Instituut voor
Kern- en Stralingsfysica
Departement Natuurkunde
en Sterrenkunde
Faculteit Wetenschappen

KATHOLIEKE UNIVERSITEIT
LEUVEN

Ion implantation in Ge:

Structural and electrical investigation of the induced lattice damage & study of the lattice location of implanted impurities.

promotor:
prof. dr. A. Vantomme

co-promotor:
dr. U. Wahl

Proefschrift ingediend tot
het behalen van de graad van
doctor in de wetenschappen
door

Stefan Decoster

2009

Instituut voor
Kern- en Stralingsfysica
Departement Natuurkunde
en Sterrenkunde
Faculteit Wetenschappen

KATHOLIEKE UNIVERSITEIT
LEUVEN

Ion implantation in Ge:

Structural and electrical investigation of the induced lattice damage & study of the lattice location of implanted impurities.

promotor:
prof. dr. A. Vantomme

co-promotor:
dr. U. Wahl

Proefschrift ingediend tot
het behalen van de graad van
doctor in de wetenschappen
door

Stefan Decoster

2009

ISBN 978-90-8649-239-8
D/2009/10.705/17

Dankwoord

Deze doctoraatsthesis is het resultaat van vier jaar onderzoek in de wereld van de halfgeleiders en met het schrijven ervan, wordt een belangrijk hoofdstuk uit mijn leven afgesloten. Alhoewel enkel mijn eigen naam als auteur op de kaft van deze thesis te vinden is, ben ik heel wat dank verschuldigd aan andere mensen. De eerste pagina's van dit werk wil ik dan ook graag aan hen opdragen.

Eerst en vooral wil ik mijn twee 'bazen' bedanken. André en Uli, Dankzij jullie heb ik de kans gekregen om me de voorbije vier jaar volledig uit te leven in de wereld van de experimentele fysica. Ik ben jullie zeer dankbaar voor de steun en het vertrouwen dat jullie getoond hebben door me vrij te laten in mijn keuzes tijdens het onderzoek. Uiteraard ben ik ook dankbaar voor de hulp als het eens wat slechter ging, en vooral voor de tijd die jullie de voorbije vier jaar in mij geïnvesteerd hebben, enerzijds voor het nalezen en verbeteren van abstracts, lezingen, proposals, projecten en artikels, en anderzijds voor de vele wetenschappelijke maar ook de niet-wetenschappelijke discussies.

I would like to thank the members of the jury prof. dr. Kristiaan Temst, prof. dr. Wilfried Vandervorst, dr. Stefaan Cottenier, prof. dr. Michel Houssa, prof. dr. Reiner Sielemann, dr. Ulrich Wahl and prof. dr. André Vantomme for the effort of reading this thesis and for the interesting discussion during the preliminary defense.

A large part of this work has been performed at institutes outside of Leuven. The emission channeling experiments have been performed at the ISOLDE facility in CERN, where many colleagues helped me with the 'radioactive' implantations and with the actual measurements. I would like to thank Guilherme and Uli to supervise the experiments, and of course also all the other (Portuguese) colleagues who helped during the several beam times over the past few years: Lino, Sergio, Tania, Elisabete, Ana Claudia, Dina, Ligia, Carlos, ... Muito obrigado! Een speciaal dankwoordje voor Bart is hier ook op zijn plaats, aangezien hij mij enorm

geholpen heeft tijdens mijn eerste stappen in de emissiekanalisatie-wereld.

Furthermore, I would like to thank my colleagues from the University of Pretoria for their major contribution in our successful collaboration about the electrical defect characterization in germanium. I really learned a lot during my 4 weeks stay in Pretoria and your hospitality was unforgettable. Prof. Auret, Johan, Cloud, Sergio, Hannes en Michael, baie dankie vir die moeite en vir die lekker tyd in Suid-Afrika!

Naast deze internationale samenwerkingsverbanden, heb ik ook veel tijd gespendeerd aan experimenten in 'ons eigen' labo, het IMBL. Verschillende mensen hebben hun best gedaan om me hier het werken zo gemakkelijk mogelijk te maken. In de eerste plaats denk ik aan Annemie, Zhao en Willy die, samen met de dienst elektronica en mechanica, altijd klaar stonden om technische problemen in het labo op te lossen. Verder wil ik ook graag het volledige IT-team bedanken, en ben ik blij dat de vriendelijke dames van het secretariaat altijd klaar stonden om me gedurende de voorbije jaren door de administratieve rompslomp te leiden. Daarnaast wil ik graag Valerie en Annelies bedanken voor hun inzet tijdens hun licentiaatsthesis en Marijke voor haar enthousiasme tijdens haar zomerstage, waardoor mijn werk op bepaalde momenten aanzienlijk verlicht werd. Ook ben ik Stefaan veel dank verschuldigd voor de tijd en de moeite die hij gestopt heeft in de theoretische berekeningen die steeds met veel enthousiasme uitgevoerd werden. Verder wil ik graag alle collega's van het IKS bedanken voor de vele nuttige discussies, maar ook voor de leuke niet-wetenschappelijke momenten die ik er tot nu toe beleefd heb.

Alhoewel ik enorm dankbaar ben voor de steun die ik gekregen heb van al deze collega's, ben ik er van overtuigd dat veel meer mensen onrechtstreeks bijgedragen hebben in het tot stand komen van deze thesis. Hierbij denk ik dan vooral aan de vele kickeravonden samen met Kristof, Pauwels, Thomas en Somettie, waarop we allemaal even onze fysicagedachten konden wegsp(o)elen; aan de Bodegemse fanfare, waar ik gedurende verschillende jaren alles van me af kon blazen; aan de vol-

leyballers waarbij ik me enkele keren per week volledig kan laten gaan en aan alle andere vrienden, die ik liever niet begin op te sommen, uit schrik om iemand te vergeten. Bedankt allemaal, om de boog ook eens te laten ontspannen!

Een enorm grote dankbetuiging gaat uit naar het thuisfront. Bedankt oma, om altijd mijn grootste fan te willen zijn. Bedankt Ilse, Kristof en Tatiana, voor jullie steun en interesse. Mama en papa, bedankt voor jullie vertrouwen in mij, om me altijd te blijven steunen en om me vrij te laten mijn eigen weg te kiezen!

Het laatste dankwoordje heb ik gereserveerd voor een heel speciaal iemand. Sjattie, het is moeilijk om in woorden uit te drukken wat je voor me betekent. Je hebt me de afgelopen vier jaar zoveel liefde en steun gegeven – zelfs als ik weer eens naar Genève of naar n of andere conferentie moest tijdens je examenperiode én je verjaardag. Je bent me achterna gevlogen naar Zuid-Afrika, je hebt geduimd voor me als het spannend werd, me getroost bij slecht nieuws en meegenoten van goed nieuws. Voor dat alles wil ik je graag bedanken. Ine, ik ben er zeker van dat we samen een mooie toekomst tegemoet gaan!

Bedankt iedereen, voor alles!
Stefan

I can no other answer make, but, thanks, and thanks.
(W. Shakespeare)

Preface

This PhD-thesis is the result of 4 years of intensive research, performed at the Instituut voor Kern en Stralingsfysica (IKS) of the Katholieke Universiteit Leuven, at the Organisation Européenne pour la Recherche Nucléaire (CERN) in Geneva, Switzerland and at the Physics Department of the University of Pretoria, South Africa. This thesis has been written, based on 7 publications which have been published in, or submitted to, international peer-reviewed journals. In a first chapter, the performed research is motivated and situated within the field of semiconductor technology. This chapter is followed by the objectives of this work and an overview of the sample preparation and the experimental methods. The obtained results, as well as the discussion of these results, are briefly summarized in the body of this PhD-thesis, and are elaborately explained in the following publications, which have been added at the end of this thesis:

I **Implantation-induced damage in Ge: Strain and disorder profiles during defect accumulation and recovery**
S. Decoster and A. Vantomme
Submitted to Journal of Physics D: Applied Physics

II **Electrical characterization of defects introduced in *n*-type Ge during indium implantation**
F. D. Auret, P. J. Janse van Rensburg, M. Hayes, J. M. Nel, W. E. Meyer, S. Decoster, V. Matias and A. Vantomme
*Applied Physics Letters **89**, 152123 (2006)*

III **Electrical characterization of defects in heavy-ion implanted *n*-type Ge**

F. D. Auret, P. J. Janse van Rensburg, M. Hayes, J. M. Nel, S. Coelho, W. E. Meyer, S. Decoster, V. Matias, A. Vantomme and D. Smeets

*Nuclear Instruments and Methods in Physics Research B **257**, 169 (2007)*

IV **Experimental evidence of tetrahedral interstitial and bond-centered Er in Ge**

S. Decoster, B. De Vries, U. Wahl, J. G. Correia and A. Vantomme

*Applied Physics Letters **93**, 141907 (2008)*

V **Transition metal impurities on the bond-centered site in germanium**

S. Decoster, S. Cottenier, B. De Vries, H. Emmerich, U. Wahl, J. G. Correia and A. Vantomme

*Physical Review Letters **102**, 065502 (2009)*

VI **Lattice location study of implanted In in Ge**

S. Decoster, B. De Vries, U. Wahl, J. G. Correia and A. Vantomme

*Journal of Applied Physics **105**, 083522 (2009)*

VII **Lattice location study of ion implanted Sn and Sn-related defects in Ge**

S. Decoster, S. Cottenier, U. Wahl, J. G. Correia and A. Vantomme

To be submitted to Physical Review B

CONTENTS

INTRODUCTION

The past two decades, germanium has drawn international attention as one of the most promising materials to replace silicon in semiconductor applications. Due to important advantages with respect to Si, such as the increased electron and hole mobility, Ge is well on its way to become an important material in future high-speed integrated circuits. Although the interest in this elemental group IV semiconductor is increasing rapidly nowadays, the number of publications about this material is still relatively scarce, especially when compared to Si.

The most widely used technique to dope semiconductors is ion implantation, due to its good control of the dopant concentration and profile, and the isotopic purity of the implanted species. However, there is a major lack of knowledge of the fundamental properties of ion implantation in Ge, which has triggered the research presented in this thesis. One of the most important and generally unwanted properties of ion implantation is the creation of damage to the crystal lattice, ranging from simple point defects such as vacancies and self-interstitials, over small and large defect clusters to even fully amorphous layers of material. These structural defects give rise to electronic (deep) levels in the semiconductor band gap, altering the electrical properties of the material, eventually resulting in the degradation of the semiconductor

device.

During implantation, the energetic ions travel through the host material while losing energy and creating defects, until they come to rest and occupy a certain lattice site within the crystal structure. The exact location of the implanted ions is known to influence the (electrical, optical and magnetic) properties of the doped material to a large extent, which makes it a very important, but barely-studied topic in Ge. It is generally assumed that most impurities simply replace the Ge host atoms – i.e. they are located on a substitutional Ge site – but the lack of accurate results on this issue puts this assumption at least into question.

In this work, we present an investigation of these two important ion implantation-related issues in germanium. First of all, we will study the accumulation of, and the recovery from implantation-induced defects in Ge, both from structural and from electrical point of view. Secondly, we present a detailed lattice location study of a number of relevant and interesting impurities in germanium.

In **chapter 1**, the research presented in this thesis is situated in its scientific and technological context. First of all, the status of *germanium* throughout the semiconductor history is highlighted, starting at the late 40s, followed by its revival during the past two decades and concluding with the current issues and problems to integrate Ge in the semiconductor technology. Secondly, the most widely used technique to dope semiconductors, i.e. *ion implantation*, is put forward, emphasizing the different types of implantation-induced defects. We also present an extended overview of the current knowledge of implantation-related damage in Ge. The third section of this chapter contains an overview of the most relevant *impurities* in Ge, i.e. electrical dopants, isovalent elements, metal impurities and optical dopants. The overall objectives of the thesis are explained in **chapter 2**. The sample preparation, which includes the ion implantation and the subsequent annealing process, is presented in **chapter 3**, while **chapter 4** contains relevant information about the experimental methods that have been used in this research. First, the techniques to structurally and electrically characterize the

implantation-induced damage are introduced – i.e. Rutherford backscattering and channeling spectrometry (RBS/C), X-ray diffraction (XRD) and deep level transient spectroscopy (DLTS) – followed by emission channeling (EC) and *ab initio* calculations, which aim at studying the lattice location of implanted impurities. Finally, **chapter 5** contains a short summary and a discussion of the results that have been obtained within the framework of this research. A more elaborate explanation and discussion of the results can be found in the articles that have been published and in the manuscripts that have been prepared for publication. These articles and manuscripts are added at the end of this thesis.

CHAPTER 1

GENERAL CONCEPTS

In this chapter, the research topics of this PhD thesis are put in their scientific and technological context. The first section contains an overview of the status of *germanium* in the field of semiconductor technology throughout history. Its important contribution during the late 40s and 50s will be highlighted, as well as the revival during the last two decades. The first section is concluded with the present status of germanium, indicating the problems that need to be solved in order to integrate this material in future semiconductor applications. In the second section, the *ion implantation* technique is addressed, with special attention to the implantation-induced structural and electrical defects. Finally, the last section gives an overview of the technologically relevant and fundamentally interesting *impurities* in Ge, together with their optical, magnetic or electrical properties. Special attention will be given to the lattice location of these impurities.

1.1 Germanium

1.1.1 History

The element 'germanium' has been discovered by C. Winkler in 1886 [1] and is a group IV elemental semiconductor, similar to silicon. Despite the fact that silicon has been on a supreme position in the world of electronic circuits and devices for almost 50 years, germanium has played a very important role in the beginning of the semiconductor technology [2, 3].

During the second world war, the driving force behind the intensive semiconductor research was the need for very high frequency rectifiers and mixers to be used in radar receivers. Lark-Horovitz performed an intensive study to investigate the possibility of germanium as a rectifying material, which eventually led to the first point contact transistor. This transistor has been built by J. Bardeen and W. H. Brattain in 1947 at Bell Labs with a slab of polycrystalline germanium [4]. Shortly afterwards, W. Shockley invented the germanium junction transistor, which is seen as one of the most important events in shaping modern day life. As E. E. Haller wrote in his overview of the history of germanium [2]: *"There is the time before, and the time after this invention. It is hard to come up with any modern day activity which is not influenced by the device called the transistor."* For their discovery of the transistor effect, Brattain, Bardeen and Shockley received the Nobel Prize in Physics in 1956. In 1958, the first germanium integrated circuit (IC) was built by J. Kilby at Texas Instruments, but at that time, many of the technological difficulties inherent to silicon had already been overcome. From the early sixties, Si took its number one position in the world of IC's, mainly due to (1) its larger band gap with respect to germanium, allowing operation at higher temperatures, (2) its stable oxide SiO_2, acting as a device protection layer and as a mask during device manufacturing, (3) a very low surface state density at the SiO_2-Si interface and finally (4) its low production price and wide availability with respect to other materials, such as Ge [3].

Despite the fact that from the early sixties on, Si was basically the only substrate material used in electronic circuits, Ge was still used at that time but its area of applicability shifted mainly towards nuclear physics. Due to its high stopping power to electromagnetic radiation, its high electron and hole mobility and the possibility to grow it into large single crystals with very low impurity concentrations, Ge became the leading material in X-ray and γ-ray detectors. These ultra-pure Ge detectors were found to be extremely stable with low noise, high-speed electronics, and have remained unsurpassed in their performance. Besides its use as an X-ray and γ-ray detector, lightly-doped germanium has also been used as a far-infrared detector.

1.1.2 Revival in IC-technology

The past 40 years, the improvements in the IC-technology have been following Moore's Law: Every 18 months, the number of devices per chip and the overall performance speed are being doubled. However, the dimensions of the devices have become so small that the scaling of the dimensions is not sufficient in order to keep following Moore's law. Therefore, further improvements have to be achieved by changing the fundamental properties of the materials in the devices or by using different materials. One of these fundamental properties is the mobility of the electrons and holes in the material, which can be increased by using strained Si instead of bulk Si [5, 6]. The mobility enhancement depends on the growth method of these strained layers, i.e. with a SiGe buffer layer (strained Si on a SiGe buffer layer on insulator – SGOI) or an ultra-thin film deposited directly on the insulator (strained silicon directly on insulator – SSDOI). For SGOI structures, a 15 to 25 % enhanced drive current has been demonstrated [7], while in SSDOI structures, the electron mobility can be easily doubled, but a large amount of strain (up to 1.5 %) is required to improve the hole mobility with a factor of 1.5 [8]. However, even larger electron and hole mobility values can be achieved by using bulk Ge instead of Si or strained Si (Tab. 1.1). In

	Si	Ge
μ_e (cm^2/V s)	1500	3900
μ_h (cm^2/V s)	450	1900

Table 1.1: Electron (μ_e) and hole (μ_h) mobility of bulk silicon and germanium at room temperature [3].

other words, integrating germanium as a replacement material for Si in the IC-technology might result in an increased performance speed of the electronic devices. The past two decades, this enhanced mobility of Ge with respect to Si has raised an internationally increased interest in this material and many groups are trying to tackle the earlier shortcomings of Ge, in order to investigate the feasibility of integrating germanium in the current IC technology.

1.1.3 Current status

One of the major advantages of Si with respect to Ge has been its stable native oxide SiO_2. However, due to the device scaling, the physical dimensions of the oxide are becoming smaller than the typical electron tunneling length (3 nm). To overcome this problem, high-κ materials (such as HfO_2, ZrO_2 and LaO_2) should replace SiO_2 as a gate dielectric. However, this replacement is not straightforward, since the interface charges and the growth of an interfacial layer between the substrate and the high-κ material overcompensate the advantages of using high-κ materials in Si.

The integration of high-κ materials on Ge is less problematic than in Si, because the instability of the native Ge oxide results in a much smaller interfacial layer. This means that the early disadvantage of the unstable native Ge oxide has turned into an important advantage with respect to Si. However, before germanium can be successfully integrated in metal-oxide semiconductor field effect transistors, several important obstacles have to be overcome first. Some of these obstacles are addressed in the following paragraphs [3].

A proper passivation of the Ge surface is an important issue in Ge-based devices, since the direct deposition of the most promising high-κ materials HfO_2 and ZrO_2 has only resulted in non-functioning devices so far. Several chemical passivation methods have been used on Ge: nitridation (N), oxidation (O), oxynitridation (ON), hydrogenation (H) and passivation with sulfur (S), selenium (Se), silicon (Si) and chlorine (Cl) ([3, 9–16] and references therein).

A second problem is the high leakage current of the Ge p-n junctions which may dominate the off-state leakage of a transistor. This problem is related to the relatively small band gap of Ge (0.67 eV at room temperature), yielding a high intrinsic carrier concentration [3].

Finally, another very challenging issue concerns the overall availability of Ge. It is known that, on earth, there is not a sufficient amount of Ge available to completely replace Si. This problem needs to be overcome by using thin films of Ge instead of bulk Ge wafers. Ideally, these thin films should be integrated in the present Si-technology. The growth of these so-called Ge-on-insulator structures, preferably on Si or on SiO_2, has received much attention, and several methods have been developed for this purpose. One of them is the condensation technique, in which a SiGe-layer is grown on top of SiO_2, followed by the oxidation of this layer which results in the Ge-enrichment of the SiGe layer [17–21]. At full completion of the oxidation process, a Ge-rich layer is obtained with a concentration which can be close to pure Ge. In other methods, thin films of Ge are grown epitaxially on Si, sometimes using strained Ge buffer layers or graded SiGe layers. [22–26].

Another important drawback, which is interrelated with all previous issues, is the fact that only very recently, Ge has come into the picture as a possible replacement material for Si. This simply implies that only little information is available on the fundamental properties in Ge, as well as on the properties of Ge-based devices, especially in comparison to Si. For instance, many steps in the complete device manufacturing process have been studied very intensively in Si over the past 50 years, but are still barely studied in Ge. One of these very well studied topics

in Si is the ion implantation process, while the Ge-related information on this topic is very scarce. This will be discussed in more detail in the next section.

1.2 Ion implantation

Besides its general use of changing the physical properties of a material, ion implantation is also one of the key processing steps in the present IC technology. Most integrated circuits are processed with more than 10 implantation steps while some of them even require up to 35 steps. The unique features of ion implantation that are relevant for device fabrication are its accurate control of the fluence, depth and purity of the implanted dopants, the high processing throughput and the high reproducibility of the doping process. Moreover, this technique has played a crucial role in the device scaling, and it is still generally accepted that doping by ion implantation is the tool of choice to meet the future challenges in the evolution of the semiconductor industry. In this section, we present the concept of energy loss in ion beam-solid interactions (1.2.1), an overview of the types of implantation defects (1.2.2) and finally a summary of the available literature on ion implantation-induced damage in Ge (1.2.3).

1.2.1 Energy loss

When an energetic ion penetrates a solid, it undergoes a series of collisions and interactions with the nuclei and electrons in the target. During these collisions the incident particle loses its energy at a typical rate of 200 eV/Å, depending on the mass, nuclear charge and the energy of the incoming ion, as well as on the nuclear charge and the atomic density of the solid material. It is customary to distinguish two different mechanisms of energy loss: (1) elastic nuclear interaction, in which energy is transmitted from the moving particle to the target atom, and (2) inelastic interaction, in which the incoming particle causes excitation of target electrons, ionization of the target atom, a collective electron motion or lattice vibrations through plasmons and phonons. The relative contributions of these energy loss mechanisms depend on the energy of the incoming ion, and can be calculated with simulation programs, such as the Monte-Carlo simulation program SRIM (The Stopping and Range

of Ions in Matter [27]), which has been used in this thesis.

1.2.2 Overview of implantation-induced defects

In this thesis, we investigate structural defects in the Ge lattice, in which the host atoms get displaced from their regular lattice site. These defects can only be induced when the energy transfer from the incoming ion exceeds the displacement threshold energy. Therefore, we are mainly interested in elastic nuclear interactions, and will not go into detail on inelastic interactions. When the energy transfer from the incoming ion to a Ge lattice atom is high enough, a so-called *primary knock-on atom* is kicked from its lattice site. In turn, this primary knock-on atom can displace other atoms (secondary knock-on atoms) and so on, thus creating an atomic collision cascade. Each of these knock-on atoms will eventually come to rest, leaving an ion track behind, surrounded by several types of defects. When the implantation fluence is sufficiently high, the ion tracks and damaged regions can overlap, thus creating a more heavily damaged layer or even a completely amorphous region. The amount of defects and the relative lattice disorder (degree of crystallinity) after ion implantation depend on several parameters such as the mass and the energy of the ions, the ion current density, the implantation angle, the total implanted fluence, the substrate temperature and of course also on the radiation hardness of the material. This radiation hardness or resistance is directly related to the bond strength in the material and can be quantified by the threshold energy for displacements, which is roughly 15 eV in Ge [28]. A detailed study of the influence of the implantation parameters on the induced lattice damage is one of the main objectives of this research work.

The different types of structural defects that are created during ion irradiation of semiconductors are categorized as point defects, line defects, planar defects and volume defects and are discussed in the following paragraphs.

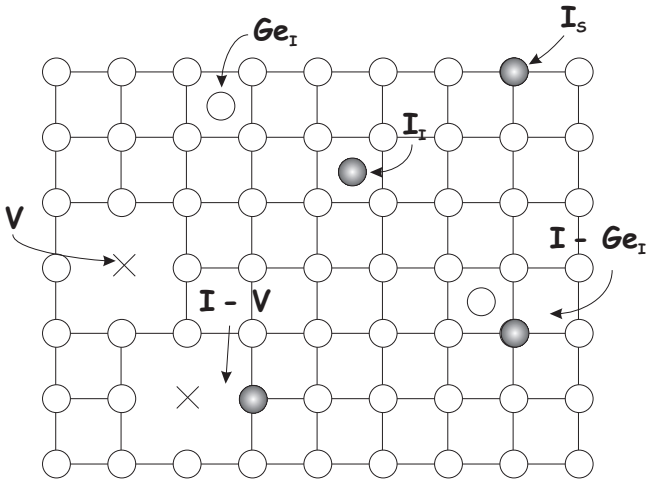

Figure 1.1: A schematic representation of several point defects: a vacancy (V), a self-interstitial (Ge_I), a substitutional (I_S) and an interstitial impurity (I_I), an impurity-vacancy (I-V) and an impurity-self-interstitial (I-Ge_I) complex. Ge atoms are represented by open circles, impurities by filled circles and vacancies by crosses.

1.2.2.1 Point defects

A point defect is a deviation in the periodicity of the lattice arising from a single point. Fig. 1.1 shows a schematic representation of a number of point defects that are discussed below.

Point defects can be sub-categorized in native defects and impurity-related defects. The simplest defects are the vacancy and the self-interstitial, which are both native defects. A vacancy (V) is an empty lattice site, while a displaced target atom, residing on a position in between the atomic positions in a perfect crystal, is called a self-interstitial (Ge_I in the case of a Ge self-interstitial). The combination of a self-interstitial and the vacancy that this atom left behind, is referred to as a Frenkel pair. When an impurity atom replaces a host atom or occupies a site in between the host atoms, it is called a substitutional (I_S) or an interstitial (I_I) impurity respectively. When a vacancy is created next to an impurity atom, it forms an impurity-vacancy (I-V) complex, and in

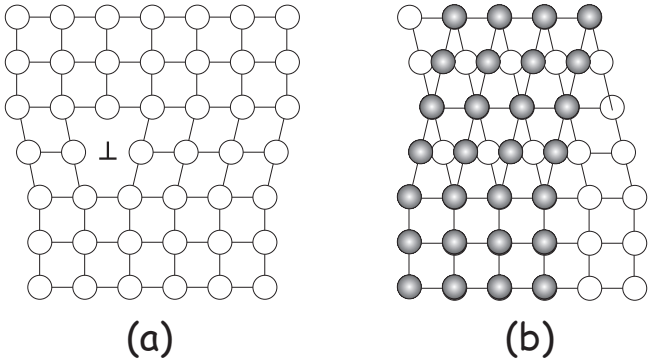

Figure 1.2: Schematic representations of (a) an edge and (b) a screw dislocation. The filled and open circles in (b) represent two planes of atoms on top of each other.

analogy, if a self-interstitial is located next to an impurity atom, it will be referred to as an impurity-self-interstitial (I-Ge$_I$) complex. The exact microscopic configuration of such impurity-related defects can vary a lot, and will be studied in this thesis.

1.2.2.2 Line and planar defects

Due to non-equilibrium conditions during ion implantation and subsequent thermal processing, also more extended defects can be produced in a crystalline material. Typical line defects that have been observed in semiconductors are edge and screw dislocations, which are schematically presented in Fig. 1.2 (a) and (b) respectively. Planar defects include so-called grain boundaries, stacking faults, twins, etc. For more information on these structures, we refer to specialized literature [29–31].

1.2.2.3 Volume defects

Extended, 3-dimensional types of defect clusters are categorized as volume defects. They can be described as irregularly shaped agglomerates of self-interstitials, vacancies and impurities, surrounded by crystalline material. A special type of volume defects are the so-called voids, which are clusters of vacancies.

All these types of ion implantation-induced structural defects drastically change the properties of the doped semiconductor, and have been intensively studied in Si by numerous groups using a wide variety of techniques, while the knowledge on this topic in Ge is rather scarce. In the next section, we present an overview of the available literature on the creation and removal of implantation-induced simple and extended defects in Ge.

1.2.3 Implantation-induced defect studies in Si and Ge

Due to its large technological significance, many groups have been investigating the ion implantation process in Si during the past 40 years, which has led to a good fundamental understanding of many implantation-related aspects. An overview of the tremendous amount of experimental results in Si, covering the influence of several implantation parameters such as the ion mass, energy, current density, substrate temperature, dopant concentration, implantation angle, ... on the accumulation of structural damage up to amorphization, as well as the influence of the annealing technique and temperature on the recovery and recrystallization of the damaged layers, can be found in review articles by Gibbons [32], Hobler and Otto [33], and Pelaz *et al.* [34]. In order to obtain a more complete understanding of the process of damage accumulation and recovery, many models have been proposed to explain and fit the experimental observations in Si [32, 35–43]. An elaborate review of these models can be found in [34].

Despite this extensive research over more than 40 years, both experimentally and theoretically, many questions about the ion implantation process still remain unanswered. This has been paraphrased in the 2001-edition of the International Technology Roadmap for Semiconductors (ITRS) as follows [44]: "*...a more detailed understanding of the implantation damage, amorphization and subsequent recrystallization is important... extensive research and model development needs to be started immediately to develop improved models for damage creation and an-*

nealing, and for temperature dependent implantation." In the 2007-edition, it was stated that "*Implantation damage, amorphization, recrystallization, and silicidation must be accurately simulated*". Hence, it can be concluded that the ion implantation process, after more than 40 years of intensive research, has not been completely understood or modeled yet, even in Si.

In comparison to Si, the information that can be found on implantation-induced structural lattice damage in Ge is very scarce. This is mainly due to the fact that by the time that the ion implantation technique was used regularly in practical applications, Si was the leading material in integrated circuit technology, with a fading general interest in Ge as a result. Although some groups have studied line and planar defects as well [45–47], in the following two paragraphs, we present an overview of the most relevant point defect studies in Ge as well as an overview of the studies on extended defects (and amorphization) after ion implantation in Ge.

1.2.3.1 Point defects

The earliest studies on point defects in Ge have been performed with electrical measurements (such as Hall measurements), and an extensive overview of these electrical data is presented in Ref. [48]. From the eighties on, deep level transient spectroscopy (DLTS) has been frequently used to characterize the electrical properties of point defects, which has been done after electron, neutron and ion irradiation in Ge [49–58]. These electrical measurements have revealed numerous defect levels (electron traps as well as hole traps) which have been related to (different charge states of) vacancies, di-vacancies, multi-vacancies, self-interstitials, di-interstitials, and other vacancy and interstitial-related defects. However, in general, it is not straightforward to attribute the measured electronic levels to specific point defects. Radioactive probe techniques, such as perturbed angular correlation (PAC) spectroscopy, have been applied to obtain complementary information about simple

defects [59–63]. In particular, the single vacancy and the germanium self-interstitial have been observed in the PAC studies. These defects were found to start migrating at 200K and 220K respectively. On the other hand, the past few years, the increased computing possibilities have resulted in many *ab initio* studies on the intrinsic properties of simple defects [64–75]. In this way, a lot of information has been gained about the electronic, structural and diffusion properties of vacancies, di-vacancies, self-interstitials and vacancy clusters.

The most relevant information on impurity-related point defects, such as impurity-vacancy and impurity-interstitial complexes, is summarized per type of impurity in Sec. 1.3.

1.2.3.2 Extended defects

The earliest relevant work on extended defects after ion implantation was done by Mayer *et al.* [76]. They implanted In ions into Ge with an energy of 40 keV and found an *amorphization threshold* (AT) of roughly 2×10^{13} – 1×10^{14} at/cm^2 from Rutherford backscattering and channeling spectrometry (RBS/C) experiments. Similar studies have been performed to determine AT values in Ge for several elements under different conditions. Sigurd *et al.* implanted 56 keV B ions, which resulted in an AT of 3.5×10^{15} at/cm^2 [77], while 300 keV Si-irradiation was found to amorphize after implanting 6×10^{13} at/cm^2 [78]. Extended X-ray absorption fine structure (EXAFS) measurements were used to investigate the AT of high-energy (1.7 MeV) self-implantation in Ge at liquid nitrogen temperature, which was found to be 1×10^{14} at/cm^2 [79]. By using focussed ion beams, Posselt *et al.* studied the amorphization process during 30 keV channeled Ga implantations and found an AT of 1×10^{14} at/cm^2. From these studies, it can be concluded that low mass implantation (B) results in a much higher AT [77]. However, due to the large variety of implantation conditions in the experiments described above, it is not straightforward to compare the other AT values with each other.

When comparing these results with corresponding amorphization threshold values in Si, it can be concluded that Ge is much more susceptible to implantation damage than Si. This has been explicitly shown by Speriosu *et al.* by comparing the implantation-induced strain [1] in Ge and Si, where similar strain values were observed for a fluence which is about 20 times larger in Si [80]. Furthermore, Lie *et al.* found an amorphization threshold which is roughly 15 times larger in Si than in Ge [78]. From molecular dynamics simulations, this large difference between Si and Ge has been explained by the higher energy density in the Ge cascades and by the lower melting temperature of Ge [81].

Several groups have investigated the influence of specific implantation parameters on the induced lattice damage. From these studies, an increased *substrate temperature* during implantation is known to cause a drastic decrease of the amount of lattice damage [77, 82]. Furthermore, the influence of the *current density* is small at room temperature, but plays an important role at elevated temperatures [82, 83]. Shallow B and P implantations – i.e. at very low *energy* (a few keV) – have been studied by Simoen and Satta *et al.* [84–86], while very high energy implantations (600 MeV Au ions) were found to create so-called thermal spikes (i.e. local regions of instantaneously melted Ge) [87]. However, the influence of the implantation energy on the crystal damage has not been studied in detail yet. Since all of the above-mentioned studies mainly consist of isolated experiments, it is clear that there is still a large knowledge gap on the role of several implantation parameters in the damage accumulation process in Ge.

Finally, a few groups have investigated the *annealing behavior* of damaged and amorphous Ge layers. Mayer *et al.* observed complete recovery of the damage for a low fluence implanted sample after annealing at 180 °C, while 380 °C was required for a high fluence implanted sample. These results have been attributed to the recovery of isolated dam-

[1] Ion implantation is known to create a locally strained or deformed crystal lattice, which is attributed to the presence of a large amount of simple defects in the crystal after implantation.

age clusters and to the recrystallization of an amorphous layer, respectively [76]. Similar results were found by Kräutle, i.e. recrystallization of the amorphous Ge layers starts after annealing at 400 – 500 °C [88]. Finally, from positron annihilation spectroscopy experiments, complete recovery of the damaged Ge samples was found after annealing at 500 °C [89]. From these results, it can be concluded that the damage recovery in Ge occurs at much lower temperature than in Si, where typically temperatures of 800 – 900 °C are required.

In general, we can conclude that the information on ion implantation-induced damage in Ge is still relatively scarce, and consists mainly of isolated studies, in particular with respect to the characterization of extended defects.

1.3 Impurities in Ge

The most important impurities in group IV elemental semiconductors are the group III and group V elements, which are used as electrical dopants. However, as will be explained in this section, other impurities can play a crucial role in semiconductors as well. Here, we present a summary of the most interesting properties of a variety of technologically relevant and fundamentally interesting impurities. Since the exact position of the impurities within the Ge crystal lattice determines their electrical, optical and magnetic properties, the lattice location of impurities is an important issue in semiconductors and will be given special attention in this section. Therefore, the first part of this section is attributed to an overview of the high-symmetry sites in a diamond lattice crystal. Subsequently, the basic properties of group III and group V impurities will be summarized, with special attention to indium. The next element that will be discussed is tin, which is a group IV element and consequently an isovalent impurity in germanium, making it fundamentally very interesting. The third group of impurities are the metal impurities, which can be effective lifetime killers and act as leakage current centers due to the introduction of deep electronic levels in the band gap of the semiconductor. Finally, potential optical dopants are highlighted.

1.3.1 Diamond lattice sites

Similar to silicon, germanium has a diamond lattice structure, which means that in a perfect crystal, all Ge atoms are tetrahedrally bonded. The lattice sites with the highest symmetry in the (110)-plane of a diamond crystal are shown in Fig. 1.3. The S (substitutional) sites are the sites which are occupied by Ge atoms in the case of a perfect crystal. When impurities are present in the crystal, they can be located substitutionally – i.e. on an S site – or interstitially – i.e. in principle anywhere in the crystal. Due to symmetry reasons, some interstitial sites are more likely than others. The most interesting interstitial positions

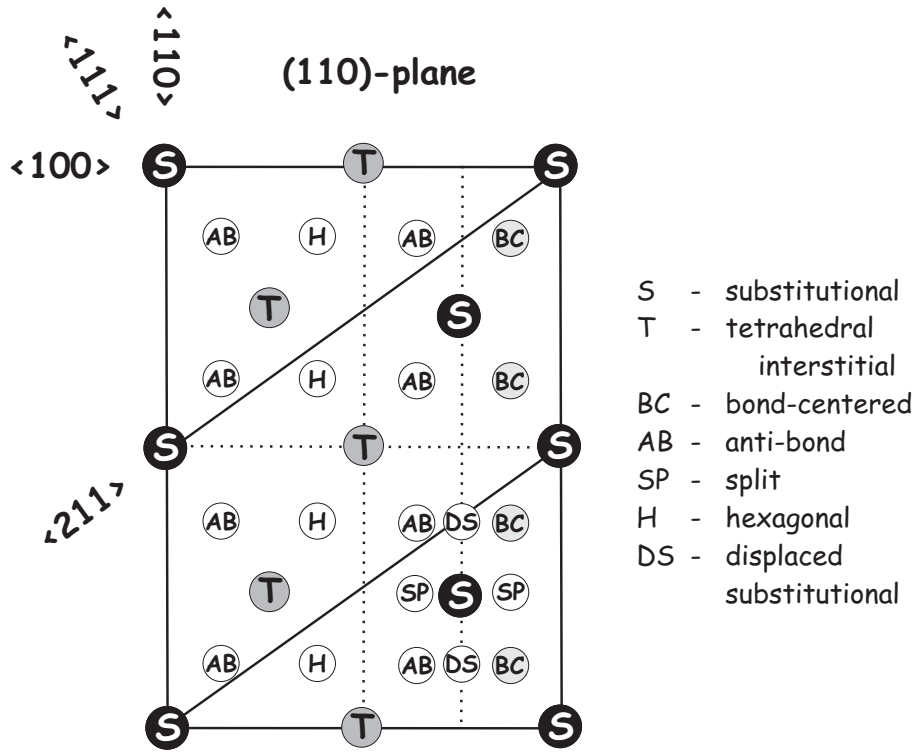

Figure 1.3: An overview of the high-symmetry sites in the (110)-plane of a diamond lattice crystal.

relevant for our work, are the tetrahedral interstitial (T) site, which is the only tetrahedrally symmetric interstitial site, and the bond-centered (BC) site, which is the site exactly in the middle of two nearest neighbor substitutional sites.

1.3.2 Group III and V impurities

1.3.2.1 Electrical properties

The most studied impurities in elemental group IV semiconductors are the group III and group V elements, which are the electrical dopants. Group III elements (B, Al, Ga and In) lack one valence electron with respect to Ge and are called acceptors or p-type dopants, while the group

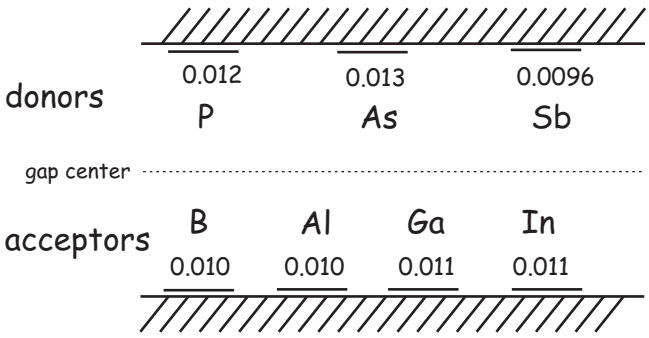

Figure 1.4: Ionization energies (eV) for substitutional donors and acceptors in germanium [90]. The energy values are relative to the conduction band in the case of donors and relative to the valence band for the acceptors.

V elements (P, As and Sb) have one extra valence electron and are called donors or n-type dopants. The shallow donor and acceptor levels in the band gap of the doped semiconductor are crucial in the working principle of diodes and transistors. This has been known since the fifties, which has resulted in many electrical characterization studies of these dopants both in Si and in Ge. Accurate values of the ionization energies of the group III and group V dopants in Ge have been summarized by Burton [90], and are shown in Fig. 1.4.

1.3.2.2 Diffusion and solid solubility

The ionization energies, shown in Fig. 1.4, are relatively close to each other, and consequently other properties will determine which electrical dopants are the most useful ones. Two such properties are the diffusion mechanism and the solid solubility of the dopant in germanium [3]. The solid solubility is defined as the maximum concentration of a certain impurity in thermodynamic equilibrium with the liquid phase of a material. In the early days of germanium crystal growth development, a substantial amount of data has been gathered on this topic. In Tab. 1.2, the solid solubility of some common dopants in Ge are summarized, showing that for the p-type dopants, Al and Ga have the best characteristics,

	Dopant	Maximum equilibrium solid solubility (at/cm^2)
p-type	B	5.5×10^{18}
	Al	$\sim 4 \times 10^{20}$
	Ga	4.9×10^{20}
	In	$\sim 4 \times 10^{18}$
n-type	P	2.0×10^{20}
	As	8.1×10^{19}
	Sb	1.2×10^{19}

Table 1.2: The maximum equilibrium solid solubility of the group III and group V dopant impurities in Ge [3].

while P and As have the highest solid solubility of the n-type dopants.

A large amount of diffusion data is available in literature, and an elaborate overview of diffusion-related properties of group III and group V elements in Ge can be found in [3]. Although both types of dopants diffuse through the vacancy-mediated mechanism, group III elements are known to diffuse typically 100 times slower than group V elements, which is related to the attractive Coulomb interaction between a positive group V impurity and a negatively charged vacancy [3, 91].

Currently, the most suitable p-type dopant in Ge is boron, since both a shallow junction (due to the low diffusivity) and a high electrical activation has been realized [92–95]. However, its major problem is the relatively low solid solubility with respect to other p-type dopants.

Due to the much higher diffusivity, the quest for a suitable n-type dopant is more problematic. So far, the most promising results have been obtained with phosphorus, despite its high diffusivity and the large difference between the chemical solid solubility and the maximum number of electrically active dopants. The past few years, many studies have been trying to solve these issues [92, 96–102].

1.3.2.3 Lattice location studies

Despite the influence of the lattice site of the dopants on the electrical properties of the doped semiconductor, not much is known about the lattice location of dopants in germanium. Some early work has been done with RBS/C, but only elements which are heavier than Ge have been considered in these studies [2]. The majority of the implanted In and Sb atoms were found on the substitutional site [103,104]. A few years later, Chemin *et al.* performed an ion-induced X-ray study, revealing that the majority of implanted P was located substitutionally as well [105]. This substitutional fraction was dependent on the implanted fluence, resulting in a decrease (from 93% to 67%) with increasing fluence (from 0.7 to 2.4×10^{15} at/cm^2).
Although it is generally accepted that the majority of the electrical dopants are located substitutionally, for most of the dopants there is still no direct evidence of their exact lattice location in the germanium crystal.

1.3.2.4 Dopant-related defects

Dopant diffusion is believed to be mediated by vacancies. Moreover, ion implantation is the most widely used technique to dope semiconductors and creates many vacancies in the implanted material. For these two reasons, many groups have studied donor-vacancy (*E center*) and acceptor-vacancy complexes. Most of the experimental results on this topic have been achieved with capacitance techniques such as DLTS, in order to determine the electrical defect levels of these dopant-vacancy complexes in the Ge band gap [102,106–109]. These DLTS experiments have been complemented with many theoretical calculations to study the electrical (binding energy, formation energy and electronic activation)

[2] The RBS spectrum of a Ge sample, doped with a heavy impurity, consists of a continuous Ge signal and a separated impurity signal. When doped with an impurity that is lighter than Ge, both signals overlap and the relatively small impurity signal has a very high background from the Ge signal, which makes it very hard to extract information about light impurities in Ge with RBS measurements.

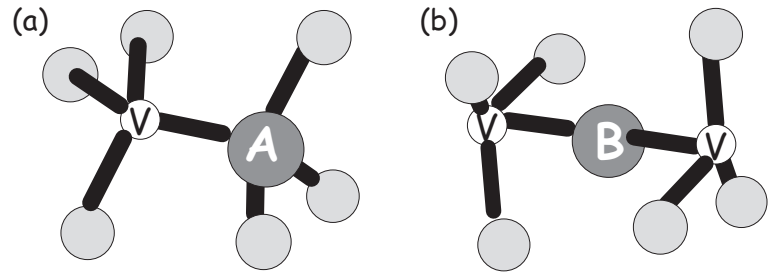

Figure 1.5: Two possible microscopic configurations of an impurity-vacancy complex: (a) The *full-vacancy* configuration with the impurity (A) on a substitutional site and a vacancy (V) as nearest neighbor and (b) the *split-vacancy* configuration with the impurity (B) on a bond-centered site with two nearest neighbor vacancies (V).

and structural properties (structural configuration, migration, stability and concentration) of these dopant-related defects [67, 110–118].

An issue that requires some extra attention in the framework of this research, is the structural configuration of these well studied impurity-vacancy complexes. There are two obvious configurations for these impurity-vacancy complexes, although other configurations can not be explicitly excluded. First of all, the *full vacancy* configuration simply consists of a substitutional impurity atom and a nearby vacancy, as shown in Fig. 1.5 (a). The second configuration (Fig. 1.5 (b)) is the so-called *split vacancy* configuration, where the impurity is displaced towards the bond-centered site and has two vacant S sites as nearest neighbors, resulting in a six-fold coordinated environment. Höhler *et al.* calculated the microscopic structure of these dopant-vacancy complexes, which resulted in the full-vacancy configuration for dopants with a Z-value smaller than Ge (Al, P, Ga and As), while the so-called *oversized* dopants In and Sb were part of a split-vacancy configuration [110–112]. Similar calculations have been performed by Coutinho *et al.* for n-type dopants, and they found that the P-, As- and Sb-vacancy complexes prefer the full-vacancy configuration [67, 114]. By comparing the results from Höhler *et al.* and from Coutinho *et al.*, it can be noted that conflicting results have been obtained for the Sb-vacancy complex. According

to Coutinho *et al.* the discrepancies between the results of both groups for Sb can be attributed to the limited size of the supercell and the k-point sampling method used by Höhler.

1.3.2.5 Indium

Indium is one of the impurities in Ge that have been studied in detail during this PhD work. Therefore, we present an extended overview of the available literature on the lattice location of In atoms in Ge, as well as on the properties of indium-related defects. As mentioned before, early RBS/C experiments have shown that the majority of the In atoms occupy the substitutional site [103, 104]. Furthermore, other techniques, such as perturbed angular correlation (PAC) spectroscopy, have been used to study implanted In atoms in a Ge crystal. Since the radioactive ^{111}In isotope is the most widely used probe for PAC spectroscopy, this technique has led to a number of detailed studies on the local environment of implanted In atoms in many materials, including Ge [59, 61–63, 119–122]. It actually probes the surroundings of the daughter atom ^{111}Cd, but due to the very small recoil energy (< 1 eV) during the radioactive $^{111}\text{In} \rightarrow {}^{111}\text{Cd}$ decay in comparison to typical lattice binding energies (10 – 20 eV), ^{111}Cd will inherit the lattice location of its precursor ^{111}In. After annealing the ^{111}In implanted Ge sample up to 600 °C, no interaction frequency was found in the PAC spectra, showing that all In atoms occupy sites with perfect cubic charge symmetry. Electron irradiation as well as ion irradiation of the annealed ^{111}In-doped Ge samples revealed two main defects: one which has been attributed to the In-vacancy (In-V) defect and another one attributed to a defect complex involving an In atom and a Ge self-interstitial (In-Ge$_I$). Both defects have an electric field gradient orientation along the $\langle 111 \rangle$-direction and disappear in the temperature range of 110 – 210 °C. Deep level transient spectroscopy measurements were used in combination with PAC, to determine the electrical levels in the Ge band gap related to In defects [63,123]. This resulted in a level at $E = E_V + 0.33$,

which has been assigned to the In-V defect.

1.3.3 Group IV impurities: Tin

Sn is a group IV element, similar to Si and Ge, which makes it a very interesting impurity in group IV semiconductors. Due to similar chemical properties, Sn impurities are expected to behave similarly to Ge lattice atoms, but are much easier to study. In particular, diffusion of Sn has been investigated to obtain information on Ge self-diffusion. Moreover, the investigation of Sn-related defects in Ge is a technologically important issue since Sn_xGe_{1-x} was found to be the first direct band gap semiconductor composed entirely of group IV elements [124–127]. The range of its band gap (between 0 and 0.67 eV) makes Sn_xGe_{1-x} a very interesting material for infrared applications, especially at low Sn concentrations ($x < 0.20$). Recent theoretical calculations indicate that strained Sn_xGe_{1-x} exhibits enhanced electron and hole mobility in the dilute limit ($x \approx 0.10$), which could make this alloy also interesting for high speed integrated circuits [128].

So far, only few groups have studied the diffusion properties of Sn in germanium. The most recent data have been obtained from secondary ion mass spectrometry studies, in which activation energies of 3.05 eV [129] and 3.26 eV [91] were found for diffusion of ion implanted Sn and for in-diffusion of a deposited Sn-layer, respectively. Very recently, electronic structure calculations were performed by Chroneos *et al.* to calculate the activation enthalpy of vacancy-mediated diffusion of Sn in Ge [130]. This resulted in an activation energy of 3.26 eV, in very good agreement with the experimental data [91, 129]. Besides these studies, Riihimäki *et al.* have investigated the diffusion properties of radioactive Sn isotopes and explained them by assuming an attractive elastic interaction between the Sn atoms and vacancies. They also proved that Sn diffusion is mediated by vacancies, and that the Sn-vacancy complexes are negatively charged in Ge [131, 132].

Similar to the results of the dopant-vacancy complexes, calculations by

Höhler *et al.* suggest that the Sn-vacancy complex prefers the split-vacancy configuration (Fig. 1.5 (b)), i.e. with the Sn atoms on the bond-centered site [112]. However, so far, there has been no experimental evidence of bond-centered Sn atoms in Ge. So far, most of the experimental information about the lattice site location of Sn in Ge is obtained from Mössbauer experiments. Weyer *et al.* found, by combining Mössbauer spectroscopy (MS) and channeling experiments, that 90% of the implanted ^{119m}Sn atoms were located substitutionally [133]. After implanting ^{119}In and ^{119}Sb as precursors for Sn, the MS data consist of several contributions (resonances) with the major one attributed to substitutional Sn and the smaller ones to isolated interstitial Sn atoms and Sn-vacancy (Sn-V) complexes in the split-vacancy and the full-vacancy configuration [134–136]. However, it should be noted that from Mössbauer experiments only, it is not possible to unambiguously determine the microscopic configuration of such defect complexes.

1.3.4 Metal impurities

Unlike the group III and group V elements, which are used as electrical dopants, transition metals are detrimental in semiconductor technology. This is due to the fact that most transition metals generate *deep* electronic levels in the band gap of silicon and germanium, which act as generation, recombination or trapping centers for the charge carriers. Typically, metals have a high diffusivity, which means that they can be easily integrated from the surface during one of the many process steps of the device manufacturing that require heating. In addition, they have a low solid solubility, which enhances precipitation during cooling. Consequently, one of the most important issues regarding metals, is their *gettering*, or their removal from the device areas. However, this gettering is not straightforward, since metals can be introduced in various processing steps such as gate dielectric deposition, germanidation, metallization and even during crystal growth or polishing [3]. Besides gettering, another means to deactivate the metals is passivation, which

has only been proven successful for Cu [137, 138]. The information presented in this section, has been mainly extracted from Ref. [3], where an elaborate overview on metals in germanium is presented. In the next sections, we present a brief summary of the most important metal impurities in Ge, including information on their electronic properties and on their lattice location within the Ge single crystal.

1.3.4.1 Relevant metal impurities in Ge

Since some metals are more likely to be introduced in the working area of the Ge device than others, and since there are large differences in their impact on the device properties, not all metals are equally important. Here, we will briefly summarize the most relevant ones.

First of all, the most widely studied metal impurity in Ge is *Cu*, which can be introduced during many process steps, and in particular during wafer polishing. Cu is known to have a very high diffusivity, and this element is a text book example of the dissociative diffusion mechanism (or the Frank-Turnbull diffusion mechanism), where a substitutional impurity diffuses interstitially throughout the lattice crystal, while leaving a vacancy behind, until it replaces a Ge host atom [139]. *Ag* and *Au* belong to the same group of elements (1B metals) as Cu, and have been studied specifically for their interesting amphoteric behavior, i.e. they behave as triple acceptors, but have a donor level as well [140–143]. Moreover, Au has been important in Ge-based infrared detectors as will be briefly explained in Sec. 1.3.5. Another thoroughly investigated element in Ge is *Ni*, which has a high diffusivity (comparable to Cu) but a lower solid solubility, which makes it somewhat more complex to study. It is known to be a fast diffuser, via the dissociative mechanism and has received much attention as one of the most promising ohmic contact elements in Ge devices [144]. Due to their low solubility and high diffusivity, other important metals such as *Fe, Co, Mn, Ti, V, Zr* and *Cr* are even harder to investigate and consequently the available data on these impurities are rather scarce. The magnetic properties of Cr, Mn,

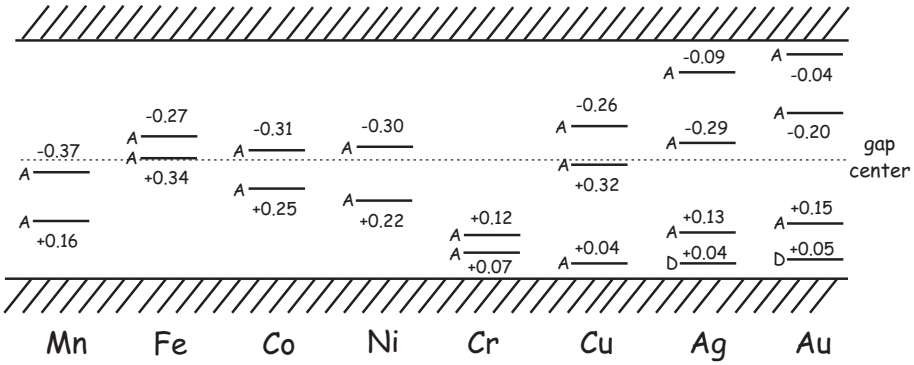

Figure 1.6: The deep acceptor (A) and donor (D) levels in the Ge band gap induced by substitutional Mn, Fe, Co, Ni, Cr, Cu, Ag and Au impurities [3, 155]. The energy values (eV) are given relative to the valence band when positive, and relative to the conduction band when negative.

Fe and Co and the possible use of these metals in Ge to create diluted magnetic semiconductors is beyond the scope of this work and will not be highlighted here. For more information, the reader is referred to the literature [145–154].

1.3.4.2 Electrical properties

As mentioned before, most metal impurities create deep energy levels in the Ge band gap and are therefore detrimental to the device operation. In Fig. 1.6, these induced energy levels are depicted schematically for a number of substitutional metal impurities. From this figure, it is clear that the group 1B metals Cu, Ag and Au are triple acceptors [140, 155], while Ag and Au also have an extra donor level. This is in accordance with the simple picture that these elements, which have one valence *s* electron in the outer shell, want to give up this electron to get the closed shell configuration, or want to take up three electrons to be tetrahedrally bonded on the substitutional site. The general chemical trend of the electronic levels in the band gap for the 1B metals is clear: For heavier (and larger) elements, the corresponding level is shifted away

from the valence band. Extrapolating this trend to Cu, its missing donor level is likely to be in the valence band, and therefore invisible for most experimental techniques. As expected, most other metals (Mn, Fe, Co, Ni and Cr) are found to be double acceptors [155], due to the two $4s$ electrons in the outer shell. In Zr, three electron levels were found [156,157], while for Ti and V, no unambiguous metal-related deep levels have been found yet [140].

1.3.4.3 Lattice location studies

The lattice location of metals is known to play a major role regarding their electrical activity. All levels in Fig. 1.6 are attributed to substitutional impurities, but when these impurities would be located on interstitial sites, their electrical behavior – and consequently electrical activity – could completely change. Although not yet proven, influencing the lattice location of metal impurities could be a promising method to deactivate these unwanted impurities.

From electrical measurements (mostly Hall and DLTS measurements), most of the metal-related energy levels have been attributed to substitutional impurities ([143,158,159] and references therein), in accordance with the simple valence model. Only for Cu, an energy level has been attributed to interstitial Cu as well [160]. Based on these studies, the overall picture that emerged, is that the majority of metal impurities occupy the substitutional site in germanium. However, other studies have shown that this is not always correct.

First of all, most metals are believed to diffuse through the dissociative mechanism, in which the substitutional impurity diffuses interstitially through the crystal, until it encounters a vacant site. This would mean that interstitial metals are present during diffusion, while no deep energy levels have been attributed to interstitial metals yet – with the exception of Cu. This could indicate that interstitial metals are invisible to techniques which only probe the electronic levels in the Ge band gap, or that they exist in much lower concentrations than the substitutional

ones, which makes them very difficult to detect.

Other experimental techniques have been applied to metal-doped Ge, in order to study the lattice location and local environment of the metal impurities. Here we will only give examples for Fe and Cu. Mössbauer spectroscopy experiments after recoil implantation of ^{57m}Fe [161] and ion implantation of ^{57}Mn in Ge [162] have revealed that the Fe atoms also partly occupy the T site and a third site believed to be related to Fe_i-V complexes. For Cu, emission channeling experiments have revealed a large fraction of ion implanted ^{67}Cu on the substitutional site, together with a smaller fraction located halfway between the substitutional and the bond-centered site [163]. Finally, from the computational side, *ab initio* calculations have been performed in order to calculate the preferred lattice site of metal impurities. These studies indicate that the S site is favored over the T site for 3d-transition metals in Ge as well as in Si [148, 164].

1.3.5 Optical dopants

Besides its application as an effective X-ray and γ-ray detector, germanium has also been used as a far-infrared photodetector, when doped with metal impurities. The photoconductivity, where an electron or a hole is released from a deep (impurity) level by absorption of a photon, has been investigated with Cd, Hg, Zn and Au as impurities, with the two latter being the most suitable ones [165–167].

More recently, Er has also received some interest as a possible optical dopant in germanium. During the past decades, the optical properties of Er integrated in semiconductors have been of great interest for photonic applications, especially in Si since the wavelength of the $^4I_{13/2} \rightarrow ^4I_{15/2}$ transition of the Er^{3+} ion corresponds to the minimum absorption of silica-based optical fibers. The properties and dependencies of the luminescence in Er-doped Si and Si-based materials have been investigated intensively. However, due to the so-called thermal and concentration quenching, its room temperature luminescence yield remains

below needs [168].
In the search for alternative semiconducting host materials, the Ge:Er system first received little attention because bulk Ge has a band gap (0.67 eV) which is smaller than the energy corresponding to the technologically interesting optical emission wavelength of Er, i.e. 1.54 μm (0.80 eV). This results in a large self absorption and consequently a very low efficiency. However, by using Ge nanoparticles, it has been shown that it is possible to tune the band gap with the size of the nanoparticles, and thus to reduce the interband absorption [169]. The stronger quantum confinement effect and a better controlled oxidation with respect to Si, makes Ge a very promising candidate as an Er-host for future photonic applications [170, 171]. Some studies have been performed on the luminescence properties of Er-doped Ge-nanoparticles [169, 172, 173], as well as on the annealing behavior of highly Er-doped Ge [174]. However, several fundamental questions remain unsolved, such as the exact lattice location of the Er atoms, which largely influences the luminescence properties in semiconductors. In silicon, the Er atoms have been found on the T site from emission channeling experiments [175,176] and several first-principles calculations [177–179], while other studies suggested Er atoms on the substitutional (S) site and the hexagonal (H) site [180,181]. In Ge, the only study on the lattice location of rare earths, is the work of Yamamoto *et al.*, who concluded from He channeling experiments that 25% of implanted Tm occupies the T site [182].

1.3.6 Other impurities

Besides electrical dopants, metal impurities and optical dopants, many other impurities have been studied as well. Oxygen and oxygen-related defects such as the oxygen-vacancy, oxygen-self-interstitial and vacancy-di-oxygen defect, have been investigated experimentally (DLTS) as well as theoretically [3,183–187]. Furthermore, a number of hydrogen, carbon and nitrogen-related studies have been performed in Ge and we refer to literature for more details on these studies [3].

CHAPTER 2

OBJECTIVES

The introduction of dopants in semiconductors is a crucial issue in the integrated circuit technology, and the most widely used technique to do so is ion implantation. As presented in the previous chapter, ion implantation in Si has been studied very intensively, however, without reaching a complete understanding of the implantation process. In germanium, which could become an important material in future semiconductor applications, the picture is even more incomplete – a huge knowledge gap of ion implantation-related topics urgently needs to be filled.

In this thesis, our goal is to investigate two important aspects in the ion implantation process in Ge. During implantation, impurities are introduced into the semiconductor material, while creating a considerable amount of (unwanted) damage to the crystal lattice. The first part of this work is dedicated to the characterization of this induced lattice damage, both structurally and electrically. Secondly, we want to investigate the final lattice site of a well-considered selection of implanted impurities in the crystal lattice, which is crucial information in order to understand and to tune the electrical, optical or magnetic properties of the doped semiconductor.

More specifically, we want to investigate the implantation induced damage accumulation up to amorphization as well as the recovery from this damage in germanium. One of our main goals is to determine the role of several implantation parameters such as the total fluence, the energy and mass of the implanted ions and the current density during implantation. The emphasis of this work is put on the structural characterization of the damage, which is done by determining the amount of displaced host atoms and the induced lattice strain in the implanted material. In cooperation with the group of prof. D. Auret (University of Pretoria, South-Africa), we also aim to study the electrical defects after ion implantation, in order to obtain complementary information about the implantation-induced defects, by measuring the induced energy levels in the band gap of germanium.

The second implantation issue that we want to address, is the lattice site location of several important impurities in germanium. More specifically, we want to study the transition metals *iron*, *copper* and *silver* because of their detrimental electrical behavior in germanium (and in semiconductors in general), *erbium* due to its interesting potential as an optical dopant in Ge nanocrystals, *indium* due to its electrical properties, which makes it a possible *p*-type dopant and finally *tin*, which is a fundamentally very interesting impurity due to its isovalency with germanium.

Ultimately, our research should lead to a better understanding of the damage accumulation process during ion implantation and the subsequent damage recovery, together with a thorough understanding of the influence of specific parameters on the implantation process. We also aim to comprehend the microscopic behavior of impurities in germanium, which could possibly lead to the observation of general trends throughout the periodic system of elements. Summarizing, in this thesis, we aim at extending the fundamental knowledge about two important implantation-related topics in germanium: the implantation-induced lattice damage and the lattice location of implanted impurities.

CHAPTER 3

SAMPLE PREPARATION

In this chapter, we briefly explain the ion implantation process and annealing procedures that have been used in this thesis. In the first section, the basic steps in the ion implantation process are highlighted, followed by an overview of the two experimental set-ups and the most relevant implantation parameters. The second part contains the experimental conditions of the applied annealing procedures. In the subsequent chapter 4, the experimental techniques that have been used to determine the implantation-induced lattice damage and to locate the implanted ions, are presented. All this experimental work has been performed at three different facilities:

- The implantation of **stable** ions for the structural and electrical characterization of the induced lattice damage, have been performed at the *Ion and Molecular Beam Laboratory* (IMBL) at the K.U.Leuven. Also the structural damage characterization with Rutherford backscattering and channeling spectroscopy (RBS/C) and X-ray diffraction (XRD), as well as the rapid thermal processing have been done in this laboratory.

- The electrical characterization of the implantation-induced damage, by means of deep level transient spectroscopy (DLTS) experiments, has been performed at the Physics Department of the *University of Pretoria* in South Africa, under supervision of prof. dr. D. Auret.

- Both sample preparation (i.e. the implantation of **radioactive** isotopes) and the determination of the occupied lattice sites by the impurities by means of the emission channeling (EC) technique, have been done at the *ISOLDE-facility* at the Organisation Européenne pour la recherche nucléaire (CERN) in Geneva, Switzerland.

3.1 Ion implantation

As mentioned in the previous chapter, the main objective of this research work is to investigate ion implantation-related issues in germanium. In the first part of this section, we will briefly explain the basic steps to perform an ion implantation, while the next part gives an overview of the experimental set-up of both implantation facilities at the IMBL and at ISOLDE. In the third section, the implantation parameters that have been used in this work are summarized.

3.1.1 Basic implantation steps

The ion implantation process can be divided into different process steps, starting with the production of the ions of the desired element at the ion source. The next step is the acceleration of these ions to a typical energy of a few keV up to several MeV. This is typically achieved by subjecting the charged particles to an electrostatic potential. The third step in this simplified presentation is the mass selection, where the ion beam passes through a magnet, resulting in a mass-separated beam. Choosing the appropriate magnetic field then allows to select the desired element or isotope. The final step of the implantation process is the

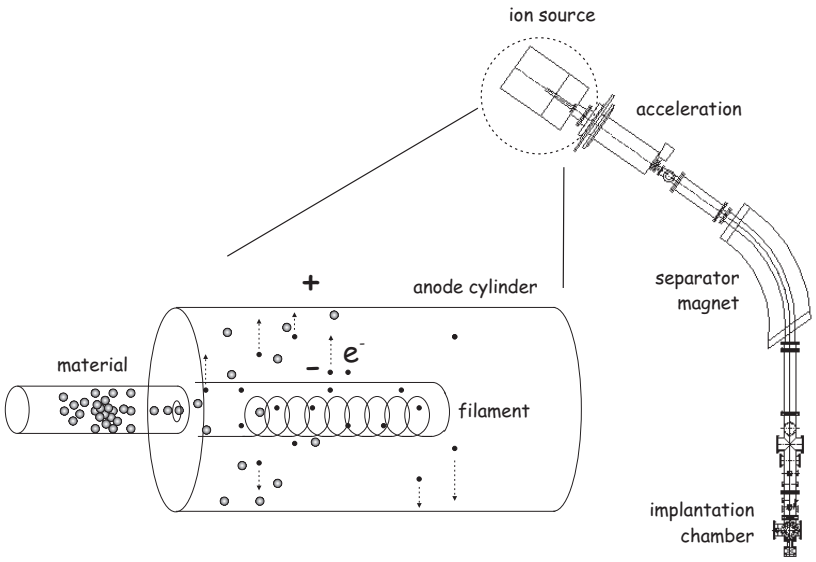

Figure 3.1: A schematic representation of the implanter at the IMBL, with a detailed view of the ion source.

actual impinging of the ions onto the target material. Deflection plates, quadrupoles and lenses are used to guide, focus and collimate the ion beam.

3.1.2 Experimental set-up

3.1.2.1 IMBL

Fig. 3.1 shows a schematic representation of the complete ion implantation set-up in the IMBL at the K.U.Leuven, showing the plasma ion source, the acceleration part, the separator magnet and the implantation chamber. The desired element (that needs to be implanted) can be in a pure gaseous, liquid or solid state or can be part of a compound. Through heating, the material is evaporated or the compound breaks up and the atoms are able to diffuse into an anode cylinder (see Fig. 3.1). Electrons emitted from a tungsten cathode filament are accelerated towards the anode and collide with the atoms, thus ionizing them and

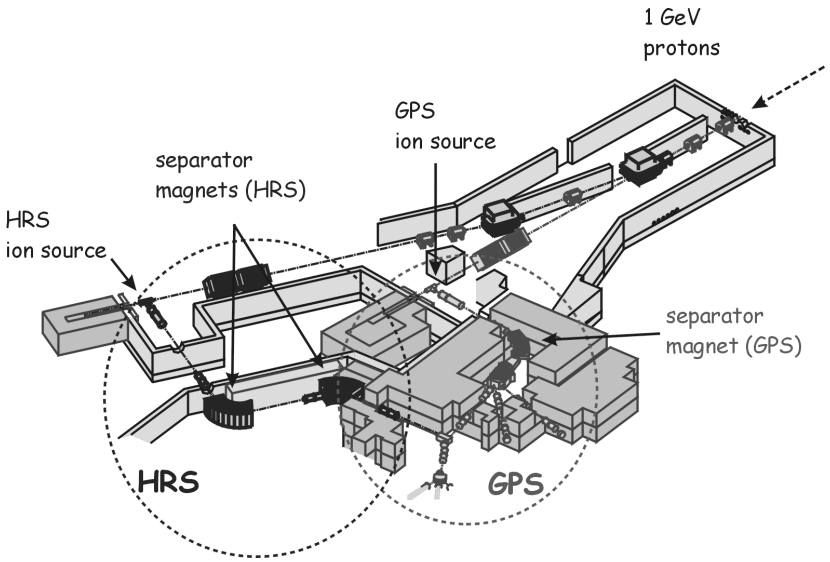

Figure 3.2: A schematic representation of the 'double' implantation facility at the ISOLDE isotope separator. High energy protons impinge on a heavy mass target at the ion source, creating a wide variety of stable and radioactive isotopes through spallation, fragmentation and fission. The desired isotope can be mass selected through the general purpose separator (GPS) or the high resolution separator (HRS) magnets.

eventually creating a plasma. From this plasma, the ions are extracted and guided towards the separator magnet, where they are separated by mass.

3.1.2.2 ISOLDE

The schematics of the implantation set-up at ISOLDE is given in Fig. 3.2. The basic implantation process consists of the same steps as presented in Sec. 3.1.1. However, since this facility uses radioactive ion beams, the ion generation process is completely different. The ion source typically contains a heavy material such as UC_2-pellets or Ta-foils. This material is irradiated with very high energy protons (1 GeV), which induce spallation, fragmentation or fission inside the ion source. In this way, a wide variety of stable, as well as radioactive atoms, are generated.

	Structural charact. [a]	Electrical charact. [b]	Lattice location of impurities [c]
isotopes	^{20}Ne, ^{40}Ar, ^{59}Co, ^{82}Kr, ^{115}In , ^{136}Xe	^{4}He, ^{10}B ^{20}Ne, ^{40}Ar, ^{76}Ge, ^{83}Kr, ^{115}In, ^{130}Xe	^{59}Mn, ^{67}Cu, ^{111}Ag, ^{111}In, ^{121}Sn, ^{167}Tm
energy	40 - 160 keV	160 keV	30 - 60 keV
angle	10°	0°	7°
fluence	5×10^{11} - 3×10^{14} at/cm^2	2×10^{11} at/cm^2	2×10^{12} - 1×10^{13} at/cm^2
current density	20 nA/cm^2 - 2μA/cm^2	$\sim$ 5 nA/cm^2	0.3 nA/cm^2 - 20 nA/cm^2
impl. area	1×1 cm^2	2×4 mm^2	0.79 mm^2

Table 3.1: Experimental implantation parameters used to study the structural (column 1) and the electrical (column 2) characterization of implantation-induced damage, and the lattice location of ion-implanted impurities (column 3) in Ge.

[a] Article I
[b] Articles II-III
[c] Articles IV-VII

The ionization of these atoms is done with different methods, depending on the desired element. The two most frequently applied methods are surface ionization, where the atoms are ionized during bouncing off a high-temperature metallic surface, and resonant laser ionization, where a laser beam ionizes one specific element in the ion beam through the stepwise excitation via two or three atomic transitions. As can be seen on Fig. 3.2, the ISOLDE facility consists of two ion source set-ups, each leading to its own mass separation system. The general purpose separator (GPS) consists of one separator magnet, while the two separator magnets of the high resolution separator (HRS) system can be used to achieve a better mass resolution.

	Structural charact.	Electrical charact.	Lattice location of impurities
supplier	Umicore	Umicore	Eagle-Picher
surface orientation	⟨100⟩	⟨111⟩	⟨111⟩
doping concentration	undoped	undoped	2-3×10^{15} Sb cm^{-3}

Table 3.2: Characteristics of the wafers used to study the structural (column 1) and the electrical (column 2) characterization of implantation-induced damage, and the lattice location of ion-implanted impurities (column 3) in Ge.

3.1.3 Implantation parameters and wafer characteristics

An overview of the implantation parameters and the characteristics of the wafers that have been used in this thesis are presented in Tab. 3.1 and Tab. 3.2 respectively. They have been divided into three groups, related to the (1) structural and (2) electrical characterization of the implantation-induced damage, for which the implantations have been performed at the IMBL in Leuven, and (3) the study of the lattice location of impurities, for which the implantation of the radioactive isotopes has been performed at the ISOLDE facility. The decay schemes of the radioactive isotopes, used in the lattice location experiments, can be found in Appendix A.

3.2 Annealing

In this research work, we have applied two different annealing procedures to the implanted samples. In order to investigate the recovery of the structural implantation-induced damage, we applied a rapid thermal annealing process. This means that the samples are annealed for only 30 s in a pure N_2-ambient, while the desired temperature is rapidly reached at a rate of 50 °C/s. Rapid thermal processing is the most widely used annealing technique in semiconductor technology due to its relatively

low thermal budget, reduced dopant diffusion, low probability of contamination and high throughput in comparison to other procedures.
To study the thermal stability of the lattice location of implanted impurities, we performed 10 min thermal annealing steps in vacuum, i.e. at a pressure $< 1\times10^{-5}$ mbar. In this way, it is possible to anneal the samples without removing them from the experimental set-up[1] (*in situ*), which is important for the sample alignment during emission channeling experiments. A similar *slow* annealing process was performed in the electrical characterization study of the lattice damage after implantation, but in an Ar-ambient instead of in vacuum.

[1] Rapid thermal processing is not possible in the experimental emission channeling set-ups.

CHAPTER 4

EXPERIMENTAL METHODS

In this chapter, we present an overview of the experimental techniques and tools, used in this work to characterize the structural (Sec. 4.1) and the electrical (Sec. 4.2) implantation-induced damage – Rutherford backscattering and channeling spectrometry, X-ray diffraction and deep level transient spectroscopy – and to determine the occupied lattice sites of implanted impurities in Ge (Sec. 4.3) – emission channeling and *ab initio* calculations.

4.1 Structural characterization of lattice damage

The implantation of ions is known to create a large amount of defects in a crystal. To quantify this lattice damage, we use two complementary techniques. First of all, the amount of displaced target atoms in the single crystal is deduced from Rutherford backscattering and channeling spectrometry (RBS/C) experiments. Secondly, since these implantation defects are known to create local lattice deformation, we use X-ray diffraction (XRD) to study the induced strain in the implanted region. Both techniques, as well as the analysis method of typical spectra are

highlighted in the following sections.

4.1.1 Rutherford backscattering and channeling spectrometry (RBS/C)

4.1.1.1 Basic principles of RBS

Rutherford backscattering spectrometry (RBS) has its roots in the famous experiment by Geiger and Marsden, where alpha particles were found to be backscattered from a thin gold foil [188]. This experiment has been explained by E. Rutherford in 1911 for the first time [189]. This technique is mainly used to characterize the compositional depth profile of a material and the thickness of thin layers.

In RBS-experiments, light ions are accelerated and lose energy by interacting with the material under investigation. As mentioned in Sec. 1.2.1, this interaction can be divided in electronic and nuclear energy loss. For relatively high energy (100 keV – MeV) light ions, the electronic energy loss predominates, while the nuclear energy loss becomes important at lower energies. Losing energy in nuclear interaction can be translated into a collision between the ion and the core of the lattice atoms. When the mass of the incoming ions is lower than the mass of the lattice atoms, these collisions can result in backscattering of the incoming ions. Moreover, the energy of the backscattered ions contains information about (1) the mass of the target atoms and (2) at what depth the collision took place (from the amount of electronic energy loss). In practice, most RBS-experiments use $^4He^+$ ions as incoming particles at an energy of 1 – 2 MeV, while in some special cases, other elements or energies can be used as well. The detection of the backscattered ions is typically done with a silicon surface barrier detector, at varying angles, according to specific needs. When a good mass resolution is required, the optimal position of the detector is as close as possible to the incoming ion beam. However, when depth information is more important, the detector is typically placed under grazing exit angles with the surface of the material under investigation. In our work, two detectors have been used

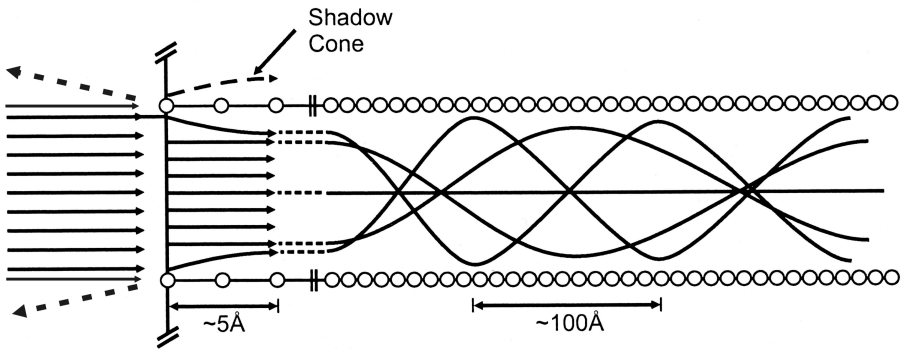

Figure 4.1: Schematic representation of the channeling effect: Incoming positively charged ions aligned with a crystallographic axis of the target material will be steered in between the rows and planes of the single crystalline material [192].

simultaneously, placed at 168° and 105° with respect to the direction of the incoming He beam.

More information about the technique itself, and a detailed theoretical description of the method, based on simple two-body collisions, can be found in literature [27, 190–192].

4.1.1.2 Channeling and RBS/C

When the trajectory of an incoming positive ion is aligned with a crystallographic axis or plane of a single crystalline target material, the repulsive force between the ion and the positively charged nuclei of the regularly-spaced atomic rows and planes of the single crystalline material will steer the incoming ion in the open space between the rows and planes through many small-angle interactions. This effect is called *channeling* and is presented schematically in Fig. 4.1. The incoming ion stays in this open channel until it encounters an obstruction or until it loses almost all of its energy through electronic stopping. This channeling effect has been theoretically described by Lindhard [193], whose work is still the basis of the analysis of modern channeling data. More information about channeling can be found in several books and arti-

cles [191, 192, 194, 195].

When using RBS in channeling geometry (RBS/C), it becomes possible to obtain structural information about the lattice. As mentioned above, when the beam of incoming He ions is aligned with a perfect single crystal axis, the channeling ions will not be backscattered and will continue to penetrate the material until they lose all their energy. However, when structural defects are present, e.g. after ion implantation, such as self-interstitials, interstitial impurities or more extended defects such as dislocations, the channels become obstructed, resulting in an increased amount of He ions that are backscattered. In this way, the backscattered yield provides information about the crystalline quality of the target material.

In order to quantify the defect density from an RBS/C experiment, it is important to note that there are two contributions to the amount of backscattered He ions: (1) A fraction of the incoming ions collides directly with defects in the lattice crystal (f_{def}) and (2) a second fraction of ions will be dechanneled (and not backscattered) from crystal impurities or defects and only collides with a lattice atom deeper into the sample (f_{dech}). Only by subtracting the fraction of dechanneled ions as a function of depth, from the total amount of backscattered He ions, it is possible to extract a quantitative profile of the amount of displaced target atoms, as will be illustrated in the next section.

4.1.1.3 Analysis of an RBS/C spectrum

Fig. 4.2 shows typical RBS/C spectra of a virgin Ge sample, measured with 1.57 MeV $^4He^+$ ions, with the detector at grazing exit angle with the sample. The spectrum with the Ge sample randomly oriented with respect to the incoming ion beam (□) will be referred to as a *random* spectrum, while the spectrum under channeling conditions (■), will be referred to as a *channeled* spectrum. As expected, the backscattered yield of the random spectrum is much higher than the yield of the channeled spectrum. By dividing both yields for a shallow depth window

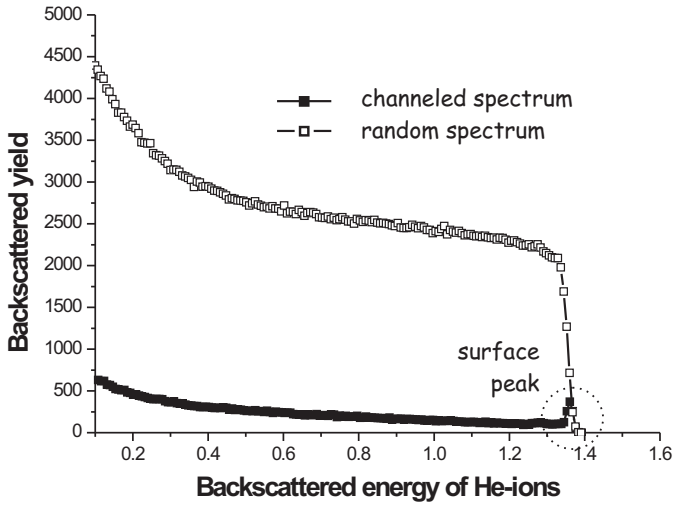

Figure 4.2: The amount of backscattered He ions as a function of energy for a virgin Ge sample. The open □ and filled ■ symbols represent the random and channeled measurement respectively.

(i.e. a narrow energy window) below the surface peak, the minimum yield χ_{min} can be obtained, which is a measure for the crystalline quality of a sample. When calculating this value for the virgin Ge sample (Fig. 4.2), we obtain a χ_{min}-value of 4.5%, which is comparable to the values obtained from high-quality single crystalline material.

The increased yield of backscattered ions, around 1.35 MeV in the channeled spectrum in Fig. 4.2 is referred to as the *surface* peak. Even when the incoming ion beam is perfectly aligned with a single crystal, a fraction of the incoming ions will impinge on the crystal surface very close to a surface atom, resulting in a large repulsive interaction between the ion and the positive nucleus of the surface atom. These ions will be backscattered, which gives rise to the surface peak[1]. This is schematically represented by the 2 dashed arrows on the left side of Fig. 4.1.

[1]To be complete, disordered surface layers can contribute to the surface peak as well.

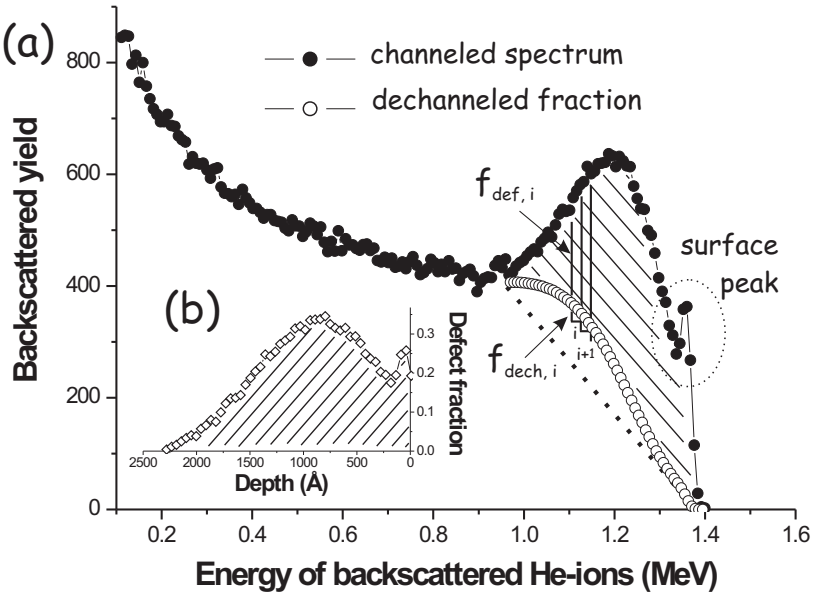

Figure 4.3: (a) The channeled spectrum (•) for a 160 keV Ar-implanted Ge sample to a fluence of 3×10^{13} at/cm^2; the total dechanneled fraction (◦), as calculated according to the procedure by Schmid [196]; the shaded part of the spectrum represents the defect fraction. (b) The defect fraction (◇), as extracted from (a) as a function of depth.

In Fig. 4.3 (a), the channeled spectrum of a Ge sample (•) is shown, after implantation of Ar ions with an energy of 160 keV to a fluence of 3×10^{13} at/cm^2. The random spectrum is comparable to the random spectrum in Fig. 4.2 and is not shown in Fig. 4.3 for the sake of clarity. Ion implantation creates damage to the crystal lattice, as is evidenced by the enhanced yield of the channeled spectrum. As mentioned above, the total amount of backscattered He ions can be divided in two contributions f_{def} and f_{dech}. As a first approximation, the total dechanneled fraction can be represented by a straight line, as shown in Fig. 4.3 (a) by the dotted line. However, it is obvious that the dechanneled fraction at a certain depth window i is related to the defect fraction in this depth

window, indicating the need of a more detailed description. Schmid [196] developed an iterative procedure to calculate the dechanneled fraction, assuming a linear relation between the dechanneled fraction and the defect fraction in a certain depth window[2] ($f_{\mathrm{dech,i}}/f_{\mathrm{def,i}} = C$), and using the straight line approximation as a first input. The iterative procedure optimizes the proportionality factor C and gives rise to a more accurate dechanneled fraction. For a more detailed explanation of this procedure, we refer to the literature [196, 197]. For our work, a C^{++} computer program has been written to extract the actual defect fraction f_{def} from the channeled spectra, based on the work by Schmid. As an illustration, Fig. 4.3 (a) shows the dechanneled fraction f_{dech} ($\circ$), derived from the channeled spectrum ($\bullet$) with this program. The shaded area in this figure represents the actual defect fraction. Finally, to reproduce the defect profile, which is shown ($\diamond$) in Fig. 4.3 (b), the energy scale needs to be converted to a depth scale. This defect fraction profile is normalized, such that 0 and 1 represent an undamaged crystal and amorphous material, respectively.

4.1.2 X-ray diffraction

4.1.2.1 Principles of XRD

X-rays are electromagnetic radiation with a wavelength of the order of 1 Å, which makes them very suitable to study interatomic distances in crystal lattices. When X-rays are incident on a crystal, they will scatter at the electrons in all directions. However, under certain geometrical conditions, constructive interference of the scattered X-rays occurs. This phenomenon has been described and explained by W. L. Bragg, resulting in his well-known law of diffraction. X-rays impinging on a crystal at an angle θ with respect to a certain crystal plane *(hkl)* will interfere constructively when the outgoing angle, with respect to this crystal plane, is similar to the incident angle and when their difference in path

[2] Here, we have used the single channels from the multichannel analyzer as the depth windows.

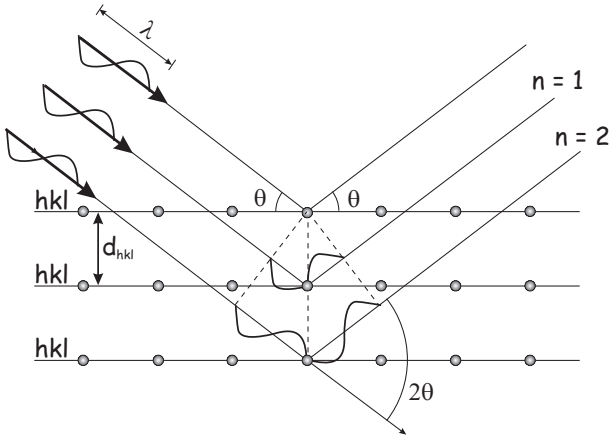

Figure 4.4: Reflection of X-rays incident on atomic planes, interfering constructively according to Bragg's law.

length is equal to an integer times the wavelength of the X-rays. Put into mathematical form, we obtain Bragg's law of diffraction

$$n\lambda = 2d_{hkl}\sin\theta,$$

with n an integer number (1, 2, ...), λ the wavelength of the X-rays, d_{hkl} the interplanar distance and θ the angle of incidence. This law is illustrated in Fig. 4.4. If the wavelength of the incoming X-rays is kept at a fixed and known value, the interplanar distance of the crystal lattice can be derived by measuring the incident angle θ for which constructive interference occurs. As a consequence, by performing a $\theta - -2\theta$-scan, in which the outgoing angle (with respect to the crystal planes) is equal to the incoming angle, it is possible to scan the interplanar distances in the crystal lattice. More information on the X-ray diffraction technique, together with its applications in the field of material characterization, can be found in Refs. [198] and [199].

As explained in Sec. 1.2, ion implantation induces damage to the crystal lattice, from simple point defects to extended volume defects. The microscopic simple defects, such as vacancies and self-interstitials, are known to induce positive strain in the implanted crystal layers, i.e. a local in-

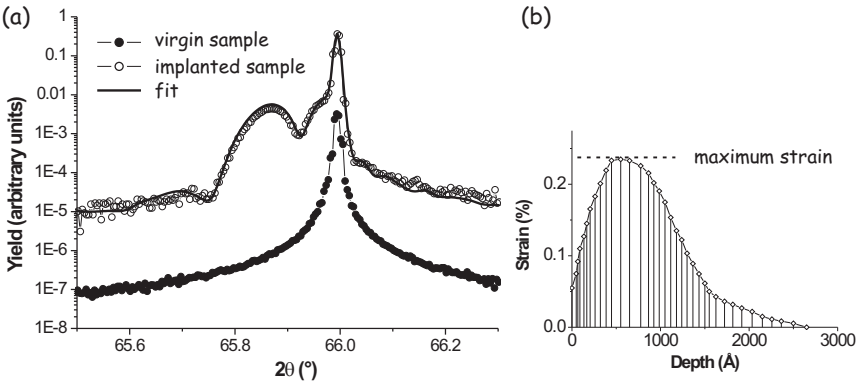

Figure 4.5: (a) (004) X-ray diffraction spectra of a virgin Ge sample (•) and a 160 keV Ar-implanted Ge sample to a fluence of 1×10^{13} at/cm^2 (○), together with a fit (solid line) through the latter spectrum. The spectra of the virgin and the implanted Ge sample have been shifted vertically for the sake of clarity. (b) The strain profile that has been used to create the fit through the spectrum of the implanted Ge sample.

crease of the interatomic and interplanar distances in the crystal. Since XRD allows us to accurately determine these distances, this technique can provide us with very useful information about the implantation-induced damage.

4.1.2.2 Analysis of an XRD spectrum

In Fig. 4.5 (a), typical X-ray diffraction spectra of the (004)-planes[3] of a virgin Ge crystal (•) and a 160 keV Ar-implanted Ge sample to a fluence of 1×10^{13} at/cm^2 (○) are shown. Monochromatic Cu K_{α_1}-irradiation with a wavelength of 1.54056 Å was used in all XRD-measurements. It is clear from this figure that X-ray diffraction on a virgin Ge sample

[3]Due to selection rules, there are forbidden reflections in crystal structures of certain symmetry. For the diamond lattice, these forbidden reflections to a plane (hkl) occur when h, k and l are mixed even and odd, or when h+k+l=2N, with N odd. This implies that the (001)-, (002)- and (003)-planes of a diamond lattice can not be observed by X-ray diffraction.

only results in a single diffraction peak at a 2θ-value of 66° which corresponds to the experimental lattice parameter of bulk Ge of 5.657 Å. As expected, the X-ray diffraction spectrum after ion implantation (∘ in Fig. 4.5 (a)) has extra features compared to the virgin Ge sample, due to the implantation-induced strain. Several side peaks are located at the low angle side of the bulk peak, corresponding with a local expansion of the Ge lattice.

In order to quantify the induced lattice strain, we have used the commercially available software package *Leptos*© to simulate the experimental data [200]. With this software, which is based on the dynamical theory of X-ray diffraction, it is possible to simulate the XRD spectra of strained samples by modeling a virtual sample consisting of several thin layers with a graded strain profile. Fig. 4.5 (b) shows the strain profile and the maximum strain that has been used to simulate the experimental data (∘) from Fig. 4.5 (a), with the simulation (solid line) plotted on top of the XRD spectrum.

4.1.2.3 Perpendicular versus parallel strain

By measuring diffraction spectra at crystal planes which are not parallel to the surface, it is possible to determine whether the strain is (in)elastic or if a preferential strain direction is present. The strain can be divided in two contributions: parallel strain ($e^{\parallel}$ – i.e. in the in-plane direction) and perpendicular strain ($e^{\perp}$ – i.e. in the out-of-plane direction). To separate both contributions, reciprocal space mapping (RSM) is the ideal measuring tool, since it provides a two-dimensional diffraction spectrum as a function of the in-plane and the out-of-plane lattice parameters.

Fig. 4.6 shows a reciprocal space map around the (224) reciprocal lattice point in Ge after implanting 160 keV Ar ions to a fluence of 1×10^{13} at/cm^2. The 3-dimensional diffraction pattern is shown as a function of the in-plane lattice parameter a and the out-of-plane lattice parameter c. We clearly see the large diffraction peak at the middle of the pattern from the bulk Ge at the experimental lattice parameter of $a = c = 5.657$ Å,

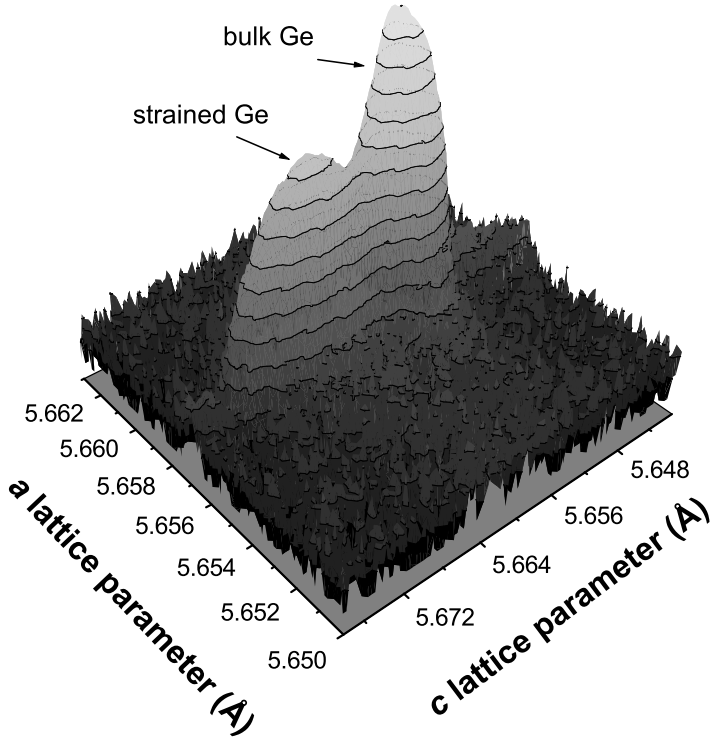

Figure 4.6: Reciprocal space map around the (224) reciprocal lattice point in Ge, implanted with 160 keV Ar ions to a fluence of 1×10^{13} at/cm^2.

together with the extra diffraction feature from the strained implanted region. It is clear that this second peak only occurs at larger c values whereas the a value remains unchanged. Hence, the lattice deformation occurs only in the out-of-plane direction and the strain in the implanted region is purely perpendicular. Therefore, in the remainder of this thesis, we will use *strain* when referring to *perpendicular strain*.

4.2 Electrical characterization of defects: Deep level transient spectroscopy

Imperfections in a semiconductor crystal lattice break the symmetry and induce electrical energy levels in the (otherwise forbidden) band gap of the semiconductor. These energy levels can be divided into *shallow* levels, which are close to the valence or the conduction band and *deep* levels. These deep levels can act as hole traps, electron traps or recombination-generation centers and are detrimental for the semiconductor device. While shallow levels are typically measured with luminescence techniques, the most popular and widely used technique to study deep levels is deep level transient spectroscopy (DLTS). With this technique, it is possible to obtain the activation energy, the capture cross section and the depth profile of the deep defect levels in the band gap [201, 202].

This technique is based on measuring the change in capacitance of a Schottky contact (or a p^+n or pn^+ diode) during the emission of charge carriers from a deep level. In the following section, the basic principle of DLTS will be explained for a Schottky contact between a metal and an n-type semiconductor, in accordance to the experimental conditions in this thesis: a Pd Schottky contact on Sb-doped Ge.

4.2.1 Capacitance transient

When a metal is put into contact with a semiconductor (i.e. a Schottky contact), a potential difference is created between the semiconductor and the metal due to the difference in Fermi level. As a consequence, electrons flow from the n-type semiconductor to the metal, which results in a depleted region with width W. By putting the Schottky contact under reverse bias, i.e. applying a negative potential to the metal with respect to the semiconductor, this depleted region becomes larger. When a certain deep level (e.g. electron trap) is present in the semiconductor at an energy value E_T and the Schottky contact is put under reverse

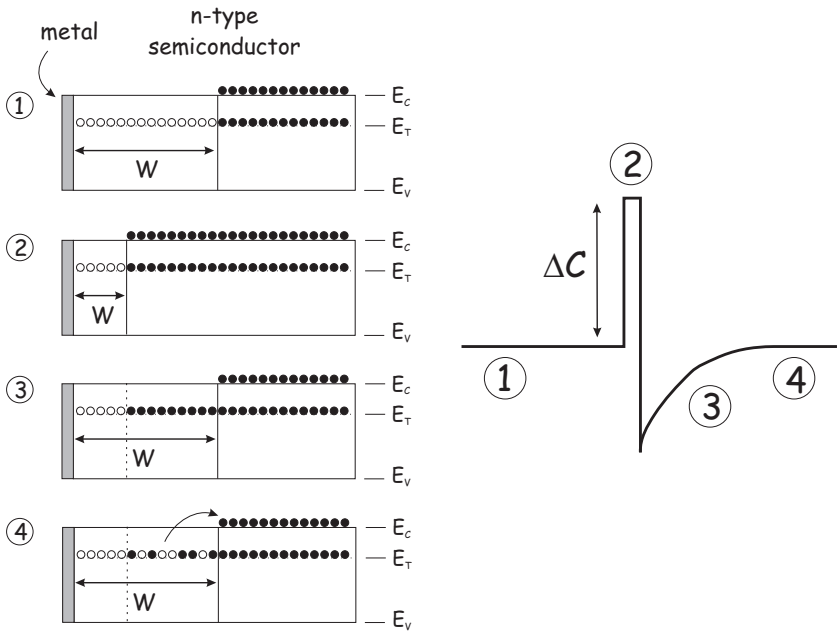

Figure 4.7: The capacitance transient due to the presence of a deep energy level in an n-type semiconductor: (1) the Schottky contact under reverse bias, (2) applying a filling pulse, (3) abruptly restoring the reverse bias and (4) after the partial emission of the deep defect level. The corresponding capacitance function is shown on the right side of the figure.

bias, this trap will not be populated in the depleted region since no mobile charge carriers are available for capture. This is schematically presented in Fig. 4.7 as step 1. The depleted region can be regarded as a parallel-plate capacitor with a capacitance C.

Next, a short filling pulse of 1 ms is applied across the Schottky contact, which results in the immediate reduction of the depletion region (Fig. 4.7 - step 2) and in the filling of the electron traps in the formerly depleted region. The smaller width of the depleted region results in an increase in the capacitance, as shown on the right side of Fig. 4.7. After this short filling pulse, the system is put back under the quiescent reverse bias and the width of the depleted region is back at the original value (step 3). The capacitance value at this point is lower than the original value C due

to the trapped carriers in the defect level. The charge carriers in the filled electron trap will start to emit at an emission rate which is proportional to the Boltzmann factor ($e^{-\Delta E/kT}$), where $\Delta E = E_C - E_T$ is the depth of the trap from the band edge to which the carrier is emitted, k the Boltzmann constant and T the temperature (step 4). The emptying of this defect level results in the increase of the capacitance, back to the equilibrium value C. This capacitance transient has a characteristic time constant equal to the emission rate of the deep level.

4.2.2 Double boxcar integrator principle

To analyze the capacitance transient as a function of temperature, the double boxcar integrator principle is used. In this procedure, a set of capacitance transients, measured at different temperatures, are sampled at two gate times t_1 and t_2 (Fig. 4.8). The output of this procedure is the difference between the capacitance values at those two instants. When the transient is either very slow or very fast, the output will be zero, while a maximum value will be obtained when the transient time constant (which is the inverse of the emission rate) is of the order of $|t_2 - t_1|$. This boxcar principle leads to a typical DLTS spectrum, where peaks are found at a particular emission rate as a function of temperature, as illustrated on the right side of Fig. 4.8 and in Fig. 4.9. By looking for emission at different rates while monitoring the temperature of the defect-associated peak, the activation energy and the capture cross-section of the defect can be obtained from a $\log e - 1/T$ Arrhenius plot of the emission rate e as a function of $1/T$.
Recently, this technique has been improved by the implementation of Laplace DLTS (LDLTS). Instead of sampling the transient at two different gate times, in LDLTS the complete capacitance transient is Laplace transformed, which leads to a significantly increased energy resolution. For more information, the interested reader is referred to literature [204].

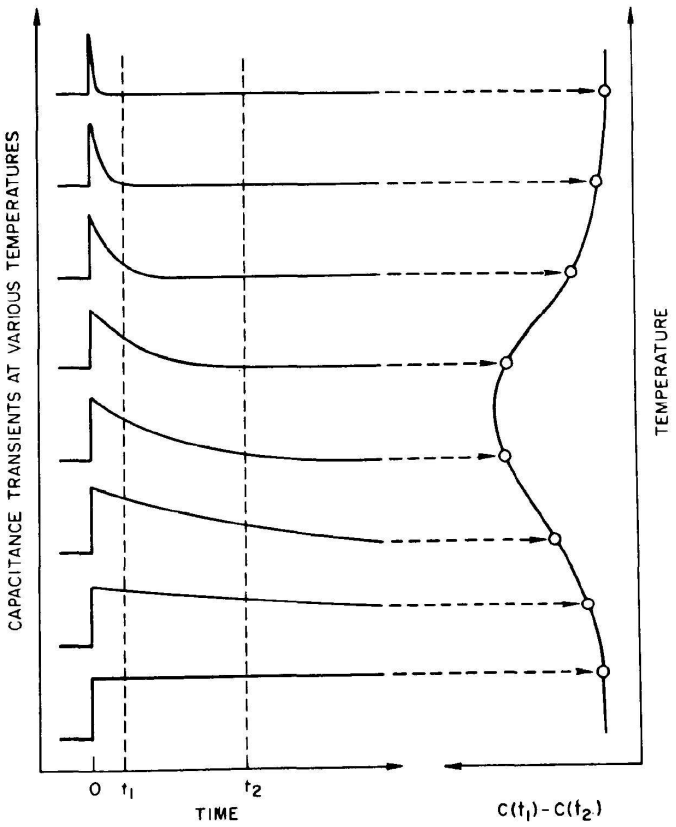

Figure 4.8: The double boxcar integrator principle, in which a set of capacitance transients, measured at different temperatures, are sampled at two gate times t_1 and t_2. The outcome is the difference in capacitance at those two instants, resulting in the peak as a function of temperature, shown at the right side of the figure [201].

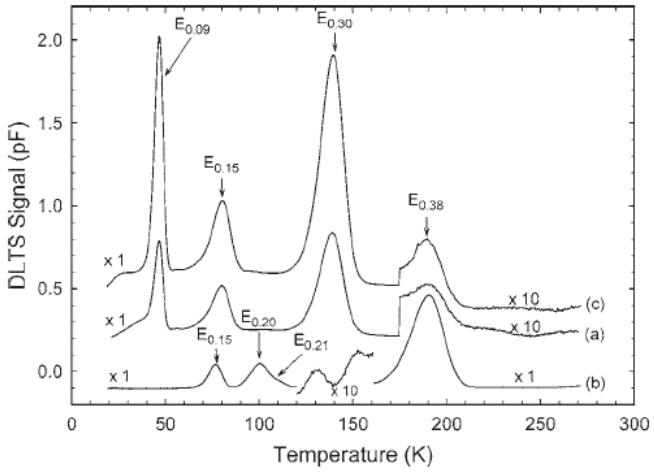

Figure 4.9: DLTS spectra of 160 keV In-implanted Ge (a), high-energy electron irradiated Ge (b) and 160 keV Xe-implanted Ge (c). These spectra were recorded using a rate window of 80 s^{-1} at a quiescent reverse bias of -2 V with a filling pulse, V_p, of 1.8 V superimposed on the reverse bias [203].

4.3 Lattice site location

In this section, we present the techniques that have been used to locate impurity atoms in a single crystal. In order to achieve this goal, we have performed electron emission channeling (EC) experiments (Sec. 4.3.1) as well as *ab initio* calculations (Sec. 4.3.2). Similar to ion channeling techniques, EC is based on the channeling of charged particles along and in between the rows (and planes) of atoms, which has been briefly discussed in Sec. 4.1.1.2. The basic principles behind the technique, the experimental emission channeling setup and a brief overview of the analysis method are presented in the first part of this section. The second part contains a brief description of the *ab initio* calculations that have been performed to obtain complementary information on the lattice location of impurity atoms.

4.3.1 Electron emission channeling

4.3.1.1 Basic principles

In short, the emission channeling technique is based on the fact that charged particles, emitted from an implanted radioactive isotope are guided by the potential of atomic rows and planes while traveling through a single crystal. The resulting anisotropic electron emission pattern around low-index crystal directions is characteristic for the lattice site occupied by the emitting atom and is measured with a 2-dimensional position- and energy-sensitive Si detector.

The first step in the determination of the lattice location of an impurity with the emission channeling technique, is the implantation of a radioactive isotope of the impurity under investigation. The radioactive isotopes that are used in the electron emission channeling experiments, emit β^--electrons or conversion electrons. Influenced by the potential of the atomic rows and planes, these emitted electrons are steered (channeled) through the crystal. The major difference between positive ion channeling and electron channeling, is the opposite charge of the channeling particles. Due to the attractive force between the positive charge of the nuclei of the lattice atoms and the negatively charged electrons, the electrons will not be channeled in between, but *along* the rows and planes of atoms.

As can be seen in Fig. 4.10, this channeling effect is largely influenced by the lattice location of the implanted impurity. When the impurity is located on a substitutional site in a single crystal (Fig. 4.10 (a)), the electrons, emitted along any crystal direction, feel the attractive force of the nuclei of the lattice atoms and will channel along this row of atoms. However, when an impurity is located interstitially, i.e. at least in one direction in between of the rows of lattice atoms (Fig. 4.10 (b)), the electrons emitted along this direction will be steered towards the lattice nuclei and will not be channeled (cfr. the vertical and the horizontal direction in Fig. 4.10 (b)). By measuring the yield of emitted electrons along several crystal directions (typically 4), which will be

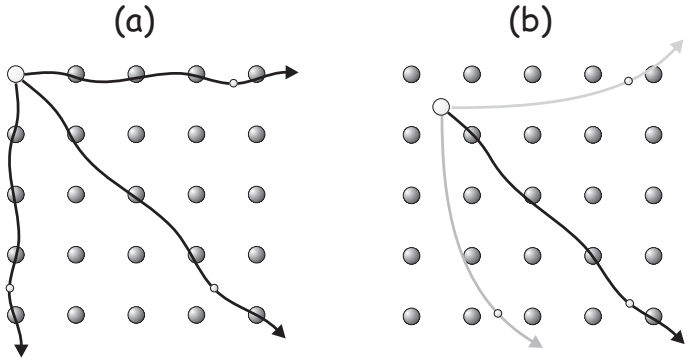

Figure 4.10: The channeling (black arrows) and blocking effect (grey arrows) for emitted electrons from (a) a substitutional and (b) an interstitial impurity in a single crystal.

larger (smaller) than average if the decaying impurity is located substitutionally (interstitially) along that direction, it becomes possible to qualitatively determine the lattice site of the impurity. Besides the axial channeling effect, planar channeling has a similar but smaller effect and will be used in the EC-analysis as well.

The major advantages of electron emission channeling[4] with respect to regular ion channeling techniques such as RBS/C, are (1) the possibility to use small impurity concentrations and thus studying isolated impurities, (2) the applicability of the technique to light impurities as well as heavy impurities[5] and (3) the increased accuracy of the lattice site determination (0.1 – 0.2 Å) due to the use of 2-dimensional patterns. More information about the channeling of electrons, and in particular about the theoretical framework of the emission channeling technique, can be found in Refs. [205–212].

[4]The same advantages are valid for α and positron emission channeling, which have not been discussed (and used) in this thesis.

[5]As mentioned before (p. 24), in RBS/C experiments it is not straightforward to investigate impurities with a lower mass than the host atoms.

4.3.1.2 Experimental setup

The implantations of radioactive isotopes in the framework of this PhD thesis have been performed at the ISOLDE facility at CERN, as was explained in Sec. 3.1.2.2. After implantation, the implanted samples are measured offline; 4 experimental setups are available for the measurements. Each setup basically consists of a vacuum chamber, a two-axis goniometer on which the sample is mounted and which can be heated in situ up to 900 °C and a detector. This 2-dimensional silicon pad detector is position-sensitive as well as energy-sensitive, and consists of 22×22 pixels, each having an active area of 1.3×1.3 mm^2. The energy resolution of the detector for electrons is roughly 5 – 6 keV, while an angular resolution of 0.1° can be reached in a typical emission channeling experiment. Fig. 4.11 shows (a) the complete emission channeling setup, (b) the goniometer and (c) the pad detector. For more information on the operation of this pad detector for emission channeling experiments, the reader is referred to Ref. [213].

4.3.1.3 Analysis method

The output of an EC experiment is a 2-dimensional pattern, which gives the anisotropic yield of emitted electrons around a certain low-index crystal axis. Examples of such patterns are shown in Fig. 4.12 (a)-(d), where the gray scale in the patterns is directly related to the electron yield. It is clear that besides the axial channeling or blocking effect, which is visible in the center of each pattern, planar channeling and blocking effects occur as well. In the EC experiments presented in this work, the patterns along four different crystal directions are measured ($\langle 111 \rangle$, $\langle 100 \rangle$, $\langle 110 \rangle$ and $\langle 211 \rangle$), in order to unambiguously determine the occupied lattice sites of the impurity. To monitor the thermal stability of the lattice sites of the impurity atoms, measurements have been performed after implantation as well as after several annealing steps for 10 min in vacuum ($< 10^{-5}$ mbar) at temperatures up to 600 °C.
In order to perform a quantitative analysis of the patterns, we make use

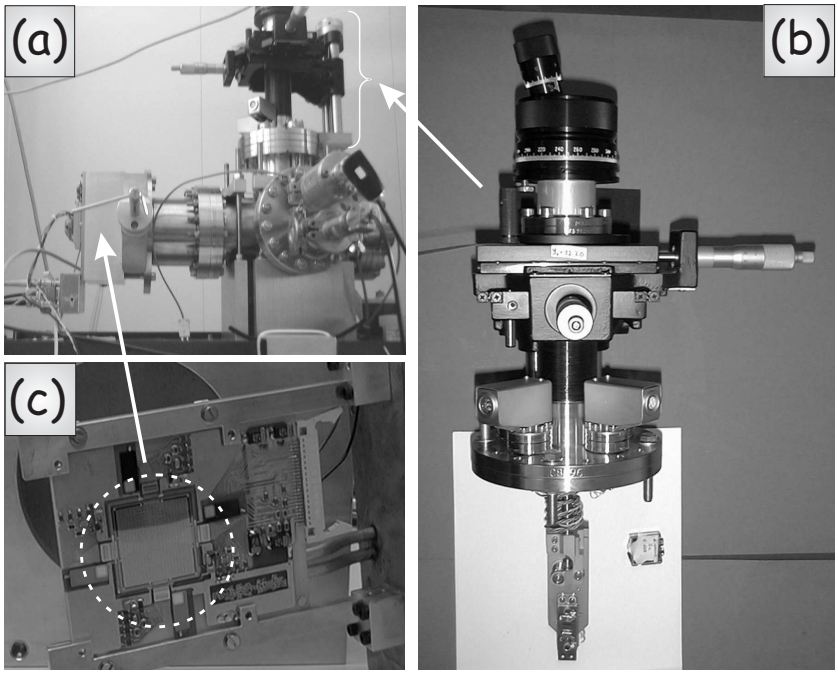

Figure 4.11: (a) The complete experimental setup and detailed pictures of (b) the goniometer and (c) the pad detector, as used in the emission channeling experiments presented in this work.

of simulations. Considering the low mass of electrons and the typical decay energies of around 100 keV to several MeV, the electrons are expected to behave quantum mechanically. Therefore, the simulations have to be based on the dynamical theory of electron diffraction. The theoretical framework of these calculations, which is based on the *many beam* formulation, is described in detail in literature [205, 207, 209, 212, 214–216]. For each emission channeling experiment, these calculations are performed for impurities on each of the high-symmetry sites shown in Fig. 1.3, as well as on discrete displacements between these sites along the ⟨111⟩, ⟨100⟩ and ⟨110⟩-directions. Finally, the experimental patterns are fitted by (a linear combination of) the simulated patterns, which results in the fractional occupation of the impurities on the considered high-symmetry sites.

As an example, Fig. 4.12 (a)-(d) show the normalized electron emission patterns of ^{111}Ag atoms, implanted to a fluence of $5 \times 10^{12}/\text{cm}^2$ in Ge, around the $\langle 111 \rangle$, $\langle 100 \rangle$, $\langle 110 \rangle$ and the $\langle 211 \rangle$-axis following a 400 °C annealing step in vacuum. Simulated patterns for this experiment are shown in Fig. 4.13, for ^{111}Ag atoms on the bond-centered site in Ge (Fig. 4.13 (a)-(d)) and on the substitutional site (Fig. 4.13 (e)-(h)). The best consistent fit for all 4 experimental patterns (Fig. 4.12 (a)-(d)) is shown in Fig. 4.12 (e)-(h), where 21(3)% of the Ag atoms are located on the substitutional site and a 33(4)% on the bond-centered site. The overall resemblance in the experimental and the simulated 2D-patterns, together with the fine structure that is present in each pattern, clearly illustrate the strength of this technique for lattice site location studies.

A final remark needs to be made concerning the background of electrons in the experimental patterns. Obviously, the simulated patterns are only representative for electrons traveling directly from the implanted sample to the detector in a straight path. However, in practice, a relatively large fraction of electrons that reach the detector have scattered on parts of the experimental setup (tubes) or even have experienced large angle scattering by the lattice atoms of the implanted material. These electrons generate a uniform background in the experimental patterns which needs to be taken into account. Using GEANT4 simulations, it is possible to determine the fraction of electrons that reach the detector in an indirect way with respect to the total amount of electrons reaching the detector. These simulations have been performed for all experiments and for the different experimental setups used in this research work. The resulting background correction factors can be found in Appendix B. For more information on these GEANT4 simulations, we refer to literature [217, 218] while a more detailed description of its use in our work is presented in the thesis of B. De Vries [212].

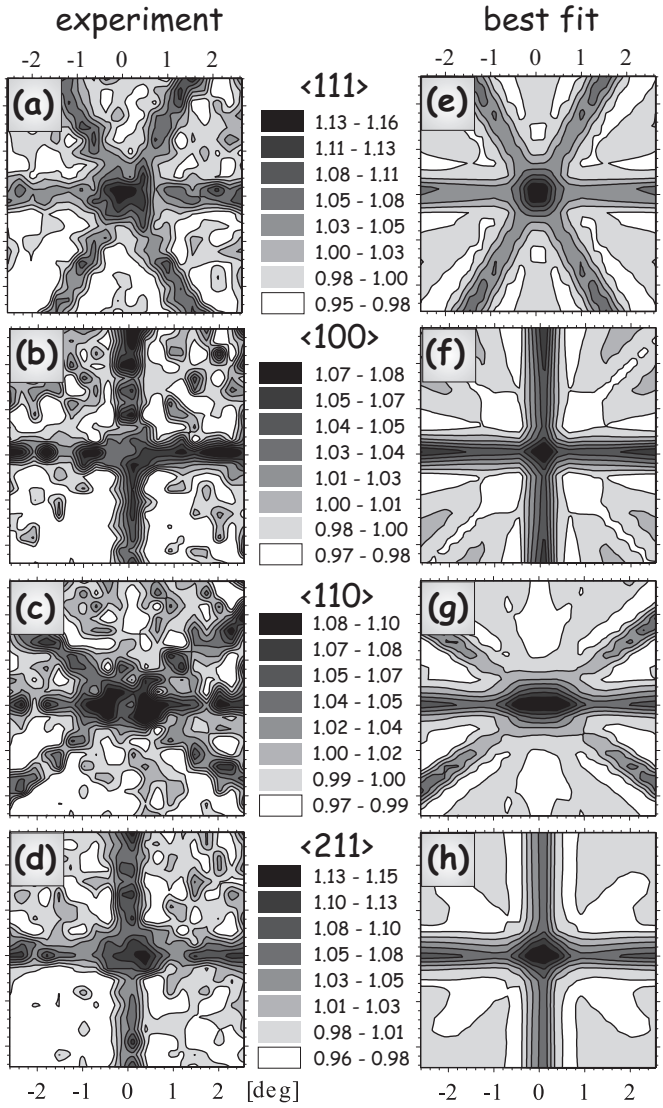

Figure 4.12: (a)-(d) Experimental normalized emission patterns for ^{111}Ag atoms in Ge, and (e)-(h) the best fit through these patterns, along the $\langle 111 \rangle$, $\langle 100 \rangle$, $\langle 110 \rangle$ and $\langle 211 \rangle$-direction, having 21(3)% of the Ag atoms on the substitutional site and 33(4)% on the bond-centered site.

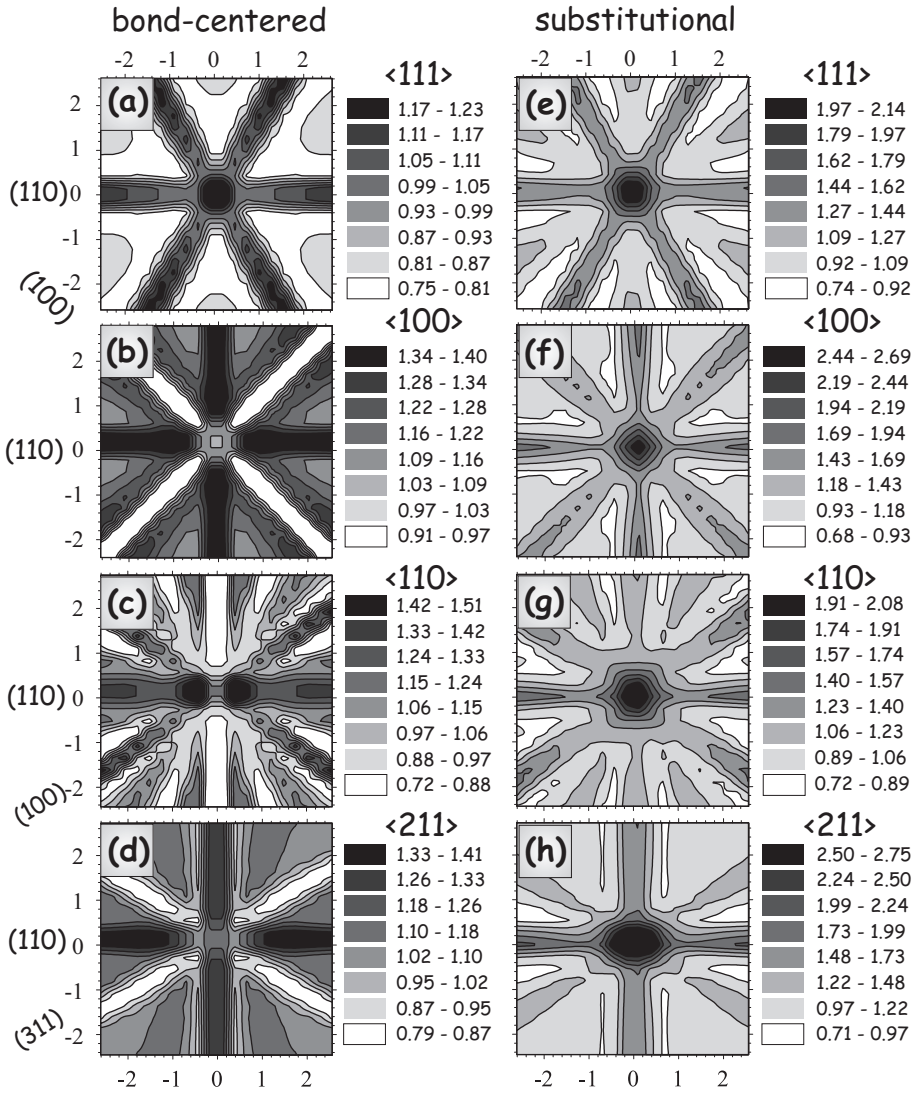

Figure 4.13: (a)-(d) Simulated electron emission patterns for ^{111}Ag atoms in Ge on the bond-centered site and (e)-(h) on the substitutional site around 4 different axial directions $\langle 111 \rangle$, $\langle 100 \rangle$, $\langle 110 \rangle$ and $\langle 211 \rangle$.

4.3.2 *Ab initio* calculations

To obtain complementary information about the lattice location of impurities in single crystals, we have performed *ab initio* calculations. The calculations were done by the APW+lo method within Density Functional Theory, as implemented in the WIEN2k code [219, 220]. The Perdew-Burke-Ernzerhof [221] exchange-correlation functional was used, with the k-space sampling done on a 4×4×4 mesh in a 64-atom cell, with a basis set corresponding to $K_{max} = 3.5$ a.u. The influence of the size of the supercell on the obtained results has been checked by performing calculations with a supercell containing up to 256 atoms.
More specifically, we have calculated the heat of formation of several impurity sites in Ge, which are calculated according to

$$\Delta H_f = E_{sup}^{imp} - \mu_{imp} - \left(32E_{sup}^{id} - n\mu_{Ge}\right) \tag{4.1}$$

where E_{sup}^{imp} is the total energy of a 63- or 64-atom supercell that contains the impurity, E_{sup}^{id} is the total energy of a pure Ge unit cell (diamond structure, 2 atoms), μ_{Ge} is the chemical potential of Ge (taken equal to the total energy per atom in bulk Ge), n is the number of Ge atoms in the ideal 64-atom supercell that are replaced by either vacancies or impurities ($n = 1, 2$) and μ_{imp} is the chemical potential of the impurity with respect to the elemental solid. For all elemental solids, the lattice constant was optimized and then fixed for the 64-atom cells, but all atoms in those supercells were allowed to move to their equilibrium positions.
Besides the information about the stability of certain impurity sites after relaxation, we have used *ab initio* calculations to investigate the hyperfine parameters – the electric field gradient and the isomer shift – at these sites as well.

CHAPTER 5

RESULTS

In this chapter, we present an overview of the results that have been obtained during this PhD research. Two major research topics have been investigated, both related to ion implantation in germanium. First, we present the characterization study of the ion implantation-induced structural and electrical damage in the Ge lattice (Sec. 5.1). The second research topic deals with the lattice location of a number of fundamentally, as well as technologically interesting impurities after implantation in germanium (Sec. 5.2). In the final section of this chapter (Sec. 5.3), both topics are brought together in a discussion about the influence of the implantation damage on the lattice location of impurities in Ge.
A detailed explanation and a more elaborate discussion of the presented results in this chapter can be found in the articles that have been published in, or submitted to international peer-reviewed journals. These articles have been added at the end of this thesis and will be referred to as Art. X, according to the following list:

I Implantation-induced damage in Ge: Strain and disorder profiles during defect accumulation and recovery (p 147)

II Electrical characterization of defects introduced in n-type Ge during

indium implantation (p 177)

III Electrical characterization of defects in heavy-ion implanted n-type Ge (p 189)

IV Experimental evidence of tetrahedral interstitial and bond-centered Er in Ge (p 199)

V Transition metal impurities on the bond-centered site in germanium (p 211)

VI Lattice location study of implanted In in Ge (p 225)

VII Lattice location study of ion implanted Sn and Sn-related defects in Ge (p 239)

5.1 Ion implantation-induced lattice damage

5.1.1 Structural characterization

The ion implantation-induced damage in Ge has been structurally characterized by measuring the strain with X-ray diffraction, and the profile of displaced Ge atoms with RBS/C, as explained in chapter 4. In this way, we studied the defect accumulation by gradually increasing the implantation fluence, as well as the recovery of the lattice damage after rapid thermal processing. A summary of the obtained results is presented here, and more details can be found in Art. I.

5.1.1.1 Damage accumulation

The damage accumulation process can be divided in three regimes, based on the implanted fluence. At the lowest fluence (*regime 1*), when the Ge lattice can still be considered single crystalline, the (small) defect fraction and the strain in the implanted layer are linearly proportional to the ion fluence, and, consequently, to each other as well. Moreover, the profile of both quantities are similar to the calculated vacancy profile from Monte-Carlo simulations, and a linear proportionality has been

found between the maximum strain in the implanted layer and the fraction of deposited energy from nuclear interactions – e.g. for the creation of vacancies. These results indicate that mainly isolated and relatively small defects are present at this fluence regime 1.

At higher implantation fluences (*regime 2*), where the defect fraction is roughly between 0.2 and 1 (=amorphous), the damage accumulation process becomes more efficient. While the defect fraction is still linearly proportional to the fluence, the proportionality constant is clearly higher than in regime 1. This implies that the fraction of retained defects, created by a single incoming ion, is larger in a pre-damaged crystal (regime 2) than in an undamaged one, or in other words that less dynamic annealing occurs in a pre-damaged crystal. This is explained by the fact that the isolated defects start to agglomerate and grow into larger defected regions, which decreases the probability that simple defects can annihilate or relax and results in a more efficient damage accumulation process. Due to the increased amount of lattice damage, it is impossible to extract a complete strain profile from the diffraction spectra. Since it is generally accepted (and intuitively comprehensible) that the strain in the implanted region is mainly caused by simple defects such as (small clusters of) vacancies and interstitials, this indicates that the type of defects in this fluence regime is different from regime 1. Besides isolated defects, also extended defects and (small or large) amorphous regions will be present in the implanted region in fluence regime 2.

At a certain fluence, the implanted region becomes amorphous (*regime 3*). This fluence, which is known as the amorphization threshold, has been determined for a variety of implantation parameters, showing that the mass of the implanted species is a crucial factor, while the implantation energy does not influence the amorphization threshold. The minor role of the energy of the incoming ions on the amorphization threshold is due to the fact that in high energy implantations, the larger amount of energy to be deposited is canceled by the larger spread in energy deposition. Therefore the defect density in the implanted region is roughly independent from the implantation energy. Moreover, we can conclude

that the chemical properties of the implanted species do not influence the overall damage accumulation process up to amorphization.

Summarizing these results, we have presented a broad overview of new experimental data on the accumulation of implantation-induced lattice damage as a function of several implantation parameters (Fig. 5.1). From these results, it is possible to accurately quantify and predict the structural damage (the amount of displaced Ge atoms as well as the strain) after ion implantation in Ge. Having this type of in-depth knowledge – and eventually control of implantation-induced defects in Ge – is also important for the interpretation of the results of dopant activation [94,97] and electrical characterization studies, such as implantation-induced defect levels in the Ge band gap, as will be shown in Sec. 5.1.2. Furthermore, the emission channeling experiments, presented in Sec. 5.2, have shown a clear influence of the overall implantation-induced damage on the analysis of the lattice location of impurities in Ge, further highlighting the importance of systematic defect studies.

5.1.1.2 Damage recovery

From the investigation of the *recovery* of the implantation-induced damage, we have revealed two annealing regimes. The first regime occurs at annealing temperatures as low as 100 °C, at which partial damage recovery was found throughout the complete implanted layer in low fluence implanted samples, and complete damage recovery at the deeper end (tail) of the implanted region for the highest fluences. Since low fluence implanted samples mainly consist of isolated and relatively small defects (such as di-vacancies, di-interstitials or small amorphous clusters), these results indicate that similar defects are present at the tail of the implantation profile. The second annealing regime starts at 350 °C, and is determined by the onset of recrystallization of amorphous Ge. From literature, recrystallization was found to occur between 380 °C and 500 °C [76,88,89], while our results show that the Ge recrystallization starts at even lower temperature. Moreover, we found that recrystallization

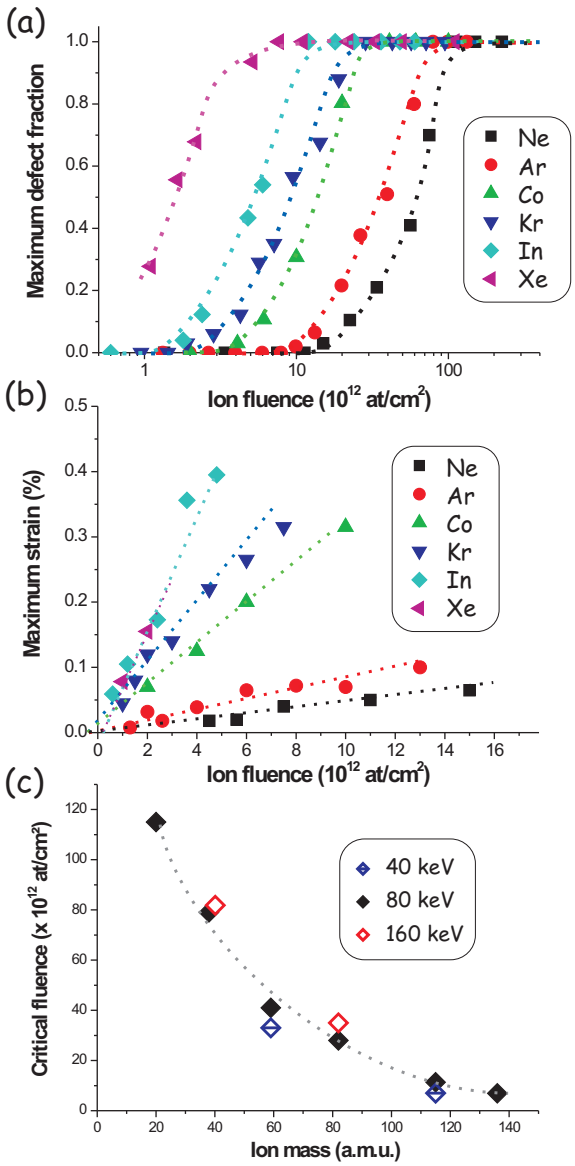

Figure 5.1: (a) Defect fraction and (b) strain at the mean projected range (i.e. maximum value) as a function of ion fluence for 80 keV Ne, Ar, Co, Kr, In and Xe implantations. (c) The amorphization threshold as a function of ion mass for implantations at an energy of 40, 80 and 160 keV.

occurs only at the amorphous-crystalline interface.

5.1.1.3 Comparison to Si

When comparing our experimental results in Ge to the extensive literature on Si, the most striking difference is found for the amorphization threshold values. It is clear that amorphization occurs at much lower fluences in Ge than in Si, in accordance with earlier studies [78, 80]. Furthermore, the recrystallization of amorphous material starts at much lower temperatures (350 °C) in Ge than in Si (>600 °C). These results are related to the lower melting temperature and the lower binding energy in the Ge lattice crystal with respect to Si. Although damage accumulation occurs at different ranges of fluence, the overall influence of implantation parameters on the damage accumulation process in Si and in Ge is similar. In accordance to what we found in Ge, the damage accumulation process in Si has been divided in three regimes, representing (I) crystalline Si containing relatively simple defects, (II) a mixture of damaged crystalline Si and amorphous Si zones and (III) an amorphous Si layer [34, 222]. Furthermore, the amorphization threshold in Si was found to be relatively insensitive to the ion energy [223], at least for the range of ion masses used in our experiments. Finally, the amount of damage after room temperature implantation in Si was found to increase with current density ([33, 34] and references therein), similar to our observations in Ge. Therefore, it can be concluded that, although Ge amorphizes at much lower fluences than Si, the influence of the investigated implantation parameters (mass, energy, current density) on the damage accumulation process is very comparable in both group IV semiconductors.

5.1.2 Electrical characterization

To electrically characterize the implantation-induced defects in Ge, deep level transient spectroscopy (DLTS) measurements have been performed to determine the electrical energy levels in the Ge band gap. The ma-

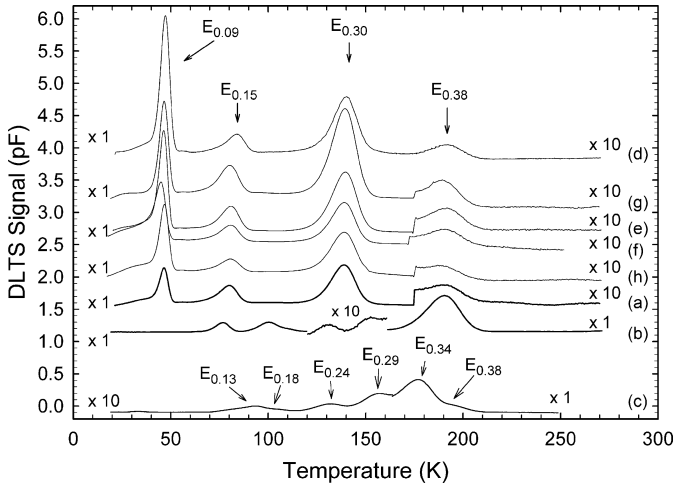

Figure 5.2: DLTS spectra of 160 keV heavy-ion implanted Ge: In [203] (a), He (c), Ne (d), Ar (e), Kr (f), Xe (g), Ge (h), high-energy electron irradiated Ge [203] (b). These spectra were recorded using a rate window of 80 s^{-1} at a quiescent reverse bias of -2 V with a filling pulse, V_p, of 1.8 V superimposed on the reverse bias.

jority of the results, summarized in this section, have been published in Art. II and III, and we refer to both articles for more details.

Four prominent defect levels[1] (electron traps) have been observed after In implantation in Ge. Moreover, these defect levels are clearly different from the induced defect levels after electron irradiation in Ge (Fig. 5.2). Since it is expected that electron irradiation mainly creates simple defects, it can be concluded that ion implantation creates more complex defects which have active levels in the Ge band gap. The observed implantation-induced defect levels are not species-related, since the implantation of other elements (B, Ne, Ar, Ge, Kr, In, Xe) has resulted in the same defects (Fig. 5.2). This indicates that the observed defects are not influenced by the chemical properties of the implanted species, but can be attributed to intrinsic defect clusters including vacancies and interstitials, or to Sb-related defects, since the Ge samples were

[1]All defect levels (e.g. $E_{0.09}$) are denoted with an energy value relative to the conduction band: $E_{0.09} = E_C$ - 0.09 eV.

Sb-doped[2]. So far, only one of the observed defects has been unambiguously attributed to a specific defect, i.e. the E center, or the Sb-vacancy complex. Although these defects are clearly not species-related, implantation with (very light) He ions has resulted in different defect levels, indicating that a different type of defects are created during very low mass ion implantation.

Annealing at 200 °C results in a drastic decrease of the defect concentration, while annealing at higher temperatures removes most of the defects that are present at room temperature, and much more complex DLTS spectra appear. This indicates that the defects, present at room temperature, anneal or transform into other defects. Finally, annealing at 600 °C removes all defect levels in the band gap. This annealing study has been done on samples with deposited Pd Schottky diodes, and germanide formation during annealing most likely interferes in the DLTS spectra. A similar annealing study, with the defect annealing performed prior to the Schottky diode deposition, is scheduled in the near future in order to investigate this phenomenon into more detail.

While most implantations have been performed with the same (very low) fluence of 2×10^{11} at/cm^2, we have investigated the influence of the implantation fluence on the induced electrical defects by implanting a number of samples with boron (B) to a range of fluences from 2×10^{11} to 2×10^{13} at/cm^2. However, preliminary results from this study indicate the presence of the same defect levels within this fluence range. This is in accordance with the structural characterization study of the implantation-induced damage: By extrapolating the results in Fig. 5.1 (a) to lower masses, it is clear that the implantation of B ions to a fluence of 2×10^{13} at/cm^2 only results in minor lattice damage, and consequently in the creation of mainly isolated defects.

More experiments are ongoing to try to attribute the different electronic levels to specific defect configurations and to investigate the annealing

[2]For this investigation, we have used Sb-doped Ge samples with a doping concentration of $2 - -3 \times 10^{15}$ at/cm^3. As a comparison, the concentration of implanted impurities in the samples used in the DLTS measurements, ranges from 5×10^{15} to 5×10^{16} at/cm^3.

behavior of the defects in more detail. Also, the difference between the defect levels for low mass (He) and high mass (heavier than B) implantations is not yet solved and is currently being investigated by performing DLTS-measurements on Li- and He-implanted Ge, with a wide range of ion fluences.

5.1.3 Comparison between structural and electrical damage characterization

The comparison between the results obtained from the structural and the electrical characterization of the implantation-induced lattice damage is not straightforward, mainly due to the difference in implantation fluences used in both studies. The electrical characterization has been performed on samples implanted to a very low fluence (2×10^{11} at/cm^2), in order to minimize the implantation damage to the Pd contact Schottky diodes[3]. At such low fluences, the techniques used to structurally characterize the defects (RBS/C and XRD), are not sensitive enough to provide detailed complementary information. However, the structural characterization study has indicated that mainly isolated defects are present at these low fluences, which is consistent with the fact that specific defects have been observed from the DLTS spectra. Large extended defects are not likely to result in a small number of energy levels, but instead to very complex DLTS spectra.

Despite the large difference in the fluences used in both studies, it can be concluded that the chemical properties of the implanted species play a minor role in the damage accumulation process. The amorphization threshold behaves similarly for the inert noble gas elements and for the more reactive elements Co and In. In the electrical characterization study, the same defects have been observed for a very wide range of elements, also indicating the relative independence of the chemical properties of the elements during ion implantation. Recent DLTS studies

[3]Most implantations have been performed after Pd deposition, since this deposition requires a slightly elevated temperature (up to 100 °C). Hence, Pd deposition after implantation can result in considerable defect annealing.

after Eu-implantation in GaN have shown Eu-related deep level defects, proving that the chemical properties do play an important role in some systems [224, 225].
It is important to note that a study of the electrical defect levels at very low fluences can be very important to understand the damage accumulation process at higher fluences. When the electrical energy levels can be attributed to specific geometrical defects, e.g. by complementary experimental techniques and by theoretical calculations, these defects are the most obvious candidates for damage nucleation sites during ion implantation.

5.2 Lattice location of ion implanted impurities

The second major research topic of this thesis concerns the lattice location of impurities in Ge, or in other words, where the ions end up after being implanted into Ge. In the previous chapter, we have explained the basics of emission channeling (EC), which is the most sensitive and most accurate direct technique for this purpose. A beam of radioactive isotopes is used, which have to fulfill certain requirements[4]. Moreover, a typical EC-experiment can take weeks or months, and a request for beam time needs to be well-founded. All these reasons indicate the need for a well-considered choice of impurities to study.
We have determined the occupied lattice site(s) for the following series of impurities, each for different reasons. Er is a suitable optical dopant in Ge nanocrystals (Art. IV); Fe, Cu and Ag are transition metals which create deep levels in the Ge band gap (Art. V); In is an electrical dopant (Art. VI) and Sn is an isovalent impurity (Art. VII). In the first section, we present an overview of the separate results obtained from the emission channeling experiments on each of these (groups of) impurities. The second section contains the results obtained from complementary *ab initio* calculations of the structural configuration and the heat of formation of impurities and impurity-related defects. In the final section, we present a general discussion about the lattice location of impurities in Ge. More information about the results presented in this section can be found in Art. IV, V, VI and VII.

5.2.1 Emission channeling results

Erbium (Art. IV): The implanted Er atoms occupy two high-symmetry sites, i.e. the tetrahedral interstitial (T) site and the bond-centered (BC) site (Fig. 5.3 (a)). In Si, Er was found on the T site as well [175, 176], which makes it an expected site for Er in a diamond crystal

[4]Important requirements are (1) a suitable half life of the radioactive isotope ($<$ 1 year and $>$ 1 day), (2) suitable electron energies, (3) only β^--decay or decay via conversion electrons, ...

structure. However, the occupation of the bond-centered site is somewhat more surprising, and can be related to the Er-vacancy defect in the split-vacancy complex configuration (Fig. 1.5 (b)). The low relative fractions of Er atoms on the T site ($< 20\%$) and on the BC site ($< 15\%$), indicate that a large fraction of Er atoms (at least 65%) is located on low-symmetry sites or is distributed randomly throughout the crystal. However, it is more likely that this large, so-called *random* fraction, is a consequence of the implantation-induced lattice damage, as will be explained in section 5.3.1. The Er atoms on the T site and on the BC site are thermally stable at least up to 500 °C. After annealing at 600 °C, the fraction of Er atoms on high-symmetry sites is drastically reduced, which indicates possible diffusion of the Er atoms. As the depth profile of the implanted atoms is an input parameter for the simulations, it implies that a larger mean projected range of the Er atoms after diffusion will lead to an underestimation of the measured and fitted fraction on high-symmetry sites. Therefore, at high annealing temperatures, the measured fractions on high-symmetry sites have to be considered as lower limits to the real values.

Transition metals (Art. V): The three investigated metal impurities Fe, Cu and Ag, have a similar lattice location behavior (Fig. 5.4). All three impurities have been found partially on the substitutional (S) site and partially on the bond-centered site. Since most transition metal (TMs) impurities are generally expected to be located substitutionally, as explained in section 1.3.4, the observation of the TMs on the bond-centered site is unexpected. The bond-centered fraction can be related to impurity-vacancy complexes in the split-vacancy configuration, which will be explained in more detail in Sec. 5.2.2. Roughly 20 – 30% of the TMs are located on the bond-centered site, while a similar fraction of Ag atoms, and roughly 40% of the Fe and Cu atoms are found on the substitutional site. All Cu and Fe atoms are thermally stable on the BC site and on the S site after annealing at least up to 350 °C and 400 °C respectively. After annealing the Ag-implanted sample at 500 °C,

the fraction of Ag atoms on the BC site almost completely disappears, which indicates the break-up of the BC-related defect (Ag-V) or, less likely, diffusion of the BC-related defect as a whole.

Indium (Art. VI): In agreement to what was found from early RBS/C experiments [103, 104], our EC experiments show that the majority of the In atoms are located on the S site after ion implantation (Fig. 5.3 (b)). After annealing the lattice damage at about 300 °C, this substitutional fraction is as high as 90%, and is thermally stable at least up to 500 °C. However, directly after implantation, as well as after the first annealing step at 150 °C, a small fraction ($< 15\%$) of the In atoms was found on the BC site as well. From the fact that In on the BC site disappears after annealing at 300 °C, an upper limit for the activation energy for dissociation of this bond-centered related defect has been extracted, i.e. 1.6 eV.
The In-V defect has been observed in perturbed angular correlation (PAC) experiments, however without attributing a particular structural configuration to this defect [59,61–63,119–122]. These PAC results have shown that the In-V defect has an electric field gradient (EFG) along the ⟨111⟩-direction and that the defect dissolves after annealing at 200 °C. Since the split-vacancy configuration of the In-V defect has an EFG along the ⟨111⟩-direction as well, and since the BC-related defect disappears after annealing between 150 °C and 300 °C, the observed BC fraction in the EC experiments can be attributed to the In-V complex in the split-vacancy configuration. In this way, our emission channeling results provide complementary structural information about one of the observed defects from earlier PAC measurements.

Tin (Art. VII): Sn impurities are isovalent impurities in Ge, and are hence expected to be located substitutionally. However, besides the large substitutional fraction (up to 80%), a smaller but still significant fraction (15%) of Sn atoms is located on the bond-centered site (Fig. 5.3 (c)). Once more, this fraction is related to the impurity-vacancy configu-

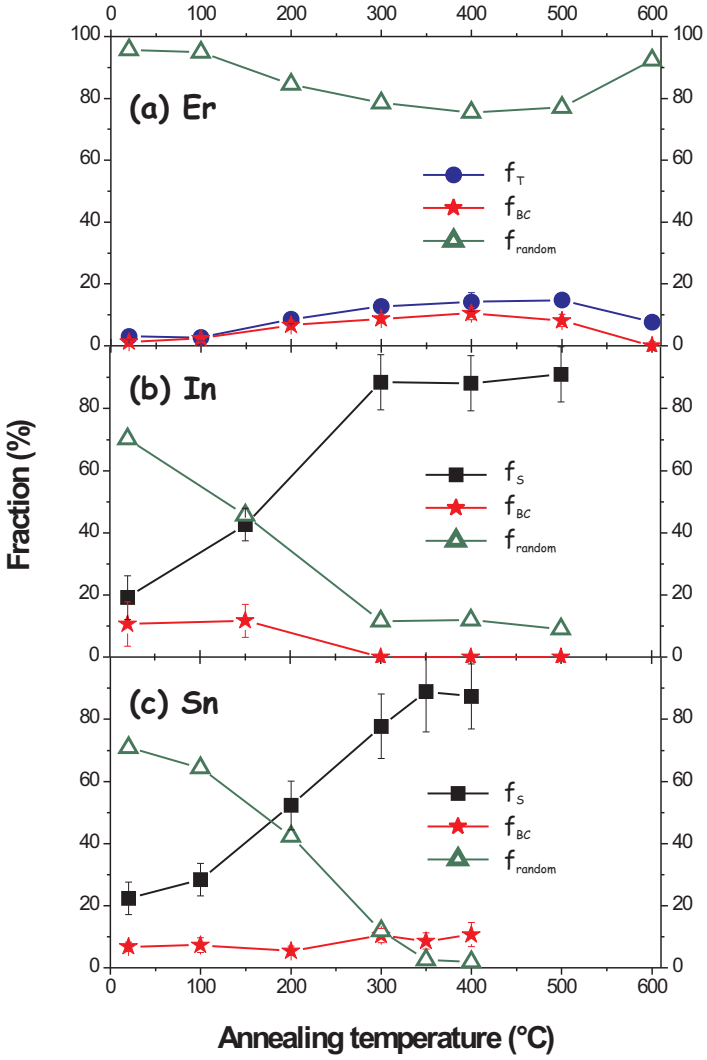

Figure 5.3: Fraction of the implanted Er (a), In (b) and Sn atoms (c) on the S site f_S (■), on the T site f_T (●) and on the BC site f_{BC} (★) in Ge, together with the random fraction f_{random} (△ = 100% - ■ (or ●) - ★), as a function of annealing temperature.

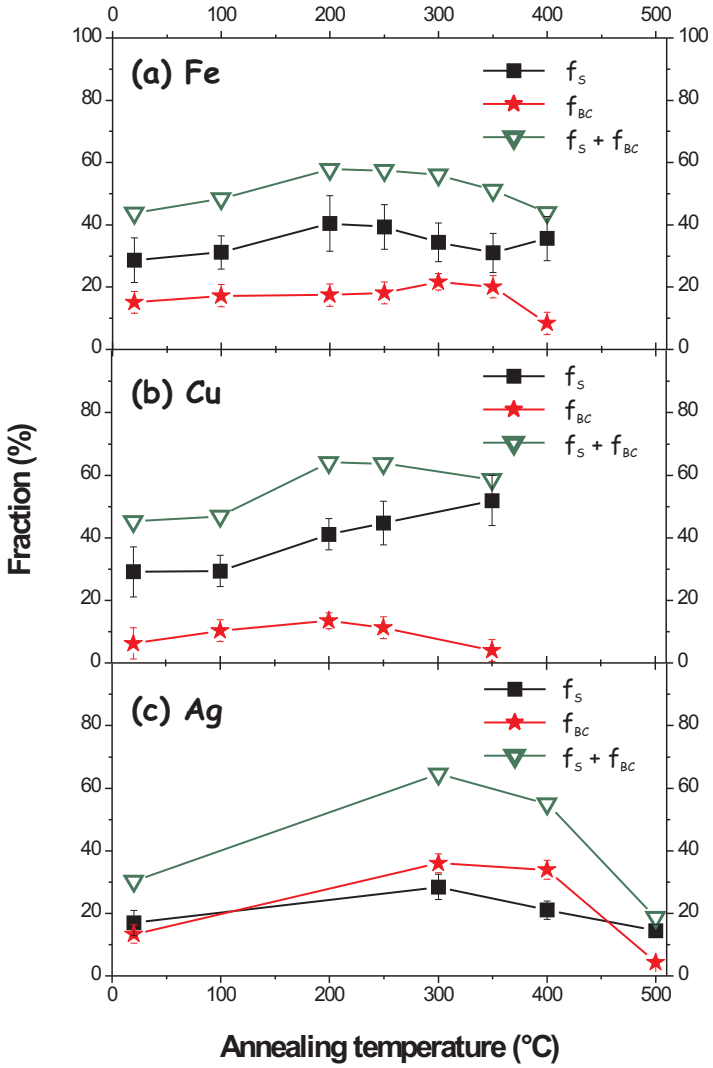

Figure 5.4: Fraction of the implanted Fe (a), Cu (b) and Ag atoms (c) on the S site f_S (■) and on the BC site f_{BC} (★) in Ge, together with the total fraction $f_S + f_{BC}$ ($\nabla = ■ + ★$) on high-symmetry sites, as a function of annealing temperature.

ration, as will be shown from *ab initio* calculations in Sec. 5.2.2. Almost complete recrystallization of the lattice is found after annealing at 300 °C, as can be concluded from the very small random fraction. The Sn atoms on the S site, as well as on the BC site, are thermally stable at least up to 400 °C.

5.2.2 Results from *ab initio* calculations

Ab initio density functional calculations have been performed to obtain complementary information on the lattice location of impurities and on the structural configuration of impurity-related defects. First of all, we have determined the structural configuration of impurity-vacancy (I-V) complexes. For this, we used an I-V complex in the full-vacancy configuration (Fig. 1.5 (a)) as the starting configuration, and allowed the system to relax. For all impurities (with the exception of Er), a large force was induced along the ⟨111⟩-direction, resulting in the impurity ending up on the ideal six-fold coordinated BC site with the vacancy *split* over the nearest neighbor positions: the *split-vacancy* configuration (Fig. 1.5 (b)). Calculations for most of the rare earth elements, such as Er, are not as straightforward as for the other impurities. However, the behavior of these elements can generally be interpolated between La and Lu, which are much easier to treat in calculations. Therefore, we have performed a similar relaxation study for the La-V and Lu-V complexes, resulting in both complexes preferring the split-vacancy configuration. From this, it can be safely concluded that the BC fraction of Er atoms is related to Er-V complexes as well.

In order to investigate whether this bond-centered behavior is a general trend for impurities in Ge, a systematic study of I-V complexes is currently ongoing for impurities throughout the periodic table of elements [226]. So far, it can be concluded that the majority (but not all) of the transition metals prefers the split-vacancy configuration, as well as most of the group III dopants. However, group V elements prefer the full-vacancy configuration, in agreement with the results from Coutinho

	Fe	Cu	Ag	Sn
S	1.90	1.34	1.63	0.18
T	3.19	1.75	2.10	3.96
S+V (BC)	3.85	3.10	2.53	1.86

Table 5.1: Heat of formation (ΔH_f) for Fe, Cu, Ag and Sn on the S site, on the T site and on the BC site in the split-vacancy configuration after relaxation of the impurity-vacancy complex. The calculated heat of formation of an isolated vacancy in Ge is 2.23 eV.

et al. [114]. All these results will be published in the near future [226].

Secondly, we have calculated the heat of formation for a number of impurities (Fe, Cu, Ag and Sn) on the S site, on the T site and on the BC site in the split-vacancy configuration (Tab. 5.1). These calculations show that all these impurities prefer the substitutional site to the tetrahedral site, in accordance with our experimental observations. Moreover, Tab. 5.1 shows that the heat of formation for an impurity on the BC site is considerably lower than the sum of the heat of formation for a substitutional impurity and that for an isolated vacancy (2.23 eV). This implies that it is energetically favorable for an impurity to trap one of the abundantly available vacancies which are created during the ion implantation process. Finally, the impurity-vacancy complex relaxes towards the split-vacancy configuration, which is consistent with the observed BC fraction in the emission channeling experiments.

Thirdly, the isomer shift δ and the quadrupole splitting ΔE_Q of Fe and Sn have been calculated, in order to compare them with the measured hyperfine parameters from Mössbauer spectroscopy (MS) experiments (Tab. 5.2). Three different Mössbauer lines have been measured for Fe in Ge, attributed to Fe on the S site, the T site and to Fe in an Fe-V complex in the full-vacancy configuration [162]. Our calculated hyperfine parameters show very good resemblance with the MS values for Fe on the S site and the T site, as can be seen in Tab. 5.2. However, calculating the isomer shift and the quadrupole splitting for Fe on the BC site in the split-vacancy configuration shows very good agreement with the

		$\delta_{(theo)}$ (mm/s)	$\Delta E_{Q,0\ (theo)}$ (mm/s)	$\delta_{(exp)}$ (mm/s)	$\Delta E_{Q,0\ (exp)}$ (mm/s)
	S	0.06	0.00	0.059	0.00
Fe	T	1.08	0.00	0.80	0.00
	BC	0.55	0.81	0.46	0.69
	S	1.75	0.00	1.90	0.00
Sn	T	3.19	0.00	3.27	0.00
	BC	2.24	0.15	2.36	0.30
				1.41	

Table 5.2: The calculated isomer shift $\delta_{0\ (theo)}$ (mm/s) and quadrupole splitting $\Delta E_{Q,0\ (theo)}$ (mm/s) for Fe and Sn on the S site, the T site and the BC site in the split-vacancy configuration at 0 K, as well as the experimental isomer shift $\delta_{0\ (exp)}$ (mm/s) and quadrupole splitting $\Delta E_{Q,0\ (exp)}$ (mm/s) as deduced from the 3 measured Mössbauer lines for Fe [162], and the 4 Mössbauer lines for Sn [133–136].

experimental values, extracted from the third Mössbauer line. Therefore, we can conclude that this Mössbauer line was correctly attributed to an Fe-V complex, but with an incorrect structural configuration.

Similar calculations have been performed for Sn atoms on the S site, the T site and the BC site in the split-vacancy configuration, in order to compare them with the isomer shift and the quadrupole splitting, extracted from the 4 experimentally measured Mössbauer lines [133–136]. Again, a good resemblance was found between the experiment and the calculations for Sn atoms on the S site and on the T site (Tab. 5.2). The two other Mössbauer lines have been attributed to Sn-V complexes in the split-vacancy and in the full-vacancy configuration. However, here as well, our calculations indicate an incorrect assignment of one of these Mössbauer lines[5]. The fourth line could not yet be attributed to a specific defect, and additional calculations are currently being performed to address this issue.

[5]The Mössbauer line was attributed to Sn-V complex in the full-vacancy configuration, while our calculations indicate that it should be attributed to the Sn-V complex in the split-vacancy configuration.

5.2.3 General discussion

Summarizing all the results from the lattice location study of impurities in Ge, it can be concluded that most of the investigated impurities are located on the substitutional site. Moreover, since the experimentally observed root mean square displacement of the substitutional impurities is equal to the expected value at room temperature, it is very likely that these impurities on the S site are embedded in an undamaged environment. Er is the only impurity without a substitutional fraction but with a fraction on the tetrahedral interstitial site.

However, the most important and most striking observation is that, besides the fraction on the S/T site, all impurities partially occupy the bond-centered site as well. Corroborated by *ab initio* calculations, this bond-centered fraction is related to impurity-vacancy complexes in the split-vacancy configuration. Moreover, the calculated heats of formation have shown that the vacancies will be trapped spontaneously by the impurities, thereby creating an impurity-vacancy complex which relaxes towards the split-vacancy configuration – i.e. with the impurity on the BC site. Hence, by introducing vacancies, which are mobile at room temperature in Ge [61], it is possible to relocate substitutional impurities towards the bond-centered site. This is a very important result, since it provides a simple method to change the properties of doped germanium. In particular, the optical properties of Er and the electrical properties of In, Fe, Cu and Ag can be changed by introducing vacancies (e.g. by e^--irradiation), resulting in the relocation of the impurities from the S site to the BC site. Moreover, the impurity-vacancy complexes are thermally stable up to relatively high temperatures (with the exception of In), which is important in order to use this method in the production process of integrated circuits.

The observation of the impurity-vacancy complex in the split-vacancy configuration is also of major importance for the diffusion properties of group III, IV and V impurities. Since these impurities are known to diffuse through the vacancy-mediated mechanism, the structural configura-

tion of the I-V complexes is important to understand the experimentally observed diffusion properties. Moreover, the split-vacancy configuration will be a crucial input factor in theoretical studies on the diffusion of impurities in Ge.

5.3 Implantation-induced damage in lattice location studies

5.3.1 Relation between lattice damage and EC analysis

As is clear from the previous section, not all implanted impurities are located on high-symmetry sites. The remaining fraction, which is called the *random* fraction, can be attributed to impurities which are located on low-symmetry sites or which are distributed randomly throughout the crystal lattice. However, it is more likely that this random fraction, which can be relatively large in some experiments, is related to the implantation-induced damage. Due to the deterioration of the crystal structure, a fraction of the implanted radioactive isotopes will be located in damaged regions with reduced local crystallinity. Moreover, a fraction of the electrons emitted from an undamaged region will pass through damaged crystal regions, enhancing the probability for dechanneling. Both effects will result in an isotropic background to the patterns and consequently in an increase of the random fraction. Therefore, the fractional occupation values should be taken as a lower limit to the actual values, especially for the EC patterns taken directly after implantation and after low-temperature annealing steps. This influence of the implantation-induced damage on the random fraction is reflected in the overall increase of the fraction of impurities on high-symmetry sites after the first annealing steps, pointing out the recovery of the crystal lattice.

In order to compare the implantation-induced damage in the different EC experiments, we have plotted the implantation fluence of each experiment as a function of mass in Fig. 5.5. The experimentally observed amorphization threshold as a function of mass has been added to the graph (dotted line), which shows that the implantation fluences used in the Er(Tm) experiments are very close to (or even above) the amorphization threshold. This is in agreement with the high random fraction observed in these EC experiments (Fig. 5.3 (a)), even after several an-

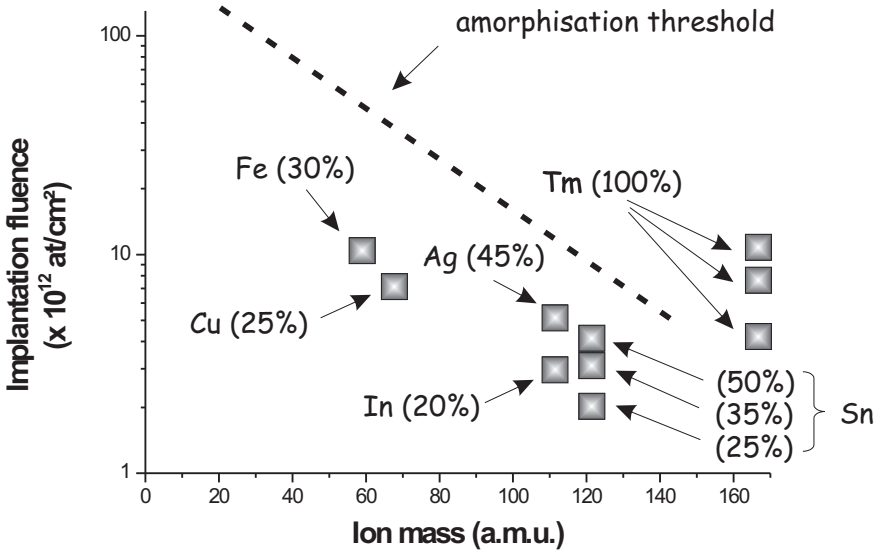

Figure 5.5: The implantation fluence of the EC experiments (■) of Fe, Cu, Ag, In, Sn and Er as a function of ion mass and the generalized amorphization threshold-ion mass dependence (dotted line), as explained in Art. I, together with the relative lattice disorder (0% is undamaged, 100% is amorphous)) for each EC experiment.

nealing steps. The implanted fluence is well below the amorphization threshold for the other EC experiments, as can be noted from the relative disorder values which have been added to Fig. 5.5. This is consistent with the overall lower measured random fraction, in comparison with the Er experiment. Therefore, we can conclude that the large number of defects influences the quantitative analysis of the EC experiments, and vice versa, that the random fraction observed in the EC experiments gives an indication of the crystal quality of the implanted Ge lattice.

5.3.2 Influence of lattice damage on lattice location of impurities

Summarizing all the emission channeling results presented in this thesis, three different high-symmetry sites have been observed. First of all, a

fraction of all investigated impurities (with the exception of Er) occupies the S site. Although it can not be completely excluded from the EC results that these substitutional impurities are part of defect complexes, they are most likely embedded in an undamaged environment. This can be concluded from the theoretical calculations, which have shown that the full-vacancy complex does not exist for the investigated impurities, and from the experimentally observed root mean square (rms) displacement of the impurities on the S site which is in very good agreement with the expected value at room temperature ($\sim$ 0.07 Å). Theoretical calculations of the structural configuration of other defects are required in order to unambiguously attribute the observed substitutional fraction to an impurity in an undamaged local environment.

Er is the only impurity that has been observed on the tetrahedral interstitial (T) site. Since the experimentally observed rms displacement of the Er atoms on the T site ($\sim$ 0.20 Å) is larger than the expected vibrational amplitude at room temperature ($\sim$ 0.07 Å), it is not unlikely that some of these Er atoms are part of small defect complexes. Calculations for Cu, Ag and Sn have shown that, when these impurities are located on the T site with a vacancy as nearest neighbor (T+V), they are pushed towards the vacant substitutional site in the Ge crystal lattice. Since no Er atoms are found on the substitutional site, it can be expected that the T+V configuration is stable for Er, but additional relaxation studies (for Lu and La) are required to confirm this conjecture. An impurity on the T site, with two nearest neighbor vacancies, can be expected to be pushed towards the BC site, since this results in the split-vacancy configuration, which is clearly a stable site for many impurities in Ge.

Finally, all impurities partly occupy the BC site after implantation, and corroborated with *ab initio* calculations, this BC fraction has been related to impurity-vacancy complexes. It is obvious that such complexes will be present, since ion implantation abundantly creates vacancies and interstitials, which are mobile at room temperature [61]. They will migrate through the Ge lattice during implantation, until they recombine, form vacancy or interstitial clusters or become trapped by impurities.

Moreover, our calculations have shown that this vacancy-trapping occurs spontaneously. Therefore, it can be concluded that by deliberately introducing vacancies (e.g. by e^--irradiation), the substitutional impurities will trap the vacancies and are relocated towards the BC site. In other words, the induced defects during ion implantation play a crucial role in the lattice location of impurities, and moreover, externally introducing defects may change the lattice location of the present impurities.

CONCLUSIONS

In this PhD thesis, we have investigated two important ion implantation-related issues in germanium: implantation-induced lattice damage and the lattice location of implanted impurities.

Ion implantation is known to create a huge amount of defects, and the accumulation and the recovery of this damage has been characterized structurally as well as electrically. More specifically, we have determined the relative lattice disorder (or crystal quality) and the induced strain in the implanted region as a function of several implantation parameters. The damage accumulation process has been divided in three fluence regimes. In the first regime, isolated defects are created and there is a linear relation between the lattice disorder and the strain on one hand, and the implanted fluence on the other hand. The second regime is characterized by a more efficient damage accumulation rate, since the present lattice damage decreases the probability that simple defects annihilate or relax, resulting in a larger fraction of retained defects during implantation. Finally, the third fluence regime starts at the critical fluence for amorphization, which has been determined for a wide range of species. Furthermore, the mass of the implanted species largely influences the damage accumulation process, while the chemical nature and the energy of the implanted species do not play a crucial role at all.

The study of the recovery of the implantation-induced damage by rapid thermal annealing has revealed two annealing regimes, clearly separated in temperature. The recovery of small defects starts already after a 100 °C annealing step. The second annealing regime starts at an annealing temperature of 350 °C, and represents the onset of recrystallization of amorphous material, which occurs at the amorphous-crystalline interface.

Although the amorphization threshold in Si and Ge is typically different by orders of magnitude, the influence of the implantation parameters on the induced lattice damage in Ge is largely similar to what is found for Si in literature.

This structural characterization study has been complemented with an electrical characterization study of the implantation-related defects, by examining the implantation-induced energy levels in the band gap of the Sb-doped germanium as a function of several implantation parameters. Four prominent defect levels have been observed, which are clearly different from the point defects that are created during electron irradiation. Furthermore, these defect levels are not species-related, which indicates that they are most likely dopant-related defect complexes, or small intrinsic defect clusters. These defect levels disappear after annealing between 200 °C and 300 °C, at which temperature a very complex spectrum appears, most likely attributed to germanide formation at the Pd Schottky contacts. Annealing at 600 °C completely removes all defects in the band gap. Very low mass implantations (He) have resulted in the creation of other energy levels, indicating a different type of implantation-induced defects.

Summarizing these results, we have presented an elaborate overview of the implantation-induced structural and electrical damage in Ge as a function of a variety of implantation parameters. This overview provides a large amount of new and fundamentally interesting information, which will be important for different types of studies on ion implanted Ge. In particular, this information has been used in the analysis of the emission channeling results that have been presented in this thesis.

Although we have presented many experimental results about the implantation-induced damage in this PhD thesis, there are still many open problems that require further investigation. With respect to the structural characterization of the lattice damage, a particularly interesting topic is the study of the influence of the temperature during implantation. Earlier studies have shown that it is possible to largely reduce the amount of defects in this way [77, 82]. It could also be very interesting to extend the range of implantation conditions used in this thesis: very low ($A < 20$) or very high mass ($A > 130$) ions, lower energy (< 30 keV), very low or very high current densities, etc. Concerning the electrical characterization of the induced defects, many questions are still unanswered and require further attention. The most challenging issues are the attribution of the measured energy levels to specific defects, and the origin of the change of defects for very low mass (He) implantations. Therefore, we propose additional DLTS measurements on Sb-implanted Ge to identify the Sb-related defects, and on Li-implanted Ge in order to study the transition region between He and the heavier ions.

The second implantation-related topic that has been investigated in this thesis is the lattice location of a selection of implanted impurities. For this research, we have used the emission channeling (EC) technique to determine the occupied lattice sites of the optical dopant Er, the transition metals Fe, Cu and Ag, the electrical dopant In, and Sn, which is an isovalent impurity in Ge. According to common expectation, almost all implanted impurities have been found partly on the substitutional site in Ge. The only exception is Er, which has been observed on the tetrahedral interstitial site. However, the most striking result is the occupation of a second high-symmetry site – the bond-centered site – by all of the investigated impurities!

In order to determine the origin of the BC fraction, we have performed complementary *ab initio* density functional calculations. These calculations have shown that the impurity-vacancy complex in the full-vacancy configuration (i.e. with the impurity on the S site) is unstable and

that the defect spontaneously evolves to the split-vacancy configuration (i.e. with the impurity on the BC site). Furthermore, the calculated heats of formation for several configurations have led to the conclusion that it is energetically favorable for the impurities to trap vacancies. These vacancies are abundantly available during the ion implantation process and will migrate through the Ge crystal until they recombine, form vacancy clusters or become trapped by an impurity.

Although this BC behavior was predicted from theoretical calculations for oversized impurities in Ge, no experimental observation of impurities on the bond-centered site in Ge has been reported in literature yet. In this PhD thesis, we have presented experimental evidence, corroborated by theoretical calculations, that the investigated impurities occupy the BC site in an impurity-vacancy complex. Moreover, by externally introducing vacancies, it should be possible to change the lattice site of the impurities, i.e. to relocate the substitutional impurities towards the BC site. In this way, one could alter the electrical (of Fe, Cu, Ag and In) and optical properties (Er) of impurities in Ge.

Via this unique combination of the experimental observation of the BC site with the EC technique and the density functional calculations, we have been able to attribute a specific structural configuration to defects, which have been observed in earlier perturbed angular correlation (PAC) and Mössbauer spectroscopy (MS) experiments. We have shown that the In-V defect, observed in PAC experiments, was incorrectly attributed to the full-vacancy configuration, and should be attributed to the split-vacancy configuration. By calculating the hyperfine parameters of Fe and Sn on different lattice sites, we have also shown that some of the MS-lines have been attributed incorrectly.

The observation of impurity-vacancy complexes is particularly important for diffusion properties in Ge as well. Since group III, IV and V dopants diffuse via the vacancy-mediated mechanism, the structural configuration of the impurity-vacancy complex is important to understand the diffusion behavior and to use as input parameter in theoretical diffusion studies.

Finally, it is noteworthy that the implantation-induced defects play an important role in the lattice location study of impurities, performed with the emission channeling technique. Firstly, due to the deterioration of the crystal structure after implantation, there is an enhanced probability that the emitted electrons will be dechanneled. This results in an isotropic background to the patterns and consequently in an increase of the random fraction, and hence influences the quantitative analysis of the emission channeling spectra. Secondly, we have shown that the introduction of vacancies can induce a relocation of the substitutional impurities towards the BC site.

In this research, we have investigated the ion implantation process in germanium from different lines of approach. Summarizing, we have performed a structural and electrical characterization study of the implantation-induced damage on one hand and a detailed experimental and theoretical lattice location study of implanted impurities in Ge on the other hand. We can conclude to have presented a significant contribution in filling the huge knowledge gap on ion implantation in Ge.

APPENDIX A

PROBE DECAY SCHEMES

This appendix contains the decay schemes of the radioactive probes that have been used in the emission channeling experiments, in order to determine the lattice location of impurities in a host single crystalline lattice. Two of these radioactive probes (^{167}Tm and ^{111}In) decay by the emission of conversion electrons, as can be seen in Fig. A.1. The other probes ^{59}Mn, ^{67}Cu, ^{111}Ag and ^{121}Sn, decay by pure β^--emission, and their decay schemes are plotted in Fig. A.2.

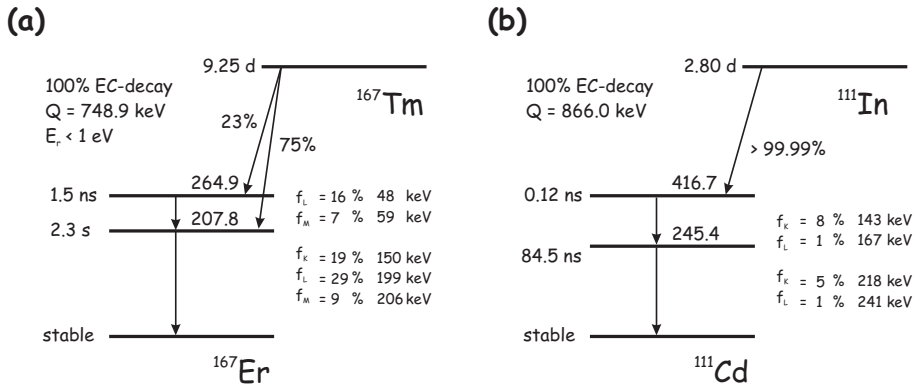

Figure A.1: The conversion electron decay schemes of (a) ^{167}Tm and (b) ^{111}In.

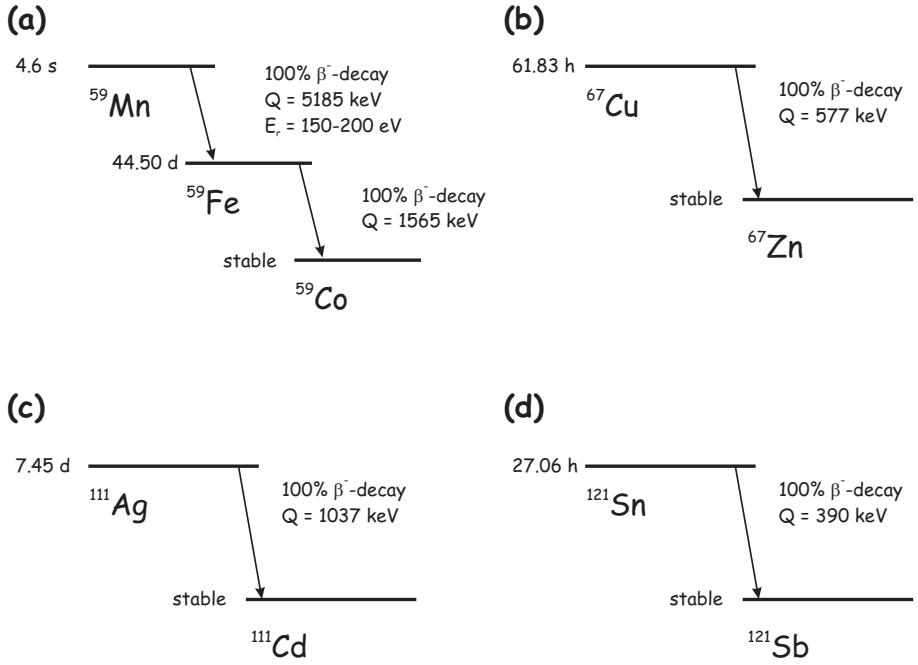

Figure A.2: The β^--decay schemes of (a) ^{59}Mn, (b) ^{67}Cu, (c) ^{111}Ag and (d) ^{121}Sn.

APPENDIX B

BACKGROUND CORRECTION FACTORS

In Tab. B.1, the background correction factors for each emission channeling experiment are given, as calculated from the Geant4 simulations. The set-up numbers in Tab. B.1 have no extra meaning for the reader, but are meant to provide a general feeling about the differences that can occur between the correction factors for different experimental set-ups. All simulations have been done for 60 keV implantations (with an exception of two ^{167}Tm experiments which have been performed with an energy of 30 keV) and with the sample perpendicular to the direction of the detector. Simulations under different angles only result in minor changes of the order of a percent.

	set-up 1	set-up 2	set-up 2b[a]	set-up 4
^{167}Tm		2.51 / 2.49[b]	1.80[b]	
^{59}Mn	1.81	3.01		
^{67}Cu	1.73	3.06	2.62	
^{111}Ag	2.09	3.95		
^{111}In	1.86	2.96	2.64	
^{121}Sn				1.76

Table B.1: Background correction factors for the isotopes and experimental set-ups used in this work.
[a] This set-up is similar to setup 2, but has an extra valve which separates the detector from the vacuum chamber.
[b] This correction factor was calculated for ^{167}Tm implanted with 30 keV instead of 60 keV.

NEDERLANDSTALIGE SAMENVATTING

Inleiding

De ontwikkelingen in de halfgeleiderindustrie kunnen fenomenologisch beschreven worden door de wet van Moore, die stelt dat elk anderhalf jaar het aantal transistoren per chip verdubbelt, net als de snelheid van de schakelingen. Om de komende jaren aan deze wet te blijven voldoen, is het echter niet voldoende om de dimensies van de transistor te blijven verkleinen, maar moeten ook de intrinsieke eigenschappen van de transistor aanzienlijk verbeterd worden. Eén van die eigenschappen, die de voorbije twee decennia intensief onderzocht zijn, is de mobiliteit van de ladingsdragers. Door het gebruik van vervormd (*strained*) silicium (Si), is het mogelijk gebleken om de mobiliteit te verhogen, en dusdanig de werkingssnelheid van elke transistor en dus van de geïntegreerde schakelingen te verhogen. Echter, aangezien de mobiliteit in germanium (Ge) 3 à 4 keer groter is dan in Si, en beide groep IV halfgeleiders gelijkaardige chemische eigenschappen hebben, geniet Ge de laatste decennia heel wat internationale belangstelling als alternatief voor Si in de geïntegreerde schakelingen van de toekomst.

De meest gebruikte techniek om halfgeleiders te doperen is ionenimplantatie. De belangrijkste voordelen van deze techniek zijn de nauwkeurige bepaling van de concentratie en het diepteprofiel van de geïmplanteerde onzuiverheden, en de isotopische zuiverheid die hiermee bereikt wordt. Aangezien het productieproces van een geïntegreerde schakeling gemakkelijk 10 tot 30 implantatiestappen bevat, is deze techniek reeds zeer intensief bestudeerd in Si. De beschikbare literatuur over implantatiegerelateerd onderzoek in Ge is echter relatief summier, en bijgevolg willen we met deze doctoraatsthesis enkele specifieke facetten van ionenimplantatie in Ge in detail bestuderen.

Een belangrijk nadeel van ionenimplantatie is de structurele roosterschade die hierbij gecreëerd wordt, waardoor de fundamentele eigenschappen van de halfgeleider in sterke mate beïnvloed worden. Bovendien kunnen deze defecten aanleiding geven tot geïnduceerde elektronische niveaus in de energiekloof van de halfgeleider. Een goed begrip van de implantatie-geïnduceerde roosterschade is bijgevolg van groot belang en vormt het uitgangspunt van het *eerste* deel van deze doctoraatsthesis. Meer bepaald zullen we het accumulatie- en het herstelproces van de roosterschade na ionenimplantatie bestuderen in functie van verschillende parameters: de energie en de massa van de geïmplanteerde ionen, de dosis en de stroomdichtheid. Zowel de structurele schade (type defecten, de roostervervorming, de amorfisatiedrempel, ...) als de elektrische schade (geïnduceerde niveaus in de energiekloof) na ionenimplantatie in Ge zullen uitvoerig gekarakteriseerd worden.

Een tweede belangrijk aspect met betrekking tot ionenimplantatie, is de plaats die de geïmplanteerde onzuiverheden innemen in het kristalrooster. De exacte roosterpositie van de onzuiverheden heeft namelijk een grote invloed op de elektrische, optische of magnetische activatie van de doperingsatomen in een halfgeleider. In het *tweede* deel van deze doctoraatsthesis zullen we daarom de roosterplaats bepalen van een selectie onzuiverheden: het optische doperingsatoom Er, de transitiemetalen Fe, Cu en Ag, het elektrische doperingsatoom In en het isovalente Sn.

1 Implantatieschade in Ge

1.1 Structurele karakterisering

Experimentele methoden

Om de structurele schade na ionenimplantatie te karakteriseren hebben we gebruik gemaakt van twee experimentele technieken. Enerzijds hebben we met behulp van Rutherford terugverstrooiings- en kanalisatiespectrometrie (RBS/C) de hoeveelheid verplaatste Ge-atomen en de relatieve kristallijne kwaliteit (defectfractie) van het Ge-rooster bepaald. Deze techniek maakt gebruik van het kanalisatie-effect dat geladen deeltjes ($^4He^+$-ionen) ondervinden wanneer ze volgens een kristalas op een éénkristallijn rooster invallen. Dit kanalisatie-effect zal echter minder uitgesproken zijn naarmate het rooster meer defecten bevat en de fractie terugverstrooide He-ionen is op die manier een maat voor het aantal verplaatste Ge-roosteratomen.

Anderzijds is het geweten dat er bij ionenimplantatie een aanzienlijke hoeveelheid defecten gecreëerd worden, waarvan de aanwezige enkelvoudige defecten (zoals vacatures en interstitiëlen) ervoor zorgen dat het kristal plaatselijk vervormd wordt. Door met behulp van X-stralen diffractie (XRD) de afstand tussen de verschillende roostervlakken van het geïmplanteerde monster te bepalen, is het mogelijk om dieptegevoelige informatie te verkrijgen over de roostervervorming, hetgeen indirect bijdraagt tot de structurele karakterisering van de implantatiegeïnduceerde roosterschade.

We hebben met behulp van beide technieken zowel het accumulatie- als het herstelproces van de structurele roosterschade bestudeerd in functie van verschillende implantatieparameters. Alle implantaties zijn uitgevoerd in het ionen- en moleculaire bundellaboratorium aan de K.U.Leuven en de gebruikte implantatieparameters staan getabelleerd op pagina 41.

Resultaten

Accumulatie van de roosterschade: Het accumulatieproces van de roosterschade is opgedeeld in drie regimes, afhankelijk van de implantatiedosis. Bij lage dosissen (*regime 1*) is het Ge-rooster nog grotendeels kristallijn en zijn zowel de roostervervorming als de defectfractie lineair afhankelijk van de implantatiedosis. Het diepteprofiel van beide grootheden is vergelijkbaar met dat van het berekende vacatureprofiel uit Monte-Carlo simulaties (SRIM [27]). Bovendien is de maximale roostervervorming lineair afhankelijk van de hoeveelheid energie die per ion afgegeven wordt aan het rooster tijdens nucleaire interacties – en dus onder andere omgezet wordt in de aanmaak van vacatures. Hieruit kunnen we afleiden dat er voornamelijk enkelvoudige en geïsoleerde defecten aanwezig zijn in het licht beschadigde Ge-kristalrooster na ionenimplantatie bij lage dosis.

In regime 2, waarbij het geïmplanteerde gebied zowel uit kristallijne als amorfe regio's bestaat, is er een duidelijke verhoging van de efficiëntie van het schade-accumulatieproces waarneembaar. Met andere woorden, een inkomend ion creëert relatief gezien meer schade in regime 2 dan in regime 1. Dit is een gevolg van het reeds beschadigde rooster, waarbij nieuwe (kleine) defecten gemakkelijker kunnen agglomereren met bestaande defecten. De kans dat enkelvoudige defecten kunnen annihileren of relaxeren wordt kleiner (i.e. minder dynamische uitgloeiing), hetgeen leidt tot een verhoogde efficiëntie van het schadevormingsproces. Aangezien de vervormingsprofielen in regime 2 totaal verschillend zijn van de profielen uit regime 1 en van de berekende vacatureprofielen, kunnen we besluiten dat er, naast geïsoleerde defecten, ook complexe defecten en zelfs amorfe gebieden aanwezig zijn in regime 2.

Uit de studie naar de invloed van de stroomdichtheid op de geïnduceerde roosterschade bij dosissen uit regime 2, is gebleken dat de hoeveelheid roosterschade toeneemt bij hogere stroomdichtheid. Een hogere stroomdichtheid zorgt voor een groter aantal defecten in het geïmplanteerde gebied in een bepaalde tijdsspanne. Deze defecten kunnen relatief

gemakkelijk agglomereren, hetgeen resulteert in minder dynamische uitgloeiing en meer remanente schade. Bij lage stroomdichtheid is de defectdichtheid binnen eenzelfde tijdsspanne lager, waardoor veel meer simpele defecten kunnen annihileren of relaxeren.
Vanaf een bepaalde kritische dosis (*regime 3*) treedt volledige amorfisatie op. Deze dosis, ook wel de amorfisatiedrempel genoemd, hebben we bepaald in functie van verschillende implantatieparameters. Hierbij is duidelijk geworden dat de amorfisatiedrempel sterk afhangt van de massa van de geïmplanteerde ionen maar niet van hun initiële energie. Dit laat ons toe om te besluiten dat niet zozeer de totale hoeveelheid gedeponeerde energie een belangrijke factor is voor amorfisatie, maar wel de defectdichtheid. Zware ionen worden sneller afgeremd dan lichte ionen, hetgeen resulteert in een hoge defectdichtheid in het geïmplanteerde gebied. Ionen met een relatief hoge energie, penetreren dieper in het materiaal, waardoor de grotere hoeveelheid te deponeren energie gecompenseerd wordt door het grotere volume waarin deze energie gedeponeerd wordt. Aangezien zowel de chemisch inerte edelgassen (Ne, Ar, Kr en Xe) als de meer reactieve elementen Co en In eenzelfde amorfisatiegedrag vertonen, kunnen we besluiten dat de chemische eigenschappen van de geïmplanteerde elementen geen grote rol spelen in het schadevormingsproces.

Herstel van de roosterschade: We hebben het herstelproces van de structurele roosterschade in kaart gebracht door de roostervervorming en de defectfractie te bestuderen na snelle thermische uitgloeiing (RTA) op verschillende temperaturen. Uit deze studie is gebleken dat we te maken hebben met twee belangrijke uitgloeiregimes. Eerst en vooral is er de uitgloeiing bij 100 °C, waarbij enerzijds defecten in het volledige implantatiegebied van licht-beschadigde monsters hersteld worden en anderzijds ook de defecten uit de staart van het implantatieprofiel bij zwaar-beschadigde of zelfs volledig amorfe monsters uitgegloeid worden. Hieruit kunnen we afleiden dat in dit uitgloeiregime (100 °C) vooral simpele, geïsoleerde defecten uit het Ge-rooster verwijderd worden. Boven-

dien kunnen we concluderen dat de defecten in licht-beschadigde monsters gelijkaardig zijn aan de defecten die aanwezig zijn in de staart van het implantatieprofiel van zwaar-beschadigde monsters.
Het tweede uitgloeiregime wordt gekarakteriseerd door de rekristallisatie van amorfe Ge-zones, na uitgloeiing bij 350 °C. Deze rekristallisatie gebeurt enkel aan het amorf-kristallijn overgangsgebied.

Vergelijking Ge versus Si: Wanneer de resultaten uit deze studie vergeleken worden met wat er in de literatuur te vinden is over implantatieschade in Si, is het duidelijk dat er een groot verschil is tussen de amorfisatiedrempel in beide groep-IV halfgeleiders. De dosis die nodig is om Si te amorfiseren is typisch 2 grootteordes groter dan in Ge, hetgeen samenhangt met de minder sterke atomaire binding in het Ge-rooster en de lagere smelttemperatuur van Ge ten opzichte van Si. Desondanks dit grote verschil, vertoont de invloed van de bestudeerde implantatieparameters op de geaccumuleerde roosterschade bij beide halfgeleiders veel gelijkenissen: de opsplitsing in verschillende regimes aan de hand van de dosis, de amorfisatiedrempel die onafhankelijk is van de energie van de ionen, het groter aantal defecten bij hogere stroomdichtheid, etc.

1.2 Elektrische karakterisering

Experimentele methode

Om de roosterschade elektrisch te karakteriseren hebben we gebruik gemaakt van ‘deep level transient spectroscopy’ (DLTS). Met deze methode is het mogelijk om de geïnduceerde elektrische niveaus in de energiekloof van de halfgeleider te bestuderen. Hiervoor wordt de lichtgedopeerde halfgeleider – waarin we de defecten willen bestuderen – in contact gebracht met een metaal of een sterk-gedopeerde halfgeleider. Hierdoor ontstaat er een ladingsvrije zone, waarin we met behulp van een spanningspuls de defectniveaus momentaan vullen. Na het verdwijnen van de spanningspuls zullen de ladingsdragers terug verdwijnen uit deze defectniveaus, en de snelheid hiervan is afhankelijk van enerzijds

de temperatuur en anderzijds de energie van het niveau. Dit vullen en leeglopen van defectniveaus induceert een variërende capaciteit, hetgeen opgemeten wordt in een typisch DLTS experiment. Uit de verandering van de capaciteit (*transient*) in functie van de temperatuur, is het mogelijk om het energieniveau en de defectconcentratie van de implantatie-geïnduceerde defecten te bepalen. Meer informatie over deze techniek kan gevonden worden in Refs. [201, 202]. In deze thesis hebben we gebruik gemaakt van Ge monsters, gedopeerd met Sb, in contact gebracht met een Pd metaallaag en geïmplanteerd met verschillende implantatieparameters (zie tabel pagina 41).

Resultaten

De elektrische karakterisering van de roosterschade na In-implantatie heeft geleid tot de observatie van vier elektronenvallen of *traps* (Fig. 1 (a)). Uit de vergelijking tussen deze vier niveaus, en de niveaus geïnduceerd na elektronenbestraling (b), kunnen we concluderen dat de defecten gecreëerd na ionenimplantatie verschillend zijn van de (enkelvoudige) defecten na elektronenbestraling. Gelijkaardige DLTS-experimenten na implantatie van B, Ne, Ar, Ge, Kr en Xe (met uitzondering van He (c)) hebben geleid tot dezelfde vier niveaus, hetgeen duidelijk maakt dat deze defecten niet element-gerelateerd zijn. Bijgevolg kunnen we deze vier defecten toekennen aan (combinaties van) intrinsieke defecten (divacatures, di-interstitiëlen, ...) en Sb-gerelateerde defecten. Eén van de vier defecten is reeds geïdentificeerd als een Sb-vacature complex (het zogenaamde *E-center*), terwijl extra studies en complementaire technieken nodig zijn om de oorsprong van de andere drie defecten te achterhalen. Om de thermische stabiliteit van deze defecten te bestuderen zijn de metingen uitgevoerd na verschillende uitgloeiingen. Hierbij hebben we gevonden dat de defectconcentratie sterk afneemt na uitgloeiing op 200 °C. Na 300 °C en meer zijn alle vier de defecten, die aanwezig waren op kamertemperatuur, volledig uitgegloeid, waarna zeer complexe DLTS-spectra verschijnen. Deze spectra worden hoogstwaarschijnlijk beïnvloed

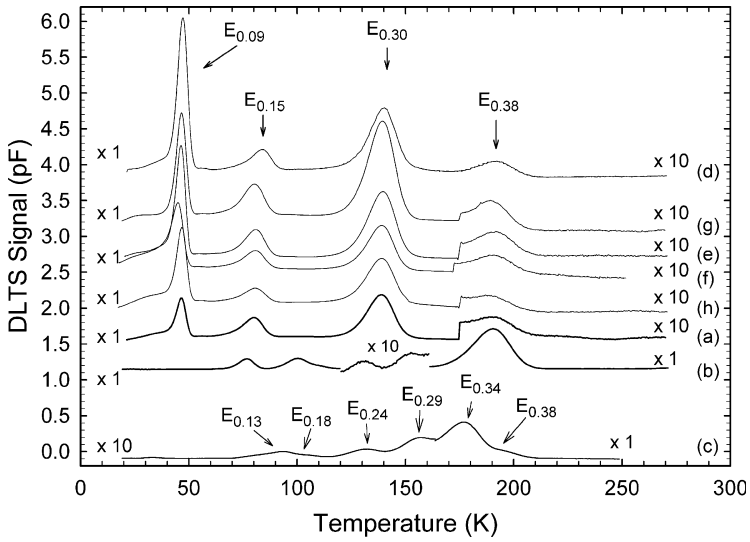

Figuur 1: DLTS spectra van Ge-monsters na implantatie van 160 keV In (a), He (c), Ne (d), Ar (e), Kr (f), Xe (g) en Ge (h) ionen, en na bestraling met hoge-energie elektronen (b).

door germanidevorming aan het grensvlak tussen de Pd-metaallaag en het bulk germanium.

1.3 Vergelijking tussen de structurele en de elektrische karakterisering

De vergelijking maken tussen de resultaten van de structurele en de elektrische karakterisering van de implantatie-geïnduceerde roosterschade is niet eenvoudig, aangezien beide studies uitgevoerd zijn bij verschillende implantatiedosissen. De elektrische karakterisering is uitgevoerd bij zeer lage dosissen (2×10^{11} at/cm^2), voornamelijk om de implantatieschade in de Pd-contacten te minimaliseren. Bij deze lage dosissen zijn de technieken die we gebruikt hebben bij de structurele karakterisering echter niet gevoelig genoeg om gedetailleerde en complementaire informatie over de geïnduceerde defecten te verschaffen. Uit de structurele karakterisering is wel gebleken dat bij de laagste dosissen voornamelijk en-

kelvoudige defecten aanwezig zijn, hetgeen in overeenstemming is met de DLTS metingen, waarbij slechts een beperkt aantal defectniveaus opgemeten zijn. Het is namelijk zeer onwaarschijnlijk dat grote complexe defecten tot de relatief eenvoudige, opgemeten DLTS spectra zouden leiden.
Ondanks de verschillende dosissen die gebruikt zijn, volgt uit beide studies dat de chemische eigenschappen van de geïmplanteerde elementen geen invloed uitoefenen op zowel het schadevormingsproces als op het type elektrische defecten die hierbij gecreëerd worden. Dit is een direct gevolg van het groot aantal defecten (typisch 1000 à 2000 vacature-interstitieel-paren) die per ion geïntroduceerd worden in het Ge-rooster tijdens implantatie. Alhoewel een grote fractie van deze defecten terug zal annihileren, zullen er nog veel intrinsieke defecten en defectclusters gecreëerd worden, tegenover slechts één defect waarvan het onzuiverheidsatoom deel uitmaakt.
Het is belangrijk om op te merken dat de elektrische karakterisering van de defecten bij heel lage dosissen van groot belang is voor een beter begrip van de structurele schadevorming bij hogere dosissen. Deze defecten zijn namelijk de meest logische kandidaten als schadenucleatie-plaatsen – i.e. de basis van de vorming van meer complexe defecten – en kunnen een belangrijke rol spelen bij theoretische berekeningen van de roosterschade na implantatie.

2 Roosterplaatsbepaling van onzuiverheden in Ge

Het tweede luik van deze doctoraatsthesis handelt over de roosterplaats die geïmplanteerde onzuiverheden innemen in het Ge-rooster. Een zeer geschikte techniek hiervoor is emissiekanalisatie (EC). Naast de experimentele resultaten (Sec. 2.1), hebben we ook complementaire theoretische berekeningen uitgevoerd (Sec. 2.2) om een zo volledig mogelijk beeld te verkrijgen over de roosterplaatsen die de onzuiverheden innemen en over de defecten waar ze op die positie deel van uitmaken.

2.1 Emissiekanalisatie-experimenten

Experimentele methode

Emissiekanalisatie is gebaseerd op het kanalisatie-effect dat geladen deeltjes ondervinden wanneer ze doorheen een éénkristallijn rooster bewegen onder invloed van de potentiaal van atomaire rijen en vlakken. In het geval van (elektronen-) emissiekanalisatie zijn deze geladen deeltjes conversie- of β^--elektronen, afkomstig van geïmplanteerde radioactieve isotopen van de te bestuderen onzuiverheid. De emissie van deze elektronen wordt opgemeten langsheen lage-index kristalassen met behulp van een 2-dimensionele energie- en positiegevoelige detector. Afhankelijk van de positie – substitutioneel of interstitieel – van het radioactieve isotoop langsheen een bepaalde kristalas in het rooster, zullen de elektronen respectievelijk een kanalisatie-effect of een obstructie-effect ondervinden langsheen die as, en zullen er respectievelijk meer of minder elektronen waargenomen worden in de detector. Door de experimentele spectra te fitten met gesimuleerde patronen is het mogelijk om de fractionele bezetting van de verschillende roosterplaatsen kwantitatief nauwkeurig te bepalen. Meer informatie over elektronen-kanalisatie in het algemeen en de emissiekanalisatietechniek en de simulaties in het bijzonder, kan gevonden worden in Refs. [205–212].

Resultaten

Erbium Na implantatie bevinden de Er-atomen zich op twee verschillende hoog-symmetrische roosterposities: de tetrahedraal interstitiële positie (T) en de bindingscentrum (BC) positie (Fig. 2 (a)). Aangezien Er ook in Si de T-positie inneemt [175–179], is deze positie niet onverwacht voor Er in een diamantstructuur. Veel minder verwacht, is de fractie Er-atomen op de BC-positie, die ongeveer even groot is als de fractie op de T-positie. Een relatief grote fractie Er-atomen bevindt zich echter niet op hoog-symmetrische roosterposities, hetgeen direct gerelateerd is met de geïnduceerde structurele roosterschade die interfereert met de analyse van de experimentele EC-spectra. Dit wordt verder uit-

gelegd in Sec. 3.

Transitiemetalen De drie bestudeerde transitiemetalen Fe, Cu en Ag bezetten dezelfde hoog-symmetrische roosterposities: enerzijds de substitutionele positie en anderzijds de bindingscentrum positie (Fig. 3). Aangezien tot voor kort algemeen aanvaard werd dat de meeste transitiemetalen zich hoofdzakelijk op de substitutionele positie bevinden, is deze fractie op de BC-positie op zijn minst merkwaardig te noemen. Zoals verder uitgelegd wordt (Sec. 2.2), is deze BC-fractie gerelateerd aan onzuiverheid-vacature complexen in de gesplitste-vacature configuratie.

Indium In overeenstemming met de resultaten uit vroegere RBS/C-experimenten [103, 104], bevindt het merendeel van de In-atomen zich op de substitutionele positie (Fig. 2 (b)). Na uitgloeiing op 300 °C bedraagt de substitutionele fractie ongeveer 90% en blijft ze thermisch stabiel na uitgloeiing tot minstens 500 °C. Direct na implantatie is er echter, net als bij de andere bestudeerde onzuiverheden, een tweede hoog-symmetrische positie die ingenomen wordt, i.e. de bindingscentrum positie. Ondanks de kleine fractie ($\sim$ 15%), kan ook deze roosterplaats gelinkt worden aan In-vacature complexen in de gesplitste-vacature configuratie, in overeenstemming met resultaten uit gestoorde hoekcorrelatie-experimenten (PAC) [59, 61–63, 119–122].

Tin Aangezien Sn een isovalente onzuiverheid is in Ge, kan er verwacht worden dat Sn de substitutionele positie prefereert. Alhoewel de EC-experimenten duidelijk aangetoond hebben dat de meerderheid van de Sn-atomen zich op de S-positie bevindt, is er ook hier een fractie van de onzuiverheden op de BC-positie gevonden (Fig. 2 (c)). Theoretische berekeningen (zie Sec. 2.2) hebben uitgewezen dat de Sn-atomen op de BC-positie deel uitmaken van Sn-vacature complexen. Alhoewel deze BC-positie nog nooit eerder op een directe manier experimenteel waargenomen is voor onzuiverheden in Ge, hebben onze berekeningen aange-

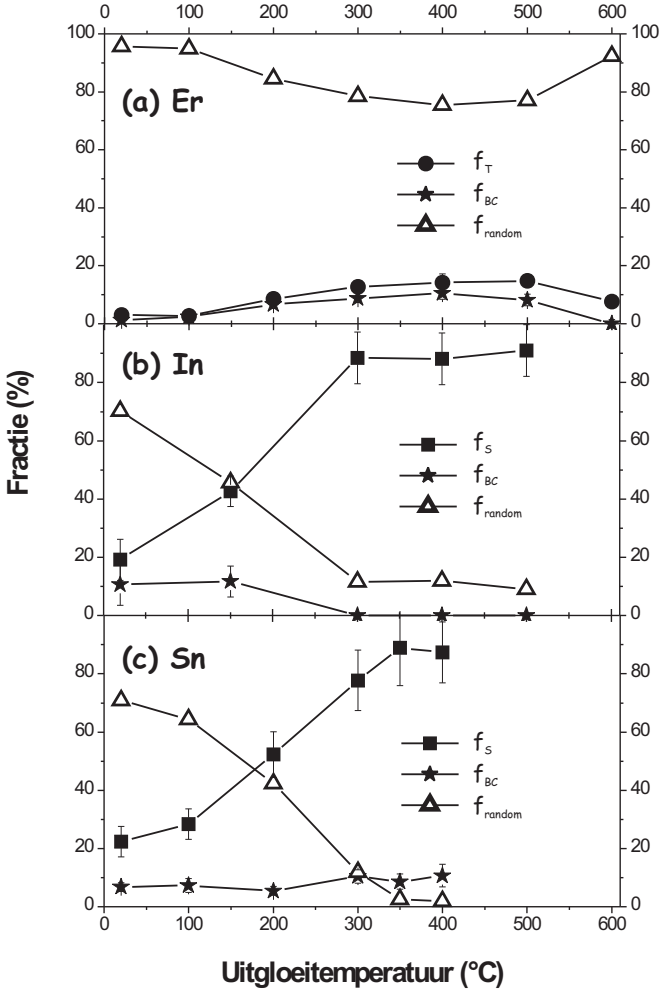

Figuur 2: Fractie van de geïmplanteerde Er (a), In (b) en Sn atomen (c) op de S-positie f_{S} (■), op de T-positie f_{T} (●) en op de BC-positie f_{BC} (★) in Ge, samen met de *random* fractie f_{random} (△ = 100% - ■ (of ●) - ★), in functie van de uitgloeitemperatuur.

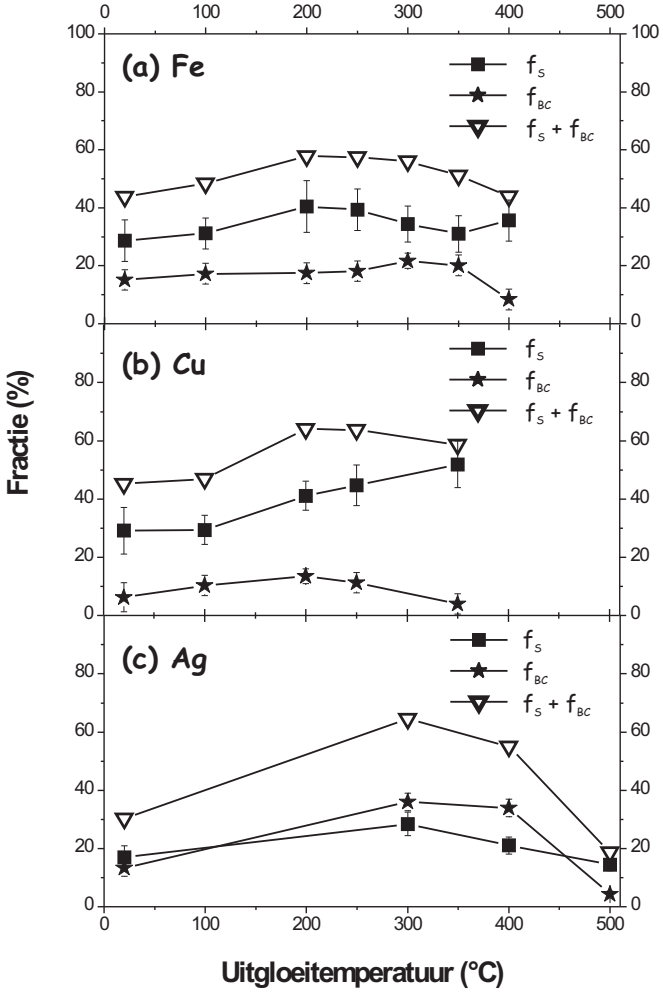

Figuur 3: Fractie van de geïmplanteerde Fe (a), Cu (b) en Ag atomen (c) op de S-positie f_{S} (■) en op de BC-positie f_{BC} (★) in Ge, samen met de totale fractie $f_{\mathrm{S}} + f_{\mathrm{BC}}$ ($\triangledown = ■ + ★$) op hoog-symmetrische posities, in functie van de uitgloeitemperatuur.

toond dat één van de signalen uit vroegere Mössbauerspectroscopie (MS) experimenten met Sn in Ge [133–136], toegewezen kan worden aan de gesplitste-vacature configuratie.

2.2 Theoretische berekeningen

Om complementaire informatie te verkrijgen over de roosterplaats van onzuiverheden en over de structurele configuratie van onzuiverheidsgerelateerde defecten, hebben we naast de EC-experimenten ook *ab initio* berekeningen uitgevoerd. Eerst en vooral hebben we onzuiverheid-vacature complexen bestudeerd. Hiervoor hebben we als startconfiguratie een Ge-matrix beschouwd, met hierin een substitutionele onzuiverheid en een naburige vacature, en deze configuratie hebben we laten relaxeren. Deze relaxatieberekeningen zijn uitgevoerd met Fe, Cu, Ag, In en Sn als onzuiverheid, en telkens werd er door de omringende Ge-atomen een grote kracht uitgeoefend op het onzuiverheidsatoom langsheen de $\langle 111 \rangle$-richting, waarbij de onzuiverheden naar de bindingscentrum (BC) positie verschoven werden met de oorspronkelijke vacature *gesplitst* over de twee naburige S-posities: de gesplitste-vacature configuratie. Deze relaxatieberekeningen zijn volledig in overeenstemming met de toewijzing van de geobserveerde BC-fractie tijdens de EC-experimenten aan de onzuiverheid-vacature complexen. Alhoewel soortgelijke berekeningen voor zeldzame aardes veel ingewikkelder zijn, is het toch mogelijk om informatie te verkrijgen uit de interpolatie van berekeningen voor La en Lu, die minder problemen veroorzaken. Aangezien La-vacature en Lu-vacature complexen ook de gesplitste-vacature configuratie prefereren, kunnen we besluiten dat de geobserveerde fractie Er-atomen op de BC-positie eveneens gerelateerd is aan Er-vacature complexen.

Ten tweede hebben we de vormingsenergie van Fe, Cu, Ag en Sn berekend op de S-positie, de T-positie en de BC-positie na relaxatie van het onzuiverheid-vacature complex. Hieruit is gebleken dat alle vier de onzuiverheden een duidelijk lagere vormingsenergie hebben op de S-positie dan op de T-positie, in overeenstemming met de experimentele

		$\delta_{0\ (theo)}$ (mm/s)	$\Delta E_{Q,0\ (theo)}$ (mm/s)	$\delta_{0\ (exp)}$ (mm/s)	$\Delta E_{Q,0\ (exp)}$ (mm/s)
Fe	S	0.06	0.00	0.059	0.00
	T	1.08	0.00	0.80	0.00
	BC	0.55	0.81	0.46	0.69
Sn	S	1.75	0.00	1.90	0.00
	T	3.19	0.00	3.27	0.00
	BC	2.24	0.15	2.36	0.30
				1.41	

Tabel 1: De berekende isomeerverschuiving $\delta_{0\ (theo)}$ (mm/s) en quadrupool-opsplitsing $\Delta E_{Q,0\ (theo)}$ (mm/s) voor Fe en Sn op de S-positie, de T-positie en de BC-positie in de gesplitste-vacature configuratie bij 0 K, samen met de experimentele isomeerverschuiving $\delta_{0\ (exp)}$ (mm/s) en quadrupool-opsplitsing $\Delta E_{Q,0\ (exp)}$ (mm/s), bekomen uit Mössbauer spectroscopie experimenten voor Fe [162] en Sn [133–136].

observaties. Uit de vergelijking tussen de vormingsenergie van de onzuiverheden op de BC-positie enerzijds, en de vormingsenergie van de onzuiverheden op de S-positie en de vormingsenergie van een geïsoleerde vacature anderzijds, kunnen we concluderen dat het voor alle vier de onzuiverheden energetisch voordelig is om een vacature in te vangen en de gesplitste-vacature configuratie in te nemen. Hieruit volgt er dat het principieel mogelijk moet zijn om substitutionele onzuiverheden te verplaatsen naar de bindingscentrum positie, door simpelweg vacatures te creëren in het Ge-monster. In de EC-experimenten worden er tijdens de implantatie een grote hoeveelheid vacatures gecreëerd, waardoor we een relatief grote fractie onzuiverheden aantreffen op de BC-positie. Andere technieken, zoals bestraling met hoge-energie elektronen zijn hiervoor waarschijnlijk beter geschikt, aangezien er op die manier zeer weinig complexe defecten worden gevormd.

Voor Fe en Sn hebben we bovendien ook de isomeerverschuiving en de quadrupool-opsplitsing berekend op de S-, T- en BC-roosterposities, om deze waarden te vergelijken met de experimentele waarden uit MS experimenten (Tab. 1) [133–136, 162]. De berekeningen voor de S- en de

T-positie zijn vergelijkbaar met de experimentele waarden. Bovendien hebben we sterke aanwijzingen dat voor beide elementen één van de geobserveerde Mössbauersignalen toe te wijzen is aan een probe op de BC-positie, in tegenstelling tot de toewijzing in de desbetreffende artikels voor Sn [133–136] en Fe [162].

2.3 Overzicht van de bezette roosterplaatsen van onzuiverheden in Ge

Samengevat hebben we de roosterplaats van verschillende onzuiverheden in Ge bestudeerd. Met uitzondering van Er, bevindt er zich van elke onzuiverheid een fractie op de S-positie in het Ge-kristal. Aangezien de experimentele trillingsamplitude van deze substitutionele onzuiverheden goed overeenkomt met de verwachte waarde op kamertemperatuur, kunnen we aannemen dat deze onzuiverheden op de S-positie zich in een niet-beschadigde directe omgeving bevinden.

Het belangrijkste resultaat van deze studie is echter de observatie dat een fractie van alle onderzochte onzuiverheden de bindingscentrum positie inneemt. Gesterkt door *ab initio* berekeningen, is deze BC-positie gerelateerd aan onzuiverheid-vacature complexen in de gesplitste-vacature configuratie. Bovendien hebben we aangetoond dat het energetisch voordelig is voor de onzuiverheden om vacatures in te vangen, waarna de configuratie spontaan relaxeert naar de gesplitste-vacature configuratie. Dit resultaat is van groot belang omdat op deze manier de roosterplaats van onzuiverheden, en als dusdanig ook de elektrische of optische (des)activering van doperingsatomen, extern beïnvloed of zelfs gecontroleerd kan worden.

De observatie van onzuiverheidsatomen op de BC-positie in de onzuiverheid-vacature complexen is ook belangrijk voor de vacaturegerelateerde diffusie van onzuiverheden in Ge. De groep III, IV en V onzuiverheden diffunderen via vacatures in Ge: het onzuiverheidsatoom vangt een vacature in, wisselt ermee van plaats waarna de vacature verdwijnt en het proces herbegint. De kennis dat de onzuiverheid-vacature complexen de

gesplitste-vacature configuratie aannemen, is (1) zeer belangrijk om diffusiemodellen op te stellen, (2) het diffusiemechanisme te doorgronden en (3) is belangrijke input voor theoretische diffusieberekeningen.

3 Invloed van de implantatieschade op de roosterplaats van onzuiverheden

In deze doctoraatsthesis hebben we enerzijds de roosterschade bestudeerd na ionenimplantatie in Ge vanuit elektrisch en structureel standpunt, en anderzijds hebben we de roosterplaats van geïmplanteerde onzuiverheden in Ge bepaald. Alhoewel beide onderzoeken niet direct gerelateerd lijken te zijn met elkaar, beïnvloedt de roosterschade toch de analyse van de EC-experimenten en is ze ook mee bepalend voor de roosterplaats die onzuiverheden innemen.
De implantatie-geïnduceerde roosterschade beïnvloedt de kanalisatie van de uitgezonden elektronen op twee manieren. Enerzijds worden elektronen van radioactieve isotopen die zich in een niet-kristallijne omgeving bevinden, isotroper uitgezonden in vergelijking met elektronen, afkomstig van isotopen in een onbeschadigde omgeving. Anderzijds hebben gekanaliseerde elektronen die doorheen een beschadigd kristalrooster bewegen, meer kans om gedekanaliseerd te worden. Beide effecten zorgen voor een minder uitgesproken kanalisatie- en obstructie-effect, en bijgevolg voor een verhoogde isotrope achtergrond in de EC-spectra. Dit resulteert in een schijnbaar lagere fractie onzuiverheidsatomen op hoogsymmetrische posities en dus zijn de opgemeten fracties, in het geval van een beschadigd kristal, een onderlimiet voor de werkelijke fracties.

Ten tweede is het mogelijk, zoals hierboven reeds werd aangehaald, om de roosterplaats van substitutionele onzuiverheden te wijzigen door vacatures toe te voegen aan het kristalrooster. In deze thesis is gebleken dat de vacatures, gecreëerd tijdens het implantatieproces, ingevangen worden door de onzuiverheden op de S-positie waarna de onzuiverheden zich verplaatsen naar de bindingscentrum positie. Op die manier is

het mogelijk om de roosterplaats van onzuiverheden te beïnvloeden door een gecontroleerde hoeveelheid defecten in het kristalrooster te brengen. Vice versa is het in principe ook mogelijk om via de bepaling van de roosterplaats van de onzuiverheden onrechtstreeks de roosterschade te bestuderen.

Conclusies

In deze doctoraatsthesis hebben we twee belangrijke implantatie-gerelateerde onderwerpen onderzocht in germanium: (1) de geïnduceerde structurele en elektrische roosterschade na implantatie en (2) de roosterplaats van geïmplanteerde onzuiverheden.

Vooreerst hebben we de structurele roosterschade na ionenimplantatie in Ge gekarakteriseerd aan de hand van de roostervervorming en de defectfractie in functie van verschillende implantatieparameters. Het schade-accumulatieproces is onder te verdelen in drie regimes naargelang de geïmplanteerde dosis. In het eerste regime, bij de laagste dosis, worden vooral geïsoleerde defecten gecreëerd, terwijl bij hogere dosissen (in het tweede regime) de geïsoleerde defecten gemakkelijker accumuleren tot grotere en meer uitgebreide defecten, met een efficiënter schade-accumulatieproces als gevolg. Het derde regime begint bij de kritische dosis voor amorfisatie. Uit deze studie is gebleken dat de massa van de geïmplanteerde atomen een cruciale rol speelt in het schade-accumulatieproces, terwijl de amorfisatiedrempel onafhankelijk is van de chemische eigenschappen en de energie van de versnelde ionen. Het herstelproces van de schade is op te splitsen in twee fases. Enerzijds is er de uitgloeiing van de kleinere geïsoleerde defecten bij 100 °C en anderzijds treedt er rekristallisatie op van amorf Ge na uitgloeiing op 350 °C. Uit de vergelijking van het schade-accumulatieproces bij Si en Ge kan geconcludeerd worden dat, ondanks het grote verschil in amorfisatiedosis bij beide materialen, de invloed van de bestudeerde implantatieparameters vergelijkbaar is in Ge en in Si.

Naast de structurele karakterisering van de roosterschade, hebben we

ook de geïnduceerde elektronenniveaus in de energiekloof van Sb-gedopeerd Ge bepaald na implantatie. Hierbij zijn er vier defectniveaus waargenomen die duidelijk verschillend zijn van de defectniveaus die gecreëerd worden bij elektronenbestraling. Bovendien zijn deze vier defectniveaus onafhankelijk van het geïmplanteerd element (behalve voor heel lichte ionen zoals He), waaruit we kunnen besluiten dat we te maken hebben met ofwel enkelvoudige intrinsieke defecten ofwel met Sb-gerelateerde defecten. Na uitgloeiing op 300 °C verdwijnen deze defectniveaus.

Samengevat hebben we een uitgebreid overzicht gegeven over de invloed van verschillende implantatieparameters op de structurele en de elektrische roosterschade. Met dit overzicht is het mogelijk om de hoeveelheid schade na ionenimplantatie in Ge te bepalen en zelfs te voorspellen. Deze dieptegevoelige kennis is ook belangrijk voor de interpretatie van resultaten uit andere studies waarin ionenimplantatie in Ge gebruikt wordt of waarin onderzoek gebeurt naar verschillende types defecten in Ge in het algemeen.

In het tweede deel van deze doctoraatsthesis hebben we, via een unieke combinatie van emissiekanalisatie-experimenten en *ab initio* berekeningen, de roosterplaats van Er, Fe, Cu, Ag, In en Sn bestudeerd na implantatie in Ge. Uit deze studie is gebleken dat een fractie van de Er-atomen de tetrahedrale interstitiële (T) positie inneemt, terwijl een fractie van de overige onzuiverheden zich op de substitutionele (S) roosterplaats bevindt. Naast dit min of meer verwacht gedrag, hebben we echter ook een fractie van alle bestudeerde onzuiverheden op een *nieuwe* hoog-symmetrische roosterplaats waargenomen: de bindingscentrum (BC) positie. Via *ab initio* berekeningen hebben we deze roosterpositie kunnen relateren aan onzuiverheid-vacature complexen in de gesplitste-vacature configuratie. Bovendien tonen de berekeningen aan dat het energetisch voordelig is voor de substitutionele onzuiverheidsatomen om vacatures, die veelvuldig geproduceerd worden tijdens het implantatieproces, in te vangen en te relaxeren naar de BC-positie.

Dit resultaat impliceert dat de externe toevoeging van vacatures leidt tot de herpositionering van de onzuiverheidsatomen. Een zeer belangrijk gevolg hiervan is dat het op die manier mogelijk is om ongewenste actieve onzuiverheden op de substitutionele roosterpositie (zoals de transitiemetalen) te verplaatsen naar de bindingscentrum (BC) positie. Met behulp van de resultaten uit deze studie hebben we bovendien enkele onjuiste toewijzingen van signalen uit Mössbauer spectroscopie-experimenten (voor Fe en Sn) en gestoorde-hoek correlatie-experimenten (voor In) aan bepaalde defectconfiguraties kunnen corrigeren, hetgeen de sterkte van deze gecombineerde (experimentele en theoretische) studie nogmaals in de verf zet.
Uiteindelijk hebben we ook aangetoond dat de roosterschade een belangrijke invloed heeft op de roosterplaatsbepaling van onzuiverheden. De implantatie-geïnduceerde roosterschade zorgt voor een verminderd kanalisatie-effect van de elektronen, hetgeen de analyse van de EC-experimenten sterk beïnvloedt. Anderzijds hebben we aangetoond dat de defecten (vacatures) die gecreëerd worden tijdens het implantatieproces, kunnen zorgen voor de herpositionering van de onzuiverheidsatomen.
Samengevat hebben we het implantatieproces in Ge vanuit verschillende standpunten onderzocht en kunnen we concluderen dat we een aanzienlijke bijdrage hebben geleverd aan het fundamentele onderzoek naar ionenimplantatie in Ge.

Bibliography

[1] H. C. A. Winkler, *Mittheilungen über das Germanium*, J. Prak. Chemie **34** (1886), 177.

[2] E. E. Haller, *Germanium: From its discovery to SiGe devices*, Mat. Sci. Semicond. Proc. **9** (2006), 408.

[3] E. Simoen and C. Claeys, *Germanium-based technologies: From materials to devices*, Elsevier, Amsterdam, 2007.

[4] J. Bardeen and W. H. Brattain, *Physical principles involved in transistor action*, Phys. Rev. **75** (1949), 1208.

[5] M. L. Lee and E. A. Fitzgerald, *Strained Si/strained Ge dual-channel heterostructures on relaxed $Si_{0.5}Ge_{0.5}$ for symmetric mobility p-type and n-type metal-oxide-semiconductor field-effect transistors*, Appl. Phys. Lett. **83** (2003), 4202.

[6] M. L. Lee, E. A. Fitzgerald, M. T. Bulsara, M. T. Currie, and A. Lochtefeld, *Strained Si, SiGe, and Ge channels for high-mobility metal-oxide-semiconductor field-effect transistors*, J. Appl. Phys. **97** (2005), 011101.

[7] M. Ieong, B. Doris, J. Kedzierski, K. Rim, and M. Yang, *Silicon device scaling to the sub-10-nm regime*, Science **306** (2004), 2057.

[8] K. Rim, K. Chan, L. Shi, D. Boyd, J. Ott, N. Klymko, F. Cardone, L. Tai, S. Koester, M. Cobb, D. Canaperi, B. To, E. Duch, I. Babich, R. Carruthers, P. Saunders, G. Walker, Y. Zhang, M. Steen, and M. Ieong, *Fabrication and mobility characteristics of ultra-thin strained Si directly on insulator (SSDOI) MOSFETs*, IEDM Tech. Dig. **2003** (2003), 03.49.

[9] A. Dimoulas, E. Gusev, P. C. McIntyre, and M. Heyns, *Advanced gate stacks for high-mobility semiconductors*, Springer Series in Advanced Microelectronics, 2007.

[10] P. W. Loscutoff and S. F. Bent, *Reactivity of the germanium surface: Chemical passivation and functionalization*, Ann. Rev. Phys. Chem. **57** (2006), 467.

[11] M. Houssa, G. Pourtois, B. Kaczer, B. De Jaeger, F. E. Leys, D. Nelis, K. Paredis, A. Vantomme, M. Caymax, M. Meuris, and M. M. Heyns, *Experimental and theoretical study of Ge surface passivation*, Microelec. Eng. **84** (2007), 2267.

[12] A. Delabie, F. Bellenger, M. Houssa, T. Conard, S. Van Elshocht, M. Caymax, M. Heyns, and M. Meuris, *Effective electrical passivation of Ge(100) for high-κ gate dielectric layers using germanium oxide*, Appl. Phys. Lett. **91** (2007), 082904.

[13] F. Bellenger, M. Houssa, A. Delabie, V. Afanasiev, T. Conard, M. Caymax, M. Meuris, K. De Meyer, and M. M. Heyns, *Passivation of Ge(100)/GeO_2/high-κ gate stacks using thermal oxide treatments*, J. Electrochem. Soc. **155** (2008), G33.

[14] J. R. Weber, A. Janotti, P. Rinke, and C. G. Van de Walle, *Dangling-bond defects and hydrogen passivation in germanium*, Appl. Phys. Lett. **91** (2007), 142101.

[15] A. Dimoulas, G. Mavrou, G. Vellianitis, E. Evangelou, N. Boukos, M. Houssa, and M. Caymax, *HfO_2 high-κ gate dielectrics on Ge(100) by atomic oxygen beam deposition*, Appl. Phys. Lett. **86** (2005), 032908.

[16] M. Houssa, D. Nelis, D. Hellin, G. Pourtois, T. Conard, K. Paredis, K. Vanormelingen, A. Vantomme, M. K. Van Bael, J. Mullens, M. Caymax, M. Meuris, and M. M. Heyns, *H_2S exposure of a (100) Ge surface: Evidence for a 2×1 electrically passivated surface*, Appl. Phys. Lett. **90** (2007), 222105.

[17] S. Nakaharai, T. Tezuka, N. Sugiyama, Y. Moriyana, and S. Takagi, *Characterization of 7-nm-thick strained Ge-on-insulator layer fabricated by Ge-condensation technique*, Appl. Phys. Lett. **83** (2003), 3516.

[18] S. Nakaharia, T. Tezuka, and S. Takagi, May 2005, U.S. Patent No. US2005/0098234 A1.

[19] S. Balakumar, C. H. Tung, G. Q. Lo, R. Kumar, N. Balasubramanian, and D. L. Kwong, *Solid phase epitaxy during Ge condensa-*

tion from amorphous SiGe layer on silicon-on-insulator substrate, Appl. Phys. Lett. **89** (2006), 032101.

[20] B. G. Min, Y. H. Pae, K. S. Jun, D. H. Koa, H. Kim, M. H. Cho, and T. W. Lee, *Formation of a Ge-rich layer during the oxidation of strained $Si_{1-x}Ge_x$*, J. Appl. Phys. **100** (2006), 016102.

[21] L. Souriau, V. Terzievaa, W. Vandervorst, F. Clemente, B. Brijs, A. Moussa, M. Meuris, R. Loo, and M. Caymax, *High Ge content SGOI substrates obtained by the Ge condensation technique: A template for growth of strained epitaxial Ge*, Thin Solid Films **517** (2008), 23.

[22] T. Schmidt, R. Kröger, T. Clausen, J. Falta, A. Janzen, M. Kammler, P. Kury, P. Zahl, and M. Horn-von Hoegen, *Surfactant-mediated epitaxy of Ge on Si(111): Beyond the surface*, Appl. Phys. Lett. **86** (2005), 111910.

[23] M. Halbwax, D. Bouchier, V. Yam, D. Débarre, L. H. Nguyen, Y. Zheng, P. Rosner, M. Benamara, H. P. Strunk, and C. Clerc, *Kinetics of Ge growth at low temperature on Si(001) by ultra-high vacuum chemical vapor deposition*, J. Appl. Phys. **97** (2005), 064907.

[24] G. Vanamua, A. K. Datye, and S. H. Zaidi, *Epitaxial growth of high-quality Ge films on nanostructured silicon substrates*, Appl. Phys. Lett. **88** (2006), 204104.

[25] T. H. Loh, H. S. Nguyen, C. H. Tung, A. D. Trigg, G. Q. Lo, N. Balasubramanian, D. L. Kwong, and S. Tripathy, *Ultrathin low temperature SiGe buffer for the growth of high quality Ge epilayer on Si(100) by ultrahigh vacuum chemical vapor deposition*, Appl. Phys. Lett. **90** (2007), 092108.

[26] M. A. Wistey, Y. Y. Fang, J. Tolle, A. V. G. Chizmeshya, and J. Kouvetakisa, *Chemical routes to Ge/Si(100) structures for low temperature Si-based semiconductor applications*, Appl. Phys. Lett. **90** (2007), 082108.

[27] J.F. Ziegler, J.P. Biersack, and U. Littmark, *The stopping and*

range of ions in solids, Pergamon Press, New York, 1985.

[28] J. J. Loferski and P. Rappaport, *Displacement thresholds in semiconductors*, J. Appl. Phys. **30** (1959), 1296.

[29] C. Claeys and J. Vanhellemont, *Recent progress in the understanding of crystallographic defects in silicon*, J. Cryst. Growth **126** (1993), 41.

[30] A. Stesmans, *Fundamentals of defects in materials*, 2003, (Doctoral Course, K.U.Leuven).

[31] R. J. D. Tilley, *Defects in solids*, John Wiley & Sons, New Jersey, 2008.

[32] J. F. Gibbons, *Ion implantation in semiconductors – Part II: Damage production and annealing*, Proceedings of the IEEE **60** (1972), 1062.

[33] G. Hobler and G. Otto, *Status and open problems in modeling of as-implanted damage in silicon*, Mat. Sci. Semicond. Proc. **6** (2003), 1.

[34] L. Pelaz, L. A. Marqués, and J. Barbolla, *Ion-beam-induced amorphization and recrystallization in silicon*, J. Appl. Phys. **96** (2004), 5947.

[35] F. Seitz., *On the disordering of solids by action of fast massive particles*, Discuss. Faraday Soc. **5** (1949), 271.

[36] N. Hecking, K. F. Heidemann, and E. Te Kaat, *Model of temperature dependent defect interaction and amorphization in crystalline silicon during ion irradiation*, Nucl. Instrum. Methods Phys. Res. B **15** (1986), 760.

[37] F. F. Morehead and B. L. Crowder, *A model for the formation of amorphous Si by ion bombardment*, Radiat. Eff. **6** (1970), 27.

[38] J. R. Dennis and E. B. Hale, *Crystalline to amorphous transformation in ion-implanted silicon: A composite model*, J. Appl. Phys. **49** (1978), 1119.

[39] L. A. Marqués, L. Pelaz, J. Hernandez, J. Barbolla, and H. Gilmer,

Stability of defects in crystalline silicon and their role in amorphization, Phys. Rev. B **64** (2001), 045214.

[40] L. A. Marqués, L. Pelaz, M. Aboy, L. Enríquez, and J. Barbolla, *Microscopic description of the irradiation-induced amorphization in silicon*, Phys. Rev. Lett. **91** (2003), 135504.

[41] L. Pelaz, L. A. Marqués, M. Aboy, J. Barbolla, and G. H. Gilmer, *Atomistic modeling of amorphization and recrystallization in silicon*, Appl. Phys. Lett. **82** (2003), 2038.

[42] K. R. C. Mok, M. Jaraiz, I. Martin-Bragado, J. E. Rubio, P. Castrillo, R. Pinacho, J. Barbolla, and M. P. Srinivasan, *Ion-beam amorphization of semiconductors: A physical model based on the amorphous pocket population*, J. Appl. Phys. **98** (2005), 046104.

[43] K. R. C. Mok, F. Benistant, M. Jaraiz, J. E. Rubio, P. Castrillo, R. Pinacho, and M. P. Srinivasan, *Comprehensive model of damage accumulation in silicon*, J. Appl. Phys. **103** (2008), 014911.

[44] International Technology Roadmap for Semiconductors, `http://public.itrs.net/`.

[45] M. Pasemann, D. Hoehl, A. L. Aseev, and O. P. Pchelyakov, *Analysis of rod-like defects in silicon and germanium by means of high-resolution electron microscopy*, Phys. Status Solidi (A) **80** (1983), 135.

[46] H. Bartsch, D. Hoehl, and G. Kästner, *Radiation-induced rod-like defects in silicon and germanium*, Phys. Status Solidi (A) **83** (1984), 543.

[47] S. Pizzini, W. Schröter, and H. Cerva, *Defect interaction and clustering in semiconductors: Interaction of point defects with dislocations in silicon and germanium: Electrical and optical effects*, Trans Tech Publications, 2002.

[48] E. E. Haller, W. L. Hansen, and F. S. Goulding, *Physics of ultra-pure germanium*, Adv. Phys. **30** (1981), 93.

[49] J. C. Bourgoin, P. M. Mooney, and F. Poulin, *Irradiation-induced*

defects in germanium, Inst. Phys. Conf. Ser. **59** (1980), 33.

[50] K. Ito, I. Baba, K. Mizuno, and T. Ito, *Interaction of point defects with implanted hydrogen in undoped germanium*, Materials Science Forum **10** (1986), 1171.

[51] N. Fourches, G. Walter, and J. C. Bourgoin, *Neutron-induced defects in high-purity germanium*, J. Appl. Phys. **69** (1991), 2033.

[52] P. Marie, M. Levalois, and P. Bogdanski, *Deep level transient spectroscopy of high-energy heavy ion irradiation-induced defects in n-type germanium*, J. Appl. Phys. **74** (1993), 868.

[53] P. Marie and M. Levalois, *Hole traps produced by swift heavy ion irradiation in p-type germanium*, J. Appl. Phys. **75** (1994), 1852.

[54] A. Colder, M. Levalois, and P. Marie, *Study of electron, proton, and swift heavy ion irradiation of n-type germanium using deep level transient spectroscopy*, J. Appl. Phys. **88** (2000), 3082.

[55] A. R. Peaker, V. P. Markevich, L. I. Murin, N. V. Abrosimov, and V. V. Litvinov, *Ion implantation and electron irradiation damage in unstrained germanium and silicon-germanium alloys*, Mat. Sci. Eng. B **124** (2005), 166.

[56] Vl. Kolkovsky, M. Christian Petersen, and A. Nylandsted Larsen, *Alpha-particle irradiation-induced defects in n-type germanium*, Appl. Phys. Lett. **90** (2007), 112110.

[57] V. P. Markevich, S. Bernardini, I. D. Hawkins, A. R. Peaker, Vl. Kolkovsky, A. Nylandsted Larsen, and L. Dobaczewski, *Electrically active defects induced by hydrogen and helium implantations in Ge*, Mat. Sci. Semicond. Proc. (2008), doi:10.1016/j.mssp.2008.09.007.

[58] A. Mesli, L. Dobaczewski, K. Bonde Nielsen, Vl. Kolkovsky, M. Christian Petersen, and A. Nylandsted Larsen, *Low-temperature irradiation-induced defects in germanium: In situ analysis*, Phys. Rev. B **78** (2008), 165202.

[59] H. Hässlein, R. Sielemann, and Ch. Zistl, *Microscopic study of*

the vacancy and self-interstitial in germanium by PAC, Materials Science Forum **258** (1997), 59.

[60] R. Sielemann, *Study of intrinsic defects in semiconductors with radioactive probes*, Nucl. Instrum. Methods Phys. Res. B **146** (1998), 329.

[61] H. Hässlein, R. Sielemann, and C. Zistl, *Vacancies and self-interstitials in germanium observed by perturbed angular correlation spectroscopy*, Phys. Rev. Lett. **80** (1998), 2626.

[62] R. Sielemann, H. Hässlein, L. Wende, and Ch. Zistl, *Frenkel pairs, vacancies, and self-interstitials in Ge: Identification and properties from PAC- and Mössbauer spectroscopy*, Physica B **273** (1999), 565.

[63] R. Sielemann, H. Hässlein, Ch. Zistl, M. Müller, L. Stadler, and V. V. Emtsev, *Vacancies and self-interstitials in germanium: A picture derived from radioactive probes*, Physica B **308** (2001), 529.

[64] A. J. R. da Silva, A. Janotti, A. Fazzio, R. J. Baierle, and R. Mota, *Self-interstitial defect in germanium*, Phys. Rev. B **62** (2000), 9903.

[65] D. Dionizio Moreira, R. H. Miwa, and P. Venezuela, *Electronic and structural properties of germanium self-interstitials*, Phys. Rev. B **70** (2004), 115215.

[66] J. Coutinho, V. J. B. Torres, R. Jones, A. Carvalho, S. Öberg, and P. R. Briddon, *Calculation of deep carrier traps in a divacancy in germanium crystals*, Appl. Phys. Lett. **88** (2006), 091919.

[67] J. Coutinho, V. J. B. Torres, A. Carvalho, R. Jones, S. Öberg, and P. R. Briddon, *Ab initio modeling of defect levels in Ge clusters and supercells*, Mat. Sci. Semicond. Proc. **9** (2006), 477.

[68] H. M. Pinto, J. Coutinho, V. J. B. Torres, S. Öberg, and P. R. Briddon, *Formation energy and migration barrier of a Ge vacancy from ab initio studies*, Mat. Sci. Semicond. Proc. **9** (2006), 498.

[69] J. Lauwaert, S. Hens, P. Śpiewak, D. Wauters, D. Poelman, I. Ro-

mandic, P. Clauws, and J. Vanhellemont, *Simulation of point defect diffusion in germanium*, Physica B **376** (2006), 257.

[70] K. Sueoka and J. Vanhellemont, *Ab initio studies of intrinsic point defects, interstitial oxygen and vacancy or oxygen clustering in germanium crystals*, Mat. Sci. Semicond. Proc. **9** (2006), 494.

[71] A. Carvalho, R. Jones, C. Janke, J. P. Goss, P. R. Briddon, J. Coutinho, and S. Öberg, *Self-interstitial in germanium*, Phys. Rev. Lett. **99** (2007), 175502.

[72] C. Janke, R. Jones, S. Öberg, and P. R. Briddon, *Supercell and cluster density functional calculations of the thermal stability of the divacancy in germanium*, Phys. Rev. B **75** (2007), 195208.

[73] P. Śpiewak, K. Sueoka, J. Vanhellemont, K. J. Kurzydłowski, K. Młyanrczyk, P. Wabínski, and I. Romandic, *Ab initio calculation of the formation energy of charged vacancies in germanium*, Physica B **401** (2007), 205.

[74] P. Śpiewak, M. Muzyk, K. J. Kurzydłowski, J. Vanhellemont, K. Młyanrczyk, P. Wabínski, and I. Romandic, *Molecular dynamics simulation of intrinsic point defects in germanium*, J. Cryst. Growth **303** (2007), 12.

[75] J. Vanhellemont, P. Śpiewak, and K. Sueoka, *On the solubility and diffusivity of the intrinsic point defects in germanium*, J. Appl. Phys. **101** (2007), 036103.

[76] J. W. Mayer, L. Eriksson, S. T. Picraux, and J. A. Davies, *Ion implantation of silicon and germanium at room temperature. Analysis by means of 1.0-MeV helium ion scattering*, Can. J. Phys. **46** (1968), 663.

[77] D. Sigurd, G. Fladda, L. Eriksson, and K. Björkqvist, *Lattice disorder in germanium by ion bombardment*, Radiat. Eff. **3** (1970), 145.

[78] D. Y. C. Lie, A. Vantomme, F. Eisen, T. Vreeland Jr., M. A. Nicolet, T. K. Carns, V. Arbet-Engels, and K. L. Wang, *Damage and strain in epitaxial GeSi films irradiated with Si*, J. Appl. Phys.

74 (1993), 6039.

[79] A. P. Byrne, M. C. Ridgway, C. J. Glover, and E. Bezakova, *Comparative studies using EXAFS and PAC of lattice damage in semiconductors*, Hyperf. Int. **158** (2004), 245.

[80] V. S. Speriosu, B. M. Paine, M. A. Nicolet, and H. L. Glass, *X-ray rocking curve study of Si-implanted GaAs, Si and Ge*, Appl. Phys. Lett. **40** (1982), 604.

[81] K. Nordlund, M. Ghaly, R. S. Averback, M. Caturla, T. Diaz de la Rubia, and J. Tarus, *Defect production in collision cascades in elemental semiconductors and fcc metals*, Phys. Rev. B **57** (1998), 7556.

[82] T. E. Haynes and O. W. Holland, *Comparative study of implantation-induced damage in GaAs and Ge: Temperature and flux dependence*, Appl. Phys. Lett. **59** (1991), 452.

[83] M. Posselt, L. Bischoff, D. Grambole, and F. Herrmann, *Competition between damage buildup and dynamic annealing in ion implantation into Ge*, Appl. Phys. Lett. **89** (2006), 151918.

[84] A. Satta, E. Simoen, T. Janssens, T. Clarysse, B. De Jaeger, A. Benedetti, I. Hoflijk, B. Brijs, M. Meuris, and W. Vandervorst, *Shallow junction ion implantation in Ge and associated defect control*, J. Electrochem. Soc. **153** (2006), G229.

[85] E. Simoen, A. Satta, A. D'Amore, T. Janssens, T. Clarysse, K. Martens, B. De Jaeger, A. Benedetti, I. Hoflijk, B. Brijs, M. Meuris, and W. Vandervorst, *Ion-implantation issues in the formation of shallow junctions in germanium*, Mat. Sci. Semicond. Proc. **9** (2006), 634.

[86] E. Simoen, G. Brouwers, A. Satta, M.-L. David, F. Pailloux, B. Parmentier, T. Clarysse, J. Goossens, W. Vandervorst, and M. Meuris, *Shallow boron implantations in Ge and the role of the pre-amorphization depth*, Mat. Sci. Semicond. Proc. (2008), doi:10.1016/j.mssp.2008.09.006.

[87] A. Kamarou, W. Wesch, E. Wendler, A. Undisz, and M. Retten-

mayr, *Radiation damage formation in InP, InSb, GaAs, GaP, Ge, and Si due to fast ions*, Phys. Rev. B **78** (2008), 054111.

[88] H. Kräutle, *Study of the annealing behaviour of high dose implants in silicon and germanium crystals*, Radiat. Eff. **24** (1975), 255.

[89] J. Slotte, M. Rummukainen, F. Tuomisto, V. P. Markevich, A. R. Peaker, C. Jeynes, and R. M. Gwilliam, *Evolution of vacancy-related defects upon annealing of ion-implanted germanium*, Phys. Rev. B **78** (2008), 085202.

[90] J. A. Burton, *Impurity centers in Ge and Si*, Physica **20** (1954), 845.

[91] M. Friesel, U Södervall, and W. Gust, *Diffusion of tin in germanium studied by secondary-ion mass-spectrometry*, J. Appl. Phys. **78** (1995), 5351.

[92] C. O. Chui, K. Gopalakrishnan, P. B. Griffin, J. D. Plummer, and K. C. Saraswat, *Activation and diffusion studies of ion-implanted p and n dopants in germanium*, Appl. Phys. Lett. **83** (2003), 3275.

[93] Y. L. Chao, S. Prussin, J. C. S. Woo, and R. Scholz, *Preamorphization implantation-assisted boron activation in bulk germanium and germanium-on-insulator*, Appl. Phys. Lett. **87** (2005), 142102.

[94] A. Satta, E. Simoen, T. Clarysse, T. Janssens, A. Benedetti, B. De Jaeger, M. Meuris, and W. Vandervorst, *Diffusion, activation, and recrystallization of boron implanted in preamorphized and crystalline germanium*, Appl. Phys. Lett. **87** (2005), 172109.

[95] S. Mirabella, G. Impellizzeri, A. M. Piro, E. Bruno, and M. G. Grimaldi, *Activation and carrier mobility in high fluence B implanted germanium*, Appl. Phys. Lett. **92** (2008), 251909.

[96] A. Chroneos, D. Skarlatos, C. Tsamis, A. Christofi, D. S. McPhail, and R. Hung, *Implantation and diffusion of phosphorous in germanium*, Mat. Sci. Semicond. Proc. **9** (2006), 640.

[97] A. Satta, E. Simoen, R. Duffy, T. Janssens, T. Clarysse, A. Benedetti, M. Meuris, and W. Vandervorst, *Diffusion, activa-*

tion, and regrowth behavior of high dose P implants in Ge, Appl. Phys. Lett. **88** (2006), 162118.

[98] S. Brotzmann and H. Bracht, *Intrinsic and extrinsic diffusion of phosphorus, arsenic, and antimony in germanium*, J. Appl. Phys. **103** (2008), 033508.

[99] M. Koike, Y. Kamata, T. Ino, D. Hagishima, K. Tatsumura, M. Koyama, and A. Nishiyama, *Diffusion and activation on n-type dopants in germanium*, J. Appl. Phys. **104** (2008), 023523.

[100] M. Naganawa, Y. Shimizu, M. Uematsu, K. M. Itoh, K. Sawano, Y. Shiraki, and E. E. Haller, *Charge states of vacancies in germanium investigated by simultaneous observation of germanium self-diffusion and arsenic diffusion*, Appl. Phys. Lett. **93** (2008), 191905.

[101] P. Tsouroutas, D. Tsoukalas, I. Zergioti, N. Cherkashin, and A. Claverie, *Diffusion and activation of phosphorous in germanium*, Mat. Sci. Semicond. Proc. (2008), doi:10.1016/j.mssp.2008.09.005.

[102] S. Brotzmann, H. Bracht, J. Lundsgaard Hansen, A. Nylandsted Larsen, E. Simoen, E. E. Haller, J. S. Christensen, and P. Werner, *Diffusion and defect reactions between donors, C, and vacancies in Ge. I. Experimental results*, Phys. Rev. B **77** (2008), 235207.

[103] K. Björkqvist, B. Domeij, L. Eriksson, G. Fladda, A. Fontell, and J. W. Mayer, *Lattice location of dopant elements implanted into Ge*, Appl. Phys. Lett. **13** (1968), 379.

[104] K. Björkqvist, D. Sigurd, G. Fladda, and G. Bjarnholt, *Lattice location of heavy group III and V elements implanted into Ge*, Radiat. Eff. **6** (1970), 141.

[105] J. F. Chemin, I. V. Mitchell, and F. W. Saris, *Lattice location of low-Z impurities in medium-Z targets using ion-induced X-rays II: Phosphorus and sulfur implants in germanium single crystals*, J. Appl. Phys. **45** (1974), 537.

[106] J. Fage-Pedersen, A. Nylandsted Larsen, and A. Mesli, *Irradiation-induced defects in Ge studied by transient spectroscopies*, Phys. Rev. B **62** (2000), 10116.

[107] V. P. Markevich, D. Hawkins, A. R. Peaker, K. V. Emtsev, V. V. Emtsev, V. V. Litvinov, L. I. Murin, and L. Dobaczewski, *Vacancy-group-V-impurity atom pairs in Ge crystals doped with P, As, Sb, and Bi*, Phys. Rev. B **70** (2004), 235213.

[108] C. E. Lindberg, J. Lundsgaard Hansen, P. Bomholt, A. Mesli, K. Bonde Nielsen, and A. Nylandsted Larsen, *The antimony-vacancy defect in p-type germanium*, Appl. Phys. Lett. **87** (2005), 172103.

[109] A. Nylandsted Larsen and A. Mesli, *The hidden secrets of the E-center in Si and Ge*, Physica B **401** (2007), 85.

[110] H. Höhler, N. Atodiresei, K. Schroeder, R. Zeller, and P. H. Dederichs, *Cd-vacancy and Cd-interstitial complexes in Si and Ge*, Phys. Rev. B **70** (2004), 155313.

[111] H. Höhler, N. Atodiresei, K. Schroeder, R. Zeller, and P. H. Dederichs, *Impurity-vacancy complexes in Si and Ge*, Hyperf. Int. **158** (2004), 37.

[112] H. Höhler, N. Atodiresei, K. Schroeder, R. Zeller, and P. H. Dederichs, *Vacancy complexes with oversized impurities in Si and Ge*, Phys. Rev. B **71** (2005), 035212.

[113] A. Chroneos, R. W. Grimes, and C. Tsamis, *Atomic scale simulations of arsenic-vacancy complexes in germanium and silicon*, Mat. Sci. Semicond. Proc. **9** (2006), 536.

[114] J. Coutinho, S. Öberg, V. J. B. Torres, M. Barroso, R. Jones, and P. R. Briddon, *Donor-vacancy complexes in Ge: Cluster and supercell calculations*, Phys. Rev. B **73** (2006), 235213.

[115] J. Coutinho, V. J. B. Torres, S. Öberg, A. Carvalho, C. Janke, R. Jones, and P. R. Briddon, *Early stage donor-vacancy clusters in germanium*, J. Mat. Sci. **18** (2007), 769.

[116] A. Chroneos, B. P. Uberuaga, and R. W. Grimes, *Carbon, dopant, and vacancy interactions in germanium*, J. Appl. Phys. **102** (2007), 083707.

[117] A. Chroneos, R. W. Grimes, B. P. Uberuaga, S. Brotzmann, and H. Bracht, *Vacancy-arsenic clusters in germanium*, Appl. Phys. Lett. **91** (2007), 192106.

[118] A. Chroneos, R. W. Grimes, B. P. Uberuaga, and H. Bracht, *Diffusion and defect reactions between donors, C, and vacancies in Ge. II. Atomistic calculations of related complexes*, Phys. Rev. B **77** (2008), 235208.

[119] U. Feuser, R. Vianden, and A. F. Pasquevich, *Defect-acceptor pairs in germanium*, Hyperf. Int. **60** (1990), 829.

[120] U. Feuser, R. Vianden, E. Alves, M. F. da Silva, E. Szilágyi, F. Pászti, and J. C. Soares, *Vacancy-acceptor complexes in germanium produced by ion implantation*, Nucl. Instrum. Methods Phys. Res. B **59** (1991), 1049.

[121] H. Hässlein, R. Sielemann, Grüßler, and H. Metzner, *PAC study of intrinsic defects in germanium: Dependence on doping and defect production*, Hyperf. Int. **84** (1998), 65.

[122] C. J. Glover, A. P. Byrne, and M. C. Ridgway, *Irradiation-induced defect configurations in Ge substrates characterized with perturbed angular correlation*, Nucl. Instrum. Methods Phys. Res. B **175** (2001), 51.

[123] C. Zistl, R. Sielemann, H. Hässlein, S. Gall, D. Bräunig, and J. Bollmann, *DLTS combined with perturbed angular correlation (PAC) on radioactive* ^{111}*In atoms in Ge*, Materials Science Forum **258** (1997), 53.

[124] A. Harwit, P. R. Pukite, J. Angilello, and S. S. Iyer, *Properties of diamond structure SnGe films grown by molecular beam epitaxy*, Thin Solid Films **184** (1990), 395.

[125] R. A. Soref and C. H. Perry, *Predicted band gap of the new semiconductor SiGeSn*, J. Appl. Phys. **69** (1990), 539.

[126] G. He and H. A. Atwater, *Interband transitions in SnGe alloys*, Phys. Rev. Lett. **79** (1997), 1937.

[127] V. R. D'Costa, C. S. Cook, A. G. Birdwell, C. L. Littler, M. Canonico, S. Zollner, J. Kouvetakis, and J. Menendez, *Optical critical points of thin film GeSn alloys: A comparative GeSn/GeSi study*, Phys. Rev. B **73** (2006), 125207.

[128] J. D. Sau and M. L. Cohen, *Possibility of increased mobility in GeSn alloy system*, Phys. Rev. B **75** (2007), 045208.

[129] P. Kringhøj and R. G. Elliman, *Diffusion of ion implanted Sn in Si, SiGe and Ge*, Appl. Phys. Lett. **65** (1994), 324.

[130] A. Chroneos, H. Bracht, R. W. Grimes, and P. Uberuaga, *Vacancy-mediated dopant diffusion activation enthalpies for germanium*, Appl. Phys. Lett. **92** (2008), 172103.

[131] I. Riihimäki, A. Virtanen, S. Rinta-Anttila, P. Pusa, J. Räisänen, and the ISOLDE Collaboration, *Vacancy-impurity complexes and diffusion of Ga and Sn in intrinsic and p-doped germanium*, Appl. Phys. Lett. **91** (2007), 091922.

[132] I. Riihimäki, A. Virtanen, H. Kettunen, P. Pusa, J. Räisänen, and the ISOLDE Collaboration, *Elastic interactions and diffusion of Sn in SiGe systems*, Appl. Phys. Lett. **90** (2007), 181922.

[133] G. Weyer, A. Nylandsted-Larsen, B. I. Deutch, J. U. Andersen, and E. Antoncik, *Covalency effects on implanted* ^{119}*Sn in group IV semiconductors studied by Mössbauer and channeling experiments*, Hyperf. Int. **1** (1975), 93.

[134] S. Damgaard, A. F. F. Olesen, J. W. Petersen, and G. Weyer, *Radiogenic Sn impurity defects in germanium*, Physica Scripta **22** (1981), 640.

[135] G. Weyer, S. Damgaard, J. W. Petersen, and J. Heinemeier, *Sn impurity defects in germanium from ion implantations of radioactive* ^{119}*In*, Phys. Lett. **76A** (1980), 321.

[136] G. Weyer, J. W. Petersen, and S. Damgaard, *The nature of ra-*

diogenic Sn defects in group-IV elements, Hyperf. Int. **10** (1981), 775.

[137] S. J. Pearton, *Hydrogen passivation of copper-related defects in germanium*, Appl. Phys. Lett. **40** (1982), 253.

[138] B. A. Andreev, G. G. Devyatykh, V. A. Gavva, D. M. Gordeev, A. V. Gusev, G. A. Maksimov, V. G. Pimenov, V. B. Shmagin, and D. A. Timonin, *Copper in ultra-pure germanium - Determination of the electrically active fraction*, Semicond. Sci. Technol. **9** (1994), 1050.

[139] F. C. Frank and D. Turnbull, *Mechanism of diffusion of copper in germanium*, Phys. Rev. **104** (1956), 617.

[140] H. H. Woodbury and W. W. Tyler, *Triple acceptors in germanium*, Phys. Rev. **105** (1956), 84.

[141] E. Simoen, P. Clauws, G. Huylebroeck, and J. Vennik, *DLTS of gold impurities in germanium*, Semicond. Sci. Technol. **2** (1987), 507.

[142] G. Huylebroeck, P. Clauws, E. Simoen, E. Rotsaert, and J. Vennik, *DLTS of silver in germanium: Evidence for an amphoteric impurity*, Semicond. Sci. Technol. **4** (1989), 529.

[143] P. Clauws and E. Simoen, *Metals in germanium*, Mat. Sci. Semicond. Proc. **9** (2006), 546.

[144] S. Gaudet, C. Detavernier, A. J. Kellock, P. Desjardins, and C. Lavoie, *Thin film reaction of transition metals with germanium*, J. Vac. Sci. Technol. A **24** (2006), 474.

[145] S. Ahlers, D. Bougeard, N. Sircar, G. Abstreiter, A. Trampert, M. Opel, and R. Gross, *Magnetic and structural properties of Ge_xMn_{1-x} films: Precipitation of intermetallic nanomagnets*, Phys. Rev. B **74** (2006), 214411.

[146] J. T. Wang, D. S. Wang, C. Chen, O. Nashima, T. Kanomata, H. Mizuseki, and Y. Kawazoe, *Vacancy induced structural and magnetic transition in $MnCo_{1-x}Ge$*, Appl. Phys. Lett. **89** (2006),

262504.

[147] A. Continenza, G. Profeta, and S. Picozzi, *Transition metal doping and clustering in Ge*, Appl. Phys. Lett. **89** (2006), 202510.

[148] A. Continenza, G. Profeta, and S. Picozzi, *Transition metal impurities in Ge: Chemical trends and codoping studied by electronic structure calculations*, Phys. Rev. B **73** (2006), 035212.

[149] H. Li, Y. Wu, Z. Guo, P. Luo, and S. Wang, *Magnetic and electrical transport properties of $Ge_{1-x}Mn_x$ thin films*, J. Appl. Phys. **100** (2006), 103908.

[150] J. T. Arantes, A. J. R. da Silva, A. Fazzio, and A. Antonelli, *Theoretical investigation of a Mn-doped Si/Ge heterostructure*, Phys. Rev. B **75** (2007), 075316.

[151] Y. X. Chen, S. Yan, Y. Fang, Y. F. Tian, S. Q. Xiao, L. Liu, Y. H. Liu, and L. M. Mei, *Magnetic and transport properties of homogeneous Mn_xGe_{1-x} ferromagnetic semiconductor with high Mn concentration*, Appl. Phys. Lett. **90** (2007), 052508.

[152] S. K. Kim, Y. C. Cho, S. Y. Jeong, C. R. Cho, S. E. Park, J. H. Lee, J. P. Kim, Y. C. Kim, and H. W. Choi, *High-temperature ferromagnetism in amorphous semiconductor Ge_3Mn thin films*, Appl. Phys. Lett. **90** (2007), 192505.

[153] A. P. Li, C. Zeng, K. van Benthem, M. F. Chisholm, J. Shen, S. V. S. Nageswara Rao, S. K. Dixit, L. C. Feldman, A. G. Petukhov, M. Foygel, and H. H. Weitering, *Dopant segregation and giant magnetoresistance in manganese-doped germanium*, Phys. Rev. B **75** (2007), 201201.

[154] E. Biegger, L. Stäheli, M. Fonin, U. Rüdiger, and Y. S. Dedkov, *Intrinsic ferromagnetism versus phase segregation in Mn-doped Ge*, J. Appl. Phys. **101** (2007), 103912.

[155] W. W. Tyler, *Deep level impurities in germanium*, J. Phys. Chem. Sol. **8** (1959), 59.

[156] S. J. Pearton, *A study of deep metal-related centers in germanium*

by capacitance spectroscopy, Solid State Electron. **25** (1982), 499.

[157] S. J. Pearton, *Hydrogen passivation of deep metal-related donor centers in germanium*, J. Appl. Phys. **54** (1982), 820.

[158] P. Clauws, J. Van Gheluwe, J. Lauwaert, E. Simoen, J. Vanhellemont, M. Meuris, and A. Theuwis, *Deep level transient spectroscopy of transition metal impurities in germanium*, Physica B **401** (2007), 188.

[159] E. Simoen, K. Opsomer, C. Claeys, K. Maex, C. Detavernier, R. L. Van Meirhaeghe, and P. Clauws, *Study of metal-related deep level defects in germanide Schottky barriers on n-type germanium*, J. Appl. Phys. **104** (2008), 023705.

[160] Y. Kamiura and F. Hashimoto, *Copper-related deep levels and their annealing kinetics in germanium*, Jpn. J. Appl. Phys. **28** (1989), 763.

[161] P. Schwalbach, M. Hartick, M. Ciani, E. Kankeleit, B. Keck, R. Sielemann, B. Stahl, and L. Wende, *In-beam Mössbauer spectroscopy: Fe in Si and Ge*, Hyperf. Int. **70** (1992), 1121.

[162] H. P. Gunnlaugsson, G. Weyer, M. Dietrich, M. Fanciulli, K. Bharuth-Ram, R. Sielemann, and the ISOLDE Collaboration, *Mössbauer spectroscopy on Fe impurities in germanium*, Physica B **340** (2003), 537.

[163] U. Wahl, J. G. Correia, J. C. Soares, and the ISOLDE Collaboration, *Lattice location and stability of implanted Cu in Ge*, Physica B **340** (2003), 799.

[164] Z. Z. Zhang, B. Partoens, K. Chang, and F. M. Peeters, *First-principles study of transition metal impurities in Si*, Phys. Rev. B **77** (2008), 155201.

[165] H. Levinstein, *Impurity photoconductivity in germanium*, Proc. IRE **47** (1959), 1478.

[166] R. Newman and W. W. Tyler, *Photoconductivity in germanium*, Solid State Phys. **8** (1959), 49.

[167] E. H. Putley, *Far infra-red photoconductivity*, Phys. Status Solidi **6** (1964), 571.

[168] A. J. Kenyon, *Erbium in silicon*, Semicond. Sci. Technol. **20** (2005), R65.

[169] S. Sato, S. Nozaki, H. Morisaki, and M. Iwase, *Tetragonal germanium films deposited by the cluster-beam evaporation technique*, Appl. Phys. Lett. **66** (1995), 3176.

[170] C. Bostedt, T. van Buuren, T. M. Willey, N. Franco, L. J. Terminello, C. Heske, and T. Möller, *Strong quantum-confinement effects in the conduction band of germanium nanocrystals*, Appl. Phys. Lett. **84** (2004), 4056.

[171] M. Jing, M. Ni, W. Song, J. Lu, Z. Gao, L. Lai, W. N. Mei, D. Yu, H. Ye, and L. Wang, *Anisotropic and passivation-dependent quantum confinement effects in germanium nanowires: A comparison with silicon nanowires*, J. Chem. Phys. B **110** (2006), 18332.

[172] C. L. Heng, T.G. Finstad, P. Storas, Y. J. Li, A. E. Gunnaes, and O. Nilsen, *The 1.54 μm photoluminescence from an (Er,Ge) co-doped SiO_2 film deposited on Si by rf magnetron sputtering*, Appl. Phys. Lett. **85** (2004), 4475.

[173] J. H. Chen, D. Pang, H. M. Cheong, P. Wickboldt, and W. Paul, *Room-temperature 1.5 μm luminescence of co-deposited erbium and germanium*, Appl. Phys. Lett. **67** (1995), 2182.

[174] S. O. Kucheyev, J. E. Bradby, S. Ruffell, C. P. Li, T. E. Felter, and A. V. Hamza, *Segregation and precipitation of Er in Ge*, Appl. Phys. Lett. **90** (2007), 221901.

[175] U. Wahl, A. Vantomme, J. De Wachter, R. Moons, G. Langouche, J. G. Marques, J. G. Correia, and the ISOLDE Collaboration, *Direct evidence for tetrahedral interstitial Er in Si*, Phys. Rev. Lett. **79** (1997), 2069–2072.

[176] U. Wahl, J. G. Correia, J. P. Araújo, A. Vantomme, G. Langouche, and the ISOLDE Collaboration, *Er-O clustering and its influence on the lattice sites of Er in Si*, Physica B **273-274** (1999), 342–345.

[177] M. Needels, M. Schlüter, and M. Lannoo, *Erbium point defects in silicon*, Phys. Rev. B **47** (1993), 15533.

[178] Y. Wan, Y. Ling, Q. Sun, and X. Wang, *Role of codopant oxygen in erbium-doped silicon*, Phys. Rev. B **58** (1998), 10415.

[179] D. Prezzi, T. A. G. Eberlein, R. Jones, J. S. Filhol, J. Coutinho, M. J. Shaw, and P. R. Briddon, *Electrical activity of Er and Er-O centers in silicon*, Phys. Rev. B **71** (2005), 245203.

[180] A. G. Raffa and P. Ballone, *Equilibrium structure of erbium-oxygen complexes in crystalline silicon*, Phys. Rev. B **65** (2002), 121309.

[181] A. Kozanecki, R. J. Wilson, B. J. Sealy, J. Kaczanowski, and L. Nowicki, *Evidence of interstitial location of Er atoms implanted into silicon*, Appl. Phys. Lett. **67** (1995), 1847.

[182] Y. Yamamoto, M. Wakaiki, A. Ikeda, and Y. Kido, *Lattice location of Tm in Si and Ge determined from ion channeling followed by Monte Carlo simulations*, Nucl. Instrum. Methods Phys. Res. B **153** (1999), 452.

[183] V. P. Markevich, V. V. Litvinov, L. Dobaczewski, J. L. Lindström, L. I. Murin, S. V. Vetrov, I. D. Hawkins, and A. R. Peaker, *Vacancy-oxygen complex in Ge crystals*, Physica B **340** (2003), 844.

[184] V. P. Markevich, A. R. Peaker, A. V. Markevich, V. V. Litvinov, L. I. Murin, and V. V. Emtsev, *Interaction of self-interstitials with oxygen-related defects in electron-irradiated Ge crystals*, Mat. Sci. Semicond. Proc. **9** (2006), 613.

[185] V. P. Markevich, A. R. Peaker, V. V. Emtsev, V. V. Litvinov, and L. I. Murin, *Vacancy defect reactions associated with oxygen and bismuth in irradiated germanium*, Physica B **376** (2006), 93.

[186] A. Carvalho, R. Jones, J. Coutinho, V. J. B. Torres, S. Öberg, J. M. Campanera Alsina, M. Shaw, and P. R. Briddon, *Local-density-functional calculations of the vacancy-oxygen center in Ge*, Phys. Rev. B **75** (2007), 115206.

[187] A. Carvalho, R. Jones, V. J. B. Torres, J. Coutinho, V. Markevich, S. Öberg, and P. R. Briddon, *Oxygen defects in irradiated germanium*, J. Mat. Sci. **18** (2007), 781.

[188] H. Geiger and E. Marsden, *On a diffuse reflection of the α-particles*, Proc. Roy. Soc. Series A **82** (1909), 495.

[189] E. Rutherford, *The scattering of α and β particles by matter and the structure of the atom*, Phil. Mag. **21** (1911), 669.

[190] W. K. Chu, M. A. Nicolet, and J. W. Mayer, *Backscattering Spectrometry*, Academic Press, New York, 1978.

[191] J. W. Mayer and E. Rimini, *Ion beam handbook for material analysis*, Academic Press, New York, 1977.

[192] L. C. Feldman and J. W. Mayer, *Fundamentals of surface and thin film analysis*, North-Holland, Amsterdam, 1986.

[193] J. Lindhard, *Influence of crystal lattice on motion of charged particles*, Mat. Fys. Medd. Dan. Vid. Selsk. **5** (1965), 1.

[194] D. V. Morgan, *Channeling*, John Wiley & Sons, London, 1973.

[195] L. C. Feldman, J. W. Mayer, and S. T. Picraux, *Materials analysis by ion channeling*, Academic Press, New York, 1982.

[196] K. Schmid, *Some new aspects for the evaluation of disorder profiles in silicon by backscattering*, Radiat. Eff. **17** (1973), 201.

[197] B. Pipeleers, *Defect accumulation in erbium implanted gallium nitride*, Ph.D. thesis, K.U. Leuven, Instituut voor Kern- en Stralingsfysica, 2005.

[198] V. Holy, U. Pietsch, and T. Baumbach, *High-resolution X-ray scattering from thin films and multilayers*, Springer-Verlag, Berlin Heidelberg, 1999.

[199] P. F. Fewster, *X-ray scattering from semiconductors*, Imperial College Press, London, 2003.

[200] Bruker, AXS GmbH, Karlsruhe, Germany, 2006.

[201] D. V. Lang, *Deep-level transient spectroscopy: A new method to characterize traps in semiconductors*, J. Appl. Phys. **45** (1974),

3023.

[202] G. L. Miller, D. V. Lang, and L. C. Kimerling, *Capacitance transient spectroscopy*, Ann. Rev. Mat. Sci. **7** (1977), 377.

[203] F. D. Auret, P. J. Janse van Rensburg, M. Hayes, J. M. Nel, W. E. Meyer, S. Decoster, V. Matias, and A. Vantomme, *Electrical characterization of defects introduced in n-type Ge in ion implantation into Ge*, Appl. Phys. Lett. **89** (2006), 152123.

[204] L. Dobaczewski, A. R. Peaker, and K. Bonde Nielsen, *Laplace-transform deep-level spectroscopy: The technique and its applications to the study of point defects in semiconductors*, J. Appl. Phys. **96** (2004), 4689.

[205] J. U. Andersen, S. K Andersen, and W. M. Augustyniak, *Channeling of electrons and positrons*, Munksgaard, Copenhagen, 1977.

[206] R. Wedell, *Electromagnetic radiation of relativistic positrons and electrons during axial and planar channeling in monocrystals*, Phys. Status Solidi (B) **99** (1980), 11.

[207] J. U. Andersen, E. Bonderup, E. Lægsgaard, B. B. Marsh, and A. H. Sørensen, *Axial channeling radiation from MeV electrons*, Nucl. Instrum. Methods **194** (1982), 209.

[208] J. U. Andersen, E. Bonderup, E. Lægsgaard, and A. H. Sørensen, *Incoherent scattering of electrons and linewidth of planar-channeling radiation*, Physica Scripta **28** (1982), 308.

[209] H. Hofsäss and G. Lindner, *Emission channeling and blocking*, Phys. Rep. **201** (1991), 121.

[210] U. Wahl, J. G. Correia, S. Cardoso, J. G. Marques, A. Vantomme, G. Langouche, and the ISOLDE Collaboration, *Electron emission channeling with position-sensitive detectors*, Nucl. Instrum. Methods Phys. Res. B **136-138** (1998), 744.

[211] U. Wahl, *Advances in electron emission channeling measurements in semiconductors*, Hyperf. Int. **129** (2000), 349.

[212] B. De Vries, *Lattice site location of impurities in group III nitrides*

using emission channeling, Ph.D. thesis, K.U. Leuven, Instituut voor Kern- en Stralingsfysica, 2006.

[213] U. Wahl, J. G. Correia, A. Czermak, S. G. Jahn, P. Jalocha, J. G. Marques, A. Rudge, F. Schopper, J. C. Soares, A. Vantomme, P. Weilhammer, and the ISOLDE Collaboration, *Position-sensitive Si pad detectors for electron emission channeling experiments*, Nucl. Instrum. Methods Phys. Res. A **524** (2004), 245–256.

[214] H. Hofsäss, G. Lindner, E. Recknagel, and Th. Wichert, *Channeling of conversion electrons from radioactive impurities for analysis of atomic structures in solids*, Nucl. Instrum. Methods B **2** (1984), 13.

[215] H. Hofsäss, U. Wahl, and S. G. Jahn, *Impurity lattice location and recovery of structural defects in semiconductors studied by emission channeling*, Hyperf. Int. **84** (1994), 27.

[216] H. Hofsäss, *Emission channeling*, Hyperf. Int. **97-98** (1996), 247.

[217] http://geant4.web.cern.ch/geant4/.

[218] S. Agostinelli *et al.*, *Geant4 - a simulation toolkit*, Nucl. Instrum. Methods A **506** (2003), 250.

[219] S. Cottenier, (Instituut voor Kern- en Stralingsfysica, KULeuven, Belgium), 2002, ISBN 90-807215-1-4 (freely available from http://www.wien2k.at/reg_user/textbooks).

[220] P. Blaha, K. Schwarz, G. Madsen, D. Kvasnicka, and J. Luitz, (Karlheinz Schwarz, Techn. Universität Wien, Austria), 1999, ISBN 3-9501031-1-2.

[221] J. P. Perdew, K. Burke, and M. Ernzerhof, *Generalized gradient approximation made simple*, Phys. Rev. Lett. **77** (1996), 3865.

[222] E. C. Baranova, V. M. Gusev, W. V. Martynenko, C. V. Starinin, and I. B. Haibullin, *On silicon amorphization during different mass ion implantation*, Radiat. Eff. Defects Solids **18** (1973), 21.

[223] J. R. Dennis and E. B. Hale, *Energy dependence of amorphizing implant dose in silicon*, Appl. Phys. Lett. **29** (1976), 523.

[224] A. Colder, T. Wojtowicz, P. Marie, P. Ruterana, V. Matias, M. Mamor, A. Vantomme, S. Eimer, and L. Mechin, *Deep level transient spectroscopy and TEM analysis of defects in Eu implanted GaN*, Phys. Status Solidi (C) **7** (2005), 2450.

[225] V. Matias, *Defect characterization of europium implanted gallium nitride*, Ph.D. thesis, K.U. Leuven, Instituut voor Kern- en Stralingsfysica, 2008.

[226] S. Cottenier, S. Decoster, and A. Vantomme, *unpublished*.

LIST OF PAPERS

Paper I

Implantation-induced damage in Ge: Strain and disorder profiles during defect accumulation and recovery,

S. Decoster and A. Vantomme

Submitted to Journal of Physics D: Applied Physics (2009)

Implantation-induced damage in Ge: Strain and disorder profiles during defect accumulation and recovery

S. Decoster and A. Vantomme

Instituut voor Kern- en Stralingsfysica and INPAC, K.U. Leuven, Celestijnenlaan 200D, B-3001 Leuven, Belgium

—

submitted to Journal of Physics D: Applied Physics

—

Abstract

We present an experimental study of structural lattice damage in Ge induced by ion implantation. From the strain and disorder profiles, calculated from ion channeling and X-ray diffraction experiments we have investigated the defect accumulation as a function of ion fluence, mass, energy and current density as well as the damage recovery and recrystallization of the implanted region upon annealing. The damage accumulation process can be divided in three different regimes, based on the ion fluence. In the lowest fluence regime, the strain and the defect fraction are linearly proportional to the ion fluence, and the amount of defects in the implanted layer is directly related to the deposited energy that is converted to the creation of vacancies. In the second regime, the damage accumulation process is more efficient, due to the increased defect density in the implanted layer. The third fluence regime starts at the critical fluence for amorphization, and this value has been determined for a wide range of ion masses and energies. The recovery study of the implantation-induced damage has revealed two distinct annealing steps. Rapid thermal annealing at temperatures as low as 100 °C results in the removal of isolated defects, which are present in the low fluence implanted samples, as well as in the tail of the implantation profile of heavily-damaged samples. Annealing at 350 °C results in the recrystallization of amorphous Ge at the amorphous-crystalline interface at a rate of 20 nm/min. Although Ge amorphizes at much lower fluences than Si, the influence of the studied implantation parameters on the damage accumulation process is comparable for both group IV semiconductors. This extended experimental overview of implantation-induced structural damage partly fills the large knowledge gap on implantation-related issues in Ge, and provides relevant and complementary information for defect studies in Ge and, in general, for any study using implanted Ge.

I. INTRODUCTION

Despite its early discovery and its use in the first point contact transistors made by researchers from Bell Labs in 1948, germanium has only been considered a really important material in semiconducting applications during the past decade. Compared to silicon, Ge has a higher free charge carrier mobility and a lower dopant activation temperature[1], which makes it an attractive material in future metal-oxide semiconductor field-effect transistors[2,3]. Ion implantation is still the most widely used technique to dope semiconductors, due to a good control of the dopant concentration and depth profile, and the high purity through mass selection. A very important consequence of this technique is the creation of lattice damage during implantation, such as vacancies, interstitials, Frenkel pairs, clusters of these simple defects and amorphous regions. Besides its direct impact on the electrical properties of the material, radiation damage can induce transient enhanced diffusion and can result in a large inactive dopant fraction.

Due to its predominant technological significance, many groups have been investigating the ion implantation process in Si during the past 40 years. An overview of the tremendous amount of experimental results in Si can be found in review articles by Gibbons[4], Hobler and Otto[5], and Pelaz *et al.*[6], covering the influence of several implantation parameters such as the ion mass, energy, current density, substrate temperature, dopant concentration and the implantation angle on the accumulation of structural damage up to amorphization, as well as the influence of the annealing technique and temperature on the recovery and recrystallization of the damaged layers. In order to obtain a better understanding of the damage accumulation and recovery process, many models have been proposed to explain and fit the experimental results. An elaborate review of such models can be found in Ref. 6. However, despite many decades of extensive research, both experimentally and theoretically, many questions about the implantation process still remain unanswered. This has been paraphrased as follows in the 2001-edition of the

International Technology Roadmap for Semiconductors[7]: " *... a more detailed understanding of the implantation damage, amorphization and subsequent recrystallization is important ... extensive research and model development need to be started immediately to develop improved models for damage creation and annealing, and for temperature dependent implantation.*" In the 2007-edition, it was stated that "*Implantation damage, amorphization, re-crystallization, and silicidation must be accurately simulated*", indicating that there are still many unsolved issues regarding ion implantation in Si.

In comparison to Si, the information that is available on implantation-induced structural lattice damage in Ge is very scarce. By the time ion implantation was regularly used in practical applications, Si had been the leading material in integrated circuit technology for many years, which explains the lack of relevant information on this topic in Ge.

One of the earliest relevant reports on the study of extended defects after ion implantation was made by Mayer *et al.*[8]. In this work, In ions were implanted in Ge with an energy of 40 keV and an amorphization threshold (AT) of roughly 2×10^{13} – 1×10^{14} atoms/cm^2 was found from Rutherford backscattering and channeling spectrometry (RBS/C) experiments. Similar studies have been performed to determine AT values in Ge for other elements as well, under a variety of implantation conditions. Sigurd *et al.*[9] implanted 56 keV B ions, which resulted in an AT of 3.5×10^{15} atoms/cm^2, while implanting 6×10^{13} Si atoms/cm^2 with an energy of 300 keV was found to be sufficient to amorphize Ge[10]. Extended X-ray absorption fine structure measurements were used to investigate the AT of high energy (1.7 MeV) self-implantation in Ge at liquid nitrogen temperature[11], which was found to be 1×10^{14} atoms/cm^2. By using focussed ion beams, Posselt *et al.*[12] studied the amorphization process during 30 keV channeled Ga implantations and found an AT of 1×10^{14} atoms/cm^2.

Other studies have been performed to investigate the influence of several implantation parameters on the induced lattice damage. By increas-

ing the *substrate temperature* during implantation, a drastic decrease of the amount of lattice damage has been observed[9,13]. The influence of the *current density* was found to be small at room temperature, while playing an important role at elevated temperatures (120 °C – 250 °C)[12,13]. Shallow B and P implantations – i.e. at a very low *energy* of a few keV – have been studied by Simoen and Satta *et al.*[14–16], and very high energy implantations (600 MeV Au ions) were performed by Kamarou *et al.*[17].

The defects after ion implantation can give rise to local deformation of the crystal structure, i.e. elastic *strain*. So far, generation of strain in Ge has been studied by two different groups. Speriosu *et al.* found a linear dependence between the maximum strain and the implanted fluence[18] after implanting 300 keV Si ions in bulk Ge, while Lie *et al.* observed a superlinear dependence, using similar implantation conditions[10].

Finally, a few groups have reported on the *annealing behavior* of damaged and amorphous Ge layers after ion implantation. Mayer *et al.* observed complete recovery of the damage for a low fluence implanted sample after annealing for 10 min at 180 °C, while 380 °C was required during 10 min for a high fluence implanted sample. These results were attributed to the recovery of isolated damage clusters and to the recrystallization of an amorphous layer respectively[8]. Similar results were found by Kräutle, where recrystallization of the amorphous Ge layers was observed after annealing for 30 min at 400 – 500 °C[19]. Csepregi *et al.* studied the regrowth kinetics of amorphous ⟨100⟩ Ge and found a regrowth rate of roughly 10 nm/min at 350°C[20]. Finally, from positron annihilation spectroscopy experiments, complete recovery of the damaged Ge samples was found after annealing at 500 °C for 30 min[21].

From the limited number of studies on implantation-induced damage in Ge, it is known that Ge is much more sensitive to implantation damage than Si. This has been shown by Speriosu *et al.* by measuring similar strain values in Si and in Ge after implanting Si to a fluence which is 20 times larger than the fluence in Ge[18]. Furthermore, Lie *et al.* found an amorphization threshold for 100 keV Si implantation in Si which is roughly 15 times larger than in Ge[10]. From molecular dynamics

simulations, this large difference between Si and Ge has been attributed to the lower melting temperature of Ge and to the higher energy density in the Ge damage cascades[22].

We can conclude that, despite the growing interest in Ge, the information on ion implantation-induced damage in Ge is relatively scarce, and consists mainly of single experiments, most of them performed with completely different implantation conditions. Here, we present a more systematic and elaborate experimental study on implantation-induced structural damage in germanium. We investigate both the lattice damage accumulation process, as well as the recrystallization process as a function of several implantation parameters in order to obtain a thorough understanding of the implantation process and the induced structural defects. In particular, the influence of the ion fluence, mass, energy, current density and annealing temperature is investigated in detail. The structural lattice damage is quantified by measuring the relative lattice disorder and the implantation-induced lattice strain, and Monte-Carlo simulations (SRIM v2006.02[23]) are used to complement our experimental results.

II. EXPERIMENTAL METHODS

All implantations have been performed in undoped ⟨100⟩-oriented Ge samples held at room temperature, with an implantation angle of 10° with respect to the surface direction, to minimize channeling effects. The influence of the ion mass on the induced lattice damage has been studied by implanting ^{20}Ne, $^{38-40}$Ar, ^{59}Co, ^{82}Kr, ^{115}In and ^{136}Xe. Three different energies have been used (40, 80 and 160 keV) to implant the bulk Ge samples to ion fluences between 5×10^{11} atoms/cm^2 and 3×10^{14} atoms/cm^2, at a typical current density of 20 – 100 nA/cm^2. To further investigate the influence of the current density on the accumulated damage, we used current densities up to 2 μA/cm^2. The recovery and the recrystallization of damaged layers has been studied after rapid thermal annealing at temperatures up to 500 °C under ni-

element	mass (a.m.u.)	energy (keV)	R_p (Å)	$f_{\mathrm{E,vac}}$ (%)	$E_{\mathrm{D,vac}}$ (eV/Å)
Ne	20	80	1141	4.4	2.6
Ar	38	80	612	5.5	6.4
	40	160	1153	4.9	6.1
Co	59	40	249	7.0	9.8
		80	449	6.8	10.5
Kr	82	80	345	6.8	13.8
		160	625	6.5	15.0
In	115	40	175	7.4	14.6
		80	291	7.2	17.4
Xe	136	80	272	7.1	18.2

TABLE I: Mass, energy and mean projected range (R_p) of the implanted ions used in this study; the fraction of the total ion energy that is converted to vacancy creation ($f_{\mathrm{E,vac}}$) and the deposited energy per depth at R_p that is converted to vacancy creation ($E_{\mathrm{D,vac}}$), as calculated from Monte Carlo simulations (SRIM v2006.02) using a Ge displacement threshold of 15 eV and a lattice binding energy of 2 eV.[24]

trogen ambient. The annealing temperature was reached at a rate of 50 °C/s and kept constant for 30 s. An overview of the species and their corresponding implantation energies that have been used in this work, is listed in Tab. I, together with the mean projected range R_p of the implanted ions in Ge, as calculated with SRIM.

The defect distribution of the implanted samples has been investigated by RBS/C using a 1 mm^2-collimated beam of 1.57 MeV $^4He^+$ ions. The samples were mounted on a three-axis goniometer and the backscattered He particles were detected with a solid-state detector positioned at a scattering angle of 105° to obtain a good depth resolution. Since the implantation-induced defects cause a partial dechanneling of the He ions in RBS/C experiments, the measured backscattering yield in channeling geometry is the sum of (1) ions directly backscattered from a defect and (2) ions which are first dechanneled by a defect and backscattered in a second event. Therefore, the depth profiles of the

defect distribution are obtained using a procedure to subtract the contribution of dechanneled $^4He^+$ ions from the total backscattered yield[25]. The maximum height of such a defect profile, relative to a completely amorphized layer, will be denoted as the *defect fraction* and has a value between 0 (undamaged) and 1 (fully amorphous). The total amount of displaced Ge atoms in the implanted layer is obtained by integrating the defect depth profile.

Due to the introduction of impurity atoms and the creation of many defects such as self-interstitials, vacancies and defect clusters in the Ge lattice, elastic strain will be induced in the single crystalline Ge lattice. This strain has been determined by X-ray diffraction (XRD) $\theta-2\theta$ scans, using Cu K_{α_1} radiation ($\lambda = 1.54056$Å). Strain depth profiles have been deduced from the diffraction patterns with the commercially available LEPTOS[26] software package, which uses the dynamical theory of X-ray diffraction. This strain profile is a direct consequence of the distribution of defects in the implanted layer, providing valuable information about the profile of implantation-induced defects.

III. RESULTS

A. Fluence dependence

Fig. 1 (a) shows the ⟨100⟩-channeled yield of backscattered He ions as a function of their energy for 160 keV Ar-implanted Ge to several ion fluences, together with a *random* spectrum, i.e. by measuring a randomly oriented Ge-crystal. The spectra clearly show an increasing dechanneling fraction as a function of ion fluence, which is a direct consequence of the increased amount of displaced Ge host atoms. At a fluence of 6.8×10^{13} atoms/cm^2, the channeled yield coincides with the yield of the random spectrum, indicating a complete loss of crystallinity in the most heavily damaged region. Further increasing the fluence results in the growth of the amorphous layer, both towards the surface and towards the bulk Ge. Applying the iterative procedure from Schmid to

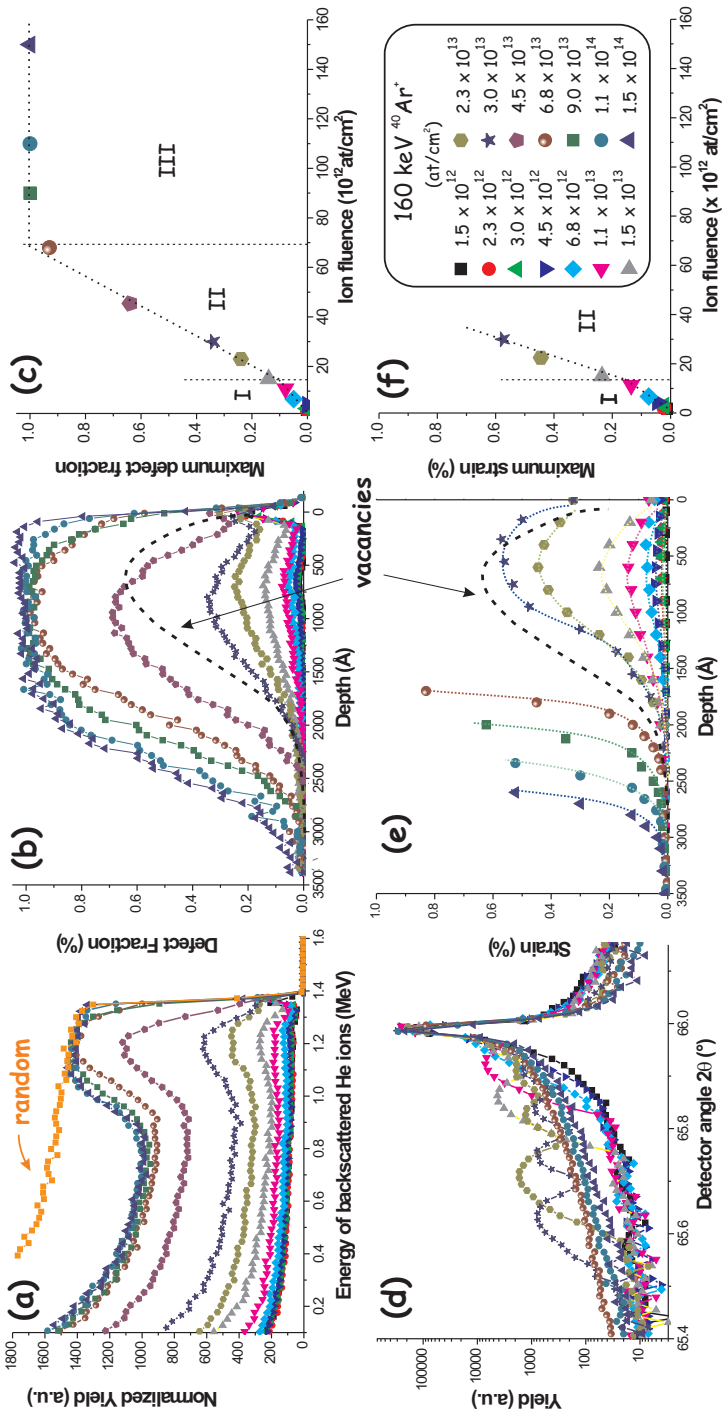

FIG. 1: (a) The yield of backscattered He ions as a function of their final energy (RBS/C-spectra) and (d) θ-2θ scans (XRD-scans) after 160 keV Ar implantations to different fluences ranging from 1.5×10^{12} to 1.5×10^{14} atoms/cm^2; (b) calculated defect profiles and (e) simulated strain profiles; (c) maximum defect fraction and (f) maximum strain value as a function of ion fluence.

subtract the dechanneled fraction of He ions[25] results in the defect depth profiles shown in Fig. 1 (b). RBS/C-experiments provide information about the profile of interstitials in the implanted material, rather than the profile of vacancies. However, the depth profile of interstitials and vacancies is known to be largely similar at these implantation conditions, and therefore, the vacancy distribution, as calculated with Monte Carlo simulations, has been added to Fig. 1. It is clear that the obtained defect depth profiles have a shape which is comparable to the vacancy (or interstitial) depth profile. When plotting the maximum defect fraction of each defect depth profile from Fig. 1 (b) as a function of ion fluence, three different fluence regimes can be observed (Fig. 1 (c)). In regime I and II, the defect fraction increases with increasing ion fluence, while saturation occurs in regime III. The damage accumulation process is more efficient in regime II than in regime I, i.e. an equal number of incoming ions will result in a larger amount of remaining defects in regime II. In regime III, the crystallinity completely disappears and an amorphous region is present. The transition fluence between regime II and III will be indicated as the amorphization threshold – i.e. the lowest ion fluence that results in a defect fraction of 100%, or in other words, in an amorphous layer. In this way, an amorphization threshold of 7×10^{13} atoms/cm^2 has been deduced for 160 keV Ar implantation in Ge.

To obtain complementary information on the damage accumulation process as a function of ion fluence, X-ray diffraction measurements have been performed to determine the strain profile of the same set of samples. These scans are shown in Fig. 1 (d) and consist of a large narrow peak around $2\theta = 66.0°$ from the diffraction on the (400)-planes of unstrained bulk Ge, and one or more smaller side peaks at lower angles, arising from the local perpendicular expansion of the lattice. From reciprocal-space X-ray mapping (not shown), it is found that ion implantation only induces perpendicular strain ($e^{\perp}$) and no lateral strain ($e^{\parallel}$). Therefore, in the remainder of this article, we will use *strain* while referring to *perpendicular strain* only. From the diffraction scans in Fig. 1 (d), the strain profiles have been extracted (Fig. 1 (e)) and can be divided in

two categories. Implantation at low fluences ($\leq 3 \times 10^{13}$ atoms/cm^2) gives rise to a strain profile with a similar shape as the defect depth profile (see Fig. 1 (b)) and the calculated vacancy profile. On the other hand, implantation at higher fluences clearly results in a completely different strain profile, consisting only of the deep-end part of a regular depth profile. This peculiar strain profile can be explained by the lack of crystallinity in the heavily-damaged implanted region (Fig. 1 (b)). Since no diffraction can occur in such heavily damaged regions, the observed strain profile of these samples must be attributed to the region below the heavily-damaged region. For the low-fluence implanted samples, the maximum strain value has been plotted as a function of ion fluence (Fig. 1 (f)). In this figure, two different regimes can be distinguished. In both regimes, the ion fluence and the strain are proportional to each other, while the amount of strain generated per incoming ion is clearly larger in regime II than in regime I.

When comparing the disorder profile with the strain profile (Fig. 1 (b) and (e)), and the maximum defect fraction with the maximum strain value (Fig. 1 (c) and (f)) for this set of samples, the following similarities are present: both profiles have a comparable shape and depth distribution, while the maximum defect fraction and the maximum strain in the implanted region behave similarly with respect to the ion fluence. The relation between the implantation-induced strain and the defect density will be addressed below for several implanted species and energies.

B. Ion mass dependence

To study the influence of the ion mass on the implantation-induced lattice damage, we have implanted Co and In, as well as the inert noble gases Ne, Ar, Kr and Xe to minimize chemical effects, with an energy of 80 keV. The strain and defect profiles have been obtained in analogy to the procedures used in Fig. 1. The results are shown in Fig. 2, where (a) the maximum defect fraction, (b) the amount of displaced Ge atoms and (c) the maximum strain are shown as a function of ion fluence. For the

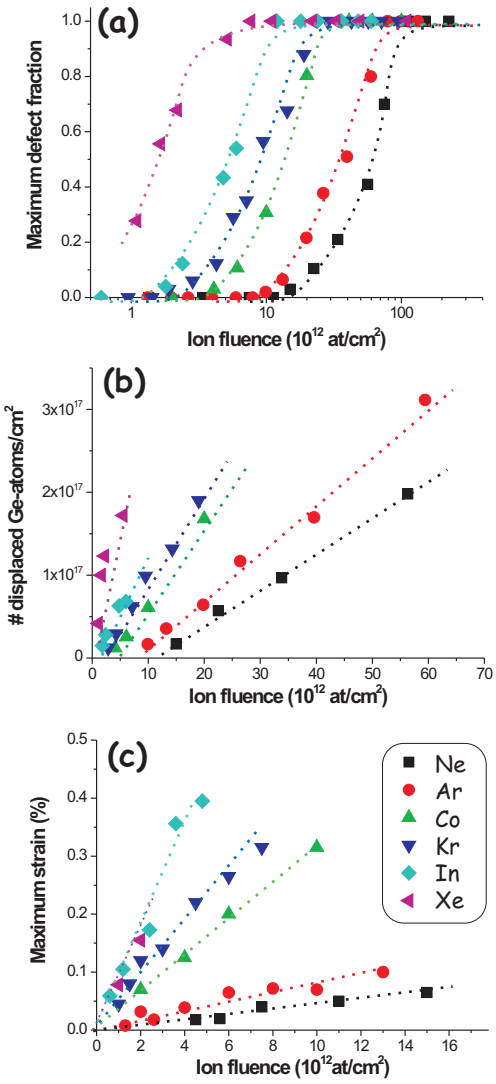

FIG. 2: (a) Maximum defect fraction, (b) total amount of displaced Ge atoms (restricted to fluence regime II) and (c) maximum strain value as a function of ion fluence (restricted to fluence regime I) for 80 keV Ne (squares), Ar (circles), Co (triangles up), Kr (triangles down), In (diamonds) and Xe (triangles left) implantations.

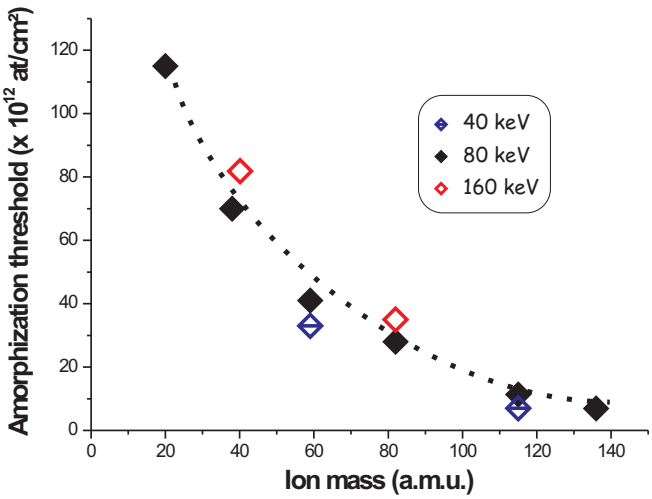

FIG. 3: The amorphization threshold as a function of ion mass for implantations at 40 keV (half open), 80 keV (filled) and 160 keV (open symbols).

sake of clarity, we have restricted the presented data in Fig. 2 (b) and (c) to fluence regime II and I respectively. However, it should be noted that the difference between both regimes is clear for low mass implantations but less distinct for high mass implantations. As expected, all three graphs in Fig. 2 show that the mass of the implanted species is a critical factor in the damage accumulation process. From Fig. 2 (b) and (c), it is found that the amount of displaced Ge atoms and the maximum strain in the implanted layer are linearly proportional to the ion fluence for all investigated elements. These results indicate a similar damage accumulation behavior for all species. Despite the same initial energy of 80 keV, it is clear that high mass ions create more displacements and induce a larger strain than low mass ions.

The influence of the mass on the damage accumulation process in Ge is visualized by plotting the amorphization threshold as a function of ion mass (Fig. 3). When comparing all elements implanted at 80 keV (filled symbols), it is obvious that a higher fluence of low mass ions can

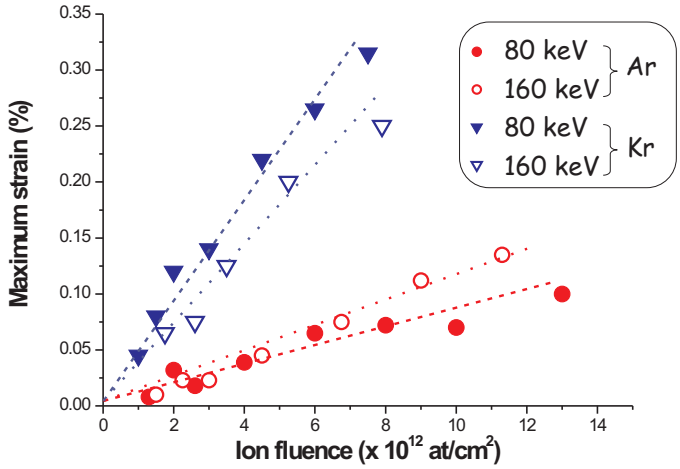

FIG. 4: Maximum strain as a function of ion fluence for Ar and Kr implantations at 80 keV (filled symbols) and 160 keV (open symbols).

be implanted in Ge before complete amorphization occurs. Since all elements – Co and In as well as the noble gases – follow the same trend, the structural implantation damage seems to be independent from the chemical properties of the implanted species. Comparison between the amorphization threshold values from literature[8–12] and our results is not straightforward, due to very different implantation conditions. While the values obtained by Mayer *et al.*[8] (40 keV In) and Lie *et al.*[10] (300 keV Si) are comparable to the values obtained in our work, the amorphization threshold values observed by Sigurd *et al.*[9] (low mass implantations - B), Byrne *et al.*[11] (implanting at 77 K) and Posselt *et al.*[12] (using focussed ion beams in channeling geometry) can not be directly compared to our results.

C. Energy dependence

The influence of the ion energy on the structural lattice damage in Ge has been investigated within the range of 40 keV to 160 keV (Fig. 3 and 4). It is clear that changing the energy of the implanted ions barely

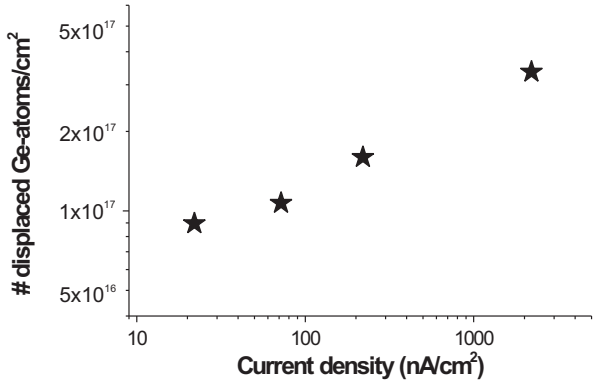

FIG. 5: The amount of displaced Ge host atoms after implanting 3×10^{13} atoms/cm^2 80 keV Ar ions, as a function of implantation current density.

influences the critical fluence required for amorphization (Fig. 3). From Fig. 4, similar conclusions can be drawn for the implantation-induced lattice strain: the energy of the implanted ion barely influences the maximum strain in the implanted layer. As will be discussed below, these results are explained by taking into account the defect density in the implanted region.

D. Current density dependence

The influence of the current density on the accumulated lattice damage has been investigated by implanting 3×10^{13} Ar atoms/cm^2 with different current densities, ranging from 20 nA/cm^2 up to 2.0 μA/cm^2. In Fig. 5, the total amount of displaced Ge atoms has been plotted as a function of current density, finding an increased amount of displacements with increasing current density. This behavior is similar to what has been observed by Haynes *et al.*[13] after implanting 100 keV Si ions at room temperature with current densities between 20 nA/cm^2 and 0.4 μA/cm^2. All implantations in this study (except for the ones presented in Fig. 5) have been performed with a current density between 20 and

100 nA/cm^2, to minimize the influence of the current density on the implantation-induced damage to less than 10%.

E. Damage recovery

The disorder and the strain depth profiles have been determined after several consecutive rapid thermal annealing steps (30 s) up to 450 °C, in order to study the recovery of the lattice damage. In Fig. 6, the disorder profiles of three samples are shown after implantation with 80 keV Xe ions to different fluences: (a) 2.2×10^{12}, (b) 1.1×10^{13} and (c) 1.1×10^{14} atoms/cm^2. In the as-implanted state, these samples consist of a partly damaged implanted region, a thin amorphous region and a thicker amorphous region of roughly 600 – 700 Å, respectively. As can be seen in all three graphs, heating the sample at 100 °C is sufficient to anneal defects at the end tail of the implantation profile. Moreover, for the lowest fluence (Fig. 6 (a)), every subsequent annealing step decreases the total defect fraction while after annealing at 300 °C, no residual damage is left. Fig. 6 (c) shows that annealing at 350 °C results in the onset of recrystallization, which occurs at the amorphous-crystalline interface, while complete recrystallization is reached after annealing at 450 °C for the highest fluence sample in this study.

To clearly visualize this annealing behavior, we have plotted the maximum defect fraction and the total amount of displaced Ge atoms versus the annealing temperature for eight different ion fluences (including the ones from Fig. 6) in Fig. 7 (a) and (b), respectively. The defect fraction of the samples with a partially damaged implanted region decreases after each annealing step, starting at 100 °C. This indicates that annealing at 100 °C is sufficient to anneal most of the damage in the implanted layer with an accordingly long annealing time. In agreement with the observations from Fig. 6, recrystallization of the amorphous layer is observed after annealing at 350 °C for all amorphized samples (Fig. 7 (a)), and complete recrystallization of all the investigated samples is reached after annealing at 450 °C. Due to the presence of two distinct temperature

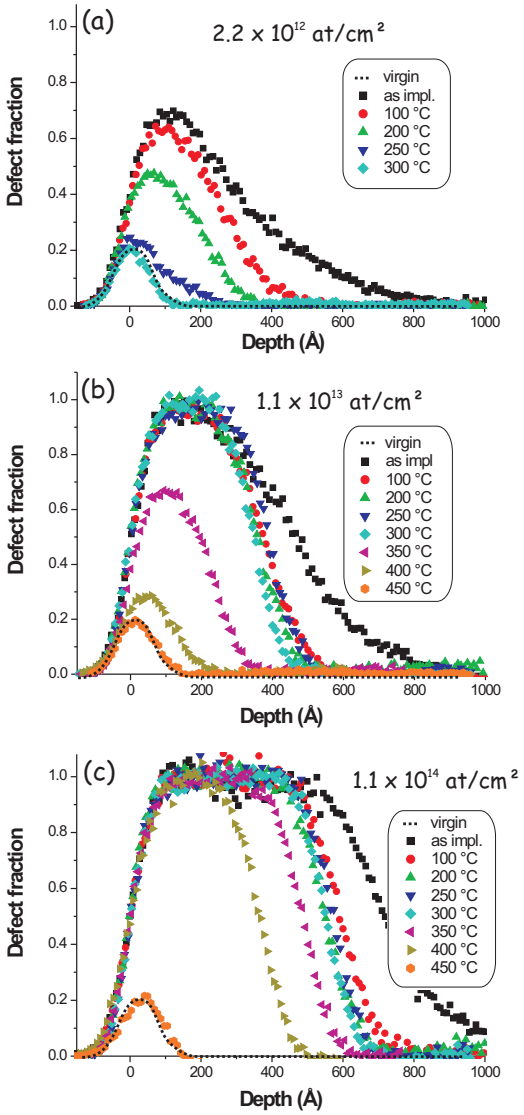

FIG. 6: Disorder profiles after 80 keV Xe-implantations to fluences of (a) 2.2×10^{12} atoms/cm^2, (b) 1.1×10^{13} atoms/cm^2 and (c) 1.1×10^{14} atoms/cm^2, directly after implantation as well as after several rapid thermal annealing steps up to 450 °C. The disorder profile of a virgin Ge sample, which only consists of the surface peak (dotted line), has been added to all three graphs.

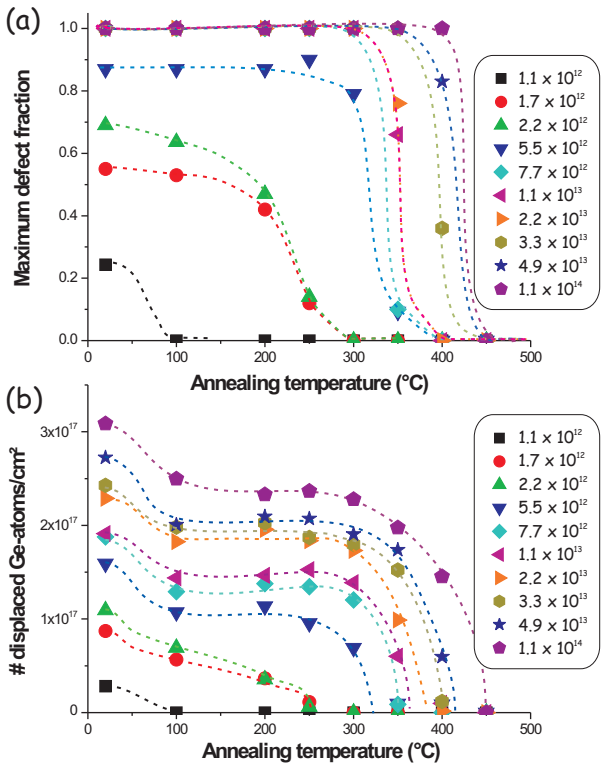

FIG. 7: (a) The maximum defect fraction and (b) the total amount of displaced Ge atoms as a function of annealing temperature after 80 keV Xe implantations for several fluences.

regions, it is clear that recrystallization does not occur via point-defect annealing, which is expected to occur in regime I and II. These observations are in agreement with earlier results where crystal reordering was found after annealing at 180 °C for low fluence implanted samples[8], and where the onset of recrystallization of amorphous Ge was found after annealing at 380 – 400 °C[8,19,21,27]. From the highest fluence samples, we have determined the regrowth rate of amorphous Ge at 350 °C to be 12 – 16 nm/min which is in good agreement with literature values where a regrowth rate of 10 – 20 nm/min has been observed[20,28].

The recovery behavior of the implantation-induced strain has been

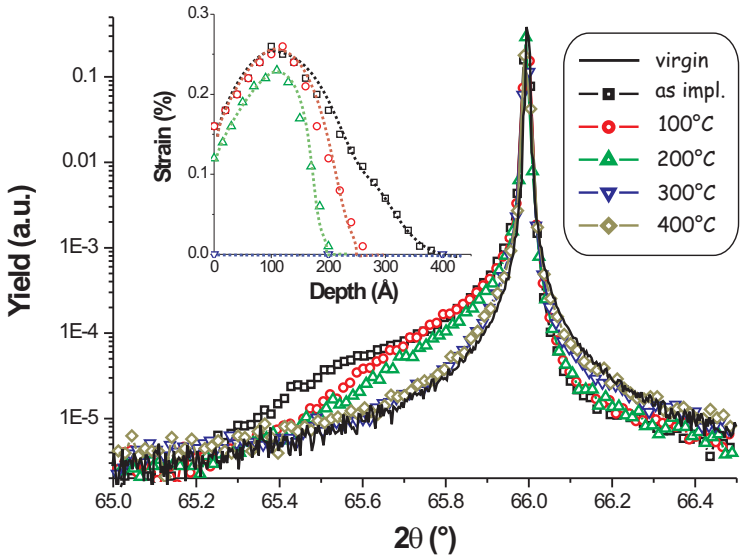

FIG. 8: θ-2θ-scans of the (400)-planes in Ge, after implanting 80 keV Xe to a fluence of 2×10^{12} atoms/cm^2, in the as-implanted state, as well as after several rapid thermal anneal stages. The XRD-scan of a virgin Ge sample (solid line) has been added for comparison. The inset shows the extracted strain profiles from the XRD-scans.

studied after implanting 80 keV Xe ions. In Fig. 8, the XRD-scans for a low fluence implanted sample (2×10^{12} atoms/cm^2) are shown after several annealing stages. The inset in Fig. 8 shows the corresponding extracted strain profile for each annealing temperature. The same trends appear in the strain profile as in the disorder profile. Annealing at 100 °C results in a narrower strain profile, indicating the recovery of defects at the end of the implantation profile. After annealing at 300 °C and 400 °C, the XRD-scans coincide with the scan of a virgin Ge sample (Fig. 8), showing the complete disappearance of strain in the implanted layer.

IV. DISCUSSION

A. Type of defects

We have divided the damage accumulation process in three fluence regimes, based on the relation between the amount of implantation-induced damage and the ion fluence. In regime I, i.e. at the lowest ion fluence, the crystalline disorder in the implanted region is small and the implantation process induces strain with a maximum value of typically a few tenths of a percent. The maximum strain, as well as the maximum defect fraction, are linearly proportional to the ion fluence. Moreover, the maximum strain $e^{\perp}$ (%) and the maximum defect fraction f_D (between 0 and 1) are linearly proportional to each other in this low fluence regime (Fig. 9), with a proportionality constant of 0.94:

$$e^{\perp} = 0.94 f_D.$$

A similar relation between the strain and the defect fraction has been found in Si, where a proportionality constant of 1.2 was found by Bai *et al.* after implanting 230 keV F and Si ions[29].

The type of defects created in this low-defect regime are mainly isolated and relatively small defects, such as pairs or clusters of vacancies (V) and/or self-interstitials (I), since large extended defect clusters are not expected to induce strain throughout the complete implanted region, in accordance with the experimental observations in this study.

In regime II, at higher fluences, the lattice becomes less and less crystalline, which inhibits the measurement of a clear strain profile above a defect fraction of roughly 0.3 – 0.4. This indicates that more extended defects will be present in the implanted region, originating from the overlap of the smaller defects. In this second regime of the damage accumulation process, the defect fraction still increases with increasing fluence, but at a significantly faster rate than in regime I. The damage accumulation process becomes more efficient, due to the higher defect density which results in an increase in the average size of the defects and

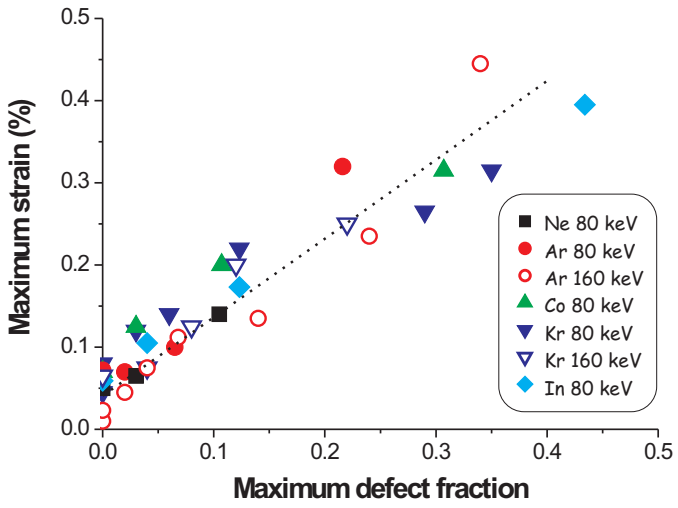

FIG. 9: The maximum strain in the implanted layer (%) as a function of maximum defect fraction.

in less annihilation and relaxation of simple defects. From the annealing study, we can conclude that the tail of the implantation profile of heavily damaged samples (fluence regime II) consists of small isolated defects or defect clusters, similar to the type of defects observed in regime I.

At the highest ion fluences (*regime III*), amorphization occurs. The amorphization threshold follows a general trend which depends on the ion mass but is independent from the energy of the implanted ions (Fig. 3). The amorphization of the implanted region starts at the mean projected range of the implanted species. When implanting to fluences larger than the amorphization threshold, the amorphous region grows both towards the surface and towards the bulk of the Ge sample. Even for samples implanted to fluences above the amorphization threshold, the tail of the damage profile consists of isolated defects or small isolated defect clusters, which can be annealed at 100 °C.

B. Energy deposition

Defects induced by ion implantation, are a consequence of the transfer of energy from the incoming ions to the Ge host lattice. The energy of the incoming ion (40, 80 or 160 keV in this study) can be transferred to the Ge atoms by many processes such as phonon creation, excitation or ionization of the host atoms, vacancy creation, etc. Monte Carlo simulations (SRIM v2006.02) have been used to deduce the relative fractions of energy lost in these particular interactions. These calculations have been performed, using a Ge displacement threshold of 15 eV and a lattice binding energy of 2 eV[30,31]. The results obtained in this work mainly depend on the fraction of energy $f_{\mathrm{E,vac}}$ converted to the creation of vacancies in the Ge crystal lattice, which is listed in Tab. I for the relevant implantation conditions in this study[24]. In the remainder of this article, we will use the term *deposited energy* to indicate the fraction of energy that is converted to vacancy creation.

From Fig. 2 (c) and 4, it is clear that the maximum strain and the ion fluence are linearly proportional in regime I. The slope of the linear fit through the data represents the amount of strain that is generated per implanted ion at its mean projected range, i.e. where most defects are present. By plotting the induced strain per incoming ion versus deposited energy (Fig. 10), it is clear that both quantities are linearly proportional:

$$e^{\perp}/\phi = K E_{D,vac},$$

where ϕ is the implanted fluence (10^{13} atoms/cm^2) and $\mathrm{E}_{D,vac}$ the deposited energy per unit depth (eV/Å), as tabulated in Tab. I. The proportionality constant K found in our study is 3.4×10^{-2} Å cm^2/eV, which is comparable to the value obtained for GaAs in Ref. 32 ($K = (5 \pm 1) \times 10^{-2}$ Å cm^2/eV). The observation that the strain per ion is proportional to the deposited energy, strengthens the assumption that mainly small isolated defects are present in the implanted region at these low fluences.

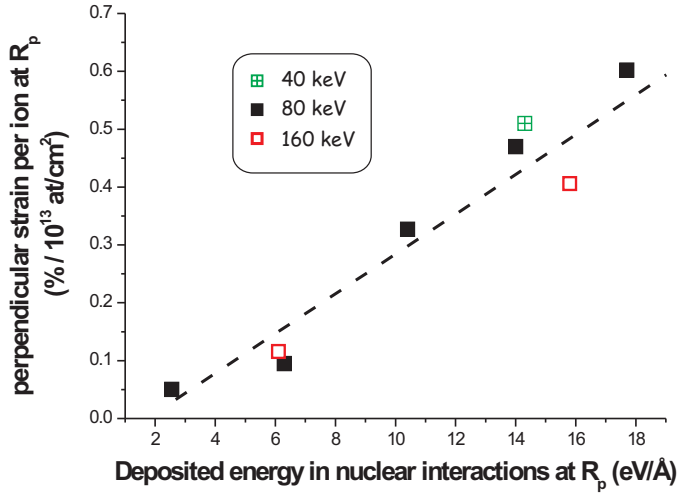

FIG. 10: Maximum strain created per incoming ion (% / 10^{13} atoms/cm^2) as a function of deposited energy (eV/Å).

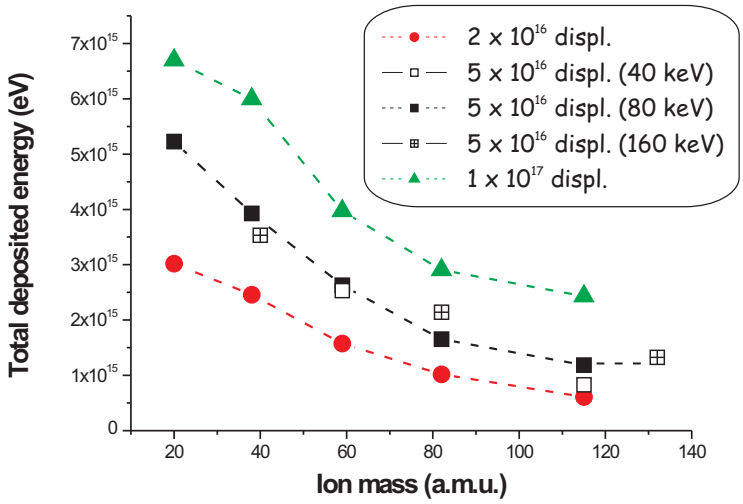

FIG. 11: The total amount of deposited energy required to displace 2×10^{16} (circles), 5×10^{16} (squares) and 1×10^{17} (triangles) Ge atoms, as a function of ion mass.

When investigating the influence of the nuclear energy deposition on the implantation-induced damage in regime II, the relation is not linear anymore. To clarify this statement, we have plotted the total amount of energy that needs to be deposited in the implanted layer to displace 2×10^{16}, 5×10^{16} and 1×10^{17} Ge host atoms, as a function of ion mass (Fig. 11). This energy value has been calculated by multiplying (1) the amount of implanted ions that results in the specified amount of displaced Ge atoms, as extracted from our experiments, (2) the implantation energy (40 – 80 – 160 keV), and (3) the calculated fraction of energy $f_{\mathrm{E,vac}}$ that is converted to the creation of vacancies (Tab. I). From this graph, it is clear that for low mass implantations, the total deposited energy to create a certain amount of displaced Ge atoms is higher in comparison to heavy ion implantation. This implies that the influence of the mass on the implantation-induced damage, can not be solely attributed to the deposited energy, but the difference in defect density, or in other words, the volume over which the deposited energy is spread, becomes important at these fluences. In comparison to low mass implantations, high mass implantations result in a shallower damage profile. Consequently, the deposited energy is confined to a smaller volume, which enhances the probability that isolated defects form extended defect clusters. This diminishes the annihilation and relaxation probability (*dynamic annealing*) of unstable defects. As a consequence, the overall effectiveness of the damage accumulation process increases, in accordance with the experimental observations in this work. A similar effect occurs when investigating the influence of the current density (Fig. 5) on the accumulated damage. At higher current densities, the local defect density increases. Hence, more unstable isolated defects will be close enough to form extended defects – instead of annihilating with other defects – which results in less dynamic annealing and a larger amount of remaining defects.

The energy of the implanted species does not significantly influence the amount of energy required to create a certain amount of displacements (Fig. 11). This is in accordance with the calculated values in

Tab. I, where the deposited energy per unit depth was found to be roughly independent from the implantation energy. These results indicate that the larger amount of energy deposited during high energy implantations is counterbalanced by the larger spread of the deposited energy. This results in a comparable defect density and a similar behavior in the damage accumulation process for the range of implantation energies used in this work, in accordance to our experimental results.

V. CONCLUSIONS

We have presented a systematic study of the accumulation and recovery of implantation-induced lattice damage in Ge as a function of ion fluence, mass, energy and current density. The damage accumulation process can be divided in three regimes, based on the implanted fluence: In the *first regime* (lowest fluences), the accumulation of strain and defects is linearly proportional with the ion fluence and with the deposited energy that is converted to the creation of vacancies. In this regime, the defects in the implanted region are mainly small isolated defect pairs or clusters of vacancies and interstitials. In the *second regime* (intermediate fluences), the damage accumulation process becomes more efficient and cannot be solely attributed to the amount of deposited energy anymore. By investigating the influence of the energy and the mass of the ions on the implantation-induced damage, we conclude that the defect density plays a crucial role in the damage accumulation process in this fluence regime. During high mass implantation, all defects are confined to a smaller volume with respect to low mass implantations, which results in a higher defect density and consequently a larger fraction of remaining defects. High energy implantations obviously result in the generation of more defects, while the implanted volume is larger. Since the implantation-induced damage was found to be independent from the energy of the implanted ions, we can conclude that both effects compensate each other for the implantation conditions used in this study. The *third regime* starts at the critical fluence for amorphization, and this

amorphization threshold has been determined for several species and energies.

The recovery of the implantation damage occurs in two distinct annealing stages. Low temperature rapid thermal annealing for 30 s (100 °C) is sufficient to remove the defects in low fluence implanted samples as well as in the tail of the defect profile in heavily damaged and even amorphized samples. The recrystallization of amorphous material starts at 350 °C at the amorphous-crystalline interface, and for the samples used in this study, complete recovery of the crystal lattice is reached after annealing at 450 °C. Furthermore, we have determined the regrowth rate of amorphous Ge to be 12 – 16 nm/min at 350 °C.

When comparing our experimental results in Ge to the extensive literature on Si, the most striking difference is found for the amorphization threshold values. It is clear that amorphization occurs at much lower fluences in Ge than in Si, in accordance with earlier studies[10,18]. Furthermore, the recrystallization of amorphous material starts at much lower temperatures (350 °C) in Ge than in Si (> 600 °C). These results are related to the lower melting temperature of Ge with respect to Si. Although damage accumulation occurs at different ranges of fluence, the overall influence of implantation parameters on the damage accumulation process in Si and in Ge is similar. In accordance to what we found in Ge, the damage accumulation process in Si has been divided in three regimes, representing (I) crystalline Si containing relatively simple defects, (II) a mixture of damaged crystalline Si and amorphous Si zones and (III) an amorphous Si layer[6,33]. For heavy mass ions (Sb), regime I and II could not be separated[33]. Furthermore, the amorphization threshold in Si was found to be relatively insensitive to the ion energy[34], at least for the range of ion masses used in our experiments. Finally, the amount of damage after implanting Si at room temperature was found to increase with current density (Ref. 5,6 and references therein), similar to our observations in Ge. Therefore, it can be concluded that, although Ge amorphizes at much lower fluences than Si, the influence of the studied implantation parameters (mass, energy, current density) on

the damage accumulation process is very comparable in both group IV semiconductors.

This work provides a detailed experimental overview of the damage accumulation and recovery process in Ge and fills one of the many gaps in the current knowledge about this important group IV semiconductor. Having in-depth knowledge – and eventually control of implantation-induced defects in Ge – is also important for the interpretation of the results of dopant activation[35,36] and electrical characterization studies, such as implantation-induced defect levels in the Ge band gap[37]. Furthermore, recent emission channeling experiments have shown a clear influence of the overall implantation-induced damage on the analysis of the lattice location of impurities in Ge[38,39], further highlighting the importance of systematic defect studies.

VI. ACKNOWLEDGEMENTS

This work was supported by FWO Flanders (G.0501.07 and G.0636.08), the K.U.Leuven projects GOA/2009/006 and INPAC EF/2005/005 and the IUAP P6/42 programme. S. D. acknowledges financial support from FWO, Flanders. We would like to thank W. Vandervorst for the helpful discussions and valuable comments.

---

[1] R. Hull and J. C. Bean, *Germanium Silicon: Physics and Materials, Semiconductors and Semimetals*, Academic, San Diego (1999).

[2] C. C. Yeo, B. J. Cho, F. Gao, S. J. Lee, M. H. Lee, C. Y. Yu, C. W. Liu, L. J. Tang, and T. W. Lee, IEEE Electron Device Letters **26**, 761 (2005).

[3] Y. J. Yang, W. S. Ho, C. F. Huang, S. T. Chang, and C. W. Liu, Appl. Phys. Lett. **91**, 102103 (2007).

[4] J. F. Gibbons, Proceedings of the IEEE **60**, 1062 (1972).

[5] G. Hobler and G. Otto, Mat. Sci. Semicond. Proc. **6**, 1 (2003).

[6] L. Pelaz, L. A. Marqués, and J. Barbolla, J. Appl. Phys. **96**, 5947 (2004).

[7] International Technology Roadmap for Semiconductors, http://public.itrs.net/.

[8] J. W. Mayer, L. Eriksson, S. T. Picraux, and J. A. Davies, Can. J. Phys. **46**, 663 (1968).

[9] D. Sigurd, G. Fladda, L. Eriksson, and K. Björkqvist, Radiat. Eff. **3**, 145 (1970).

[10] D. Y. C. Lie, A. Vantomme, F. Eisen, T. Vreeland Jr., M. A. Nicolet, T. K. Carns, V. Arbet-Engels, and K. L. Wang, J. Appl. Phys. **74**, 6039 (1993).

[11] A. P. Byrne, M. C. Ridgway, C. J. Glover, and E. Bezakova, Hyperfine Interactions **158**, 245 (2004).

[12] M. Posselt, L. Bischoff, D. Grambole, and F. Herrmann, Appl. Phys. Lett. **89**, 151918 (2006).

[13] T. E. Haynes and O. W. Holland, Appl. Phys. Lett. **59**, 452 (1991).

[14] A. Satta, E. Simoen, T. Janssens, T. Clarysse, B. De Jaeger, A. Benedetti, I. Hoflijk, B. Brijs, M. Meuris, and W. Vandervorst, J. Electrochem. Soc. **153**, G229 (2006).

[15] E. Simoen, A. Satta, A. D'Amore, T. Janssens, T. Clarysse, K. Martens, B. De Jaeger, A. Benedetti, I. Hoflijk, B. Brijs, et al., Mat. Sci. Semicond. Proc. **9**, 634 (2006).

[16] E. Simoen, G. Brouwers, A. Satta, M.-L. David, F. Pailloux, B. Parmentier, T. Clarysse, J. Goossens, W. Vandervorst, and M. Meuris, Mat. Sci. Semicond. Proc. p. doi:10.1016/j.mssp.2008.09.006 (2008).

[17] A. Kamarou, W. Wesch, E. Wendler, A. Undisz, and M. Rettenmayr, Phys. Rev. B **78**, 054111 (2008).

[18] V. S. Speriosu, B. M. Paine, M. A. Nicolet, and H. L. Glass, Appl. Phys. Lett. **40**, 604 (1982).

[19] H. Kräutle, Radiat. Eff. **24**, 255 (1975).

[20] L. Csepregi, R. P. Küllen, and J. W. Mayer, Solid State Commun. **21**, 1019 (1977).

[21] J. Slotte, M. Rummukainen, F. Tuomisto, V. P. Markevich, A. R. Peaker, C. Jeynes, and R. M. Gwilliam, Phys. Rev. B **78**, 085202 (2008).

[22] K. Nordlund, M. Ghaly, R. S. Averback, M. Caturla, T. Diaz de la Rubia, and J. Tarus, Phys. Rev. B **57**, 7556 (1998).

[23] J. Ziegler, J. Biersack, and U. Littmark, *The stopping and range of ions in solids*, Pergamon Press, New York © www.srim.com (1985).

[24] Care should be taken when interpreting the absolute values of $f_{E,vac}$ and $E_{D,vac}$, as calculated with SRIM, since they are highly dependent on the

Ge displacement threshold and the Ge lattice binding energy used in the calculations. Here, we have used 15 eV and 2 eV respectively, however, these quantities are not very accurately known yet. However, the relative values of $f_{E,vac}$ and $E_{D,vac}$ for different elements and energies are stable for different displacement threshold and lattice binding energy values.

[25] K. Schmid, Radiat. Eff. **17**, 201 (1973).

[26] A. Ulyanenkov, Proc. of SPIE **5536**, 1 (2004), LEPTOS: A universal software for X-ray reflectivity and diffraction.

[27] K. Kuitunen, F. Tuomisto, J. Slotte, and I. Capan, Phys. Rev. B **78**, 033202 (2008).

[28] E. Simoen and W. Vandervorst, private communication.

[29] G. Bai and M. A. Nicolet, J. Appl. Phys. **70**, 3551 (1991).

[30] J. J. Loferski and P. Rappaport, Phys. Rev. **111**, 432 (1958).

[31] J. J. Loferski and P. Rappaport, J. Appl. Phys. **30**, 1296 (1959).

[32] B. M. Paine, N. N. Hurvitz, and V. S. Speriosu, J. Appl. Phys. **61**, 1335 (1987).

[33] E. C. Baranova, V. M. Gusev, W. V. Martynenko, C. V. Starinin, and I. B. Haibullin, Radiat. Eff. Defects Solids **18**, 21 (1973).

[34] J. R. Dennis and E. B. Hale, Appl. Phys. Lett. **29**, 523 (1976).

[35] A. Satta, E. Simoen, T. Clarysse, T. Janssens, A. Benedetti, B. De Jaeger, M. Meuris, and W. Vandervorst, Appl. Phys. Lett. **87**, 172109 (2005).

[36] A. Satta, E. Simoen, R. Duffy, T. Janssens, T. Clarysse, A. Benedetti, M. Meuris, and W. Vandervorst, Appl. Phys. Lett. **88**, 162118 (2006).

[37] F. D. Auret, P. J. Janse van Rensburg, M. Hayes, J. M. Nel, W. E. Meyer, S. Decoster, V. Matias, and A. Vantomme, Appl. Phys. Lett. **89**, 152123 (2006).

[38] S. Decoster, B. De Vries, A. Vantomme, U. Wahl, and J. G. Correia, Appl. Phys. Lett. **93**, 141907 (2008).

[39] S. Decoster, S. Cottenier, B. De Vries, H. Emmerich, U. Wahl, J. G. Correia, and A. Vantomme, Phys. Rev. Lett. **102**, 065502 (2009).

Paper II

Electrical characterization of defects introduced in *n*-type Ge during indium implantation,

F. D. Auret, P. J. Janse van Rensburg, M. Hayes, J. M. Nel, W. E. Meyer, S. Decoster, V. Matias and A. Vantomme,

Applied Physics Letters ***89****, 152123 (2006)*

Electrical characterization of defects introduced in *n*-type Ge during indium implantation

F. D. Auret, P. J. Janse van Rensburg,
M. Hayes, J. M. Nel, and W. E. Meyer
Department of Physics, University of Pretoria, Pretoria 0002, South Africa

S. Decoster, V. Matias, and A. Vantomme
Instituut voor Kern- en Stralingsfysica and INPAC, K.U. Leuven, Celestijnenlaan 200D, B-3001 Leuven, Belgium

—

Applied Physics Letters **89**, (2006) 152123

—

Abstract

We have employed deep level transient spectroscopy to investigate the defects introduced in *n*-type Ge during 160 keV indium (In) ion implantation. Our results show that In implantation introduces three prominent electron traps with energy levels at E_C - 0.09 eV, E_C - 0.15 eV and E_C - 0.30 eV respectively. We have found that these defects are different from the point defects introduced by electron irradiation but that they do not involve In. Annealing at 600 °C removed all the defects introduced during In implantation but results in a single prominent defect with a level at E_C - 0.35 eV.

The low effective mass of holes in Ge has opened up the possibility of using Ge in ultrafast complimentary metal-oxide-semiconductor devices[1]. This, in turn, has sparked renewed interest in the properties of defects in Ge because defects ultimately determine the performance of devices. In recent studies the properties of the defects introduced during high-energy gamma-, electron- and proton irradiation of Ge[2–6] were reported. The defects introduced during electron beam deposition of Pt Schottky contacts on n-Ge, where particles heavier than electrons create the defects, have also been characterized[7]. However, little data are available regarding the electronic properties of defects introduced during the implantation of Ge with heavy ions. Implantation with heavy ions typically occurs during doping as well as pre-doping amorphization[8]. These implantations will introduce, among others, extended defects (e. g. clusters) that have different electronic and annealing characteristics than those of the well-studied point defects introduced during electron irradiation. In general, irradiation and implantation-induced defects will influence device performance, but neither the nature of heavy ion implantation-induced defects nor their influence on devices has yet been established for Ge. Depending on the application, these defects may either be beneficial for or detrimental to optimum device functioning. For example, for Si it has been shown that the defects introduced during high-energy electron and proton irradiation increase the switching speed of devices[9].

In this study we report on the electronic properties of defects introduced in n-type Ge during 160 keV In ion implantation. It has recently been demonstrated that In can be implanted in Si as a p-type dopant[10]. It is reasonable to expect that similar results may be obtained for In implantation into Ge. We show here that In implantation introduces three prominent electron traps in Ge. These defects were found to be different from the point defects introduced during high-energy electron irradiation of the same material. For this investigation we have used bulk-grown, (111) oriented, n-type material doped with Sb to a level of $(2-3)\times 10^{15}$ cm^{-3}. Before metallization and implantation the samples

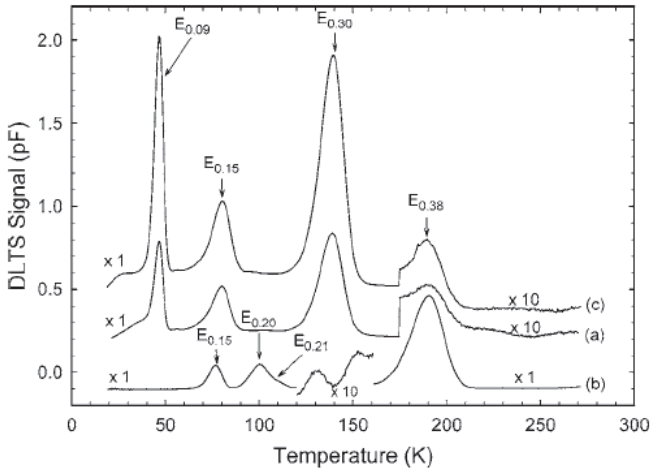

FIG. 1: DLTS spectra of 160 keV In-implanted Ge (curve (a)), high-energy electron irradiated Ge (curve (b)) and 160 keV Xe-ion implanted Ge (curve (c)). These spectra were recorded using a rate window of 80 s^{-1} at a quiescent reverse bias of -2 V with a filling pulse, V_p, of 1.8 V superimposed on the reverse bias.

were first degreased and subsequently etched in a mixture of H_2O_2:H_2O (1:5, 30% H_2O_2) for one minute. Directly after cleaning they were inserted into a vacuum chamber where AuSb (0.6 % Sb) was resistively deposited on their back surfaces as ohmic contacts. The samples were then annealed at 350 °C in Ar for 10 minutes. Thereafter the front sides of the samples were implanted at room temperature with 160 keV In ions at an angle of 0 degrees to a dose of 2×10^{11} cm^{-2}. After implantation and chemical cleaning, the 0.6 mm diameter and 200 nm thick Pd contacts were resistively deposited on the implanted side of the Ge samples[7]. Deep level transient spectroscopy (DLTS) was used to study the defects introduced in Ge during implantation.

In curve (a) of Fig. 1 we depict the DLTS spectrum for an In-implanted sample. Note that, although not shown, the unimplanted Ge did not contain any defects in detectable concentrations[7]. The most significant electron traps in curve (a) of Fig. 1 are $E_{0.09}$, $E_{0.15}$ and $E_{0.30}$

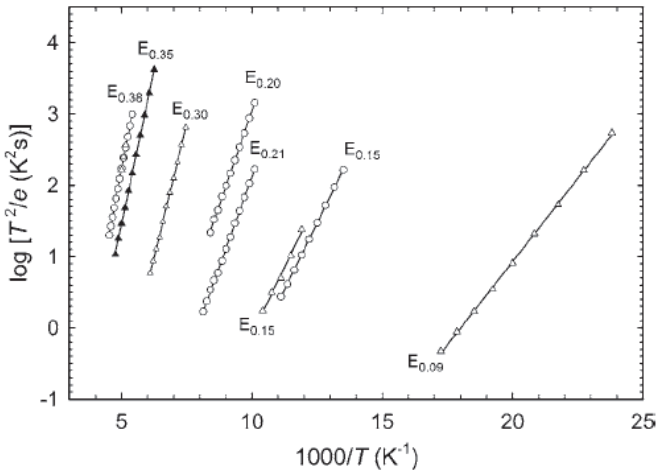

FIG. 2: Arrhenius plots for defects in In-implanted Ge (triangles) and MeV electron irradiated Ge (circles). The solid triangles represent measurements after annealing at 600 °C. All data were acquired using the bias and pulsing conditions defined in the caption of Fig. 1.

with levels at E_C - 0.09 eV, E_C - 0.15 eV and E_C - 0.30 eV, respectively. A defect, $E_{0.38}$, in a much lower concentration, was also detected. The electronic properties of all the implantation-induced defects are summarized in Table I.

In order to establish the possible nature of the implantation-induced defects, we compare the spectrum of In-implanted Ge to that of identical Ge that was irradiated with MeV electrons from a ^{90}Sr radionuclide to a dose of 2×10^{14} cm^{-2} (curve (b))[7]. The energy distribution of electrons from this source is continuous with a primary peak energy of about 200 keV, a secondary maximum of about 1 MeV and then it tails off to about 2 MeV. Note that from Fig. 1 and the Arrhenius plots in Fig. 2 the only defect that is clearly introduced both during MeV electron irradiation and implantation is $E_{0.38}$ and it is only introduced in a low concentration in the implanted Ge. $E_{0.38}$ has been identified as the (- -/-) charge state of the E-center (V-Sb) in Sb-doped Ge[2,3]. This implies that single vacancies are only produced in small quantities during implantation with

Process	Defect	E_T (eV)	σ_a (cm^2)	T_{peak} [a] (K)	Similar defects/defect ID
Indium	$E_{0.09}$	E_C - 0.09	1.0×10^{-13}	47	
implantation	$E_{0.15}$	E_C - 0.15	1.6×10^{-14}	81	
	$E_{0.30}$	E_C - 0.30	3.0×10^{-14}	140	
	$E_{0.38}$	E_C - 0.38	1.0×10^{-14}	191	$E_{0.377}$ [b], $E_{0.37}$ [c], V-Sb (- -/-) [b c]
	$E_{0.35}$	E_C - 0.35	6.0×10^{-15}	177	
MeV	$E_{0.15}$	E_C - 0.15	5.0×10^{-14}	77	
electron	$E_{0.20}$	E_C - 0.20	1.4×10^{-14}	100	$E_{0.19}$ [c], Sb and I related? [c]
irradiation	$E_{0.21}$	E_C - 0.21	3.6×10^{-14}	109	$E_{0.21}$ [c], Sb related? [c]
	$E_{0.38}$	E_C - 0.38	1.1×10^{-14}	191	$E_{0.377}$ [b], $E_{0.37}$ [c], V-Sb (–/-) [b c]

[a] Peak temperature at a rate window of 80 s^{-1}
[b] See Ref.[3]
[c] See Ref.[2]

TABLE I: Electronic properties of prominent defects introduced in n-type Ge during In implantation and MeV electron irradiation of Schottky contacts.

In, otherwise the $E_{0.38}$ concentration would have been much higher. We also note from Fig. 2 that the signatures of the $E_{0.15}$ in the irradiated and implanted samples do not correspond exactly, meaning that they may not be the same defect. Finally, we deduce from these two figures that the three main implantation-induced defects do not correspond to any of the defects introduced during electron irradiation. It should also be pointed out that although the level of $E_{0.30}$ is close to that found for the divacancy after electron irradiation (E_C - 0.29 eV[2], not shown here), the divacancy anneals out at 150 °C whereas $E_{0.30}$ is still present after annealing at 200 °C, as discussed below. From these results it is clear that the only typical radiation induced point defect that we observed after implantation is the E-center. This implies that the $E_{0.09}$, $E_{0.15}$ and $E_{0.30}$ defects are different from the point defects introduced during high-energy electron and proton irradiation[2–5]. We speculate that the origin of these defects is that an In ion creates multiple point defects in the same physical environment due to the high energy loss per unit length compared to electrons or protons. These defects can interact to form defects that are physically and therefore electronically different from the typical radiation-induced point defects. In order to determine if any of these defects involves In ions we have implanted identical Ge samples with 160 keV Xe ions. Xe is expected to be chemically inert and has a mass only slightly higher from In. The spectrum recorded from a Xe-implanted sample is shown in curve (c) of Fig. 1. From curves (a) and (c) it is clear that In and Xe introduce the same main three electron traps, as well as the E-center in small concentrations, but in different relative concentrations. The DLTS "signatures" of the Xe implantation-induced defects coincided well with those of the In ion defects and are omitted from Fig. 2 for the sake of clarity. The electronic properties of these defects are therefore independent of the implanted species (In or Xe).

Finally, we have investigated the thermal stability of the defects introduced during In implantation by isochronal annealing in argon (10 minute periods, 100 °C steps). Fig. 3 shows that annealing at 100 °C

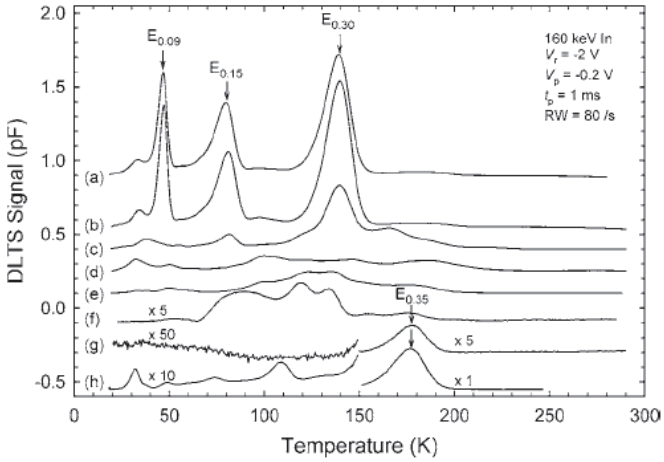

FIG. 3: DLTS spectra of Pd Schottky contacts on In-implanted Ge: (a) - room temperature, and subsequently annealed at (b) - 100 °C, (c) - 200 °C, (d) - 300 °C, (e) - 400 °C, (f) - 500 °C, (g) - 600 °C. Curve (h) was recorded from a new Schottky contact deposited on In-implanted Ge that was annealed at 600 °C before metallization.

does not noticeably change the defect spectra. Annealing at 200 °C removes $E_{0.09}$, drastically reduces the $E_{0.15}$ concentration by 90% and reduces the concentration of $E_{0.30}$ by a factor of two. At the same time a new defect appears at the high temperature side of $E_{0.30}$. During the 300 °C, 400 °C and 500 °C anneal cycles complex DLTS spectra evolve, the detailed characterization of which lies beyond the scope of this letter. Finally, after annealing at 600 °C, only a single defect, $E_{0.35}$, with a well-defined DLTS peak is present. When interpreting these thermal stability results it should be borne in mind that the annealing was performed with the Pd Schottky contact on top of the Ge. It has been shown that Pd germanide is formed during annealing above 330 °C[11]. Also bear in mind that most of the implantation-induced defects are located in a shallow region below the Pd contact and that the thickness of the Pd is 200 nm. This means that during the germanide formation, some or all of the Ge containing the implantation defects may be con-

sumed. It is therefore not clear if defect removal in the 400 °C - 500 °C region occurs because defects dissociate or interact, or because they are consumed during germanidation. To answer this question, and in order to establish if $E_{0.35}$ is the result of germanidation, we formed new Pd Schottky contacts on samples annealed at 600 °C, right next to the Pd germanide contacts, i. e. on sections of the samples that did not contain any Pd germanide. DLTS [curve (h) in Fig. 3] from these new contacts revealed the presence of the same level but in about six times the concentration of $E_{0.35}$ in the germanided material. This indicates that the germanidation is not responsible for the introduction of this defect, but, rather, that it reduces its concentration due to Ge consumption. Interestingly, DLTS depth profiling (not shown) indicated that, in contrast to defects observed directly after implantation, the concentration of $E_{0.35}$ is more or less uniformly distributed in the first 1.5 micron that could be probed by DLTS. This suggests that $E_{0.35}$ is the product of a diffusion process. Finally, note that curve (h) shows that the Ge below the ungermanided contacts contains a series of defects not observed below the germanided contacts. Their concentrations are about an order of magnitude lower than that of $E_{0.35}$. Clearly, germanidation consumed these defects as well as some of $E_{0.35}$.

Our results reveal that the main defects introduced during In implantation of n-type Ge have energy levels at E_C - 0.09 eV, E_C - 0.15 eV and E_C - 0.30 eV. We have also demonstrated that these defects are different from the defects introduced during high-energy electron and proton irradiation of the same material. By comparing the DLTS of In-implanted Ge to Xe-implanted Ge, we could establish that these defects are observed for both implantations and are therefore not species (In or Xe) related. Annealing at 200 °C removes all the defects directly introduced during In implantation whereas annealing in the 300 °C – 500 °C region introduced defects with complex DLTS spectra. This could be the result of clusters of defects dissociating and / or agglomerating. After annealing at 600 °C only one defect with a level at E_C - 0.35 eV could be observed in the Pd germanide contacts. Although its origin is not

clear at the moment, we have demonstrated that germanidation is not responsible for the formation of this defect but, rather, that it reduces its concentration. The authors gratefully acknowledge financial support of the South African National Research Foundation, the Fund for Scientific Research, Flanders (FWO), IUAP P5/10 and the KULeuven Research Council (GOA/2004/02 and INPAC EF/05/005).

[1] R. Hull and J. C. Bean, *Germanium Silicon: Physics and Materials, Semiconductors and Semimetals* (Academic Press, San Diego, 1999).

[2] J. Fage-Pedersen, A. Nylandsted Larsen, and A. Mesli, Phys. Rev. B **62**, 10116 (2000).

[3] V. P. Markevich, A. R. Peaker, V. V. Litvinov, V. V. Emtsev, and L. I. Murin, J. Appl. Phys. **95**, 4078 (2004).

[4] V. P. Markevich, D. Hawkins, A. R. Peaker, K. V. Emtsev, V. V. Emtsev, V. V. Litvinov, and L. Dobaczewski, Phys. Rev. B **70**, 235213 (2004).

[5] V. P. Markevich, I. D. Hawkins, A. R. Peaker, V. V. Litvinov, L. Dobaczewski, and J. L. Linström, Appl. Phys. Lett. **81**, 1821 (2002).

[6] C. E. Lindberg, J. Lundsgaard Hansen, P. Bomholt, A. Mesli, K. Bonde Nielsen, and A. Nylandsted Larsen, Appl. Phys. Lett. **87**, 172103 (2005).

[7] F. D. Auret, W. E. Meyer, S. Coelho, and M. Hayes, Appl. Phys. Lett. **88**, 242110 (2006).

[8] D. C. Sawko and J. Bartko, IEEE Nucl. Sci. **30**, 1756 (1983).

[9] I. D. Desnica-Francovic, K. Furic, U. V. Desnica, M. C. Ridgway, and C. J. Glover, Nucl. Inst. Methods B **178**, 192 (2001).

[10] R. Duffy, V. C. Venezia, A. Heringa, B. J. Pawlak, M. J. P. Hopstaken, Y. Tamminga, T. Dao, F. Roozeboom, C. C. Wang, C. H. Diaz, et al., J. Vac. Sci. Technol. **22**, 865 (2004).

[11] S. Gaudet, C. Detavernier, A. J. Kellock, P. Desjardins, and C. Lavoie, J. Vac. Sci. Technol. **24**, 24 (2006).

Paper III

Electrical characterization of defects in heavy-ion implanted *n*-type Ge,

F. D. Auret, P. J. Janse van Rensburg, M. Hayes, J. M. Nel, S. Coelho, W. E. Meyer, S. Decoster, V. Matias, A. Vantomme and D. Smeets,

Nuclear Instruments and Methods in Physics Research B ***257****, 169 (2007)*

Electrical characterization of defects in heavy-ion implanted *n*-type Ge

F. D. Auret, P. J. Janse van Rensburg, M. Hayes,
J. M. Nel, S. Coelho, and W. E. Meyer
Department of Physics, University of Pretoria, Pretoria 0002, South Africa

S. Decoster, V. Matias, A. Vantomme, and D. Smeets
Instituut voor Kern- en Stralingsfysica and INPAC, K.U. Leuven, Celestijnenlaan 200D, B-3001 Leuven, Belgium

—

Nuclear Instruments and Methods in Physics Research B **257** (2007) 169

—

Abstract

Deep-level transient spectroscopy was used to investigate the electrically active defects introduced in *n*-type Ge during heavy-ion implantation of 160 keV ions. Various noble heavy-ions were used for implantation and the main defects introduced were found to be electron traps with energy levels at E_C - 0.09 eV, E_C - 0.15 eV and E_C - 0.30 eV. Another defect with a level at E_C - 0.38 eV, shown to be the E-center (VSb defect), is also present in a very low concentration. The main defects in heavy-ion implanted Ge are different from those introduced by MeV electron irradiation, where the main defect is the E-center. Since electron irradiation introduces mainly point defects, this indicates that heavy-ion implantation introduces defects of a more extended nature, such as vacancy and/or interstitial clusters and their combinations with impurities or foreign species in the Ge. We have also demonstrated that these defects are not species related.

I. INTRODUCTION

The low effective mass of holes in Ge has opened up the possibility of using Ge in ultra fast complimentary metaloxide semiconductor devices[1]. There is renewed interest in the properties of defects in Ge because defects ultimately determine the performance of devices. In recent studies, the properties of the defects introduced during high-energy gamma, electron and proton irradiation of Ge were reported[2–6]. The defects introduced during electron beam deposition of Pd Schottky contacts on n-Ge, where particles heavier than electrons create the defects, have also been characterized[7]. Little data are available regarding the electronic properties of defects introduced during the implantation of Ge with heavier ions, such as dopants. Implantation by heavy-ions is typically encountered during doping as well as pre-doping amorphization[8]. These implantations will introduce, among others, extended defects (e. g. clusters) that have different electronic and annealing characteristics compared to those of the well-studied point defects introduced during electron irradiation. The effect of indium implantation has been studied and the formation of these extended defects reported[8]. In general, irradiation and implantation-induced defects will influence device performance, but neither the nature of heavy-ion implantation-induced defects nor their influence on devices has yet been established for Ge. Depending on the application, these defects may either be beneficial for or detrimental to optimum device functioning. For example, for Si it has been shown that the defects introduced during high-energy electron and proton irradiation increase the switching speed of devices[9].

In this study, we report on the electronic properties of defects introduced in n-type Ge using several different noble heavy-ions for implantation. The noble ions are chemically inert and provide a large range of ion sizes and masses that can be used to study implantation damage of other ions with a similar size or mass.

We show here that all the heavy-ion implantation introduces three prominent electron traps in Ge similar to that observed for In[10]. In

order to investigate if the foreign species have any effect on the defects observed, we also implanted Ge samples with 160 keV Ge-ions.

II. EXPERIMENTAL

To study the implantation-related defects, we have used bulk-grown, (111) oriented, n-type material doped with Sb to a level of $(2-3)\times10^{15}$ cm^{-3}. Before metallization and implantation, the samples were first degreased and subsequently etched in a mixture of H_2O_2:H_2O (1:5, 30% H_2O_2) for 1 min. Immediately after cleaning and drying, they were inserted into a vacuum chamber where AuSb (0.6% Sb) was resistively deposited on their back surfaces for ohmic contacts. The samples were then annealed at 350 °C in Ar for 10 min to minimize the contact resistivity of the ohmic contacts. Thereafter the front sides of the samples were implanted at room temperature with 160 keV ions at an angle of 0° to a fluence of 2×10^{11} cm^{-2}. Before Schottky contact deposition, the samples were chemically cleaned again as described above. Palladium contacts, 0.6 mm diameter and 200 nm thick, were then resistively deposited on the implanted side of the Ge through a mechanical mask[7]. Deep-level transient spectroscopy (DLTS) was used to study the defects introduced in the Ge after implantation.

III. RESULTS AND DISCUSSION

In curves (a) and (b) of Fig. 1, we depict the DLTS spectra for an In-implanted and electron irradiated sample, respectively[10]. Note that, although not shown, the unimplanted Ge did not contain any defects in detectable concentrations[7]. Curves (c), (d), (e), (f) and (g) show the spectra obtained for noble ion implantation of He, Ne, Ar, Kr and Xe, respectively. The most significant electron traps indicated are $E_{0.09}$, $E_{0.15}$ and $E_{0.30}$ with levels at E_C - 0.09 eV, E_C - 0.15 eV and E_C - 0.30 eV, respectively. The defect signatures in Fig. 2 indicate that the

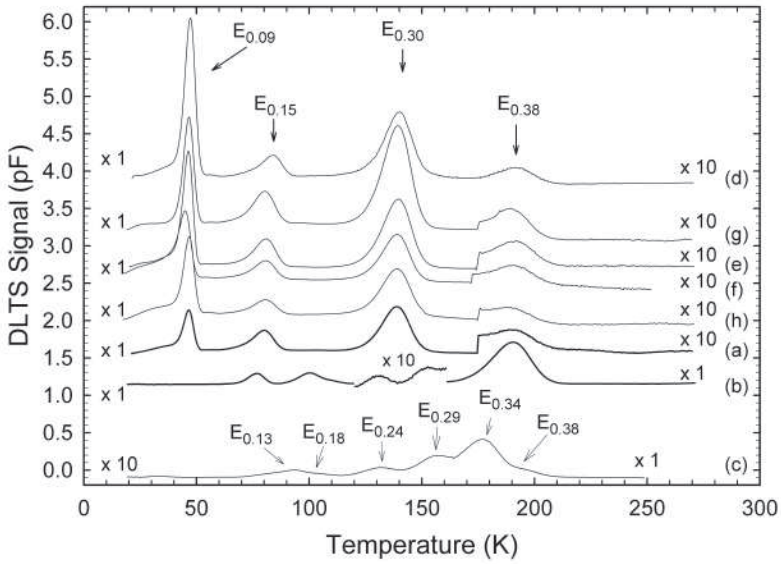

FIG. 1: DLTS spectra of 160 keV heavy-ion implanted Ge: In[10] (curve (a)), He (curve (c)), Ne (curve (d)), Ar (curve (e)), Kr (curve (f)), Xe (curve (g)), Ge (curve (h)), high-energy electron irradiated Ge[10] (curve (b)). These spectra were recorded using a rate window of 80 s^{-1} at a quiescent reverse bias of -2 V with a filling pulse, V_p, of 1.8 V superimposed on the reverse bias.

$E_{0.30}$ defect is virtually the same for all the different implanted ions. The apparent capture cross section for this defect was found to be 1.1×10^{-13} cm^{-2}. Although the level of $E_{0.30}$ is very close to that found for the divacancy after electron irradiation E_C - 0.29 eV[2], the divacancy anneals out at 150 °C whereas $E_{0.30}$ is still present after annealing at 200 °C[10]. This also suggests that this defect is of a more extended nature. The defect signatures for the $E_{0.09}$ and $E_{0.15}$ defects do not align completely, indicating that they may not be exactly the same defect. The energy levels for these two defects were found to be E_C - 0.09 $\pm$ 0.005 eV and E_C - 0.15 $\pm$ 0.005 eV, respectively. It has been observed (not shown here) that the $E_{0.09}$ defect exhibits emission rate dependence on biasing, which is characteristic of field enhanced emission possibly due to the Poole-Frenkel effect. This can possibly explain the different apparent

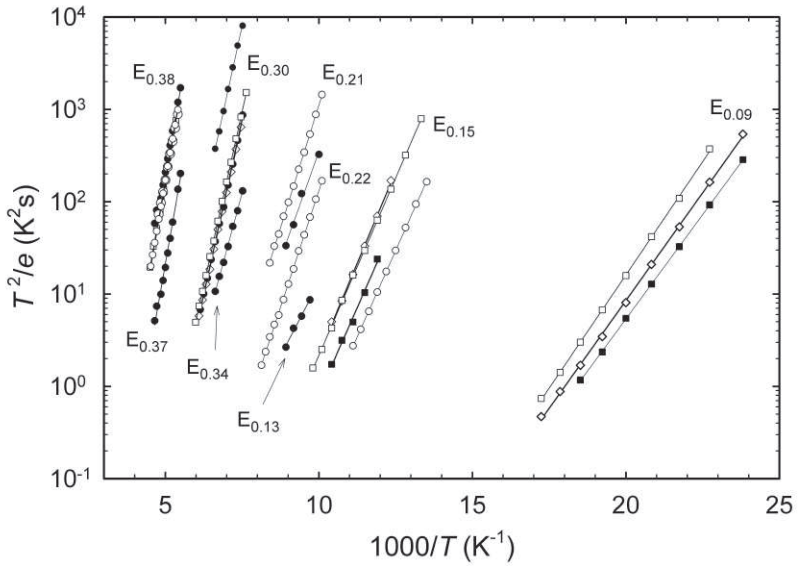

FIG. 2: Arrhenius plots for defects in heavy-ion implanted Ge: He (•), Ar (□), Xe (◇), In (■), and MeV electron irradiated Ge (○). All data were acquired using the recording conditions defined in the caption of Fig. 1.

capture cross sections observed for the various ion implantations because implantation with the different ions results in a slightly different free carrier concentrations for each of these samples. The apparent capture cross section for the $E_{0.09}$ defect varies between 7.6×10^{-14} and 1.2×10^{-13} cm^{-2} and that of the $E_{0.15}$ defect from 8.6×10^{-15} to 1.8×10^{-14} cm^{-2}.

A defect, $E_{0.38}$, in a much lower concentration, is also indicated at around 190 K. Note that from Fig. 1 and the Arrhenius plots in Fig. 2, the only defect that is clearly introduced both during MeV electron irradiation and implantation is $E_{0.38}$ and it is only introduced in a low concentration in the implanted Ge. $E_{0.38}$ has been identified as the (- -/-) charge state of the E-center (VSb) in Sb-doped Ge[2,3,10]. This implies that single vacancies are only produced in small quantities during implantation with heavy-ions, otherwise the $E_{0.38}$ concentration would have been much higher. This is understandable because heavy-ions de-

posit much more energy per unit length than electrons, thereby increasing the probability of the formation of defects larger than the single vacancy that is required for the formation of the E-center.

Note that the spectrum obtained for the He-implanted Ge (curve (c)) does not share the same features as the other heavy-ion implanted spectra. Comparing it to the electron irradiated spectrum (curve (b)), we see that the two small peaks at about 130 and 150 K are similar to the defects $E_{0.21}$ and $E_{0.22}$[10]. However, we found that these two defects have levels E_C - 0.24 eV and E_C - 0.29 eV which are different than the $E_{0.21}$ and $E_{0.22}$ found for electron irradiated Ge. Also note the $E_{0.18}$ and $E_{0.13}$ defects indicated with levels E_C - 0.18 eV and E_C - 0.13 eV and capture cross sections 3.1×10^{-15} and 6.9×10^{-16} cm^{-2}, respectively. The $E_{0.38}$ defect is also observed, closely spaced to another defect, labelled $E_{0.34}$. The defects associated with these peaks have energy levels E_C - 0.37 eV and E_C - 0.34 eV and apparent capture cross section of 4.6×10^{-14} and 1.8×10^{-14} cm^{-2}, respectively. It is therefore clear that the He-ions, which have a much lower mass compared to the other heavy-ions implanted, do not create the same structural defects in Ge. The defects that are created are present in very low concentrations and do not correspond to the three prominent defects introduced by implantation of heavier ions. As above, this is the result of the very different energy deposited per unit length for He-ions compared to heavier ions.

Finally, we deduce from Fig. 1 and Fig. 2 that the three main implantation-induced defects do not correspond to any of the defects introduced during electron irradiation. This implies that the $E_{0.09}$, $E_{0.15}$ and $E_{0.30}$ defects have a different physical structure than the defects introduced during electron irradiation. We speculate that they are related to higher order vacancy complexes, larger than the divacancy, or interstitial clusters, formed when an ion creates multiple point defects in the same physical environment that interact to become clusters.

In order to investigate the effect of lattice damage without introducing foreign species, we also investigated the implantation damage

introduced by implanting Ge-ions into the Ge substrate. The DLTS spectrum recorded for a Ge-implanted sample is shown in curve (h) of Fig. 1. It is clear that Ge introduce the same main three electron traps, as well as the E-center in small concentrations. The DLTS signatures of the Ge implantation-induced defects coincided well with those of the other heavy-ion defects (not shown in Fig. 2 for clarity). The electronic properties of these defects therefore do not depend on the implanted ion and we can thus conclude that they are simply physically different, possibly larger than the divacancy, introduced during ballistic collisions, and independent of the implanted ions.

IV. CONCLUSION

We have investigated, using conventional DLTS, the defects introduced during heavy-ion implantation of n-type Ge. Our results reveal that the main defects introduced have energy levels at E_C - 0.09 eV, E_C - 0.15 eV and E_C - 0.30 eV. Low concentrations of the VSb complex, or E-center, with an energy level at E_C - 0.38 eV, were also found to be introduced during implantation.

We have also demonstrated that the main defects are different from the point defects introduced by electron irradiation because the two sets of defects have very different electronic properties. By comparing the DLTS spectra of the heavy-ion implanted Ge (except for He), we could establish that these defects are observed for all implantations, including Ge implantation, and are therefore not species related. Since we have shown that these defects are not the same as the point defects introduced by electron irradiation, we propose that they are related to vacancy or interstitial clusters of various sizes, but larger than the divacancy.

Acknowledgements

The authors gratefully acknowledge financial support of the South African National Research Foundation, the Fund for Scientific Research, Flanders (FWO), IUAP P5/10 and the KULeuven Research Council (GOA/2004/02 and INPAC EF/05/005).

---

[1] R. Hull and J. C. Bean, *Germanium Silicon: Physics and Materials, Semiconductors and Semimetals* (Academic Press, San Diego, 1999).

[2] J. Fage-Pedersen, A. Nylandsted Larsen, and A. Mesli, Phys. Rev. B **62**, 10116 (2000).

[3] V. P. Markevich, A. R. Peaker, V. V. Litvinov, V. V. Emtsev, and L. I. Murin, J. Appl. Phys. **95**, 4078 (2004).

[4] V. P. Markevich, D. Hawkins, A. R. Peaker, K. V. Emtsev, V. V. Emtsev, V. V. Litvinov, L. I. Murin, and L. Dobaczewski, Phys. Rev. B **70**, 235213 (2004).

[5] V. P. Markevich, I. D. Hawkins, A. R. Peaker, V. V. Litvinov, L. Dobaczewski, and J. L. Linström, Appl. Phys. Lett. **81**, 1821 (2002).

[6] C. E. Lindberg, J. Lundsgaard Hansen, P. Bomholt, A. Mesli, K. Bonde Nielsen, and A. Nylandsted Larsen, Appl. Phys. Lett. **87**, 172103 (2005).

[7] F. D. Auret, W. E. Meyer, S. Coelho, and M. Hayes, Appl. Phys. Lett. **88**, 242110 (2006).

[8] I. D. Desnica-Francovic, K. Furic, U. V. Desnica, M. C. Ridgway, and C. J. Glover, Nucl. Inst. Methods B **178**, 192 (2001).

[9] D. C. Sawko and J. Bartko, IEEE Nucl. Sci. **30**, 1756 (1983).

[10] F. D. Auret, P. J. Janse van Rensburg, M. Hayes, J. M. Nel, W. E. Meyer, S. Decoster, V. Matias, and A. Vantomme, Appl. Phys. Lett. **89**, 152123 (2006).

Paper IV

Experimental evidence of tetrahedral interstitial and bond-centered Er in Ge,

S. Decoster, B. De Vries, U. Wahl, J. G. Correia and A. Vantomme

Applied Physics Letters ***93****, 141907 (2008)*

Experimental evidence of tetrahedral interstitial and bond-centered Er in Ge

S. Decoster, B. De Vries, and A. Vantomme
Instituut voor Kern- en Stralingsfysica and INPAC,
K.U. Leuven, Celestijnenlaan 200D, 3001 Leuven, Belgium

U. Wahl and J.G. Correia
Instituto Tecnológico e Nuclear, Estrada
Nacional 10, 2686-953 Sacavém, Portugal
and Centro de Física Nuclear da Universidade de Lisboa, Avenida
Prof. Gama Pinto 2, 1649-003 Lisboa, Portugal

—

Applied Physics Letters **93**, 141907 (2008)

—

Abstract

We report on an emission channeling study of the lattice site location of implanted Er in Ge together with its thermal stability. We found direct experimental evidence of Er atoms located on the tetrahedral interstitial site (T) and on the bond-centered (BC) site, with a maximum total occupancy after annealing at 400 °C. Whereas Er is expected to occupy the T site in a diamond crystal structure, the observation of bond-centered Er in Ge is more surprising and believed to be related to the Er-vacancy defect in the split-vacancy complex configuration.

During the past decades, the optical properties of Er integrated in semiconductors have been of great interest for photonic applications, especially in Si since the wavelength of the $^4I_{13/2} \rightarrow ^4I_{15/2}$ transition of the Er^{3+}-ion corresponds to the minimum absorption of silica-based optical fibers. The properties and dependencies of the luminescence in Er-doped Si or Si-based materials have been investigated intensively. However, due to the so-called thermal and concentration quenching, its room temperature luminescence yield remains below needs.[1]

In the search for alternative semiconducting host materials, the Ge:Er system received little attention so far because bulk Ge has a band gap (0.67 eV) which is smaller than the energy corresponding to the technologically interesting optical emission wavelength of Er, i.e. 1.54 μm (0.80 eV). This results in a large self absorption and consequently a very low efficiency. However, by using Ge nanoparticles, it has been possible to tune the band gap with the size of the nanoparticles, and thus to reduce the interband absorption.[2] The stronger quantum confinement effect and a better controlled oxidation with respect to Si, makes it a promising candidate as an Er-host for future photonic applications.[3,4] The growth of these Er-doped Ge-nanoparticles and their luminescence properties have been studied in detail,[2,5,6] as well as the annealing behavior of highly Er-doped Ge.[7] Despite the increased interest in this system, a number of fundamental questions remain unsolved. A particular one is the lattice location of the Er atoms, which largely influences the luminescence properties in semiconductors.[8] In Si, the lattice location of implanted Er has been investigated quite thoroughly. From emission channeling experiments[9,10] and several first-principles calculations,[11–13] the tetrahedral (T) interstitial site was found to be the preferred site in oxygen-lean Si. However, other studies suggested Er-atoms on the substitutional (S) site and the hexagonal (H) site.[14,15] In Ge, the only study on the lattice location of rare earths, is the work of Yamamoto *et al.*, who concluded from He channeling experiments that 25% of implanted Tm occupies the T site.[16]

In this letter, we present a direct lattice location study of Er in Ge,

measured with the emission channeling technique[17]. We make use of the fact that charged particles, emitted from an implanted radioactive isotope will be guided by the potential of atomic rows and planes while traveling through the crystal. The resulting anisotropic electron emission pattern around low-index crystal directions is characteristic for the lattice site occupied by the emitting atom and is measured with a 2-dimensional (2D) energy- and position-sensitive Si detector of 22×22 pixels. The advantages of this technique with respect to ion beam channeling techniques such as RBS/C, are a considerable improvement in accuracy due to the use of 2D-patterns instead of 1D-scans and the use of low implantation fluences which allows us to measure the lattice location of isolated atoms.

Implantations with radioactive ^{167}Tm ($t_{1/2}$=9.25 d) were performed at room temperature at the ISOLDE facility in CERN. This isotope decays into ^{167m}Er ($t_{1/2}$=2.27 s), emitting K, L, and M conversion electrons of respectively 150, 199 and 206 keV. Three undoped Ge samples were studied with varying implantation fluence, energy and sample orientation, and will be labeled sample A (3.6×10^{12} cm^{-2}; 30 keV; $\langle 100 \rangle$), B (1.1×10^{13} cm^{-2}; 60 keV; $\langle 100 \rangle$) and C (7.7×10^{12} cm^{-2}; 30 keV; $\langle 111 \rangle$). To obtain unambiguous results, emission patterns around the four crystal directions ($\langle 100 \rangle$, $\langle 111 \rangle$, $\langle 211 \rangle$ and $\langle 110 \rangle$) were measured, analyzed consistently and fitted to a set of simulated patterns.[18] These simulations, based on the dynamical theory of electron diffraction, were performed for several high-symmetry sites such as the S, T, H, bond-centered (BC) and the so-called AB, SP, Y and C sites,[19] as well as for discrete displacements between these sites along the $\langle 111 \rangle$-, $\langle 100 \rangle$- and $\langle 110 \rangle$-direction. To monitor the thermal stability of the lattice location of the Er atoms, the measurements were performed after implantation as well as after annealing for 10 min in vacuum ($< 10^{-5}$ mbar) at temperatures up to 600 °C.

Figures 1(a)-(d) show the normalized experimental electron emission patterns around the four investigated crystal directions for sample C after annealing at 400 °C. Along the $\langle 111 \rangle$- and $\langle 100 \rangle$-direction, we clearly

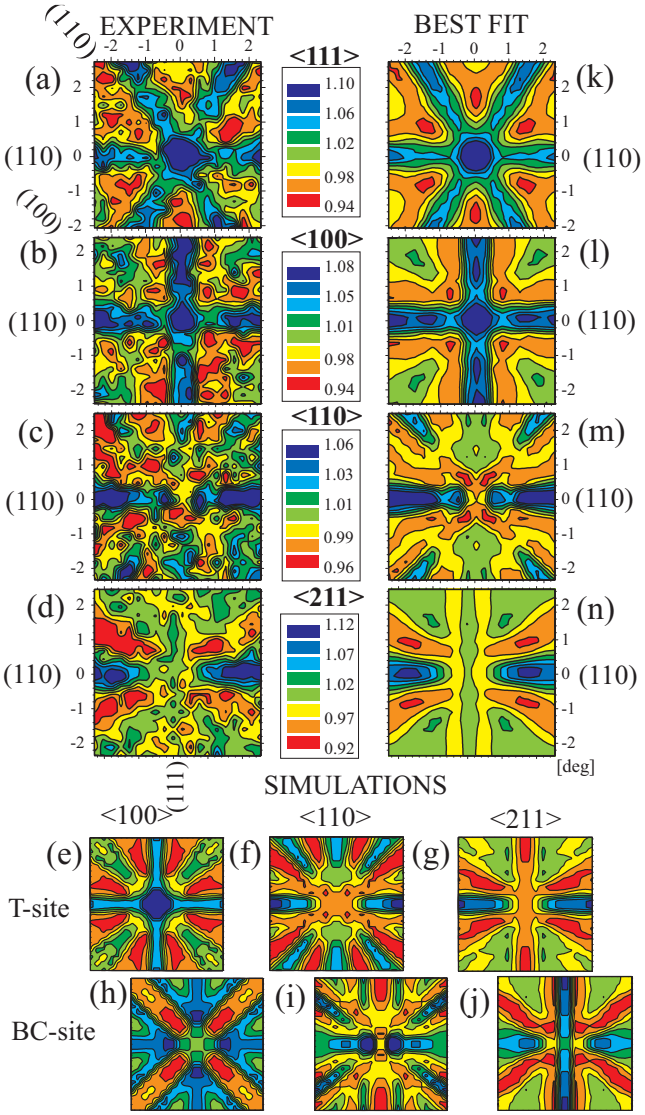

FIG. 1: (a)-(d) Two-dimensional conversion electron patterns emitted from ^{167m}Er in Ge around the ⟨111⟩, ⟨100⟩, ⟨110⟩ and ⟨211⟩-axes, following a 400 °C annealing in vacuum; (e)-(g) Calculated patterns for Er-atoms occupying the T site and (h)-(j) the BC site around the ⟨100⟩, ⟨110⟩ and ⟨211⟩-axis respectively; (k)-(n) Best fits to the experimental patterns. The anisotropy is depicted with a color scale between red (low) and blue (high).

see an enhanced number of electrons emitted along the crystal axis, while the ⟨110⟩ and ⟨211⟩ patterns show a blocking effect, which is characteristic for the T site. However, when comparing the experimental patterns for the ⟨100⟩-, ⟨110⟩- and ⟨211⟩-direction (Fig. 1(b)-(d)) to the corresponding calculated patterns for Er on a pure T site (Fig. 1(e)-(g)), a number of major discrepancies are obvious. This leads to the conclusion that the Er-atoms occupy at least a second high-symmetry site. Therefore, a detailed fitting procedure was applied, considering all possible combinations of 2 and even 3 different high-symmetry sites, including possible displacements. While adding most of the high-symmetry sites (H, S, SP, AB, Y and C) resulted only in marginal improvements of the fit (χ^2-improvement $< 3\%$), including a BC fraction results in a consistent fit in all four directions, with an average χ^2-improvement of more than 25%. Superposing the simulations for the T site (e)-(g) and the BC site (h)-(j), solves the discrepancies, as can be seen from Fig. 1. This is further clarified in Fig. 2 (a-c), showing the residual experimental pattern from Fig. 1 (d) after subtracting the fit with a BC fraction only, a T fraction only and both T and BC fractions respectively. Fig. 2 (a) clearly shows remaining features of a T site pattern, while Fig. 2 (b) exhibits the same features as a BC pattern. On the other hand, Fig. 2 (c) results in a featureless pattern, clearly indicating that the only satisfying fit is obtained by including a fraction on the BC and the T site. Adding a third fraction did not significantly improve the fit, indicating that only relatively small fractions ($< 2\%$) of Er-atoms occupy other high-symmetry sites. Similar fit results have been found for the other two samples, resulting in average χ^2 improvements between 15% and 40%.

Figures 1(k)-(n) show the best fit to the experimental patterns. Averaging the results of the 4 measured directions, 16(2)% of the Er-atoms are found on the BC site and 20(4)% on a slightly displaced T site. The Er-atoms on the T site were found to have an average root mean square displacement of about 0.18(3) Å, which is somewhat larger than the Ge host vibration amplitude at room temperature of 0.08 Å. The

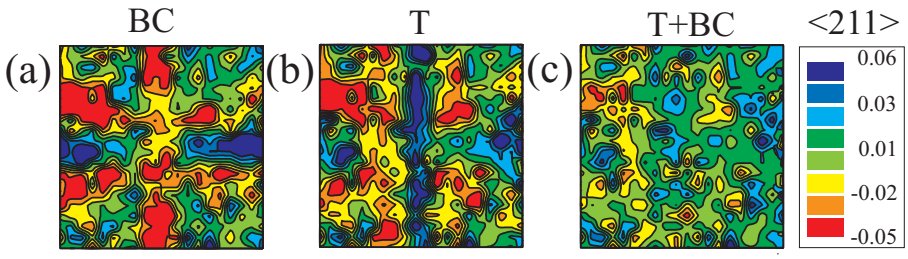

FIG. 2: The experimental ⟨211⟩-pattern from Fig. 1(d) after subtracting the best fit when allowing a fraction on (a) the BC site, (b) the T site and (c) both T and BC sites.

large remaining fraction of Er-atoms (64%) is referred to as the random fraction. This random fraction partly consists of Er-atoms that are distributed randomly within the crystal lattice, but a large contribution will be related to the implantation-induced lattice damage. Even for the low fluences used in this study, heavy-ion implantation produces highly damaged regions, especially in materials with small lattice binding energies such as Ge. Firstly, due to the deterioration of the crystal structure, a fraction of the implanted radioactive isotopes will be located in damaged regions with reduced local crystallinity. Secondly, a fraction of the electrons emitted from an undamaged region will pass through damaged crystal regions, enhancing the probability for dechanneling. Both effects will result in an isotropic background to the patterns and consequently in the high random fraction observed in this work. However, it is important to notice that this high random fraction will not affect the qualitative analysis of the spectra.

In Fig. 3, the temperature dependence of the Er-fractions on the T and BC site is plotted for all 3 samples. Despite the slightly different implantation conditions, the same behavior is present in all three samples. Annealing up to 400 °C results in an increasing fraction of Er-atoms on high-symmetry sites, which is a direct consequence of the partial lattice recovery of damaged regions. This fraction decreases again after annealing at temperatures higher than 450 °C, which is most likely related

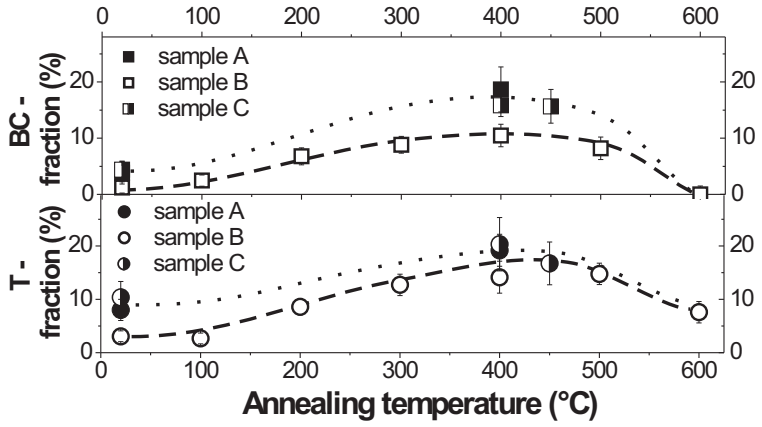

FIG. 3: Annealing temperature dependence of the fraction Er-atoms on the T site (circles) and the BC site (squares) for sample A (filled), B (open) and C (half open symbols). The dotted lines are a guide to the eye.

to diffusion of the Er-atoms. As the depth profile of the implanted Er-atoms is an input parameter for the simulations, it implies that a larger mean projected range of the Er-atoms after diffusion will lead to an underestimation of the measured and fitted fraction on high-symmetry sites. Alternatively, the trapping of Er-atoms by migrating defects, may result in Er-atoms occupying low-symmetry sites in defect complexes.

The existence of tetrahedral interstitial Er in Si has been proven both from experiments and calculations. Due to the similar lattice structure of Si and Ge, Er can be expected to occupy the T site in Ge as well, which was found experimentally in this study. So far, there is no clear explanation for the small displacement of the Er-atoms on the T site. However, it could be originating from lattice relaxations as was predicted from density functional computations.[14] Applying stress related arguments, Er is not expected to occupy a BC site in an undamaged Ge crystal. However, we believe this site is related to an Er-vacancy (Er-V) complex. From ab-initio density functional calculations, a range of high-Z impurities (from Cd to Bi) were found to be unstable on the S site with a vacancy on the nearest neighbor S site.[20] The impurity prefers to

shift towards the BC site, with the vacancy *split* between the two sites. Ion implantation is known to produce many vacancies and interstitials, which are mobile at room temperature in Ge.[21] This implies that during the implantation, they are free to migrate through the crystal until they either recombine, form complex clusters or get trapped by impurity atoms. Although no calculations have been performed for Er, interpolating the trend that high-Z impurities are stable on the BC site, allows us to conclude that our experimental observation of Er on the BC site in Ge might be indirect evidence of the Er-V complex in the split-vacancy configuration. It can not be excluded that other (more complex) defect configurations may also contribute to the observed bond-centered behavior.

In conclusion, we have found experimental evidence of implanted Er atoms located on the T site and on the BC site in Ge. While the occupation of the T site could be expected from comparison with similar studies in Si, this study offers direct evidence of the occupation of the BC site in Ge. This site has been predicted by ab-initio density functional calculations for heavy impurities in Ge and we believe it is related to the Er-V complex in the split-vacancy configuration. Since the luminescent properties of dopants are significantly influenced by their lattice site, the observation of Er on two different sites can be of great importance in understanding – and even tuning – the optical properties of the Ge:Er system.

This work was supported by FWO Flanders, the K.U.Leuven projects GOA/2004/02 and INPAC EF/05/2005, the IUAP P6/42 program and the Portuguese Foundation for Science and Technology (POCI-FP-81921-2007) and the ISOLDE collaboration. S. D. acknowledges financial support from FWO, Flanders.

---

[1] A. Kenyon, Semicond. Sci. Technol. **20**, R65 (2005).

[2] S. Sato, S. Nozaki, H. Morisaki, and M. Iwase, Appl. Phys. Lett. **66**, 3176

(1995).

[3] C. Bostedt, T. van Buuren, T. Willey, N. Franco, L. Terminello, C. Heske, and T. Moller, Appl. Phys. Lett. **84**, 4056 (2004).

[4] M. Jing, M. Ni, W. Song, J. Lu, Z. Gao, L. Lai, W. Mei, D. Yu, H. Ye, and L. Wang, J. Chem. Phys. B **110**, 18332 (2006).

[5] C. Heng, T. Finstad, P. Storas, Y. Li, A. Gunnaes, and O. Nilsen, Appl. Phys. Lett. **85**, 4475 (2004).

[6] J. Chen, D. Pang, H. Cheong, P. Wickboldt, and W. Paul, Appl. Phys. Lett. **67**, 2182 (1995).

[7] S. Kucheyev, J. Bradby, S. Ruffell, C. Li, T. Felter, and A. Hamza, Appl. Phys. Lett. **90**, 221901 (2007).

[8] Y. Tang, K. Heasman, W. Gillin, and B. Sealy, Appl. Phys. Lett. **55**, 432 (1989).

[9] U. Wahl, A. Vantomme, J. De Wachter, R. Moons, G. Langouche, J. Marques, J. Correia, and the ISOLDE Collaboration, Phys. Rev. Lett. **79**, 2069 (1997).

[10] U. Wahl, J. Correia, J. Araújo, A. Vantomme, G. Langouche, and the ISOLDE Collaboration, Physica B **273-274**, 342 (1999).

[11] M. Needels, M. Schluter, and M. Lannoo, Phys. Rev. B **47**, 15533 (1993).

[12] Y. Wan, Y. Ling, Q. Sun, and X. Wang, Phys. Rev. B **58**, 10415 (1998).

[13] D. Prezzi, T. Eberlein, R. Jones, J. Filhol, J. Coutinho, M. Shaw, and P. Briddon, Phys. Rev. B **71**, 245203 (2005).

[14] A. Raffa and P. Ballone, Phys. Rev. B **65**, 121309 (2002).

[15] A. Kozanecki, R. Wilson, B. Sealy, J. Kaczanowski, and L. Nowicki, Appl. Phys. Lett. **67**, 1847 (1995).

[16] Y. Yamamoto, M. Wakaiki, A. Ikeda, and Y. Kido, Nucl. Inst. Meth. Phys. Res. B **153**, 452 (1999).

[17] U. Wahl, J. Correia, A. Czermak, S. Jahn, P. Jalocha, J. Marques, A. Rudge, F. Schopper, J. Soares, A. Vantomme, et al., Nucl. Inst. Meth. Phys. Res. A **524**, 245 (2004).

[18] H. Hofsäss and G. Lindner, Phys. Rep. **201**, 121 (1991).

[19] U. Wahl, Phys. Rep. **280**, 145 (1997).

[20] H. Höhler, N. Atodiresei, K. Schroeder, R. Zeller, and P. Dederichs, Phys. Rev. B **71**, 035212 (2005).

[21] H. Hässlein, R. Sielemann, and C. Zistl, Phys. Rev. Lett. **80**, 2626 (1998).

Paper V

Transition metal impurities on the bond-centered site in germanium,

S. Decoster, S. Cottenier, B. De Vries, H. Emmerich, U. Wahl, J. G. Correia and A. Vantomme

Physical Review Letters ***102****, 065502 (2009)*

Transition metal impurities on the bond-centered site in germanium

S. Decoster, B. De Vries, and A. Vantomme
Instituut voor Kern- en Stralingsfysica and INPAC, K.U. Leuven, Celestijnenlaan 200D, 3001 Leuven, Belgium

S. Cottenier
Instituut voor Kern- en Stralingsfysica and INPAC, K.U. Leuven, Celestijnenlaan 200D, 3001 Leuven, Belgium and Computational Materials Engineering (CME), Institute for Minerals Engineering (GHI), Center for Computational Engineering Science (CCES) & Jülich-Aachen Research Alliance (JARA), RWTH Aachen University, DE-52064 Aachen, Germany Center for Molecular Modeling, Ghent University, Proeftuinstraat 86, BE-9000 Ghent, Belgium

H. Emmerich
Computational Materials Engineering (CME), Institute for Minerals Engineering (GHI), Center for Computational Engineering Science (CCES) & Jülich-Aachen Research Alliance (JARA), RWTH Aachen University, DE-52064 Aachen, Germany Center for Molecular Modeling, Ghent University, Proeftuinstraat 86, BE-9000 Ghent, Belgium

U. Wahl and J.G. Correia
Instituto Tecnológico e Nuclear, UFA, Estrada Nacional 10, apt. 21, 2686-953 Sacavém, Portugal

—

Physical Review Letters **102**, 065502 (2009)

—

Abstract

We report on the lattice location of ion implanted Fe, Cu and Ag impurities in germanium from a combined approach of emission channeling experiments and *ab initio* total energy calculations. Following common expectation, a fraction of these transition metals (TMs) was found on the substitutional Ge position. Less expected is the observation of a second fraction on the 6-fold coordinated bond-centered site. *Ab initio* calculated heats of formation suggest this is the result of the trapping of a vacancy by a substitutional TM impurity, spontaneously forming an impurity-vacancy complex in the split-vacancy configuration. We also present an approach to displace the TM impurities from the electrically active substitutional site to the bond-centered site.

Compared to silicon, free charge carriers have a higher mobility and dopants have a lower activation temperature in Ge[1], which makes it an increasingly important and attractive material in metal-oxide semiconductor field-effect transistors[2]. Despite intensive research, several fundamental properties of this semiconductor are still poorly known. Transition metals (TMs) produce deep-level states in the semiconductor band gap and are hence detrimental for the electrical properties of integrated circuits, even in small concentrations[3]. Since the lattice site of TMs has a major influence on their electrical activity, lattice location studies are important. For Ge, the electrical behavior of ion implanted as well as in-diffused TM impurities has been studied quite extensively ([4–6] and references therein), but the information about their lattice location in Ge is rather puzzling. From electrical characterization, the TMs are found to act as multiple acceptors in Ge, and in accordance with the simple valence model, most of the induced deep level states in the band gap have been attributed to TMs on the substitutional (S) site. However, the full picture seems to be more complicated. Mössbauer spectroscopy experiments after recoil implantation of ^{57m}Fe and ion implantation of ^{57}Mn in Ge have revealed that the Fe atoms also partly occupy the tetrahedral interstitial (T) site and a third site believed to be related to Fe_i-V complexes[7,8]. From emission channeling experiments similar to the ones presented here, a large fraction of ion implanted ^{67}Cu was found on the S site, together with a smaller fraction located halfway between the S and the bond-centered (BC) site[9]. On the computational side, *ab initio* calculations indicate that the S site is favored over the T site for 3d-transition metals in Ge as well as in Si[10,11]. Other theoretical studies in Ge focussed on impurity-vacancy complexes with impurities from the *sp*-series, with conflicting geometrical results[12,13].

To clarify these puzzling experimental data, we present a direct lattice location study of Fe, Cu and Ag in Ge with the emission channeling (EC) technique[14]. In an EC experiment, charged particles, emitted from an implanted radioactive isotope are guided by the potential of atomic rows and planes while traveling through the crystal. The re-

sulting anisotropic electron emission pattern around low-index crystal directions is characteristic for the lattice site occupied by the emitting atom and is measured with a 2D energy- and position-sensitive Si detector of 22×22 pixels. The advantages of this technique are its high accuracy in comparison with regular ion channeling techniques and the use of very low implantation fluences which allows us to study isolated atoms.

The radioactive isotopes ^{59}Mn, ^{67}Cu and ^{111}Ag have been implanted at the ISOLDE facility in CERN to study the lattice location of Fe, Cu and Ag, respectively. ^{59}Mn (4.6 s) rapidly decays into the long-lived β^--emitter ^{59}Fe (44.6 d), which decays to ^{59}Co. The ^{59}Fe nucleus receives an average recoil of 200 eV which assures the atom gets reimplanted and is not influenced by the lattice site of its precursor. ^{67}Cu (61.9 h) decays into stable ^{67}Zn by emitting β^--particles and in a similar way ^{111}Ag (7.45 d) decays into stable ^{111}Cd. The implantations have been performed at room temperature in undoped $\langle 111 \rangle$-Ge with an energy of 60 keV to fluences of 1.0×10^{13} cm^{-2} for Fe, 6.6×10^{12} cm^{-2} for Cu and 5.0×10^{12} cm^{-2} for Ag. To obtain accurate and unambiguous results, emission patterns along the four crystal directions $\langle 100 \rangle$, $\langle 111 \rangle$, $\langle 211 \rangle$ and $\langle 110 \rangle$ were measured, analyzed consistently and fitted to a set of simulated spectra. These simulations[15] have been performed for several high-symmetry sites such as the S, T, BC, hexagonal (H) and the so called AB, SP, Y and C sites[16], as well as for discrete displacements between these sites along the $\langle 111 \rangle$-, $\langle 100 \rangle$- and $\langle 110 \rangle$-direction. To monitor the thermal stability of the lattice location of the implanted impurities, the measurements were performed on as-implanted samples, as well as after annealing up to 500 °C in vacuum ($< 10^{-5}$ mbar) during 10 min.

Figures 1 (a)-(d) show the normalized electron emission patterns around the $\langle 111 \rangle$, $\langle 100 \rangle$, $\langle 110 \rangle$ and $\langle 211 \rangle$-axes for ^{111}Ag in Ge. In all directions, an increased normalized yield along the measured axis is visible (i.e. axial channeling), indicating that at least a fraction of the implanted Ag atoms will be located substitutionally. However, compar-

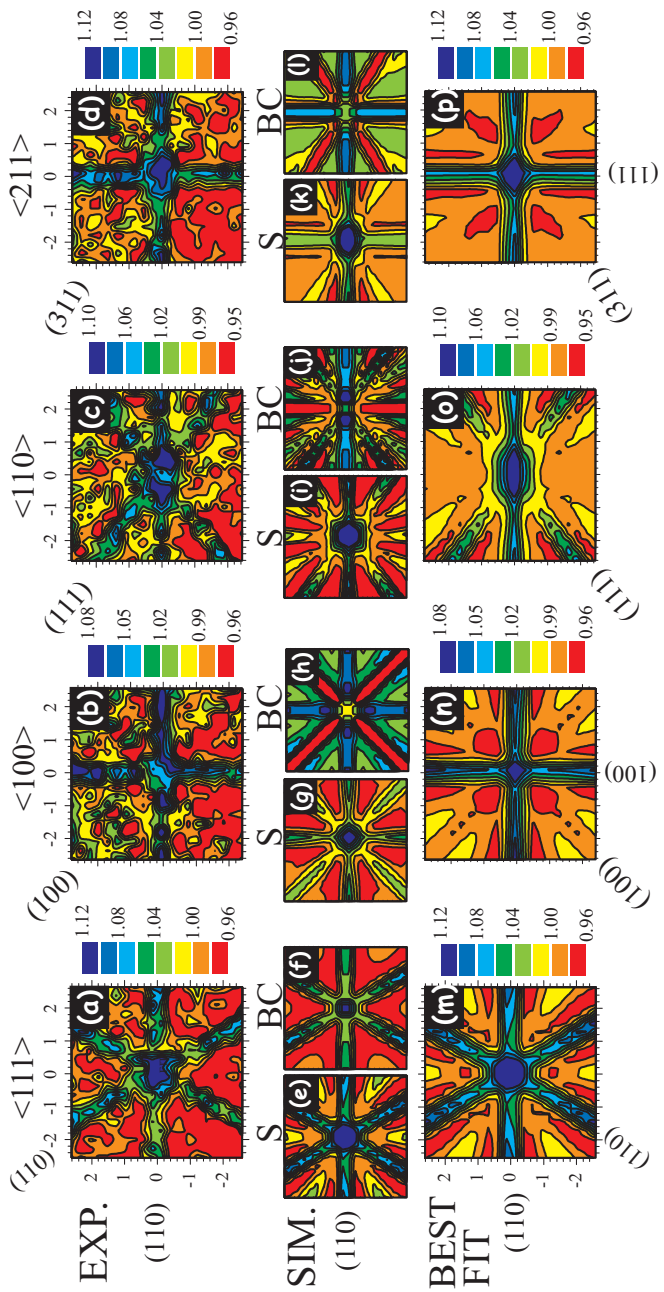

FIG. 1: (a)-(d) Two-dimensional electron patterns emitted from ^{111}Ag in Ge around the ⟨111⟩, ⟨100⟩, ⟨110⟩ and ⟨211⟩-axes, following a 400 °C annealing step in vacuum; simulated patterns around the (e)-(f) ⟨111⟩, (g)-(h) ⟨100⟩, (i)-(j) ⟨110⟩ and (k)-(l) ⟨211⟩-axes for Ag on the S site and on the BC site respectively; (m)-(p) the best fits to the experimental patterns.

ing the experimental patterns on panels (a) to (d) with the simulated patterns for purely substitutional ^{111}Ag atoms on respectively panels (e), (g), (i) and (k) reveals a number of discrepancies. The experimental pattern along the ⟨110⟩-direction shows a split channeling peak in the center of panel (c) – which is not present in the simulation on panel (i) – while along the ⟨100⟩-direction the measured axial channeling effect on panel (b) is much less pronounced than the simulated one on panel (g). More discrepancies can be found by investigating the measured planar channeling effects.

This visual analysis indicates that the Ag impurities occupy at least a second high-symmetry site. Therefore, a quantitative fitting procedure has been applied, allowing the Ag atoms to occupy up to three different sites. Adding either T, H, SP, AB, Y or C sites to the substitutional fraction results only in an insignificant fit improvement (χ^2 improvement $< 2\%$), while adding a fraction on the BC site remarkably improves the fit, up to 25%. Visual inspection of the simulations for the S and BC site in Fig. 1 (e)-(l), shows that a linear combination of these simulations is able to solve the discrepancies described above, leading to the acceptably accurate fits in Fig. 1 (m)-(p). Adding more high-symmetry sites results in only marginal improvements of the fits (i.e. χ^2 improvement $< 2\%$), allowing us to conclude that only small Ag fractions ($< 3\%$) occupy other high-symmetry sites.

In the best fit to the experimental patterns, 21(3)% of the implanted Ag atoms occupy the S site and 33(4)% the BC site. The remaining fraction, which will be referred to as the *random* fraction, will be discussed in the next paragraph. After analyzing the patterns for Fe, Cu and Ag as implanted and after several annealing stages, the general trend is clear (Fig. 2): the three TMs are partially found on the S site and partially on the BC site.

Heavy ion implantation produces highly damaged regions, especially in materials with small lattice binding energies such as Ge, even for the low fluences used in this study. This implantation damage has a double influence on the results shown here, and more specifically on

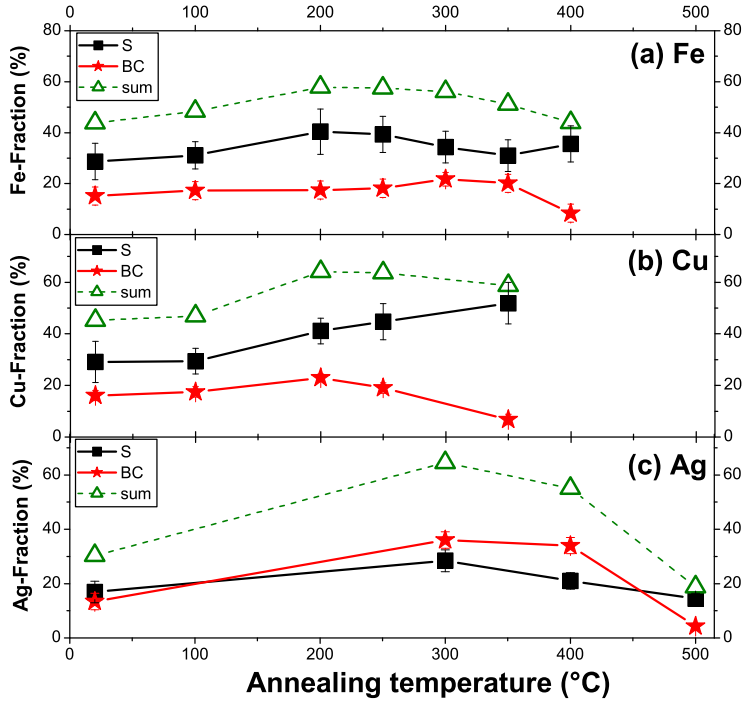

FIG. 2: Fraction of the implanted Fe (a), Cu (b) and Ag atoms (c) on the S site (■) and the BC site (★) in Ge, together with the total fraction (△ = ■ + ★) on high-symmetry sites, as a function of annealing temperature.

the random fraction. Firstly, due to the deterioration of the crystal structure, a fraction of the implanted radioactive isotopes will be located in damaged regions with reduced local crystallinity. Secondly, a fraction of the electrons emitted from an undamaged region will pass through damaged crystal regions, enhancing the probability for dechanneling – thus masking the impurity's lattice site. Both effects will result in an isotropic background to the patterns and consequently in the random fraction, observed in the experiments. This damage effect implies that the fractions presented in this work should be treated as lower limits to the real ones. The increasing fraction of TMs on high-symmetry sites after the first annealing steps (Fig. 2) indicates that the implantation

damage is at least partly recovered. The drastic decrease of this fraction in the case of Ag (Fig. 2(c)) after annealing at 500 °C is related to the diffusion of Ag atoms and will not be discussed in more detail here.

In accordance with the studies discussed in the introduction[4–10], we found a large fraction of the TMs on the S site in Ge after ion implantation. The prevalence of the S site is consistent with theoretical work[10,11] where it was found to be more favorable than the T and H sites. More intriguing is the occupation of the BC site, for which we found no unambiguous experimental evidence in literature. In order to understand the existence of this BC site, a complementary *ab initio* study has been performed. We have calculated the heat of formation of 3 impurity sites in Ge: the S site, the T site and the impurity on the S site with one vacancy in the nearest neighbor shell (S+V). The latter complex was taken into account because ion implantation produces a large amount of vacancies, which are mobile at room temperature in Ge[17] and might be trapped by impurities. The heats of formation reported in Tab. I are calculated according to

$$\Delta H_f = E_{sup}^{imp} - \mu_{imp} - \left(32E_{sup}^{id} - n\mu_{Ge}\right) \tag{1}$$

where E_{sup}^{imp} is the total energy of a 63- or 64-atom supercell that contains the impurity, E_{sup}^{id} is the total energy of a pure Ge unit cell (diamond structure, 2 atoms), μ_{Ge} is the chemical potential of Ge (taken equal to the total energy per atom in bulk Ge), n is the number of Ge atoms in the ideal 64-atom supercell that are replaced by either vacancies or impurities ($n = 1, 2$) and μ_{imp} is the chemical potential of the impurity with respect to the elemental solid (ferromagnetic bcc-Fe, fcc-Cu, fcc-Ag). For all elemental solids, the lattice constant was optimized and then fixed for the 64-atom cells, but all atoms in those supercells were allowed to move to their equilibrium positions. The calculations were done by the APW+lo method within Density Functional Theory, as implemented in the WIEN2k code[18,19]. The Perdew-Burke-Ernzerhof[20] exchange-correlation functional was used, the k-space sampling was done on a 4×4×4 mesh in the 64-atom cell, and a basis set corresponding to

	Fe				Cu		Ag	
	ΔH_f (eV)	d (%)	δ_0 (mm/s)	$\Delta E_{Q,0}$ (mm/s)	ΔH_f (eV)	d (%)	ΔH_f (eV)	d (%)
S	1.90	-6.7	0.06		1.34	-4.6	1.63	+0.0
T	3.19	+0.1	1.08		1.75	+1.7	2.10	+4.8
S+V	3.85	-19.8	0.55	0.81	3.10	-13.2	2.53	-11.0

TABLE I: Heat of formation (ΔH_f) for the 3 impurity environments considered in this work, the relative displacements of the first nearest neighbor shell (d) with respect to the starting configuration and the calculated values for the isomer shift (δ_0) and the quadrupole splitting ($\Delta E_{Q,0}$) for Fe at 0 K.

$K_{max} = 3.5$ a.u. was taken. The influence of the size of the supercell (up to 256 atoms) as well as the influence of the magnetic state of the Fe impurities on the calculations were verified and found to be small. After relaxation of the configuration with the impurities on the S and the T site, small displacements were found (Tab. I). A slightly reduced distance to the first nearest neighbor (d) shell has been calculated in the case of the substitutional impurity, while the impurity on the T site pushes the neighbors slightly away. This is in agreement with previous calculations for Fe in Ge[10,11]. Adding a vacancy to the substitutional impurity (S+V), induces a large force on the TMs along the $\langle 111 \rangle$-direction, resulting in the impurity ending up on the ideal 6-fold coordinated BC site with the vacancy *split* on the nearest neighbor positions: the *split-vacancy* configuration[12,13]. As can be seen from Tab. I, the nearest neighbor distance in this configuration is considerably reduced.

By comparing the heats of formation in Tab. I, it is clear that the three studied TMs prefer the S site to the T or BC site. At first sight, this contradicts the experimental observation of the BC site. The following arguments show this is not true, however. We calculated the heat of formation for a single neutral vacancy in Ge to be 2.23 eV (in agreement with Ref.[21]). The total energy needed to have an impurity on the S site and an isolated vacancy is larger than the heat of formation of the BC configuration for all three TMs. Therefore, S site

impurities will trap the abundantly available mobile vacancies created during implantation, and – as the structural relaxation process in our calculations shows – will spontaneously evolve into the BC site. Our results strengthen the hypothesis that the Fe atoms found on the T site in Mössbauer experiments[8] are mainly produced by the 40 eV recoil energy received during the β-decay of the ^{57}Mn atoms. This recoil energy is high enough to overcome the energy barrier between S and T, but not enough to get reimplanted. *Ab initio* values for the isomer shift and electric-field gradient of non-magnetic Fe on the S, T and BC sites (Tab. I) are in agreement with Mössbauer experiments[8], and suggest that an unidentified BC site has been encountered before in such experiments. The Fe_i-V complex, with Fe on the T site, as postulated in Ref. 8 would lead to $\delta = 0.67$ mm/s and $\Delta E_Q = 1.01$ mm/s, in worse agreement with experiment. Reanalysis of the spectra from an earlier EC-experiment on Cu[9], indicates a large fit improvement by adding a BC fraction to the S fraction and only minor improvement after allowing displacements to the site halfway between the S and BC site, in accordance with our results.

In conclusion, we found direct experimental evidence that the ion implanted transition metals Fe, Cu and Ag do not solely occupy the substitutional site, but the bond-centered site as well. This result contributes significantly to the understanding of the electrical properties of transition metals in germanium, since they are known to be electrically active on the S site, while no active defect levels have been attributed to TMs on the BC site. Corroborated by theory, this BC fraction is attributed to impurity-vacancy complexes in the split-vacancy configuration. By investigating the heat of formation of this complex, it can be concluded that the mobile vacancies, created during the ion implantation process, will be trapped by substitutional impurities, resulting in the spontaneous occupation of the BC site. Hence, this BC behavior is a direct consequence of the presence of mobile vacancies, which were, in this specific study, created during the ion implantation process. However, these results are more generally valid since a wide variety of tech-

nologically important treatments are known to produce a large number of vacancies, such as the growth of Ge-films on Si[3], sputter deposition of metals on a Ge surface[22], and annealing of those deposited films to form germanides as Ohmic or Schottky contacts[23]. Furthermore, by intentionally introducing vacancies, e. g. with electron irradiation, we have presented an approach to relocate the TMs from the electrically active S site to the BC site.

This work was supported by FWO Flanders (G.0501.07 and G.0636.08), the K.U.Leuven projects GOA/2009/006 and INPAC EF/2005/005, the IUAP P6/42 programme, the Portuguese Foundation for Science and Technology (POCI-FP-81921-2007) and the ISOLDE collaboration. S. D. acknowledges financial support from FWO.

---

[1] R. Hull and J. C. Bean, *Germanium Silicon: Physics and Materials, Semiconductors and Semimetals*, Academic, San Diego (1999).

[2] Y. J. Yang, W. S. Ho, C. F. Huang, S. T. Chang, and C. W. Liu, Appl. Phys. Lett. **91**, 102103 (2007).

[3] C. Claeys and E. Simoen, *Germanium-based technologies: From materials to devices*, Elsevier, Amsterdam (2007).

[4] P. Clauws and E. Simoen, Mat. Sci. Semicond. Proc. **9**, 546 (2006).

[5] P. Clauws, J. Van Gheluwe, J. Lauwaert, E. Simoen, J. Vanhellemont, M. Meuris, and A. Theuwis, Physica B **401-402**, 188 (2007).

[6] E. Simoen, K. Opsomer, C. Claeys, K. Maex, C. Detavernier, R. L. Van Meirhaeghe, and P. Clauws, J. Appl. Phys. **104**, 023705 (2008).

[7] P. Schwalbach, M. Hartick, M. Ciani, E. Kankeleit, B. Keck, R. Sieleman, B. Stahl, and L. Wende, Hyperfine Interactions **70**, 1121 (1992).

[8] H. P. Gunnlaugsson, G. Weyer, M. Dietrich, M. Fanciulli, K. Bharuth-Ram, R. Sielemann, and the ISOLDE Collaboration, Physica B **340-342**, 537 (2003).

[9] U. Wahl, J. G. Correia, J. C. Soares, and the ISOLDE Collaboration, Physica B **340**, 799 (2003).

[10] A. Continenza, G. Profeta, and S. Picozzi, Phys. Rev. B **73**, 035212 (2006).

[11] Z. Z. Zhang, B. Partoens, K. Chang, and F. M. Peeters, Phys. Rev. B **77**,

155201 (2008).

[12] H. Höhler, N. Atodiresei, K. Schroeder, R. Zeller, and P. H. Dederichs, Phys. Rev. B **71**, 035212 (2005).

[13] J. Coutinho, S. Öberg, V. J. B. Torres, M. Barroso, R. Jones, and P. R. Briddon, Phys. Rev. B **73**, 235213 (2006).

[14] U. Wahl, J. G. Correia, A. Czermak, S. G. Jahn, P. Jalocha, J. G. Marques, A. Rudge, F. Schopper, J. C. Soares, A. Vantomme, et al., Nucl. Inst. Meth. Phys. Res. A **524**, 245 (2004).

[15] H. Hofsäss and G. Lindner, Phys. Rep. **201**, 121 (1991).

[16] U. Wahl, Phys. Rep. **280**, 145 (1997).

[17] H. Haesslein, R. Sielemann, and C. Zistl, Phys. Rev. Lett. **80**, 2626 (1998).

[18] S. Cottenier, (Instituut voor Kern- en Stralingsfysica, KULeuven, Belgium) (2002), (freely available from http://www.wien2k.at/reg_user/textbooks), ISBN 90-807215-1-4.

[19] P. Blaha, K. Schwarz, G. Madsen, D. Kvasnicka, and J. Luitz, (Karlheinz Schwarz, Techn. Universität Wien, Austria) (2001).

[20] J. P. Perdew, K. Burke, and M. Ernzerhof, Phys. Rev. Lett. **77**, 3865 (1996).

[21] A. Fazzio, A. Janotti, A. J. R. da Silva, and R. Mota, Phys. Rev. B **61**, R2401 (2000).

[22] E. Simoen, K. Opsomer, C. Claeys, K. Maex, C. Detavernier, R. L. Van Meirhaeghe, and P. Clauws, Appl. Phys. Lett. **89**, 202114 (2006).

[23] E. Simoen, K. Opsomer, C. Claeys, K. Maex, C. Detavernier, R. L. Van Meirhaeghe, and P. Clauws, J. Electrochemical Society **154**, H857 (2007).

Paper VI

Lattice location study of implanted In in Ge,

S. Decoster, B. De Vries, U. Wahl, J. G. Correia and A. Vantomme

Journal of Applied Physics ***105****, 083522 (2009)*

Lattice location study of implanted In in Ge

S. Decoster, B. De Vries, and A. Vantomme
Instituut voor Kern- en Stralingsfysica and INPAC,
K.U. Leuven, Celestijnenlaan 200D, B-3001 Leuven, Belgium

U. Wahl and J.G. Correia
Instituto Tecnológico e Nuclear, Unidade
de Física e Aceleradores, Estrada Nacional
10, apt. 21, 2686-953 Sacavém, Portugal

—

Journal of Applied Physics ***105***, *083522 (2009)*

—

Abstract

We report on emission channeling experiments to determine the lattice location and the thermal stability of implanted ^{111}In atoms in Ge. The majority of the In atoms was found on the substitutional site, which is a thermally stable site at least up to 500 °C. We also found strong indication that directly after implantation, a fraction of the implanted ^{111}In atoms occupies the bond-centered site. This fraction disappears after annealing at 300 °C. From comparison with *ab initio* calculations, electrical studies and perturbed angular correlation experiments, the In atoms on the bond-centered site can be related to In-vacancy and In-self-interstitial defect complexes. The activation energy for dissociation of this bond-centered related defect was found to be below 1.6 eV.

I. INTRODUCTION

During the past decade, germanium has become an increasingly important material in semiconductor applications. When compared to silicon, Ge has a higher free carrier mobility and a lower dopant activation temperature[1], which makes it an attractive material in metal-oxide semiconductor field-effect transistors[2,3]. One of the possible p-type dopants in Ge is indium, introducing a shallow acceptor level of 0.0112 eV above the Ge valence band[4]. Since the electrical properties of dopants in semiconductors are drastically influenced by their exact lattice site, a detailed understanding of the lattice site occupation of In atoms in the Ge lattice – together with its thermal stability – is crucial to understand their electrical behavior.

A particular technique that has been applied to investigate the local environment of In atoms in many materials, including Ge, is perturbed angular correlation spectroscopy (PAC). Since the radioactive ^{111}In isotope is the most widely used probe for PAC spectroscopy, it has been frequently used in the past to study the local environment of In atoms in Ge[5–12]. This technique actually probes the surroundings of the daughter atom ^{111}Cd, but due to the very small recoil energy (< 1 eV) during the radioactive ^{111}In $\rightarrow^{111}$Cd decay compared to typical lattice binding energies (10-20 eV), ^{111}Cd will inherit the lattice location of its precursor ^{111}In. After annealing the ^{111}In-implanted Ge sample up to 600 °C, no interaction frequency was found in the PAC spectra, showing that all In atoms occupy sites with perfect cubic charge symmetry. Electron irradiation as well as ion irradiation of the annealed ^{111}In-doped Ge samples revealed two main defects: one which has been attributed to the In-vacancy (In-V) defect and another one attributed to a defect complex involving an In atom and a Ge self-interstitial (In-Ge$_I$). Both defects have an electric field gradient orientation along the $\langle 111 \rangle$-direction and disappear within the temperature range of 110–210 °C. Deep Level Transient Spectroscopy (DLTS) measurements were used in combination with PAC, to investigate the electrical levels in the Ge

band gap related to In defects[12,13]. This study resulted in a level at $E = E_V + 0.33$, which was assigned to the In-V defect. As the PAC technique can only give indirect information about the lattice location of the In atoms and as it can not distinguish between In atoms on substitutional (S) or on tetrahedral interstitial (T) sites, both being subject to perfect cubic charge symmetry, other or complementary techniques are required to obtain a complete understanding of the lattice location of the In atoms. In early Rutherford channeling spectroscopy (RBS/C) experiments, the majority of the In atoms were found on the S site after annealing[14,15], in accordance with the PAC results where no interaction frequency was found. In order to understand the structural configuration of simple defects such as the In-vacancy defect, *ab initio* density functional calculations were performed, resulting in In atoms occupying the bond-centered (BC) site[16]. The occupancy of the bond-centered site was calculated for many high-Z impurity atoms in the impurity-vacancy complexes, as well as for Cd in the Cd-self-interstitial defect complex[16,17]. Similar theoretical results have been found for the In-V defect in Si, where the In atom was found to occupy the BC site as well[16,18]. Since most of these results on the lattice location of the In atoms in Ge have been obtained through indirect techniques (with the exception of high fluence RBS/C experiments) or from calculations that have not been corroborated by experiments so far, in this article, we present a *direct* lattice location study of ion implanted In in Ge with the emission channeling (EC) technique. The important advantages of this technique with respect to ion channeling techniques (such as RBS/C) are its significantly higher accuracy due to the use of a 2-dimensional detection technique and the use of very low implantation fluences which allows to study isolated atoms.

II. EXPERIMENTAL METHOD

In EC experiments, charged particles emitted from an implanted radioactive isotope, are guided by the potential of atomic rows and planes

while traveling through the crystal. The resulting anisotropic electron emission pattern around low-index crystal directions is characteristic for the lattice site occupied by the emitting atom and is measured with a 2-dimensional energy- and position-sensitive Si detector of 22×22 pixels. More information about this technique can be found in Ref. 19. The radioactive isotope ^{111}In has been implanted at the ISOLDE facility in CERN. It decays with a half life of 2.81 days to ^{111}Cd, emitting K (143 and 218 keV) and L (167 and 241 keV) conversion electrons. A fluence of 2.9×10^{12} In atoms/cm^2 has been implanted with an energy of 60 keV and a beam current density of 200 pA/cm^2 in an undoped $\langle 111 \rangle$-Ge sample, held at room temperature. The Ge sample was implanted at an angle tilted 10° with respect to its surface direction to minimize channeled implantation. To obtain accurate and unambiguous results, emission patterns along the four crystal directions $\langle 111 \rangle$, $\langle 100 \rangle$, $\langle 211 \rangle$ and $\langle 110 \rangle$ were measured, analyzed consistently, and fitted to a set of simulated spectra. The simulations are based on the dynamical theory of electron diffraction and have been performed for several high-symmetry sites such as the S, BC, tetrahedral interstitial (T), hexagonal (H) and the so called AB, SP, Y and C sites, as well as for small discrete displacements between these sites along the $\langle 111 \rangle$-, $\langle 100 \rangle$- and $\langle 110 \rangle$-direction. The exact location of these sites within the diamond lattice structure and more information about the simulations can be found in Ref. 20 and Ref. 21 respectively. To monitor the thermal stability of the lattice location of the implanted In atoms, the measurements were performed in the as-implanted state as well as after 10 min isochronal annealing steps in vacuum ($< 10^{-5}$ mbar) up to 500 °C.

III. RESULTS

In Fig. 1 (a)-(d) we show the normalized two-dimensional emission yields along the four measured crystal directions after annealing the ^{111}In-implanted Ge sample at 400 °C. The high yield in the center of each pattern is a signature for the strong channeling effect of the conver-

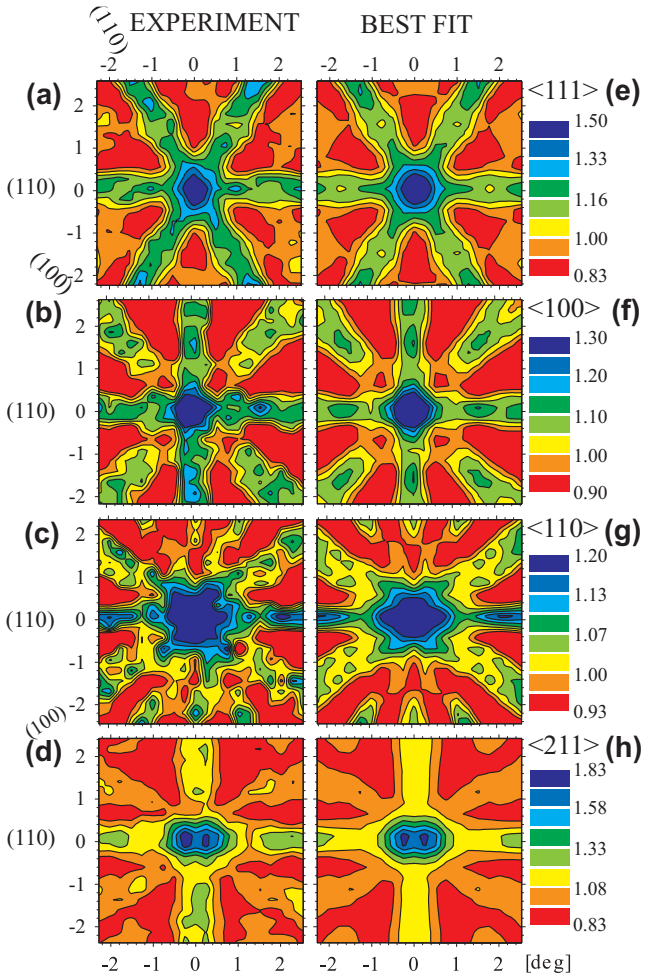

FIG. 1: (a)-(d) Two-dimensional normalized conversion electron patterns emitted from ^{111}In in Ge around the ⟨111⟩, ⟨100⟩, ⟨110⟩ and ⟨211⟩-axes, following a 400 °C annealing in vacuum; (e)-(h) Best fits to the experimental patterns. The anisotropy is depicted with a color scale between red (low) and blue (high).

sion electrons along all crystal axes. This indicates that a large fraction of the In probe atoms is located on the substitutional site. To quantify the fraction of In atoms on the substitutional site, and to investigate whether any other high-symmetry site(s) is (are) present in the spec-

tra, a quantitative fitting procedure with the simulated patterns was performed.

Up to three fractions on different high-symmetry sites were used to search for the best fit, allowing displaced sites as well. The fitting procedure unambiguously shows that the majority of the In atoms are located on undisturbed substitutional sites – as was already inferred from visual inspection of the spectra. It was found that by adding the high-symmetry sites T, H, AB, SP, Y or C, it is not possible to fit the experimental patterns in all four directions in a consistent way with a significant fit improvement. However, adding a fraction of In atoms at the bond-centered (BC) site results in consistent fits with relative improvements in χ^2 as presented in Fig. 2 (a). These results show that the χ^2 improvement after adding a BC fraction to the fit, is reduced from roughly 3.5% to less than 1% for annealing temperatures exceeding 150 °C. This analysis gives strong indication that the addition of a BC fraction is only relevant for the measurements after implantation and after annealing at 150 °C. Taking this into account, the resulting fraction of atoms on the S (f_{S}) and on the BC site (f_{BC}) as a function of annealing temperature, as obtained from the best fits, are shown in Fig. 2 (b). The best fits to the experimental patterns in Fig. 1 (a)-(d) are shown in Fig. 1 (e)-(h), matching the experimental patterns very well. In this fit, 88% of the implanted In atoms were found to occupy the S site.

IV. DISCUSSION

Apart from the fraction of In atoms on the BC and on the S site, Fig. 2 further shows the remaining fraction (as calculated from $100\% - f_{\mathrm{BC}} - f_{\mathrm{S}}$) which will be referred to as the *random* fraction (f_{random}). This random fraction is a direct consequence of implantation-induced lattice damage. Even for the low fluence used in this study, heavy-ion implantation produces damaged regions, especially in materials with small lattice binding energies such as Ge. Firstly, due to the deterioration of the crystal structure, a fraction of the implanted radioactive isotopes will be located in

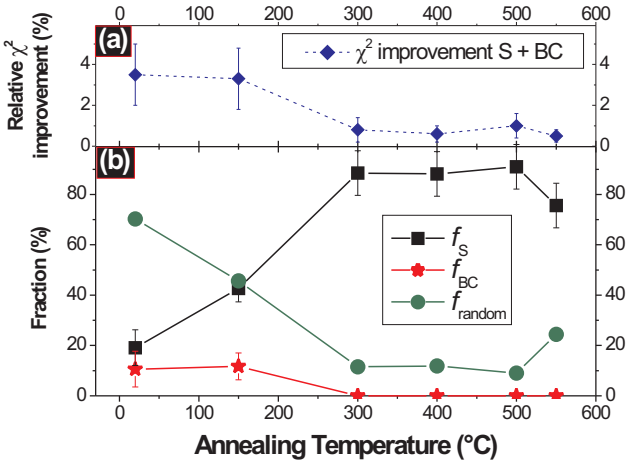

FIG. 2: (a) Relative improvements in χ^2 (%) as a function of annealing temperature when adding a BC fraction to the fit with purely substitutional In atoms; (b) the fraction of In atoms on the S site (f_S - squares) and on the BC site (f_{BC} - stars), together with the random fraction (f_{random} - circles), as a function of annealing temperature.

damaged regions with reduced local crystallinity. Secondly, a fraction of the conversion electrons emitted from an undamaged region will pass through damaged crystal regions, enhancing the probability for dechanneling. Both effects will result in an isotropic background to the patterns and, consequently, in the random fraction observed in this study. The large random fraction in the as-implanted measurement is due to the presence of implantation-induced crystal lattice damage, while its drastic decrease after annealing at 150 °C and 300 °C is a direct consequence of almost complete recrystallization, as is confirmed by RBS/C lattice recovery studies.

The majority of the In atoms are located on the substitutional site, in agreement with the results from the previously mentioned RBS/C and PAC studies[5–7,9,11,14,15]. The root mean square displacement of the substitutional In atoms was found to be comparable to the expected thermal vibration amplitude at room temperature of 0.07 Å. This indi-

cates that the majority of the In atoms on the S site are embedded in an unperturbed local environment. Besides the fraction of In atoms on the S site, we also found a significant fit improvement when including a fraction on the bond-centered (BC) site. The fraction of In atoms on the BC site, relative to the total fraction of In atoms on high-symmetry sites, was found to be 36% in the as implanted case and 22% after annealing at 150 °C. This BC fraction disappears between the 150 °C and 300 °C annealing step. In the previously mentioned PAC studies two defects have been identified as being caused by ion irradiation[5–12], and have been attributed to In-V and In-Ge_I defects. These defects were both found to have an electric field gradient (EFG) along the ⟨111⟩-direction. Since an In atom on the BC site with an axially symmetric surrounding is subject to an EFG along the ⟨111⟩-direction, we have strong indications that the In atoms on the BC site observed in this work, are related to the In-V and/or In-Ge_I defect. Moreover, the temperature range at which these defects disappear in the PAC studies (110–210 °C) is comparable to what is found here, i. e. the BC fraction partly disappears at 150 °C and completely vanishes after annealing at 300 °C. Also, we would expect the BC fraction to increase similarly to the S fraction, if it were governed by the recrystallization of the lattice at this temperature, which is clearly not the case as shown in Fig. 2(b). Furthermore, *ab initio* calculations have shown that in the In-V, the Cd-V and the Cd-Ge_I defects, the impurity prefers the BC site to the S site[16,17]. All of these results strongly point to the fact that the In atoms observed on the BC site in our study are part of the In-V and/or In-Ge_I defect complex. By introducing vacancies and/or interstitials, e. g. by electron irradiation, it might be possible to even tune the relative fraction of In atoms on the BC and the S site with the defect density. This occupancy of the bond-centered site has been observed for some transition metals and for erbium atoms in Ge as well, possibly indicating a more general trend for (several) impurities in Ge: impurity-vacancy and/or impurity-self-interstitial defect complexes with the impurity atom located on the BC site[22,23].

The occupancy of the BC site within the In-V complex can influence the diffusion process of In in Ge. In consistency with experimental studies[24,25], the In atoms are found to diffuse through the bulk Ge by the mediation of vacancies. The proposed diffusion mechanism is called the ring mechanism[26] in which the impurity atoms will change places with vacancies, but will occupy a substitutional site. Recent electronic structure calculations have been used by Chroneos *et al.* to calculate the activation enthalpies of vacancy-mediated diffusion for several impurity atoms, including indium[27]. Although the activation enthalpy for In (2.79 eV) obtained in that study[27] was found to be consistent with early experimental values (2.78 eV)[24], later experiments have suggested a much larger value (3.61 eV)[25]. Chroneos *et al.* also calculated the actual migration barrier of a vacancy near an In atom, which was found to be 1.18 eV[27].

It can be assumed that the In-V complexes as observed in our work – with the In atom on the bond-centered site with two nearest neighbor vacancies – will play a major role in this diffusion model, and that the microscopic behavior of the In atom in the ring mechanism might need revision. From the fact that the BC fraction disappears completely below 300 °C we are able to estimate the activation energy for the break-up of the BC-related complex. The activation energy E_a is calculated from

$$E_a = k_B T_n \ln\left[\frac{\nu_0 \Delta t}{N} \cdot \frac{1}{\ln\left[f(T_{n-1})/f(T_n)\right]}\right],$$

where k_B is the Boltzmann constant, T_n and Δt the temperature and duration of the n^{th} annealing step, ν_0 the attempt frequency (which has been taken $\nu_0 \approx 10^{12} s^{-1}$, i. e. of the order of the lattice vibrations), N the amount of times the vacancy will be retrapped before it escapes, and $f_{(T_{n-1})}$ and $f_{(T_n)}$ the occupied fraction after the $(n-1)^{th}$ and the n^{th} annealing step. More background information on this formula can be found in Ref 28. When using a one-step model without retrapping ($N = 1$) and 300 °C as the temperature at which the BC-fraction disappears completely, the activation energy was found to be 1.64 eV. Increasing

the retrapping rate to $N = 10$ only lowers this value slightly to 1.53 eV. Due to the uncertainty in the temperature at which the BC fraction is substantially reduced – most likely somewhere between 150 °C and 300 °C, but it could be even at lower temperatures, since the annealing of the lattice damage at 150 °C might compensate the decrease of the BC fraction – we have calculated the activation energy for $T_n = 200$ °C and $T_n = 100$ °C as well, resulting in lower activation temperatures of 1.35 eV and 1.07 eV respectively. In this way we obtain a maximum activation energy of 1.64 eV for the break-up of the BC-related complex. In order to relate this value to the literature values for the activation enthalpy of In[25,27] and the migration barrier of a vacancy near an In atom[27], as presented above, more information about the atomic break-up mechanism of this complex is required.

V. CONCLUSION

In conclusion, we have determined the lattice location of ion implanted In atoms in Ge together with its thermal stability, using the emission channeling technique. The majority of the In atoms were found to occupy the substitutional site, with a maximum occupation of 90% after annealing at 300 °C. This site was found to be thermally stable up to at least 500 °C. We found strong indications that In atoms occupy a second high-symmetry, i. e. the bond-centered site, which is thermally stable up to 150 °C. From comparison with previous PAC experiments and theoretical studies, this BC fraction can be attributed to In-vacancy and/or In-self-interstitial defect complexes. Moreover, we have determined an upper limit for the activation energy of the BC-related complex around 1.6 eV. This In-V complex, where the In atom occupies the BC site, will be important in the vacancy-mediated diffusion mechanism for In, and possibly also for other impurities in Ge.

VI. ACKNOWLEDGEMENTS

This work was supported by FWO Flanders (G.0501.07 and G.0636.08), the K.U.Leuven projects GOA/2009/006 and INPAC EF/2005/005, the IUAP P6/42 programme, the Portuguese Foundation for Science and Technology (CERN-FP-83506-2008) and the ISOLDE collaboration. S. D. acknowledges financial support from FWO, Flanders.

---

[1] R. Hull and J. C. Bean, *Germanium Silicon: Physics and Materials, Semiconductors and Semimetals*, Academic, San Diego (1999).

[2] C. C. Yeo, B. J. Cho, F. Gao, S. J. Lee, M. H. Lee, C. Y. Yu, C. W. Liu, L. J. Tang, and T. W. Lee, IEEE Electron Device Letters **26**, 761 (2005).

[3] Y. J. Yang, W. S. Ho, C. F. Huang, S. T. Chang, and C. W. Liu, Appl. Phys. Lett. **91**, 102103 (2007).

[4] T. H. Geballe and F. J. Morin, Phys. Rev. **95**, 1085 (1954).

[5] U. Feuser, R. Vianden, and A. F. Pasquevich, Hyperfine Interactions **60**, 829 (1990).

[6] U. Feuser, R. Vianden, E. Alves, M. F. da Silva, E. Szilagyi, F. Paszti, and J. C. Soares, Nucl. Inst. Meth. Phys. Res. B **59**, 1049 (1991).

[7] H. Haesslein, R. Sielemann, M. Brüßler, and H. Metzner, Hyperfine Interactions **84**, 65 (1994).

[8] H. Haesslein, R. Sielemann, and C. Zistl, Materials Science Forum **258**, 59 (1997).

[9] H. Haesslein, R. Sielemann, and C. Zistl, Phys. Rev. Lett. **80**, 2626 (1998).

[10] R. Sielemann, H. Haesslein, L. Wende, and C. Zistl, Physica B **273**, 565 (1999).

[11] C. J. Glover, A. P. Byrne, and M. C. Ridgway, Nucl. Inst. Meth. Phys. Res. B **175**, 51 (2001).

[12] R. Sielemann, H. Hässlein, C. Zistl, M. Müller, L. Stadler, and V. V. Emtsev, Physica B **308**, 529 (2001).

[13] C. Zistl, R. Sielemann, H. Hässlein, S. Gall, D. Bräunig, and J. Bollmann, Materials Science Forum **258**, 53 (1997).

[14] K. Björkqvist, B. Domeij, L. Eriksson, G. Fladda, A. Fontell, and J. W.

Mayer, Appl. Phys. Lett. **13**, 379 (1968).
[15] K. Björkqvist, D. Sigurd, G. Fladda, and G. Bjarnholt, Radiat. Eff. **6**, 141 (1970).
[16] H. Höhler, N. Atodiresei, K. Schroeder, R. Zeller, and P. H. Dederichs, Phys. Rev. B **71**, 035212 (2005).
[17] H. Höhler, N. Atodiresei, K. Schroeder, R. Zeller, and P. H. Dederichs, Phys. Rev. B **70**, 155313 (2004).
[18] P. Alippi, A. La Magna, S. Scalese, and V. V. Privitera, Phys. Rev. B **69**, 085213 (2004).
[19] U. Wahl, J. G. Correia, A. Czermak, S. G. Jahn, P. Jalocha, J. G. Marques, A. Rudge, F. Schopper, J. C. Soares, A. Vantomme, et al., Nucl. Inst. Meth. Phys. Res. A **524**, 245 (2004).
[20] U. Wahl, Phys. Rep. **280**, 145 (1997).
[21] H. Hofsäss and G. Lindner, Phys. Rep. **201**, 121 (1991).
[22] S. Decoster, B. De Vries, A. Vantomme, U. Wahl, and J. G. Correia, Appl. Phys. Lett. **93**, 141907 (2008).
[23] S. Decoster, S. Cottenier, B. De Vries, H. Emmerich, U. Wahl, J. G. Correia, and A. Vantomme, Phys. Rev. Lett. **102**, 065502 (2009).
[24] V. A. Pantaleev, Soviet Physics - Solid State **7**, 734 (1965).
[25] P. Dorner, W. Gust, A. Lodding, H. Odelius, B. Predel, and U. Roll, Z. Metallkunde **73**, 325 (1982).
[26] S. M. Hu, phys. stat. sol. (b) **60**, 595 (1973).
[27] A. Chroneos, H. Bracht, R. W. Grimes, and P. Uberuaga, Appl. Phys. Lett. **92**, 172103 (2008).
[28] U. Wahl, J. G. Correia, E. Rita, J. P. Araújo, J. C. Soares, and the ISOLDE Collaboration, Nucl. Inst. Meth. Phys. Res. B **253**, 167 (2006).

Paper VII

Lattice location study of ion implanted Sn and Sn-related defects in Ge,

S. Decoster, S. Cottenier, U. Wahl, J. G. Correia and A. Vantomme

to be submitted to Physical Review B

Lattice location study of ion implanted Sn and Sn-related defects in Ge

S. Decoster and A. Vantomme
Instituut voor Kern- en Stralingsfysica and INPAC,
K.U. Leuven, Celestijnenlaan 200D, 3001 Leuven, Belgium

S. Cottenier
Instituut voor Kern- en Stralingsfysica and INPAC,
K.U. Leuven, Celestijnenlaan 200D, 3001 Leuven, Belgium,
Center for Molecular Modeling, Ghent University,
Proeftuinstraat 86, BE-9000 Ghent, Belgium

U. Wahl and J.G. Correia
Instituto Tecnológico e Nuclear, Unidade
de Física e Aceleradores, Estrada Nacional
10, apt. 21, 2686-953 Sacavém, Portugal

—

to be submitted to Physical Review B (2009)

—

Abstract

In this work, we present a lattice location study of Sn in Ge. From emission channeling experiments, we have determined the exact lattice location of ion implanted Sn atoms, and compared the results to predictions from density functional calculations. The majority of the Sn atoms are positioned on the substitutional site, as can be expected from an isovalent impurity, while a second significant fraction has been found to occupy the six-fold coordinated bond-centered site. Corroborated by *ab initio* calculations, we were able to attribute this fraction of bond-centered Sn atoms to the Sn-vacancy defect complex in the split-vacancy configuration.

I. INTRODUCTION

Ge is considered as an important future material to replace Si in semiconducting applications. When compared to silicon, Ge has a higher free carrier mobility and a lower dopant activation temperature[1], which makes it an attractive material in future metal-oxide semiconductor field-effect transistors[2,3]. To control the growth of Ge-based devices, a thorough understanding of the diffusion properties and mechanism is needed. It is generally accepted that most group III and V dopants (with the exception of B) in Ge diffuse by vacancy mediation via the so-called *ring mechanism*[4]. This mechanism proposes that an impurity atom swaps places with a nearby vacancy, followed by the breakup of the impurity-vacancy complex and the migration of the vacancy along a ring-path to end up at the other side of the impurity atom, at which time the process can restart.

Among all impurities in group IV semiconductors, the diffusion behavior of Sn is one of the most interesting to investigate: Sn is an isovalent impurity in Ge, which means that its diffusion properties can be used to study Ge self-diffusion. Moreover, the investigation of Sn-related defects in Ge is a technologically important issue since Sn_xGe_{1-x} was found to be the first direct band gap semiconductor composed entirely of group IV elements[5–8]. The tunability of its band gap makes Sn_xGe_{1-x} a highly interesting material for infrared applications, especially at low Sn concentrations ($x < 0.20$). Recent theoretical calculations indicate that strained Sn_xGe_{1-x} ($x < 0.10$) exhibits enhanced electron and hole mobility, which could make this alloy also interesting for high speed integrated circuits[9].

A number of studies have been performed to investigate the diffusion of Sn in germanium with secondary ion mass spectrometry. Kringhøj *et al.* studied the diffusion of ion implanted Sn in Ge, finding an activation energy of 3.05(8) eV[10], while Friesel *et al.* investigated the in-diffusion of a deposited Sn-layer, resulting in a slightly larger activation energy of 3.26(7) eV[11]. More recently, the diffusion mechanism of Sn in Ge

was studied by Riihimäki *et al.*, explaining its behavior by assuming an attractive elastic interaction between the Sn atoms and vacancies. They showed that Sn diffusion is mediated by vacancies, and that the Sn-vacancy (Sn-V) complex is negatively charged in Ge[12,13]. Electronic structure calculations were performed by Chroneos to investigate the effect of C atoms on the binding of Sn-V pairs, although no information is given on the microscopic configuration of the Sn-V pair[14]. Furthermore, similar calculations have been performed to determine the activation enthalpy of vacancy-mediated diffusion of Sn in Ge[15]. This resulted in an activation energy of 3.26 eV, in very good agreement with the experimental data.

Although it is clear from these recent studies that Sn diffusion is mediated by vacancies, little is known about the microscopic configuration of Sn atoms in Ge, in particular when they are part of small defect complexes, such as the Sn-V complex. It is generally accepted that the majority (if not all) of the Sn atoms are located substitutionally in Ge due to its isovalency. So far, most of the experimental information about the lattice site location of Sn and Sn-related defects in Ge is obtained from Mössbauer spectroscopy. Weyer *et al.* found, by combining Mössbauer and ion beam channeling experiments, that 90% of the implanted ^{119m}Sn atoms were located substitutionally[16]. However, after implanting ^{119}In and ^{119}Sb as precursors for Sn, the Mössbauer spectra for Sn were found to consist of several contributions (resonances) with the most pronounced line attributed to substitutional Sn and the others to several other configurations, such as isolated interstitial Sn atoms and Sn-vacancy (Sn-V) complexes[17–19]. It should be pointed out that from Mössbauer spectroscopy alone, it is not possible to unambiguously determine the microscopic configuration of such defect complexes.

The situation is different in theoretical work, where the atomic arrangement in a specific complex, e. g. the Sn-V complex can be imposed. The two most simple configurations for such an impurity-vacancy complex have been studied with density functional theory[20]: (1) the so-called *full vacancy* configuration in which the impurity is located on a substitu-

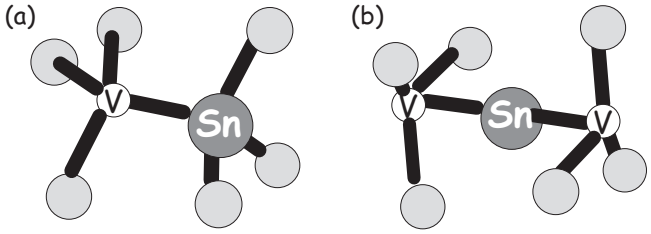

FIG. 1: (a) The full-vacancy configuration and the (b) split-vacancy configuration of the Sn-vacancy complex in Ge.

tional site with a vacancy as nearest neighbor, and (2) the *split-vacancy* configuration where the impurity atom occupies the bond-centered (BC) site in between of two vacant nearest neighbor sites. These configurations are schematically represented in Fig. 1.

Höhler *et al.* found that the split-vacancy configuration is energetically the most favorable one for the high-Z elements Cd, In, Sn, Sb and Bi, while the full-vacancy configuration is preferred for the lower-Z elements Al, Si, P, Ga, As, and Se[20]. One year later, comparable calculations were performed by Coutinho *et al.*, where all studied donor-vacancy complexes (P, As, Sb and Bi) were calculated to be in the full-vacancy configuration[21]. Coutinho *et al.* attribute the contradicting results between the two groups for the high-Z elements Sb and Bi to the size of the supercell (64 atoms) and the k-point sampling method used by Höhler *et al.* However, it must be noted that other configurations – besides the split-vacancy and full-vacancy configuration – of the impurity-vacancy complex have not been considered in this theoretical work[20,21], and therefore cannot be explicitly excluded.

Hence, it is clear from literature that experimental information about the microscopic structure of Sn-V complexes is largely lacking, while the theoretical results obtained by Höhler *et al.*[20] have raised some doubt. Although electron paramagnetic resonance experiments in silicon have indicated that the Sn atom occupies the bond-centered site in a Sn-V complex[22], no unambiguous experimental evidence has been provided concerning the microscopic configuration of the Sn-V complex in germa-

nium.

In this study, we have determined the exact lattice location of ion implanted Sn atoms, both experimentally, with the emission channeling (EC) technique, as well as theoretically. The use of ion implantation ensures that many vacancies, which are known to be mobile at room temperature[23], are present, to form Sn-V complexes. Recent emission channeling (EC) experiments on the optical dopant Er, the electrical dopant In and on the transition metals Fe, Cu and Ag in Ge, have proven that this technique is very effective in determining the lattice location of impurities and impurity-related defects in Ge[24–26] in a direct way. Besides these experimental results, we have also performed theoretical calculations on substitutional and tetrahedral interstitial Sn atoms and on the Sn-V complex, using a different k-point sampling method and a larger supercell than in Ref. 20, as proposed by Coutinho *et al.*[21], in order to validate our experimental results. These calculations allowed us to compare the deduced hyperfine parameters to the experimental values from the Mössbauer experiments[17–19] and to unravel the inconsistency between the previously mentioned theoretical articles[20,21].

II. EXPERIMENTAL METHOD

Electron emission channeling (EC) makes use of the fact that charged particles, emitted from implanted radioactive isotopes are guided by the potential of atomic rows and planes while traveling through the crystal. The resulting anisotropic electron emission patterns around low-index crystal directions are characteristic for the lattice site occupied by the emitting atom and are measured with a two-dimensional energy- and position-sensitive Si detector of 22×22 pixels. Applying this technique, it becomes possible to measure the lattice location of impurities with a sensitivity which is typically more than one order of magnitude higher with respect to regular channeling spectroscopy techniques (such as Rutherford channeling spectroscopy). More information about the technique can be found in the article by Wahl *et al.*[27] To obtain un-

ambiguous quantitative results about the lattice location of the element under investigation, the electron emission patterns are measured around four independent crystal directions (⟨100⟩, ⟨111⟩, ⟨211⟩ and ⟨110⟩), analyzed consistently and fitted to a set of simulated patterns. These simulations are based on the dynamical theory of electron diffraction, and are calculated for the substitutional (S), tetrahedral interstitial (T), bond-centered (BC), and the so called SP, H, Y and C sites[28], together with discrete displacements between all of these sites along the ⟨111⟩- and ⟨100⟩-direction. More information about the simulations can be found in Ref. 29.

To study the lattice location of Sn, we implanted the radioactive isotope ^{121}Sn which decays to ^{121}Sb with a half life of 27 h, emitting β-electrons with an endpoint energy of 390 keV. The implantations were performed at the ISOLDE facility in CERN at room temperature, in undoped ⟨111⟩-Ge, with an energy of 60 keV and at an offset angle of 7° with respect to the surface normal. Three slightly different implantation fluences have been used: 2×10^{12}, 3×10^{12} and 4×10^{12} at/cm^2. The current density used during implantation was $0.3 - 0.4$ nA/cm^2. All measurements were performed at room temperature. To monitor the thermal stability of the lattice location of the implanted ions, spectra were taken directly after implantation as well as after 10 min annealing stages in vacuum ($< 10^{-5}$ mbar) at temperatures ranging up to 400 °C.

III. EXPERIMENTAL RESULTS

Figure 2 (a)-(d) shows the measured electron emission patterns from the implanted ^{121}Sn atoms in Ge (3×10^{12} at/cm^2) around the ⟨111⟩, ⟨100⟩, ⟨110⟩ and ⟨211⟩-axes, following a 300 °C annealing. All patterns are dominated by pronounced channeling effects, indicating that the majority of the probe atoms are located along the rows of atoms in the measured directions, i. e. on the substitutional (S) site. To investigate small contributions of other high-symmetry sites and to obtain accurate quantitative information about the fractional occupation of the lattice

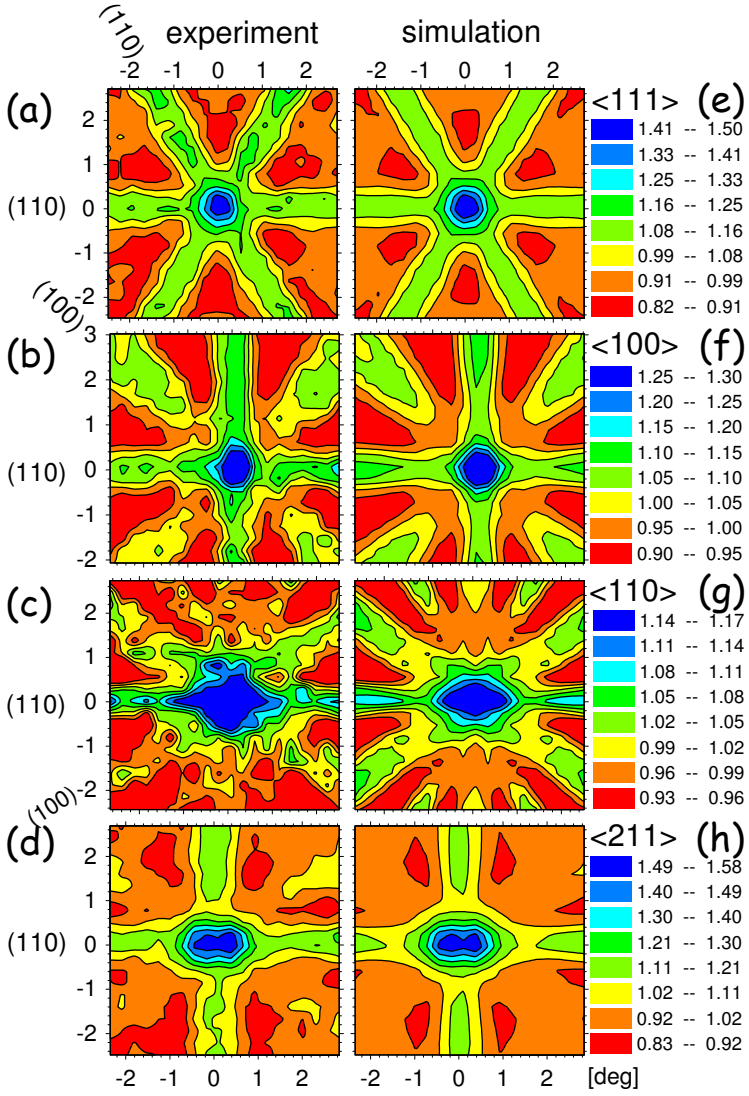

FIG. 2: (a)-(d) Two-dimensional normalized electron emission patterns from ion implanted ^{121}Sn in Ge to a fluence of 3×10^{12} at/cm^2, measured around the ⟨111⟩, ⟨100⟩, ⟨110⟩ and ⟨211⟩-axes, following a 300 °C annealing in vacuum; (e)-(h) the best fits to these patterns, with the major fraction (76%) of ^{121}Sn atoms occupying the substitutional site and a smaller fraction (11%) on the bond-centered site.

sites, the experimental patterns are fitted by simulated patterns. Up to three different high-symmetry sites are used in the fitting procedure, including small displacements of these sites as well. The only high-symmetry site that, when added to the substitutional fraction, results in a consistent and significantly improved fit in the four measured directions (average χ^2-improvement of 4%), is the bond-centered (BC) site. Adding a third high-symmetry site to both fractions, does not further improve the fit (χ^2-improvement $\ll 1\%$). Using slightly displaced S and/or BC sites, results in very small fit improvements only ($\chi^2 < 1\%$), which is most likely due to the extra degree of freedom in the fitting procedure. In Fig. 2 (e)-(h) the best fit to the experimental patterns is shown, using undisplaced S and BC sites. The fractions used to produce these fits are 78%, 79%, 70% and 75% on the S site and 11%, 9%, 14% and 11% on the BC site for the $\langle 111 \rangle$, $\langle 100 \rangle$, $\langle 110 \rangle$ and $\langle 211 \rangle$-direction respectively, clearly showing a good consistency in the fits among the four measured directions.

As can be seen in Fig. 3, similar results are obtained for all three investigated samples, directly after implantation as well as after several annealing stages. The majority of the Sn atoms is located substitutionally (f_S), with a smaller but significant fraction occupying the BC site (f_{BC}). The remaining fraction of the Sn atoms, $f_{rand} = 100\% - f_S - f_{BC}$ is the so-called *random* fraction and is plotted in Fig. 3 as well. This random fraction represents the fraction of Sn atoms that are not located on high-symmetry sites, only adding up to the homogeneous background of the pattern.

The results in Fig. 3 show no direct influence of the implantation fluence on the lattice location behavior of the Sn atoms, within the range of $2 - 4 \times 10^{12}$ at/cm^2. It is clear that directly after ion implantation, a relatively high random fraction is present. This is a direct consequence of the implantation-induced lattice damage, which has a dual influence on the results shown here. Firstly, due to the deterioration of the crystal structure, a fraction of the implanted radioactive isotopes will be located in damaged regions with reduced local crystallinity. Secondly, a fraction

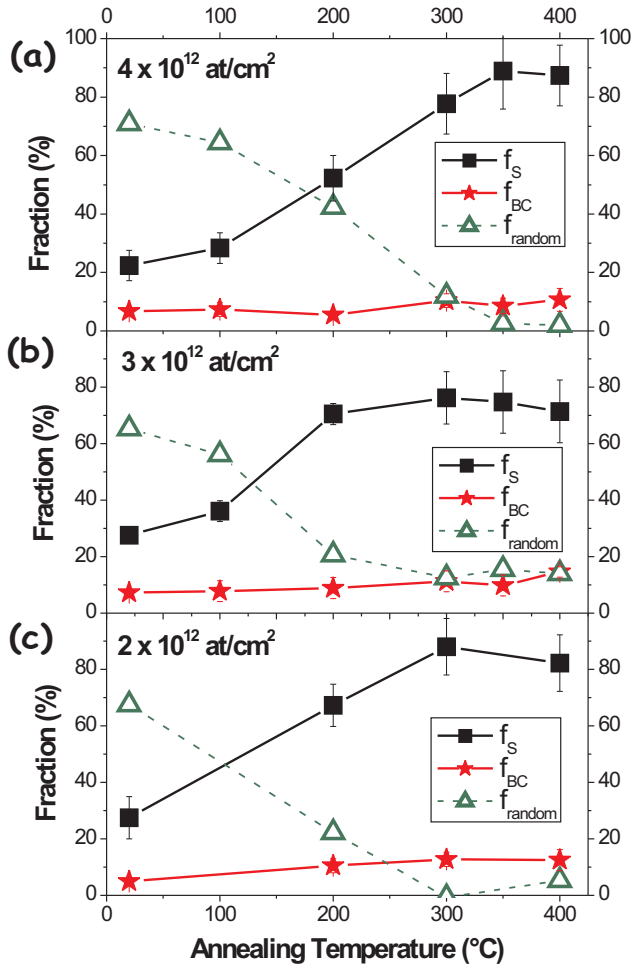

FIG. 3: Fraction of the implanted Sn atoms on the substitutional (squares) and bond-centered site (stars) in Ge, together with the random fraction f_{rand} = 100% - f_S - f_{BC} (triangles); three slightly different implantation fluences were used: (a) 4×10^{12}, (b) 3×10^{12} and (c) 2×10^{12} at/cm^2.

of the electrons emitted from an undamaged region will pass through damaged crystal regions, enhancing the probability for dechanneling – thus masking the impurity's lattice site. Both effects will result in an isotropic background to the patterns and consequently in the random fraction, as observed in the experiments. Therefore, the presented frac-

tional occupation of the Sn atoms on the high-symmetry sites for the lower temperature annealing steps ($<$ 300 °C) must be regarded as a lower limit to the real values. The recovery of the lattice damage after annealing is reflected in the significant decrease of the random fraction after annealing the samples at 300 °C, resulting in almost all Sn atoms on high-symmetry sites.

IV. CALCULATIONS

As expected, the majority of the isovalent Sn impurities are located substitutionally in the Ge lattice. Most likely, many of these impurities are embedded in an undamaged environment, although it cannot be excluded that some of them are surrounded by simple defects, without influencing their substitutional position. A smaller but significant fraction of Sn atoms is found to occupy the BC site, which has not been unambiguously observed in Ge-experiments so far. As mentioned above, this BC fraction is possibly related to the Sn-vacancy defect in the split-vacancy configuration. To strengthen this assumption, a complementary *ab initio* study has been performed.

We have calculated the heat of formation of 3 impurity sites for Sn in Ge: the S site, the T site and the occupied site in the Sn-vacancy complex after complete relaxation (S+V). The latter complex can be expected to occur since ion implantation produces a large amount of vacancies, which are mobile at room temperature in Ge[23] and may be trapped by impurities. The heats of formation reported in Tab. I are calculated according to

$$\Delta H_f = E_{sup}^{imp} - \mu_{imp} - \left(32E_{sup}^{id} - n\mu_{Ge}\right) \tag{1}$$

where E_{sup}^{imp} is the total energy of a 63- or 64-atom supercell that contains the impurity, E_{sup}^{id} is the total energy of a pure Ge unit cell (diamond structure, 2 atoms), μ_{Ge} is the chemical potential of Ge (taken equal to the total energy per atom in bulk Ge), n is the number of Ge atoms in

	ΔH_f	d	$\delta_{0(theo)}$	$\Delta E_{Q(theo)}$	MB	$\delta_{(exp)}$	$\Delta E_{Q,0(exp)}$
	(eV)	(%)	(mm/s)	(mm/s)	line nr	(mm/s)	(mm/s)
S	0.18	+4.9	1.75	0.00	2	1.90	0.00
T	3.96	+8.2	3.19	0.00	4	3.27	0.00
S+V (BC)	1.86	-5.8	2.24	0.15	3	2.36	0.30
					1	1.41	

TABLE I: Heats of formation ΔH_f (eV), the relative displacements d (%) of the first nearest neighbor shell with respect to the initial configuration, the calculated isomer shift $\delta_{0(t)}$ (mm/s) and the quadrupole splitting $\Delta E_{Q,0(t)}$ (mm/s) for the 3 relaxed impurity environments considered in this work. A comparison is made to the experimental isomer shift $\delta_{0(e)}$ (mm/s) and quadrupole splitting $\Delta E_{Q,0(e)}$ (mm/s) as deduced from the 4 Mössbauer lines in Refs 16–19.

the ideal 64-atom supercell that are replaced by either vacancies or impurities ($n = 1, 2$) and μ_{imp} is the chemical potential of Sn (taken equal to the total energy per atom in bulk α-Sn). The Ge lattice constant was optimized and fixed for the 64-atom cells, but all atoms in those supercells were allowed to move to their equilibrium positions. The calculations were done by the APW+lo method[30] within Density Functional Theory[31], as implemented in the WIEN2k code[32,33]. The Perdew-Burke-Ernzerhof[34] exchange-correlation functional was used, the k-space sampling was done on a 4×4×4 mesh in the 64-atom cell, and a basis set corresponding to $K_{max} = 3.5$ a.u. was taken. The influence of the size of the supercell (up to 256 atoms) on the calculations was verified and found to be negligible. In this way, the suggestions of Coutinho *et al.* are taken into account, i. e. increasing the number of k-points and the size of the supercell[21], with respect to the calculations by Höhler *et al.* Calculations for the Sb-vacancy complex, not shown here, result in a configuration with the Sb atom on a site halfway between the S and the BC site, in accordance with Coutinho *et al.* and opposed to the results from Höhler *et al.*, supporting the reliability of our results.

V. DISCUSSION

After relaxation of the configuration with the impurity on the S or the T site, small relative displacements of the surrounding Ge atoms were found as can be seen from Tab. I. The oversized Sn atom induces a local lattice expansion, when located on the T site as well as on the S site. Adding a vacancy to the substitutional impurity (S+V), induces a large force on the Sn atom along the ⟨111⟩-direction, resulting in the impurity on the ideal 6-fold coordinated BC site with the vacancy *split over* the nearest neighbor positions: the *split-vacancy* configuration. Although having a different k-point sampling method and an increased supercell size, these results are in agreement with what was found by Höhler *et al*[20]. As can be seen from Tab. I, the nearest neighbor distance in this configuration is considerably reduced with respect to the starting configuration. Since the transition metals Fe, Cu and Ag, as well as the acceptor In were experimentally observed and calculated to be on the BC site in the impurity-vacancy complex in Ge, a more general trend can be expected for the transition metals, group III and group IV elements. Preliminary results of similar calculations for group V elements indicate that this trend can not be generalized for all impurities in Ge[35], in accordance with the results of Coutinho *et al.*[21].

By comparing the heats of formation in Tab. I, it is clear that the Sn atoms prefer the S site to the T or the BC site. This is consistent with previous experiments, with our emission channeling results and with what one would expect for isovalent impurities. At first sight, this contradicts the experimental observation of the BC site. The following arguments show this is not true, however. We calculated the heat of formation for a single neutral vacancy in Ge to be 2.23 eV (in agreement with Ref. 36). The total energy needed to have an impurity on the S site and an isolated vacancy not bound to it (0.18 eV + 2.23 eV = 2.41 eV) is significantly larger than the heat of formation of the BC configuration of the Sn-vacancy complex (1.86 eV). This result is in agreement with the attractive interaction between Sn atoms and vacancies found by

Riihimäki *et al.*[13]. Therefore, substitutional Sn atoms will trap the abundantly available mobile vacancies created during implantation, and – as the structural relaxation process in our calculations shows – will spontaneously evolve into the BC site. Consequently, we can conclude that our experimental results are well corroborated by the presented calculations.

Additionally, we have calculated the isomer shift (relative to $CaSnO_3$) and the electric field gradient for neutral Sn atoms in the three considered configurations (S, T and BC), to allow comparison to the Mössbauer experiments. In Ref. 16–19, four Mössbauer resonances were identified; their hyperfine parameters are listed in Tab. I. The lines 2 and 4 were assigned to Sn atoms on the S and T site, respectively. These assignments are in good agreement with our calculated hyperfine parameters for these sites. The hyperfine parameters of the bond-centered Sn atoms (S+V in Tab. I), are in good agreement with line 3 from the Mössbauer spectra, in disagreement with the tentative assignment of this line to the Sn-vacancy complex in the full-vacancy configuration in the Mössbauer literature[17–19]. Our calculations indicate that the Sn-vacancy complex in the split-vacancy configuration has been measured indirectly before, without having been identified as such. As a quality check, we note that the isomer shift values calculated by Höhler – i. e. 1.88 mm/s for substitutional Sn and $2.16 - 2.19$ mm/s for Sn in the split-vacancy configuration[20] – are in good agreement with our results. Line 1, as observed in the Mössbauer spectra, has been tentatively assigned to Sn in the split-vacancy configuration[17–19], in disagreement with our calculations.

VI. CONCLUSION

We have determined the structural configuration of the Sn-vacancy complex from emission channeling experiments combined with theoretical calculations. The majority of the isovalent Sn impurities are found to be located substitutionally (S), although a significant fraction ($\sim 15\%$)

of the Sn atoms was found on the bond-centered (BC) site. Backed up by ab-initio density functional calculations, we have been able to assign the bond-centered Sn atoms to the impurity-vacancy complex in the split-vacancy configuration. Moreover, calculations of the hyperfine parameters of this defect indicate that this Sn-vacancy defect complex has probably been present in Mössbauer experiments before, without having been identified as such. In this work, we have presented strong evidence, both experimentally as well as theoretically, that the Sn-vacancy defect prefers the split-vacancy configuration. This result contributes to the study of Sn-diffusion and self-diffusion in Ge, as well as to the study of simple point defects in elemental group IV semiconductors.

Acknowledgments

This work was supported by the Fund for Scientific Research, Flanders (FWO G.0501.07 and G.0636.08), the Concerted Action of the K.U.Leuven (GOA/2009/006), the Inter-University Attraction Pole (IUAP P6/42), the Center of Excellence Programme (INPAC EF/2005/005), the Portuguese Foundation for Science and Technology (CERN-FP-83506-2008) and the ISOLDE collaboration. S. D. acknowledges his fellowship from FWO, Flanders.

[1] R. Hull and J. C. Bean, *Germanium Silicon: Physics and Materials, Semiconductors and Semimetals*, Academic, San Diego (1999).

[2] C. C. Yeo, B. J. Cho, F. Gao, S. J. Lee, M. H. Lee, C. Y. Yu, C. W. Liu, L. J. Tang, and T. W. Lee, IEEE Electron Dev. Lett. **26**, 761 (2005).

[3] Y. J. Yang, W. S. Ho, C. F. Huang, S. T. Chang, and C. W. Liu, Appl. Phys. Lett. **91**, 102103 (2007).

[4] S. M. Hu, Phys. Status Solidi (B) **60**, 595 (1973).

[5] A. Harwit, P. R. Pukite, J. Angilello, and S. S. Iyer, Thin Solid Films **184**, 395 (1990).

[6] R. A. Soref and C. H. Perry, J. Appl. Phys. **69**, 539 (1990).

[7] G. He and H. A. Atwater, Phys. Rev. Lett. **79**, 1937 (1997).
[8] V. R. D'Costa, C. S. Cook, A. G. Birdwell, C. L. Littler, M. Canonico, S. Zollner, J. Kouvetakis, and M. J., Phys. Rev. B **73**, 125207 (2006).
[9] J. D. Sau and M. L. Cohen, Phys. Rev. B **75**, 045208 (2007).
[10] P. Kringhøj and R. G. Elliman, Appl. Phys. Lett. **65**, 324 (1994).
[11] M. Friesel, U. Sodervall, and W. Gust, J. Appl. Phys. **78**, 5351 (1995).
[12] I. Riihimäki, A. Virtanen, S. Rinta-Anttila, P. Pusa, J. Räisänen, and the ISOLDE Collaboration, Appl. Phys. Lett. **91**, 091922 (2007).
[13] I. Riihimäki, A. Virtanen, H. Kettunen, P. Pusa, J. Räisänen, and the ISOLDE Collaboration, Appl. Phys. Lett. **90**, 181922 (2007).
[14] A. Chroneos, Phys. Status Solidi (B) **244**, 3206 (2007).
[15] A. Chroneos, H. Bracht, R. W. Grimes, and B. P. Uberuaga, Appl. Phys. Lett. **92**, 172103 (2008).
[16] G. Weyer, A. Nylandsted-Larsen, B. I. Deutch, J. U. Andersen, and E. Antoncik, Hyperf. Int. **1**, 93 (1975).
[17] S. Damgaard, A. F. F. Olesen, P. J. W., and G. Weyer, Physica Scripta **22**, 640 (1981).
[18] G. Weyer, S. Damgaard, J. W. Petersen, and J. Heinemeier, Phys. Lett. **76A**, 321 (1980).
[19] G. Weyer, J. W. Petersen, and S. Damgaard, Hyperf. Int. **10**, 775 (1981).
[20] H. Höhler, N. Atodiresei, K. Schroeder, R. Zeller, and P. H. Dederichs, Phys. Rev. B **71**, 035212 (2005).
[21] J. Coutinho, S. Öberg, V. J. B. Torres, M. Barroso, R. Jones, and P. R. Briddon, Phys. Rev. B **73**, 235213 (2006).
[22] G. D. Watkins, Phys. Rev. B **12**, 4383 (1975).
[23] H. Haesslein, R. Sielemann, and C. Zistl, Phys. Rev. Lett. **80**, 2626 (1998).
[24] S. Decoster, B. De Vries, A. Vantomme, U. Wahl, and J. G. Correia, Appl. Phys. Lett. **93**, 141907 (2008).
[25] S. Decoster, S. Cottenier, B. De Vries, H. Emmerich, U. Wahl, J. G. Correia, and A. Vantomme, Phys. Rev. Lett. **102**, 065502 (2009).
[26] S. Decoster, B. De Vries, A. Vantomme, U. Wahl, and J. G. Correia, J. Appl. Phys. **105**, 083522 (2009).
[27] U. Wahl, J. G. Correia, A. Czermak, S. G. Jahn, P. Jalocha, J. G. Marques, A. Rudge, F. Schopper, J. C. Soares, A. Vantomme, et al., Nucl. Instrum. Methods Phys. Res. A **524**, 245 (2004).
[28] U. Wahl, Phys. Rep. **280**, 145 (1997).
[29] H. Hofsäss and G. Lindner, Phys. Rep. **201**, 121 (1991).

[30] E. Sjöstedt, L. Nordström, and D. J. Singh, Solid State Commun. **114**, 15 (2000).

[31] P. Hohenberg and W. Kohn, Phys. Rev. **136**, 864 (1964).

[32] S. Cottenier, (Instituut voor Kern- en Stralingsfysica, KULeuven, Belgium) (2002), (freely available from http://www.wien2k.at/reg_user/textbooks), ISBN 90-807215-1-4.

[33] P. Blaha, K. Schwarz, G. Madsen, D. Kvasnicka, and J. Luitz, (Karlheinz Schwarz, Techn. Universität Wien, Austria) (1999), ISBN 3-9501031-1-2.

[34] J. P. Perdew, K. Burke, and M. Ernzerhof, Phys. Rev. Lett. **77**, 3865 (1996).

[35] S. Cottenier, S. Decoster, and A. Vantomme, unpublished (2009).

[36] J. Vanhellemont, P. Spiewak, and K. Sueoka, J. Appl. Phys. **101**, 036103 (2007).

PUBLICATION LIST

- **Electrical characterization of defects introduced in *n*-type Ge during indium implantation**
  F. D. Auret, P. J. Janse van Rensburg, M. Hayes, J. M. Nel, W. E. Meyer, S. Decoster, V. Matias and A. Vantomme
  *Applied Physics Letters **89**, 152123 (2006)*

- **Electrical characterization of defects in heavy-ion implanted *n*-type Ge**
  F. D. Auret, P. J. Janse van Rensburg, M. Hayes, J. M. Nel, S. Coelho, W. E. Meyer, S. Decoster, V. Matias, A. Vantomme and D. Smeets
  *Nuclear Instruments and Methods in Physics Research B **257**, 169 (2007)*

- **Hydrogen-induced Ostwald ripening at room temperature in a Pd nanocluster film**
  M. Di Vece, D. Grandjean, M. J. Van Bael, C. P. Romero, X. Wang, S. Decoster, A. Vantomme, and P. Lievens
  *Physical Review Letters **100**, 236105 (2008)*

- **Experimental evidence of tetrahedral interstitial and bond-centered Er in Ge**
  S. Decoster, B. De Vries, U. Wahl, J. G. Correia and A. Vantomme
  *Applied Physics Letters **93**, 141907 (2008)*

- **Transition metal impurities on the bond-centered site in germanium**
  S. Decoster, S. Cottenier, B. De Vries, H. Emmerich, U. Wahl, J. G. Correia and A. Vantomme
  *Physical Review Letters **102**, 065502 (2009)*

- **Lattice location study of implanted In in Ge**
  S. Decoster, B. De Vries, U. Wahl, J. G. Correia and A. Vantomme
  *Journal of Applied Physics **105**, 083522 (2009)*

- **Effect of fluence on the lattice site of implanted Er and implantation induced strain in GaN**
  U. Wahl, B. De Vries, S. Decoster, A. Vantomme and J. G. Correia
  *Nuclear Instruments and Methods in Physics Research B **267**, 1340 (2009)*

- **Changing the three dimensional magnetization exchange coupling of mixed Fe and V nanoclusters with hydrogen**
  V. Valev, M. Van Bael, D. Grandjean, S. Decoster, A. Vantomme, T. Verbiest and P. Lievens
  *Journal of Applied Physics **105**, 114907 (2009)*

- **Direct evidence for Sb as a Zn site impurity in ZnO**
  U. Wahl, J. G. Correia, T. Mendonça and S. Decoster
  Accepted for publication in Applied Physics Letters (2009)

- **Implantation-induced damage in Ge: Strain and disorder profiles during defect accumulation and recovery**
  S. Decoster and A. Vantomme
  Submitted to Journal of Physics D: Applied Physics (2009)

- **Lattice location study of ion implanted Sn and Sn-related defects in Ge**
  S. Decoster, S. Cottenier, U. Wahl, J. G. Correia and A. Vantomme
  In preparation for submission to Physical Review B